THÈSE DE DOCTORAT DE

L'INSTITUT NATIONAL DES
SCIENCES APPLIQUÉES RENNES
co-tutelle avec
INSTITUT DE TECHNOLOGIE DU CAMBODGE

ÉCOLE DOCTORALE N° 602
Sciences pour l'Ingénieur
Spécialité : *Génie Civil*

Par
Sokvisal MOM

Multi-scale modeling of thermal properties of cement-based materials

Thèse présentée et soutenue à INSA Rennes, le 20 décembre 2022
Unité de recherche : Laboratoire Génie Civil et Génie Mécanique (LGCGM), Material Sciences and Structure (MSS)
Thèse N° : 22ISAR 43 / D22 - 43

Rapporteurs avant soutenance :

Joseph ABSI	Professeur des Universités, Université de Limoges
Eric GARCIA-DIAZ	Professeur de l'IUT, École des Mines d'Alès
Sophy CHHANG	Enseignant, Institut de Technologie du Cambodge

Composition du Jury :

Président :	Farid BENBOUDJEMA	Professeur des Universités, École normale supérieure Paris-Saclay
Examinateurs :	Joseph ABSI	Professeur des Universités, Université de Limoges
	Eric GARCIA-DIAZ	Professeur de l'IUT, École des Mines d'Alès
	Sophy CHHANG	Enseignant-chercheur, Institut de Technologie du Cambodge
	Ali ZAOUI	Professeur des Universités, Université de Lille
Dir. de thèse :	Fabrice BERNARD	Maître de Conférences HDR, INSA Rennes
Co-dir. de thèse :	Virak HAN	Enseignant-chercheur, Institut de Technologie du Cambodge
Encardrant de thèse :	Siham KAMALI-BERNARD	Professeur des Universités, INSA Rennes
Invité :	Frédéric GRONDIN	Professeur des Universités, École Centrale de Nantes

ACKNOWLEDGEMENT

The two opening pages of this manuscript were the last to be completed during my dissertation study. It is my opportunity to express gratitude to everyone I have met who has accompanied, supported, mentored, and advised me in person and remotely. Thus, these two initial pages are meaningful to me.

First and foremost, I would like to convey my heartfelt gratitude to my dissertation supervisors, Fabrice BERNARD, Virak HAN, and Siham KAMALI-BERNARD, for their patience, motivation, encouragement, and immersive knowledge. Their wealth of experience has boosted my confidence to develop my academic research and to achieve this result. At the end of this dissertation, I can only realize the privilege I had of being able to work alongside them. For this, I would like to thank them and I can only wish to be able to continue working with them in my future career as a researcher.

I am very grateful to prof. Joseph ABSI, prof. Eric GARCIA-DIAZ, Dr. Sophy CHHANG, prof. Ali ZAOUI, prof. Farid BENBOUDJEMA, and prof. Frédéric GRONDIN for accepting being the reporters, examiners, and invited guest of my dissertation presentation, for having taken the time to read and analyze this manuscript, for their feedback, their questions, and encouragement which allow me to reflect and foresee my future research. I would like to thank prof. Thierry GLORIANT and again to prof. Frédéric GRONDIN for being the thesis monitoring committee since the first year of the dissertation.

I could not have taken this journey without financing organizations such as the French Embassy in Cambodia, the Ministry of Education, Youth, and Sport of Cambodia, Erasmus+, and the Laboratory of Mechanical and Civil Engineering (LGCGM). I am deeply grateful to these organizations for their financial support. I also would like to thank my institutes, INSA Rennes and ITC, as well as the laboratory, LGCGM, and research unit, MSS, for providing me with a priceless opportunity to facilitate my research at the institute.

I would like to express my most profound appreciation to Sela HOUEN and Chanbrosoeu MEAS, who have helped me during their Master 2 internships. Suppose I had been able to highlight the results of a relatively substantial numerical modeling in this

manuscript; in that case, I could never have done it without their help. The quality of their work, humanity, knowledge, efficiency, and ability to analyze the results have enabled me to excel in my research and contribute the results in scientific journals as well as in this manuscript. I would to extend my sincere thanks to Raveth HIN and my friend, Panha MENH, for helping me with codings such as Python, VBA, and Fortran. I also would like to credit Abderrahmane RHARDANE for his advice on take-and-place method.

I would be remiss not to mention my PhD colleagues who I have met frequently such as Nelson ALVARADO, Simon GUIHÉNEUF, Lina AMMAR, Pengzhi WANG, Josue YOKOPI, Elodie PIOLET, Malang BODIAN, Noubough ALHAJ SLEIMAN, Prince Momar GUEYE, Run Qi HAO, Marwan JOHRA, and Lei LI. I would like to thank my friends, Jérôme CLAVERIE, Boyuan YANG, and Camille FOLLET and my compatriots, Davin SANG, Sounean HENG, Piseth HENG, Lynita SAROU, Theany TO, Rithymarady HORM, Pisey KEO, Thaileng OENG, Rathanarainsey HOK, Khunpanha HEM, Sereyvathana SOK, Try MENG, Khundadino LENG, Vanthet OUCH, Borivath TAN, Loby HENG, Bunpo EAR and many others for being around while I am doing my PhD in France. I am so thankful for this friendship and you are the one that I can go to when everything else seems hard or impossible in my life.

I would like to thank my wonderful parents, Sokany MOM and Sreymom ROS for supporting me in all the good and bad times. Thank you for making me believe that I can do anything and everything in life. All I want to be in life is a good parent like you so that I can raise my children just the way you two have raised me. Thank you, mom and dad! I cannot forget my beloved younger brother and sister, Attitya MOM and Sokanyta MOM, for always being my good siblings.

Lastly, words cannot express my gratitude to my only woman, Yeakleang MUY who has been very supportive to me over the last 10 years. For no reason, and for all reasons, I have to thank you for your patience, encouragement, understanding, care, and protection toward me. I want to thank you for everything. Today and always, beyond tomorrow, we are together and forever soul mate.

Finally, I would like to mention that without their tremendous support and encouragement in the past few years, especially, when our society experienced the worst health crisis, it would not be possible for me to complete this dissertation.

TABLE OF CONTENTS

Introduction **1**

1 Literature Review **5**

1.1 Cement-based materials 5

1.1.1 Cement-based materials composition 5

1.1.1.1 Chemical composition and groups of **CEM** cement 5

1.1.1.2 Hydration of Portland Cement 7

1.1.1.3 Aggregate 8

1.1.1.4 Internal Transition Zone (**ITZ**) 11

1.1.1.5 Additives and admixtures 13

1.1.2 Cement hydration and microstructure development 14

1.1.2.1 Cement hydration kinetic 14

1.1.2.2 The heat of cement hydration 17

1.1.2.3 Microstructure development 18

1.2 Multi-scale modeling 19

1.2.1 Cement-based materials at different scale 19

1.2.2 Homogenization for continuum mechanics 23

1.2.2.1 Analytical homogenization 23

1.2.2.2 Numerical homogenization 26

1.2.2.3 Geometry generation 26

1.2.2.4 Take-and-place method 30

1.2.2.5 Representative Volume Element (**RVE**) 31

1.2.2.6 Multi-scale Modeling of Computational Concrete (**MuMoCC**) 32

1.3 Heat transfer problem 33

1.3.1 Volumetric mass density of cement-based materials 34

1.3.2 Thermal properties of cement-based materials 34

1.3.2.1 Thermal conductivity 35

1.3.2.2 Specific heat 35

1.3.2.3 Coefficient of thermal expansion (coefficient of dilatation) 36

1.3.3 Thermal Contact Conductance (**TCC**) effect on heat transfer problem 37
1.3.3.1 Domain of application . . . 38
1.3.3.2 Interface parameters . . . 39
1.3.3.3 Existing theoretical and experimental analyses of TCC . . 39
1.4 Massive concrete structure problem and solution . . . 40
1.4.1 Early-age crack . . . 42
1.4.1.1 Internal heat generation . . . 42
1.4.1.2 Restraint in massive concrete structure . . . 43
1.4.2 Solutions to the problem . . . 45

2 Theoretical framework, hypotheses, and homogenization 48
2.1 Cement-based materials . . . 48
2.1.1 Cement paste . . . 48
2.1.2 Mortar . . . 49
2.2 Heat transfer in Multi-scale Modeling of Computational Concrete (MuMoCC) 50
2.2.1 Analytical homogenization . . . 50
2.2.2 Numerical homogenization . . . 51
2.2.2.1 Cement paste representative volume element . . . 51
2.2.2.2 Take-and-place methods . . . 52
2.2.2.3 Heat transfer simulation with Abaqus FEA . . . 56
2.2.3 Thermal properties of cement-based materials . . . 58
2.3 Thermal conductivity of cement-based materials . . . 58
2.3.1 Analytical homogenization of thermal conductivity . . . 58
2.3.2 Numerical homogenization of thermal conductivity . . . 61
2.3.2.1 Initial, boundary conditions, and thermal conductivity calculation . . . 61
2.3.2.2 Verification of Representative Volume Element (RVE) . . 62
2.3.2.3 Results from numerical simulation . . . 63
2.3.3 Conclusion . . . 64
2.4 Specific heat of cement-based materials . . . 65
2.4.1 Analytical homogenization of specific heat . . . 65
2.4.2 Numerical homogenization of specific heat . . . 68
2.4.2.1 Analytical approach in heat conduction problem . . . 68
2.4.2.1.1 Equation of heat conduction problem . . . 68

2.4.2.1.2 Initial and boundary conditions 68
2.4.2.1.3 Fourier solution 69
2.4.2.2 Numerical approach in heat conduction problem 69
2.4.2.3 Fitted curve analysis (inverse analysis) for specific heat . . 71
2.4.3 Results and discussion 72
2.5 Coefficient of thermal expansion (coefficient of dilatation) 74
2.5.1 Analytical homogenization of coefficient of thermal expansion . . . 74
2.5.2 Numerical homogenization of coefficient of thermal expansion . . . 76
2.5.2.1 Thermo-mechanical sequential simulation 76
2.5.2.2 Thermo-mechanical coupled simulation 77
2.5.3 Results and discussion 79
2.5.4 Comparison with analytical homogenisation methods and discussion 80
2.6 The effect of Thermal Contact Conductance (TCC) on thermal conductivity 81
2.6.1 Analytical formulation for TCC 81
2.6.2 Numerical simulation for TCC 82
2.6.3 TCC influence on cement-based materials 82
2.6.4 TCC estimation with numerical simulation 85
2.6.5 Result and discussion on TCC 89
2.7 Conclusion 93

3 Application **96**
3.1 The influence of crack on thermal conductivity 96
3.1.1 Brief presentation of the hypotheses of the mechanical simulations . 97
3.1.2 Crack characteristic under compression and tension 98
3.1.3 Heat transfer simulation respect to crack's orientation 101
3.1.3.1 Thermal conductivity of mortar under compression 101
3.1.3.2 Thermal conductivity of mortar under tension 102
3.1.4 Conclusion - Influence of crack on thermal conductivity of cement-based materials 103
3.2 The influence of specific heat on heat evolution in massive concrete 103
3.2.1 Materials properties 104
3.2.2 Geometries of massive concrete 105
3.2.3 Initial and boundaries conditions 106
3.2.4 Cumulative heat and rate of hydration heat 107

3.2.5 Implement hydration heat rate in Abaqus FEA 108
3.2.6 Primary results and discussion 109
3.2.6.1 Temperature evolution inside the concrete block 109
3.2.6.2 Influence of specific heat on temperature development inside concrete 110
3.2.6.3 Influence of initial temperature on the maximum temperature of concrete 111
3.2.7 Equivalent age concrete of massive concrete 113
3.2.8 Thermal stress 115
3.2.8.1 Stress and strain curve from *fib*'s model 116
3.2.8.2 Concrete Damage Plasticity (CDP) model 123
3.2.8.3 Time-dependant Mechanical properties 127
3.2.9 Result and discussion 128
3.3 Conclusion 130

Conclusion **132**

Bibliography **139**

List of Figures

1.1 Cement fabrication 6
1.2 Rock type 8
1.3 The process of **NA** manufacturing 9
1.4 The process of **RA** manufacturing 10
1.5 Apparent activation energy $\mathbf{E_a}$ at different temperatures 17
1.6 Hydration heat and strength development of concrete 18
1.7 CEMHYD3D flow diagram 19
1.8 Cubic model of Calcium oxide (**CaO**) and Magnesium oxide (**MgO**) 20
1.9 Hexagonal model of Portlandite (**CH**) and Calcite ($\mathbf{CaCO_3}$) 20
1.10 A monoclinic polymorph of Alite ($\mathbf{C_3S}$) unit cell 20
1.11 Image of hardened cement paste with different water to cement ratio (**W/C**) obtained from Scanning Electron Microscopy (**SEM**) 21
1.12 Image of **CH** and **C-S-H** obtained from Scanning Electron Microscopy (**SEM**) 21
1.13 **ITZ** at the interface of bulk cement paste and aggregate 22
1.14 **ITZ** at the interface of mortar and aggregate 22
1.15 Upper bound of Voigt 23
1.16 Lower bound of Reuss 24
1.17 Maxwell 24
1.18 Rayleigh 25
1.19 Hashin-Shtrinkman 25
1.20 **XCT** scanning system 27
1.21 2D cross section of cement paste from **CEMHYD3D** 27
1.22 **DEM** result validation with experimental result 28
1.23 Concrete geometry generation by Voronoi cells 29
1.24 Lattice network of a continuous model 29
1.25 **XCT** scanning for pseudo-3D model 30
1.26 Pseudo-3D mesoscale of concrete 30
1.27 Take-and-place with zone of influence by Rhardane 31

1.28 Multi-scale Modeling of Computational Concrete (**MuMoCC**) platform . 32
1.29 Thermal conductivity and density of hemp concrete 34
1.30 Heat flow at the interface 37
1.31 Temperature drop at the interface 38
1.32 Massive concrete structure examples 41
1.33 Heat transfer in massive concrete 41
1.34 Accumulated hydration heat and rate 43
1.35 Thermal stress-strain diagram 44
1.36 Normal stress structural member 44
1.37 Flexural stress structural member 45
1.38 Restraint by supports 45
1.39 Influence of aggregate on thermal expansion of concrete 46
1.40 Cooling the concrete truck by injecting nitrogen 47
1.41 Post cooling concrete pipe layouts in different type of structure 47

2.1 Morphology of cement-based materials for analytical homogenisation . . . 50
2.2 FEM meshes of cement paste imported from **CEMHYD3D** with different degrees of hydration (α) 52
2.3 FEM meshes of mortar imported from **CEMHYD3D** 52
2.4 Fuller's grading curve 53
2.5 Methodology of original take-and-place (Method A) 54
2.6 Methodology of improved take-and-place method proposed by Rhardane . 55
2.7 Original take-and-place (Method A) 55
2.8 Take-and-place by Rhardane (Method B) 56
2.9 Algorithms for Finite Element Analysis 57
2.10 Thermal Conductivity of cement paste in function of hydration degree for various homogenisation schemes 59
2.11 Thermal Conductivity of mortar in function of hydration degree for various homogenisation schemes 59
2.12 Analytical result of thermal conductivity in function of saturation degree . 60
2.13 Initial and boundary conditions for thermal conductivity calculation 61
2.14 Representative Volume Element's (RVE) size for mortar 62
2.15 Numerical simulation result of thermal conductivity in function of saturation degree 63

2.16 Numerical simulation result of thermal conductivity with different types of sand . . . 64
2.17 Specific heat of cement paste in function of hydration degree . . . 66
2.18 Specific heat of mortar in function of hydration degree . . . 67
2.19 Analytical result of specific heat in function of saturation degree . . . 67
2.20 Initial and boundary conditions for specific heat calculation . . . 69
2.21 Sample for specific heat calculation (hydrated cement paste) . . . 70
2.22 Temperature profile of mortar at α=0.83 . . . 70
2.23 Flowchart for calculating the specific heat . . . 71
2.24 Fitted curve of temperature profile of mortar at α=0.83 . . . 72
2.25 Specific heat from fitted curve analysis . . . 73
2.26 Coefficient of thermal expansion of cement paste in function of hydration degree . . . 75
2.27 Coefficient of thermal expansion of mortar in function of hydration degree 75
2.28 Algorithm for thermo-mechanical sequential simulation in Abaqus FEA . . 76
2.29 Initial and boundary conditions for thermo-mechanical sequential simulation 77
2.30 Algorithm for thermo-mechanical coupled simulation in Abaqus FEA . . . 78
2.31 Initial and boundary conditions for thermo-mechanical coupled simulation 78
2.32 Numerical result of coefficient of thermal expansion in function of saturation degree . . . 79
2.33 Analytical result of coefficient of thermal expansion in function of saturation degree . . . 80
2.34 Maximum paste thickness of two particles under homogeneous dilatation procedure . . . 83
2.35 Simple model with one inclusion . . . 83
2.36 Simple model with 27 inclusions . . . 84
2.37 Flux (a) and temperature (b) profile of the 27 inclusions simple model without TCC . . . 84
2.38 The influence of TCC on thermal conductivity of cement-based material . . 85
2.39 Interface of matrix/aggregates captured by SEM . . . 86
2.40 Interface of matrix/aggregates regenerated in Abaqus/CAE . . . 86
2.41 Interface of paste/inclusion hypotheses for FEM simulation . . . 87
2.42 Temperature profile, temperature drop at variety of interfaces (1/2) 90
2.42 Temperature profile, temperature drop at variety of interfaces (2/2) 91

3.1 Mortar's mesh for finite element modeling 97
3.2 Boundary conditions for mechanical simulation 99
3.3 Mortar meshes with removed elements 99
3.4 Stress and strain curve for compression test 100
3.5 Stress and strain curve for tension test 100
3.6 Thermal conductivity of mortar after crack (compression) 102
3.7 Thermal conductivity of mortar after crack (tension) 103
3.8 Evolution of specific heat in function of time 105
3.9 Geometry of massive concrete block 105
3.10 Boundary conditions for massive concrete simulation 106
3.11 Equivalent exchange coefficient 107
3.12 Accumulative hydration heat and hydration heat rate 108
3.13 Implement of subroutine HETVAL in Abaqus FEA 108
3.14 Temperature evolution at different positions inside concrete block and temperature cartography 109
3.15 Temperature evolution with specific heat constant and varies 110
3.16 Temperature evolution with different initial temperatures 111
3.17 Different temperature between maximum, initial, and surface temperature for each initial temperature 112
3.18 Temperature cartography with different initial temperatures 112
3.19 Time equivalent and temperature at core on concrete in function of time . 114
3.20 Accumulated hydration heat in function of time and equivalent time 114
3.21 Temperature evolution at the core of concrete simulated with t and t_e . . . 115
3.22 Compression stress and strain curve from the *fib*'s codes 117
3.23 Tension stress and strain curve from the *fib*'s codes 119
3.24 Compression stress and strain curve 121
3.25 Tension stress and strain curve 122
3.26 Tension stress and crack opening curve 122
3.27 Concrete Damage Plasticity (CDP) model for tension 123
3.28 Concrete Damage Plasticity (CDP) model for compression 124
3.29 Stress, elastic and inelastic strain for compression 125
3.30 Stress, inelastic strain, and d_c for compression 126
3.31 Stress, crack opening, and d_t for tension 126
3.32 Compressive stress and elastic modulus in function of time 128

3.33 Maximum thermal stress 128
3.34 Thermal stress and tension strength of concrete 129
3.35 Crack status of at the maximum thermal stress 129

List of Tables

1.1 Cement additives classification [104] 14

2.1 Mineralogical composition cement CEM I 42.5 (in %) 49
2.2 Mineralogical compositions and hydration products of cement paste (in %) 49
2.3 Percentage of each sand's diameter 54
2.4 Heat transfer simulation in Abaqus FEA 57
2.5 Thermal properties of cement-based materials' compositions [5], [271]–[275] 58
2.6 Thermal properties of porosity homogenized with regard to saturation degree 60
2.7 Hypotheses for solid-to-solid contact points of TCC 82
2.8 Interface of paste/inclusion hypotheses 87
2.9 Thermal properties of mortar's composition 88
2.10 Thermal properties of cement paste with porosity 88
2.11 Thermal properties of ITZ and bulk cement paste 89
2.12 Temperature drop, thermal conductivity and TCC of each study case (1/2) 92
2.12 Temperature drop, thermal conductivity and TCC of each study case (2/2) 93

3.1 Thermal properties for massive concrete simulation 104
3.2 Constants used in equation 1.34 107
3.3 Maximum temperature inside the concrete block 110
3.4 New constants used in equation 1.34 114
3.5 Mechanical properties calculated for compression curve 120
3.6 Mechanical properties calculated for tension curve 121

INTRODUCTION

General introduction

Cement-based materials are the most widely used material in the construction industry, for instance, building, bridge, road, hydraulic dam, storage, power station, etc., because of the significant benefits it offers in terms of load-bearing capacity, durability, maneuverability, flowability, and many other attributes. Furthermore, although most of these attributes have been widely investigated, they are confined to macroscopic mechanical properties such as in [1]–[4]. Nevertheless, thermal properties, which also reflect some aspects of the durability of cement-based products, have received little attention [5].

In the context of building energy management and thermal comfort, precise assessment of thermal properties of cement-based materials is critical. Moreover, the thermal properties of cement-based materials are investigated in this PhD thesis. The thermal properties of cement-based materials are thermal conductivity ($\mathbf{k}$), specific heat ($\mathbf{C_p}$), and coefficient of thermal expansion ($\boldsymbol{\alpha}$). These properties are critical for investigating the influence of temperature gradient on the durability of concrete, particularly massive concrete. In massive concrete, there are two different kinds of thermal gradients that are significant: one of them is relative to time, which means that the temperature at a specific point of the structure changes throughout its lifetime; and the other kind is a spatial gradient that corresponds to the difference in temperature that exists between two different points of the structure at a specific point in time [6].

To get a better knowledge of conduction phenomena, it is pertinent to separate the cement-based materials into components and facets and investigate heat transfer through each of them to determine the relative relevance and contribution of component heat transfer to the overall thermal properties of the cement-based materials [7]. Moreover, in order to represent the heterogeneity of cement-based materials, such as concrete, mortar and cement paste, the hierarchical multi-scale modelling approaches are adopted. The hierarchical multi-scale modelling of cement-based materials consists of several scales such as mesoscale, sub-mesoscale, microscale, and nanoscale [5]. For instance, the nanoscale is the scale of elements cells of hardened cement paste's components; the microscale

is the scale of hardened cement paste consisting of Calcium Silicate Hydrates (**C-S-H**), Portlandite (**CH**), Ettringite (**AFt**), and Monosulfoaluminate (**AFm**); the sub-mesoscale is the scale of mortar which has the finest fraction of aggregates connected by cement paste; the mesoscale is the scale of concrete that has the largest fraction of aggregates embedded in the mortar.

Computational techniques (numerical modeling) have been suggested as an alternative to experiments for investigating the properties of cement-based materials. Several works have adopted the numerical and multi-scale modelling approaches to study the mechanical properties [8]–[14], thermal properties [5], [15], [16], shrinkage and creep [17]–[21], and durability [9], [10], [12], [22], [23] of cement-based materials. Besides cement-based materials, numerical modeling has also been used elsewhere, such as in bitumen [24]–[27]. In addition, various commercial programs and algorithms were utilized to generate the Representative Volume Element (**RVE**) of cement-based materials for numerical simulations. At microscale, the National Institute of Standards and Technology (**NIST**) developed a three-dimensional Cement Hydration and Microstructure Development model (**CEMHYD3D**) to simulate the microstructure and hydration of cement paste [28]. The **CEMHYD3D** model was well-known and was utilized by various researchers in applications, for example, leaching of mortar [9], [23], [29], Supplementary Cementitious Materials (**SEM**) [30], aggregate's shape analysis [31], etc. Several other models have also been used in this scale such as **HYMOSTRUC** [32]–[39], **HydratiCA** [40]–[45], ***μ*ic** [46]–[50], **PHREEQC** [51], [52], etc. Moreover, these commercial software were also seen used in sub-mesoscale and mesoscale. A detailed review of mesoscale modeling at the sub-mesoscale and mesoscale scales was made [53]. Mesoscale modeling is divided into two categories depending on the application: continuous and discrete approaches. Digital image-based and parameterization modeling approaches are considered continuum methods, while discrete methods include the Discrete Element Method (**DEM**), Rigid Body Spring Model (**RBSM**), and Lattice element methods. Among them, continuum methods are frequently used by researcher, for example, to generate **RVE** of concrete and identify its homogenized thermo-mechanical behavior, a numerical model called Digital Concrete model was utilized and developed using Finite Element (**FE**) code called **SYMPHONIE** [13] and the Finite Element Model for Concrete Analysis Method (**FEMCAM**) was used to construct two-phases concrete made of granular materials embedded in mortar [11]. One of the most popular parameterization modeling approaches is the **take-and-place** method [54]. This method was eventually refined to be more time efficient [55].

A 3D numerical modeling platform, Multi-scale Modelling of Computational Concrete (**MuMoCC**), has been built using a multi-scale approach. It was used to examine the leaching of cement-based materials and utilizes two numerical tools, **CEMHYD3D** from **NIST** and **Abaqus FEA** from **Dassault Systèmes SE** [23], [29], [56]. Furthermore, this platform may be utilized to investigate the mechanical, thermal, and durability properties of cement-based materials. To conclude, the **MuMoCC** was undertaken in this PhD thesis.

Objective and methodology

The objective of this PhD thesis is to use **MuMoCC** to evaluate the temperature properties of cement-based materials at the microscale (cement paste) and sub-mesoscale (mortar), such as thermal conductivity ($\mathbf{k}$), specific heat ($\mathbf{C_p}$), and coefficient of thermal expansion ($\boldsymbol{\alpha}$). In these simulations, the imposed elevation temperature is restricted to no water evaporation. In **MuMoCC**, the results obtained from microscale are used as the input data in sub-mesoscale [5].

Several software, including **CEMHYD3D** and **Abaqus FEA**, will be utilized to model, build the **RVE**, and simulate heat transfer simulation. Furthermore, Microsoft Excel, Visual Basic for Applications (**VBA**), Python, and Fortran will be employed as additional software and programming codes to aid and speed up the modeling and analysis process.

Finally, the multi-scale approach and thermal property assessment are extended to examine the impact of cracking on thermal conductivity and estimate temperature and damage within concrete at a young age.

Manuscript organization

The content for this PhD thesis is structured into three main chapters: literature reviews, theoretical framework and hypothesis, and application. There will be a conclusion with prospects for future study concepts at the end of the manuscript.

In the first chapter, a literature review is presented. This section discusses cement-based materials, multiscale modeling, heat transfer problem, and massive concrete. In the section on cement-based materials, a short explanation is presented about the composition of cement-based materials, hydration, and the formation of their microstruc-

tures. In addition, the definition of cement-based materials and analytical and numerical homogenization methods are also elaborated in multiscale modeling. Along with their thermo-mechanical properties, the thermal properties of cement-based materials are also addressed in this article. In conclusion, a brief literature review on massive concrete is presented to understand the factors that contributed to the formation of cracks inside the massive concrete structure.

This PhD thesis work focuses mainly on the second chapter as its main chapter. This section defines cement-based materials and describes the homogenization methods used in this study. This chapter focuses on the homogenization of the three thermal properties of cement-based materials, including thermal conductivity ($\mathbf{k}$), specific heat ($\mathbf{C_p}$), and coefficient of thermal expansion ($\boldsymbol{\alpha}$). Analytical and numerical homogenization are described in detail in this chapter as two distinct homogenization methods. In the last part, the influence of thermal contact conductance (**TCC**) on the thermal conductivity of materials based on cement is also examined.

The implications of the findings presented in the preceding chapter are discussed in the last chapter. The first discussion is the effect of cracks caused by mechanical stress on the thermal conductivity of cement-based materials. This investigation is the prime importance in the context of building energy control and thermal comfort since cracks are known one of the main cause of energy loss in the building and CO_2 emission into the atmosphere. Second, the investigation of the impact that hydration heat and the specific heat of cement-based materials have on a massive structure is explored.

This manuscript of the PhD thesis includes a conclusion and a perspective on the work done. The conclusion will begin with an analytical and numerical homogenization of the thermal properties of cement-based materials. After that, there will be a discussion on the **RVE** of cement-based materials in heat transfer problem and heat transfer coupled with mechanical problem. The last topic of discussion is the effect mechanical cracks have on the thermal properties of cement-based materials and the impact of the hydration heat of cement-based materials on massive structures. Finally, the perspective paragraph will conclude this manuscript.

Chapter 1

Literature Review

1.1 Cement-based materials

1.1.1 Cement-based materials composition

Cement-based materials are typically defined by the materials in which the binder is cement paste. Cement, which is referred to as **CEM** cement in **NF EN 197-1** [57], is the hydraulic binder that is reacted with water to form a cement paste. Then, the cement paste sets, hardens, and gains strength due to hydration reactions between cement and water. When sand and gravel are added to the cement paste, it produces mortar and concrete.

1.1.1.1 Chemical composition and groups of CEM cement

Cement production consists of several steps, from mining raw materials to crushing and grounding them to cement powder. For instance, natural materials such as limestone, clay, and marl, which are usually composed of **CaO**, **SiO_2**, **Al_2O_3**, **Fe_2O_3**, and a small percentage of other materials, are mined from the environment. This production is a thermal energy-intensive process in which the raw materials are heated in a rotary kiln around 1450°C and then quenched to the ambient temperature [58]. The obtained material, which is called Portland clinker, is then crushed and grounded with small quantity of gypsum to form Portland cement (**CEM I**) as shown in figure 1.1.

According to **NF EN 197-1**, the mineral compositions of the Portland cement clinkers are tricalcium silicates or alite (**$3CaO.SiO_2$** or **C_3S** in cement chemistry notation), dicalcium silicates or belite (**$2CaO.SiO_2$** or **C_2S**), tricalcium aluminate (**$3CaO.Al_2O_3$** or **C_3A**), and calcium aluminoferrite (**$4CaO.Al_2O_3.Fe_2O_3$** or **C_4AF**). In addition to Portland cement clinkers, there are also several other minerals of the **CEM** cement such as granulated blast furnace slag, natural and calcined pozzolana, silicious and calcareous fly ash, burnt shale, limestone, silica fume, and other minor additional constituents.

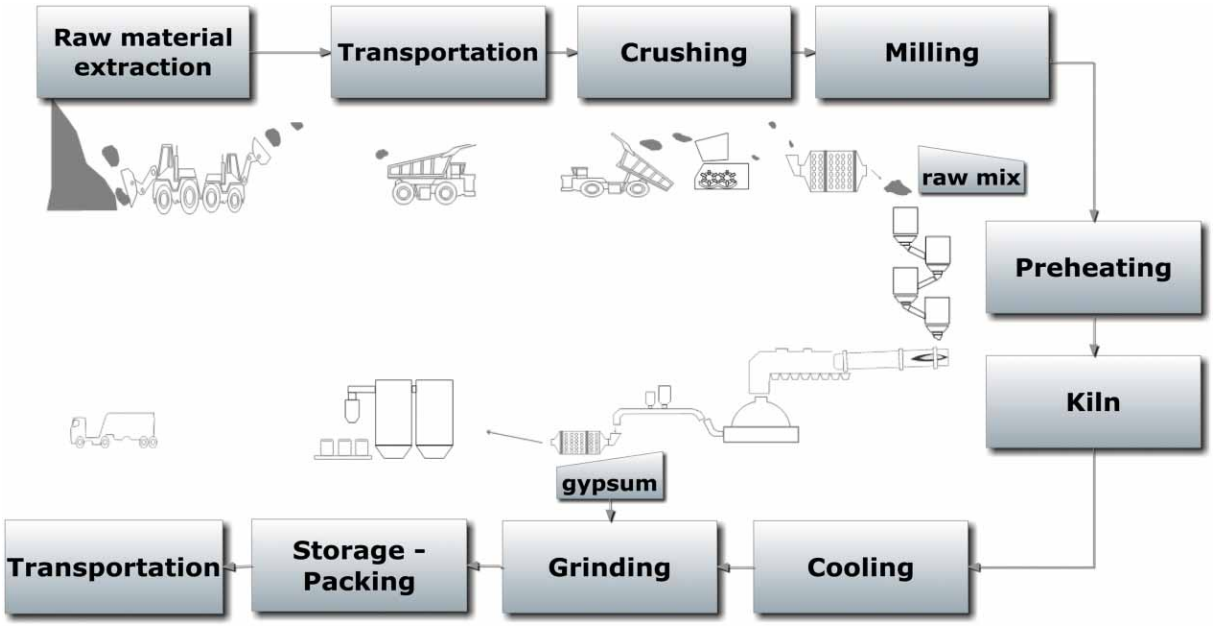

Figure 1.1 – Cement fabrication [59].

There are about 34 types of **CEM** cement, and each type is formed with different percentages of the compositions mentioned above. These **CEM** cements are used for various purposes, and they have been grouped into six main types such as:

- **CEM I**: Portland cement (minimum 95% clinker),
- **CEM II**: Portland-composite cement (minimum 65% clinker and maximum 35% others),
- **CEM III**: Blast furnace cement (5 to 64% clinker and 36 to 95% blast furnace slag),
- **CEM IV**: Pozzolanic cement (45 to 89% clinker and 11 to 55% silica fume, pozzolana, and fly ash),
- **CEM V**: Composite cement (20 to 64% clinker, 18 to 49% blast furnace slag, and 18 to 49% pozzolana and fly ash),
- **CEM VI**: Composite cement (35 to 49% clinker with 6 to 20% of natural pozzolana or siliceous fly ash or limestone) in **NF EN 197-5**.

In addition, the **CEM** cement such as **CEM I**, **CEM III**, and **CEM IV** are also used as sulfate resisting common cement which have a small percentage of $\mathbf{C_3A}$. Apart from these main compositions, researchers are also studying Supplementary Cementitious Materials (**SCMs**) to fully or partially replace the Portland cement clinkers.

1.1.1.2 Hydration of Portland Cement

The hydration of cement occurs immediately when the Portland cement contact water, which means that the cement particle react with the water molecule. The approximate chemical reactions between Portland cement clinkers and water are shown in equations 1.1-1.8 below [60]:

$$C_3S + 6\,H \longrightarrow C{-}S{-}H + CH \tag{1.1}$$

$$C_2S + 4\,H \longrightarrow C{-}S{-}H + CH \tag{1.2}$$

$$C_3A + 6\,H \longrightarrow C_3A \cdot 6\,H \tag{1.3}$$

$$C_3A + 3\,C\bar{S}H_2 + 26\,H \longrightarrow C_6A\bar{S}_3H_{32}\,(\text{ettringite}) \tag{1.4}$$

$$2\,C_3A + C_6A\bar{S}_3H_{32} + 4\,H \longrightarrow 3\,C_4A\bar{S}H_{12}\,(\text{calcium monosulfoaluminate}) \tag{1.5}$$

$$C_4AF + 3\,C\bar{S}H_2 + 30\,H \longrightarrow C_6A\bar{S}_3H_{32} + CH + FH_3 \tag{1.6}$$

$$2\,C_4AF + C_6A\bar{S}_3H_{32} + 12\,H \longrightarrow 3\,C_4A\bar{S}H_{12} + 2\,CH + 2\,FH_3 \tag{1.7}$$

$$C_4AF + 10\,H \longrightarrow C_3A \cdot 6\,H + CH + FH_3 \tag{1.8}$$

These chemical reactions give hydration products such as Calcium silicate hydrate (**C-S-H**), Portlandite (**CH**), ettringite (**AFt**), and monosulfoaluminate (**AFm**), which contribute to the mechanical strength of the cement-based materials [61]. In addition, in these chemical equations, the **C-S-H** is not stoichiometry equilibrium because the state of bound water is not transparent, and it is the reason why there is "-" between C, S, and H. Moreover, these reactions are time-dependent, so cement-based materials develop mechanical strength over time [62].

As far as it is concerned, cement hydration kinetic is divided into five stages: mixing, dormancy, hardening, cooling, and densification [63]. In general, as has been mentioned in the section 1.1.1.1above, each cement type has different mineral compositions, so the hydration kinetics of each type is also different. In 95% of clinkers of **CEM I 52,5 N CE CP2 NF**, for example, there are about 63% of $\mathbf{C_3S}$, 14% of $\mathbf{C_2S}$, 9% of $\mathbf{C_3A}$, and 9% of $\mathbf{C_4AF}$. In addition, the $\mathbf{C_3S}$, which is dominant in Portland cement, has a fast reaction in the first few seconds after the water is added into the cement. It starts to slow down because of the thin metastable layer (or barrier)of **C-S-H** around the surface of $\mathbf{C_3S}$ grain and then begins to accelerate again. Moreover, the $\mathbf{C_3A}$ has a rapid reaction with no slow-down period and an almost instantaneous setting. To coup with this fast setting

of $\mathbf{C_3A}$, gypsum ($\mathbf{CaSO_4.2H_2O}$ or $\mathbf{C\bar{S}H_2}$) is added into the cement and, as a result, it produces ettringite ($\mathbf{C_3A.3CaSO_4.32H_2O}$ or **AFt**) and calcium monosulfoaluminate ($\mathbf{C_3A.3CaSO_4.12H_2O}$ or **AFm**) as the main products [64].

1.1.1.3 Aggregate

As far as cement-based materials are concerned, aggregates, for example, sand, gravel, crushed stone, and fillers, are generally inert materials used to mix with cement paste to produce mortar and concrete. They strongly influences mortar and concrete, such as weight, strength, durability, workability, and price. Aggregates are divided into natural aggregates (**NA**) and Recycled Aggregates (**RA**).

NA originally comes from bedrocks extracted, eroded, transported, and disposed of by weathered fragments and mainly consist of mineral particles and rock fragments. For instance, sand and gravel can be found in natural deposition near streams and rivers [65]. The **NA** are classified into five main categories: igneous rocks, sedimentary rocks, metamorphic rocks, sediments or unconsolidated rocks, and mineral ore (figure 1.2) [66].



(a) (b) (c) (d)

Figure 1.2 – (a) Dark-colored igneous rock (Crushed Trap Rock) [67], (b) Sedimentary rock (Limestone) [68], (c) Metamorphic rock (Pure calcite marble) [69], (d) Unconsolidated rock (gravel) [70].

RA have been used to fully or partially replace the **NA** to reduce the environmental impact of concrete waste [71]–[74]. In such a comprehensive review on **RA** and based on the origin of Construction and Demolition Waste (**CDW**), the **RA** have been classified into four different types as Recycled Concrete Aggregate (**RCA**), Recycled Clay Brick

Aggregate (**RCBA**), Recycled Ceramic Tile Aggregate (**RCTA**), and Reclaimed Asphalt Pavement aggregate (**RAP**) [75]. The replacement level of **RA** in concrete can be up to 100% [76]. The cement-based materials made with **RA** generally have lower compressive strength, lower density, more porous, very absorbent, lower dry shrinkage, less workability, and similar freeze and thaw resistance [77]–[79].

Regardless of their categories, aggregates are supposed to be good quality, clean, and standard range of sizes that require processing technology [80]. For instance, the figure 1.3 describes the process of **NA** manufacturing and reffig:The process of **RA** manufacturing illustrates the **RA** manufacturing process starting from **CDW**. Depending on the use of mortar and concrete, aggregates have been classified for different purposes, such as normal-weight, lightweight, heavyweight, and special aggregates. The commonly used aggregates are normal-weight aggregates, including limestone, quartz, quartzite, sandstone, dolomite, trap rock, and granite.

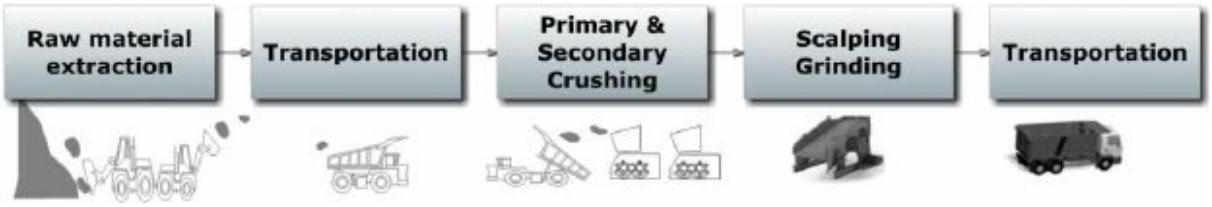

Figure 1.3 – The process of **NA** manufacturing [59].

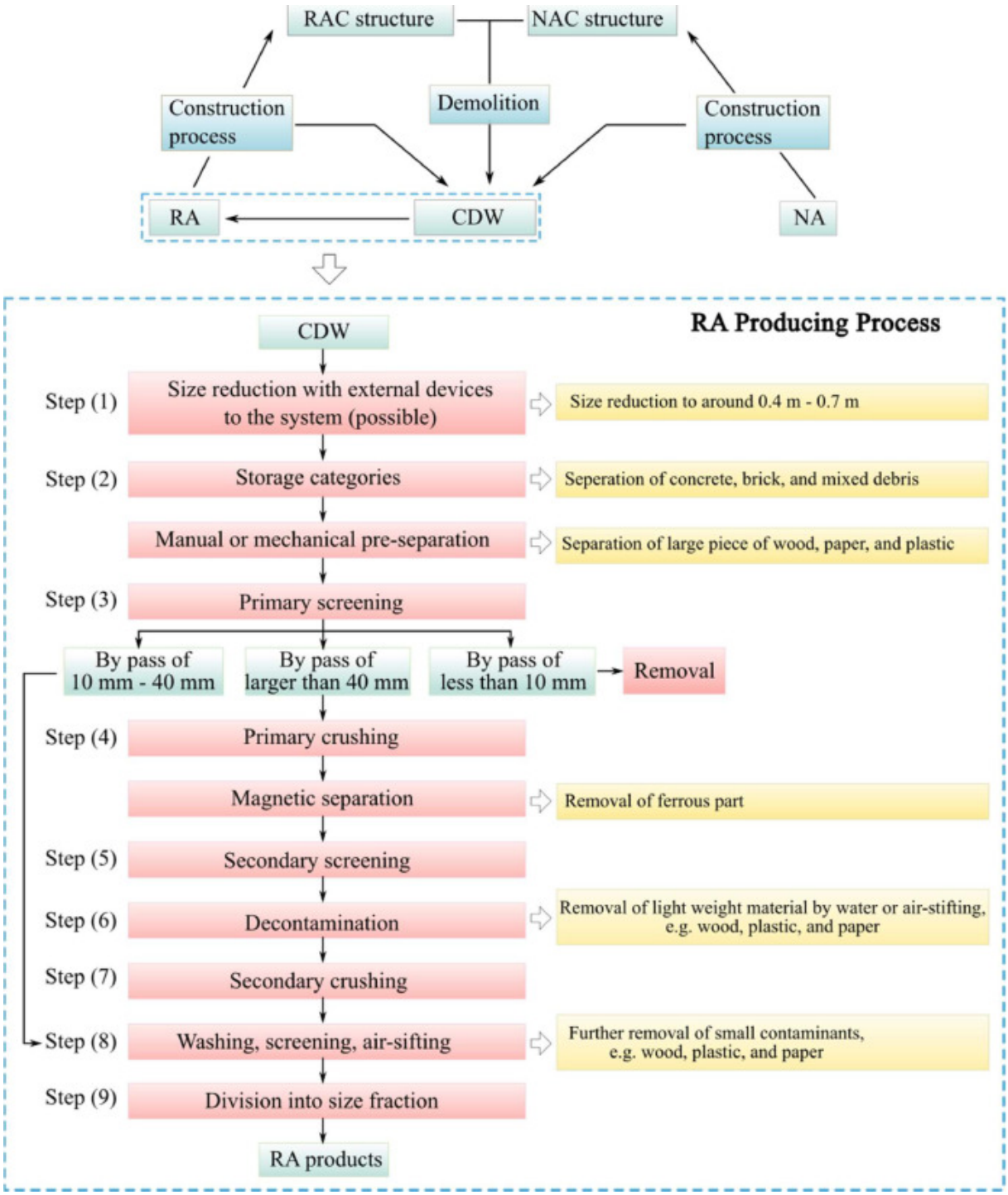

Figure 1.4 – The process of **RA** manufacturing [75].

1.1.1.4 Internal Transition Zone (ITZ)

When aggregates (inclusions) are introduced in cement-based materials (matrix), for instance, cement paste and mortar, there is an effect at the interface between matrix and inclusion called the *wall effect*. This effect leads to abnormal cement grain packing in cement-based materials, which means the small cement grains are close to the aggregate surface and large cement grains are further away. This phenomenon produces a porous band surrounding the aggregate with many parameters, including water/cement ratio, aggregate texture, aggregate roughness, aggregate size distribution, and curing age, which may influence the geometrical and mechanical characteristics [81]. This band is called *Internal Transition Zone* or **ITZ** which is more porous, has a higher **W/C** ratio, has less anhydrous materials, and is filled with a higher concentration of calcium hydroxide ($\mathbf{Ca(OH)_2}$) and ettringite than the bulk cement paste [82]–[85]. The distinction between (original) cement paste, bulk cement paste, and **ITZ** is that when aggregates are added to the actual cement paste, the paste is transformed and separated into two phases: **ITZ** near the aggregates and bulk cement paste further away from the aggregates.

As far as the mechanical properties are concerned, **ITZ** is known as the weakest link in cement-based materials such as mortar and concrete. Based on experimental data, the inverse model presents that the shear and Young's moduli for the **ITZ** are around 50 percent of those of bulk paste [86]. Several authors have studied the significance of the **ITZ** presence on the mechanical properties of cement-based materials. For instance, the results predicted using a conventional method, i.e., the two-phase model (without **ITZ**), revealed a stiffer material than both experimental results and the three-phase model (with **ITZ**) for mortar and concrete. Because of the significant number of aggregates in concrete, the effect of **ITZ** is more critical than in mortar [87]. A quantitative study was conducted to investigate the implications of the **ITZ** thickness choice on the anticipated concrete tensile behavior while considering several meso-scale characteristics such as aggregate shape, maximum aggregate size, **ITZ** strength, and aggregate volume percentage. The study can conclude that the **ITZ** thickness has a significant impact on the tensile behavior of concrete. Still, it is significantly affected by the volume proportion of aggregates and the **ITZ**/mortar strength ratio. Moreover, the aggregate geometry does not influence the tensile strength of concrete [81]. Another researcher demonstrated a novel way of incorporating **ITZ** into concrete modeling. As a result, the impact of the **ITZ** is relatively localized, and the selection of their properties influences the effective mechanical behavior of concrete [88]. With 3D numerical modeling, it is possible to predict

that **ITZ** has little influence on mortar's overall unconfined compression behavior [89]. Another study on the influence of **ITZ** on concrete fracture energy has been conducted, and it suggests that fracture energy decreases as the porosity of **ITZ** increases [90]. The appearance of **ITZ** indeed leads to a more dense cement paste core. Thus, a more significant porosity in **ITZ** is counterbalanced by a lower porosity in the paste core. It is also true that some researches have shown that the aggregate's mineralogical nature effects the aggregate/matrix bond. The influence on mechanical resistances might be significant if the binding is weak [91]. In summary, various research in terms of experimental and modeling has been undertaken to understand the influence of **ITZ** on the mechanical properties of cement-based materials, and the results demonstrate that **ITZ** has little effect on the overall mechanical characteristics of mortar and concrete.

The transport properties of cement-based materials define their durability and include absorption, permeation, and diffusion [92]. A scanning electron microscope (**SEM**) was used for the microstructure examination, which included image analysis of the **ITZ** around the coarse aggregate. The results showed that as the fraction of bigger size aggregate in the mix increased, so did the local porosity at the **ITZ** and the overall durability. It has also been discovered that lowering the average aggregate size in a mix improves the pore structure and increases the concrete's durability [93]. The existence of **ITZ** around aggregates increases the permeability of concrete [94]. Nevertheless, the water porosity can be enhanced by improving the microstructure of **ITZ** using nano-SiO_2, nano-TiO_2, and nano-alumina [95], [96].

A researcher has mentioned that the **ITZ** that forms between the aggregate and matrix allows for faster access and migration of chloride ions, increasing the chloride migration coefficient of concrete [94]. Furthermore, the thickness of the **ITZ**, the quantity of coarse aggregate, and the grade of the coarse aggregate also impact the **ITZ**'s chloride migration, but the water-cement ratio has no effect [97]. The chloride migration coefficient in the mortar was calculated experimentally using an electrochemical approach with regression analytical results. The study found that the approximate **ITZ** migration coefficient varies with thickness, ranging from 1.55 to 2.83 times that of the matrix [98]. By using the accelerated chloride diffusion test, another recent study has shown that the diffusion coefficient in **ITZ** was 74 times greater than the diffusion coefficient in mortar [99]. With thicknesses ranging from 30 to 100 μm, and using an empirical prediction model, the reference chloride diffusion coefficient of **ITZ** was around 8–40 times greater than that of the mortar [100]. Concerning the impact of **ITZ** on chloride migration of mortar, it has

been proven that the volume fraction of aggregate does not affect percolation behavior, such as chloride migration, of cement-based material, although the **ITZ** does [101], [102]. The average value and variance of concrete carbonation depth grow as **ITZ** thickness and porosity increase. Compared to the thickness of **ITZ**, the carbonation depth of concrete is more susceptible to porosity [103].

1.1.1.5 Additives and admixtures

According to European Standard **EN 197-1**, additives are the constituents that are not stated in section 1.1.1.1 and used to improve the production and the qualities of cement. Additives should not promote corrosion in reinforced concrete or weaken the qualities of cement-based materials [57]. The cement additives have been classified into several groups, as shown in the table 1.1, depending on the function of the cement [104]. Water-soluble polymers, for example, were used as viscosity modifying agents to improve the viscosity and cohesion of cement-based materials [105]. Alkaline solution, a mixture of hydroxides and silicates, is used to activate flyash and Ground Granulated Blast Furnace Slag (**GGBS**) to generate geopolymers. These geopolymers are combined with foam to create Light Weight Geopolymer Concrete (**LWGC**) [106]. Calcium Nitrite ($\mathbf{Ca(NO_2)_2}$), Calcium Nitrate ($\mathbf{Ca(NO_3)_2}$), and Urea ($\mathbf{CO(NH_2)_2}$) were utilized as antifreeze agents in cement paste backfill (**CBP**) at sub-zero temperatures [107]. Another good example that has been studied recently is the use of organic addtives such as polyhexamethyleneguanidine hydrochloride, tetraphelylphosphonium chloride, polyethyleneimine, and thiocarbamide to stabilize Pertechneatate (**Tc**) Ions in a cement matrix [108].

Cement additives classification
Basic cements
Accelerators and salts
Extenders and density-reducing additives
Silica to reduce or prevent high-temperature strength retrogression
Dispersants
Bond improving and expanding agents
Retarders
Fluid loss additives
Antigas migration agents
Antifoam and defoaming agents
Additives and mixtures to reduce or prevent lost circulation
Density-increasing or weighting agents
Free water control and solid suspending agents
Spacers and chemical washes or preflushes
Specialty cement blends

Table 1.1 – Cement additives classification [104]

1.1.2 Cement hydration and microstructure development

1.1.2.1 Cement hydration kinetic

Since the cement hydration process is very complex and up to date, there is no unifying theory on the hydration kinetic yet [109]. Generally, the rate of hydration is affected by the ambient temperature, reinforcing bars, formwork type, and thickness [110], [111]. Nevertheless, researchers have used a law called *Arrhenius law* to predict the properties of concrete as the hydration of cement develops at different temperatures [111]. The Arrhenius law, which is based on experimental observation, is shown in the equation 1.9 and 1.10 below.

$$K(T) = Ae^{-\frac{E_a}{RT}} \tag{1.9}$$

or

$$K(T) = Ae^{-\frac{E_a}{k_B T}} \tag{1.10}$$

where K(T) : reaction rate constant depends on temperature,
A : constant (=1/s),
E_a : apparent activation energy of cement-based materials (in J/mol),
k_B : boltzmann constant (= 1.380649×10^{-23} J/K),
R : gas constant (= 8.314 J/mol.K),
T : absolute temperature (in K or °R).

The idea of maturity and equivalent age of cement-based materials was established to forecast the influence of time and temperature on the development of chemical, physical, and mechanical properties of hydrating cement-based material systems [111]–[127]. By definition, the maturity of concrete is *concrete of the same mix at the same maturity (reckoned in temperature-time) has approximately the same strength whatever combination of time and temperature go to make up that maturity* [128]. This idea can be expressed in the mathematical formulation in the equation 1.11 below [111].

$$M(t, H(T)) = \int_0^t K(T(\tau))d\tau \tag{1.11}$$

where M(t,H(T)) : maturity index at time t (in °C × hours or °C × days),
H(T) : temperature history: T(τ), $\tau \in$[0,t],
K(T) : rate constant,
T(t) : temperature (in K).

Based on the experimental results working with accelerated curing methods of Nurse and Saul [128], [129], this concept was named as *Nurse-Saul maturity function* and standardized in **ASTM C1074** as below [130], [131]:

$$M(t) = \sum (T_a - T_0)\Delta t \tag{1.12}$$

where M(t) : temperature-time factor at time t (in °C × hours or °C × days),
Δt : time interval (in hours or days),
T_a : average temperature during Δt (in °C),
T_0 : datum temperature (in °C).

Moreover, the concept of the equivalent age is defined as *the equivalent age represents the age of curing at the reference temperature that would result in the same strength as would result from curing at other temperatures* [111]. By using the equation 1.11, mathematical formulation of the equivalent age is:

$$t_{eq} = \int_0^t e^{\left(-\frac{E_a}{R}\left(\frac{1}{T(\tau)}-\frac{1}{T_{ref}}\right)\right)} d\tau \tag{1.13}$$

where t_{eq} : equivalent age at the reference temperature T_{ref} (in days or hours),
T_{ref} : reference temperature usually 20 °C (or 293.15 K),
T(t) : temperature (in K).

The equivalent age has also been standardized in **ASTM C1074** by using Freiesleben Hansen and Pedersen formulation as below:

$$t_e = \sum e^{\left[-\frac{E_a}{R}\left(\frac{1}{T_a}-\frac{1}{T_s}\right)\right]} \Delta t \tag{1.14}$$

where t_e : equivalent age at a specified temperature T_s (in days or hours),
T_a : average temperature during time interval Δt (in K),
T_s : specified temperature (in K),
Δt : time interval (in days or hours).

Despite the equations of maturity and equivalent age proposed by **ASTM C1074** above, these equations have been modified to satisfy the application of cement-based materials. A review of predicting concrete strength by using modified maturity and equivalent age formulations can be found in [132].

One of the essential parameters in these equations above is the *Apparent activation energy of cement-based materials* ($\mathbf{E_a}$) which represents the sensitivity of concrete mixture and has to be experimentally determined. The mix design (cement type, aggregate type, water to cement ($\mathbf{W/C}$) ratio, and additions), degree of advancement, and temperature influence the activation energy [111]. $\mathbf{E_a}$ can be determined by using mechanical (compressive) and calorimetric (isothermal, semi-adiabatic, and adiabatic) tests on concrete or equivalent mortar. Then, several calculation methods had been used by researchers such as superposition method, speed method, derivative of speed method, single linear approximation, linear fit, hyperbolic-E, hyperbolic-U, two steps, exponential-E, exponential-U, initial time of set, and final time of set [111], [133]. For instance, $\mathbf{E_a}$ has been determined at different temperatures by using isothermal calorimetric and speed method. The *Arrhenius law* is valid only for the hydration degree between 0.05 and 0.5 since the hydration of cement-based material is controlled by chemical reaction [134]. Additionally, the superposition method, along with the isothermal calorimetric and mechanical test, was used to calculate the $\mathbf{E_a}$ of concrete using a superplasticizer can be found in [135].

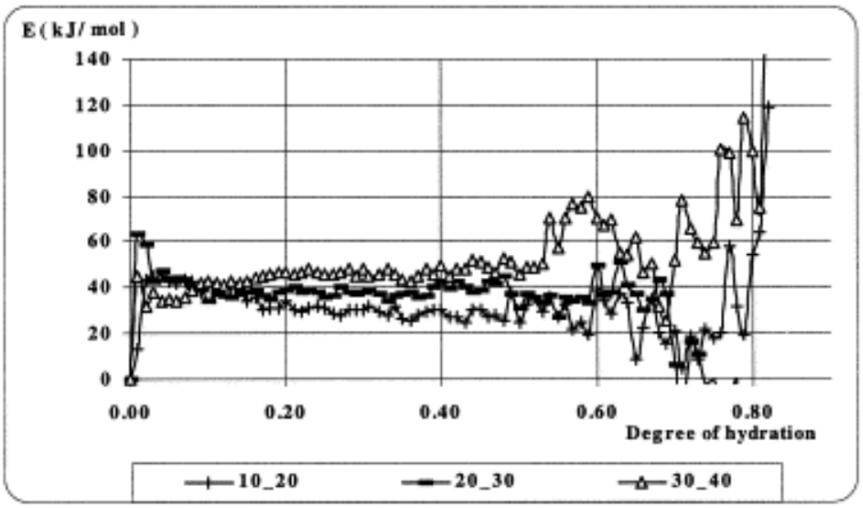

Figure 1.5 – Apparent activation energy $\mathbf{E_a}$ at different temperatures [134].

1.1.2.2 The heat of cement hydration

The hydration of Portland cement clinkers is an exothermal reaction [136] and thermal effects from this reaction are significant at young age [111]. Moreover, this heat of hydration causes an increase in temperature within a concrete block, and it dissipates into the environment. For massive structure, delay of heat dissipation causes greater temperature at young age in the structure's core and it causes chemical processes in the core to accelerate [137].

Like being mentioned in previous section, the heat of hydration can be measured in several ways by using calorimetry such as isothermal calorimetry [138]–[149], adiabatic calorimetry [138], semi-adiabatic calorimetry [150], and solution method [151]. Moreover, it also can be measured on massive concrete [138]. The result from calorimetry is used for several applications. As an example, the isothermal calorimetry was used along side with X-ray diffraction and Rietveld analysis (**XRD-Rietveld**), thermogravimetric analysis (**TGA**), and mercury instrusion porosimetry (**MIP**) to monitor the hydration process at long term of Portland cement and fly ash blended cement mortar [139]. In addition, it also can be used to study the early-age hydration, for example, in case of Portland cement cement paste blended with carbon nanotubes (**CNTs**) [140]. However, for adiabatic calorimetry, the heat production rate (**q**) is calculated by measuring the temperature rise of perfectly insulated concrete. Furthermore, the semi-adiabatic calorimetry was used to simulate the cement hydration, temperature rise and it's evolution, setting time, heat

release and heat flow of cement-based materials [152]–[155].

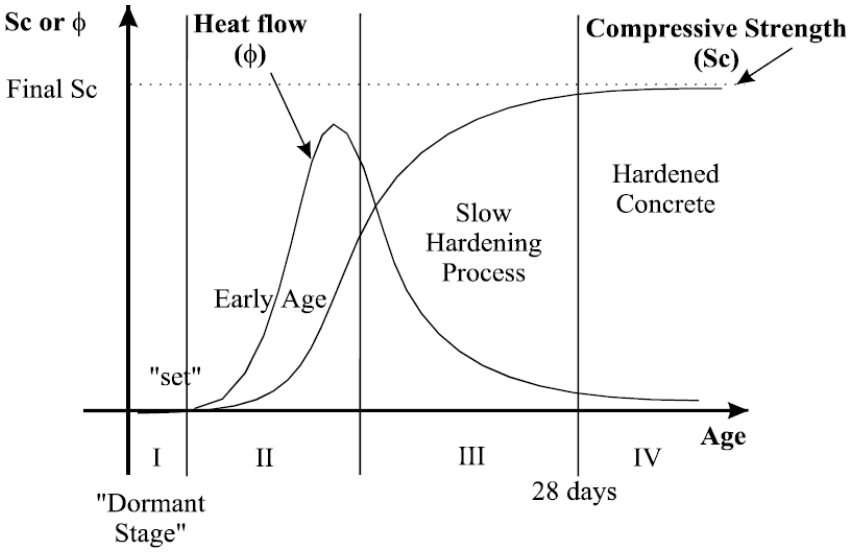

Figure 1.6 – Hydration heat and strength development of concrete [111]

1.1.2.3 Microstructure development

Despite these complex processes, several mathematical models, numerical simulations, and experimental approaches have been proposed to predict and understand the hydration kinetic of cement-based materials [156]. The **CEMHYD3D**, for example, is a program created by **NIST** that can provide three-dimensional microstructure, hydration degree, heat release, and chemical shrinkage from particle size distribution (**PSD**), water-to-cement ratio, and two-dimensional **SEM** images of cement (figure 1.7) [157]. Several researchers have used **CEMHYD3D** in the application of studying leaching of mortar [9], [23], [29], Supplementary Cementitious Materials (**SEM**) [30], aggregate's shape analysis [31], etc.

In a similar manner to that of the **CEMHYD3D**, the **HYMOSTRUC** program was used to develop the properties of cement paste by using the PSD, the chemical composition of cement, the w/c ratio, and the temperature [32]. In addition, the cement grains have the shape of spheres, and the size of the cement's hydration products increases gradually over time and as a function of the hydration reaction. Several applications of **HYMOSTRUC** can be found in [32]–[39]. In addition, **HydratiCA** was designed in a different way to model the diffusion and chemical reactions and is based on the core concepts of kinetic cellular automatons [43], [158], [159]. It's application can be found in

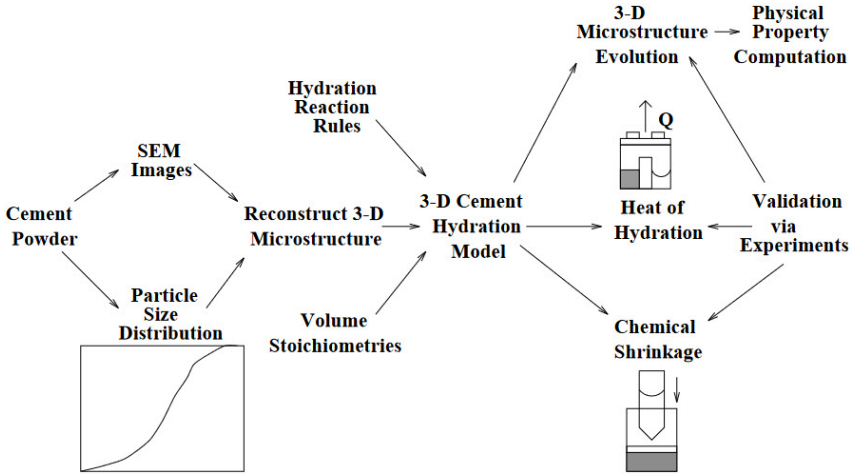

Figure 1.7 – CEMHYD3D flow diagram [157]

[40]–[42], [44], [45]. There are also other models such as **μic** [46]–[50], and **PHREEQC** [51], [52] that have been widely utilized to simulate the microstructure of cement-based materials at various scales.

1.2 Multi-scale modeling

1.2.1 Cement-based materials at different scale

Since cement-based materials are heterogeneous materials and consider all the constituents' properties, it has been divided into four different scales: nanoscale, microscale, sub-mesoscale, and mesoscale [5]. The definition of cement-based materials is defined as below:

— **Nanoscale:** it is the scale of individual element cells of hardened cement-paste [8]. For instance, the unit cells of Calcium oxide (**CaO**), Magnesium oxide (**MgO**), Portlandite (**CH**), Calcite ($\mathbf{CaCO_3}$), and Alite ($\mathbf{C_3S}$) are illustrated in figure 1.8, 1.9, and 1.10 respectively. In this scale, the element cells of harden cement-paste are in form of anisotropic structure and their elastic properties are usually calculated using Density Functional Theory (**DFT**), Molecular Dynamics (**MD**), and Atomic-Scale Finite Element Method (**AFEM**) [5], [160]–[168].

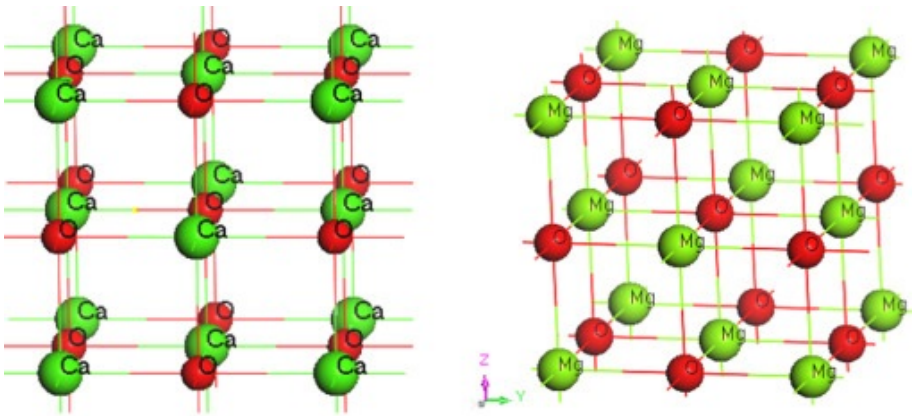

Figure 1.8 – Cubic model of Calcium oxide (**CaO**) and Magnesium oxide (**MgO**) [8].

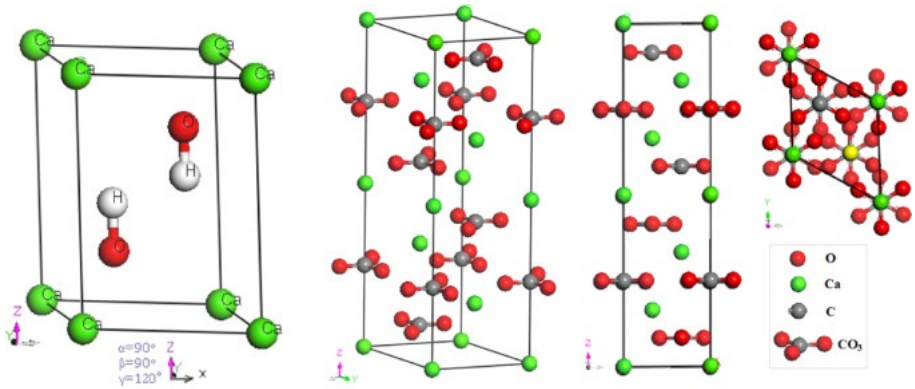

Figure 1.9 – Hexagonal model of Portlandite (**CH**) and Calcite ($\mathbf{CaCO_3}$) [8].

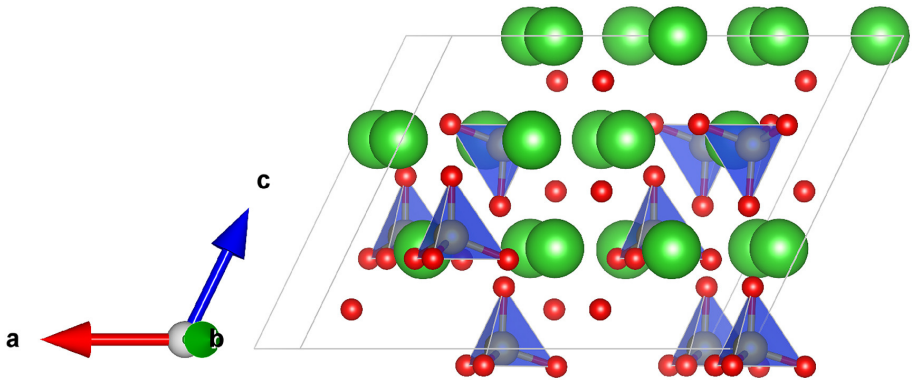

Figure 1.10 – A monoclinic polymorph of Alite ($\mathbf{C_3S}$) unit cell [169].

— **Microscale:** it is the scale of hardened cement-paste which consists of two main phases: solid and porosity phases. The solid phases are Calcium Silicate Hydrates (**C-S-H**), Calcium Hydroxydes so called Portlandite (**CH**), anhydrous clinkers, Hydrated Aluminates also known as Ettringite (**AFt**), and Monosulfoaluminates (**AFm**). The porosity phase is usually filled with excessive solution (in general, water) in the paste or yet to react with solid phases [170]. Figure 1.11 and 1.12 show the image of hardened cement paste obtained from Scanning Electron Microscopy (**SEM**) at microscale.

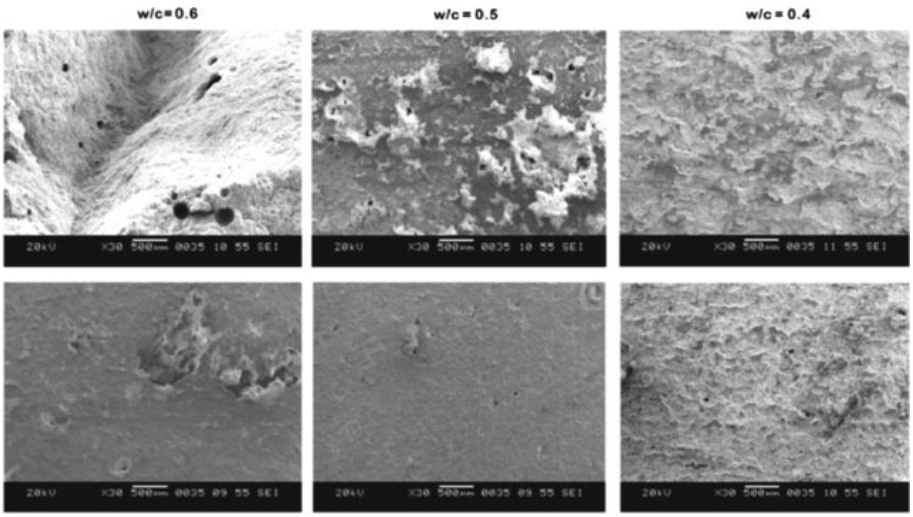

Figure 1.11 – Image of hardened cement paste with different water to cement ratio (**W/C**) obtained from Scanning Electron Microscopy (**SEM**) [171].

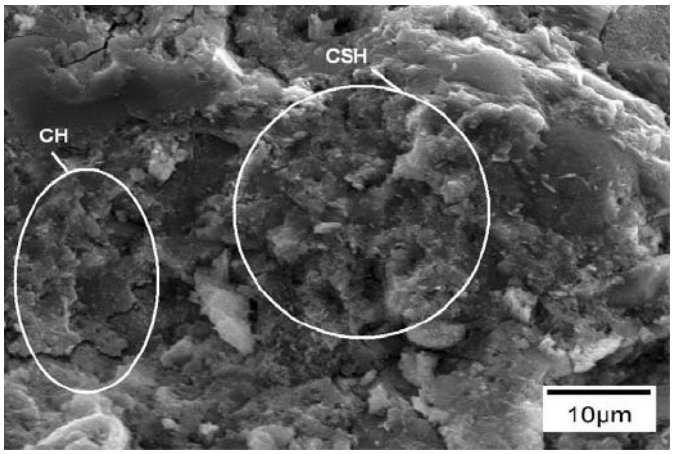

Figure 1.12 – Image of **CH** and **C-S-H** obtained from Scanning Electron Microscopy (**SEM**) [172].

— **Sub-mesoscale:** it is the scale of mortar with the smallest proportion of particle from particle size distribution enclosed by the cement paste. This one is considered homogeneous at sub-mesoscale.

— **Mesoscale:** it is the scale of concrete with the large proportion of particle from particle size distribution is enclosed by the mortar which is considered homogeneous at mesoscale.

As mentioned in the section 1.1.1.4, with the introduction of inclusion in the cement-based materials, **ITZ** appears at the interface between aggregate and the matrix. Thus, in sub-mesoscale and mesoscale, these bands of **ITZ** do exist and could effect the mechanical and diffusivity of the cement-based materials [89]. Figure 1.13 and 1.14 show the **ITZ** in sub-mesoscale and mesoscale for mortar and concrete respectively.

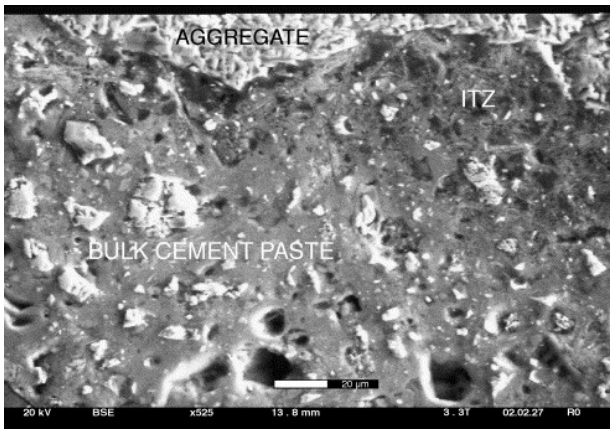

Figure 1.13 – **ITZ** at the interface of bulk cement paste and aggregate [173].

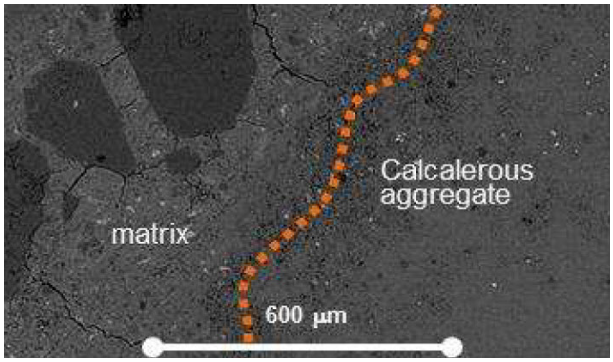

Figure 1.14 – **ITZ** at the interface of mortar and aggregate [91].

1.2.2 Homogenization for continuum mechanics

By definition, homogenization idea is to provide simple approaches for forecasting the corresponding behaviours of composite materials [174]. In this idea, the **Eshelby's inclusion problem** is well known for the homogenization of elastic field outside the inclusion which is enclosed by infinite surrounding materials [175], [176]. Moreover, the solutions given by Eshelby are in form of analytical equations. The homogenization methods are classified into analytical and numerical homogenization methods. Regardless of any types, these homogenization methods are used to predict the mechanical, thermal, and mass diffusivity properties of composite materials which are important for materials performance optimization and new materials design [177].

1.2.2.1 Analytical homogenization

Analytical homogenization, also known as Effective Medium Approximation (**EMA**), is a straightforward method that directly involves the percentage and properties of each component of composite materials [177]. Several methods have been widely used by researchers such as *upper bound of Voigt*, *lower bound of Reuss*, *Voigt-Reuss-Hill*, *Maxwell*, *Rayleigh*, and *Hashin-Shtrinkman*. The concept and analytical formulation of these methods are shown as below:

— **Upper bound of Voigt**

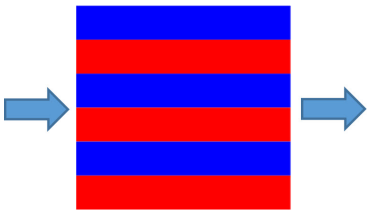

Figure 1.15 – Upper bound of Voigt

$$\lambda_v = \sum_{i=1}^{n} f_i \cdot \lambda_i \tag{1.15}$$

where f_i : volume ratio of each phase,
λ_i : properties of each phase.

— **Lower bound of Reuss**

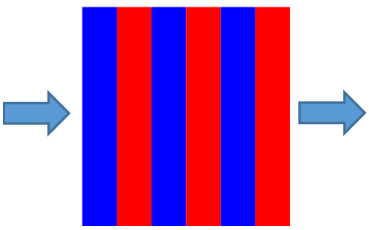

Figure 1.16 – Lower bound of Reuss

$$\lambda_R^{-1} = \sum_{i=1}^{n} f_i \cdot \lambda_i^{-1} \tag{1.16}$$

where f_i : volume ratio of each phase,
λ_i : properties of each phase.

— **Voigt-Reuss-Hill (VRH)**

$$\lambda_{VRH} = \frac{\lambda_V + \lambda_R}{2} \tag{1.17}$$

where λ_V : properties from upper bound of Voigt,
λ_R : properties from lower bound of Reuss.

— **Maxwell**

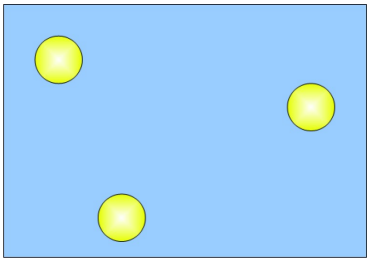

Figure 1.17 – Maxwell [178]

$$\frac{\lambda_{eff}}{\lambda_m} = 1 + \frac{3f}{\left(\frac{\lambda_1 + 2\lambda_m}{\lambda_1 - \lambda_m}\right) - f} \tag{1.18}$$

where f : volume ratio of particle,
λ_m, λ_1 : properties of the matrix and particle.

— **Rayleigh**

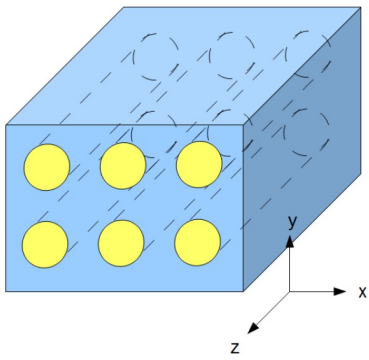

Figure 1.18 – Rayleigh [178]

$$\frac{\lambda_{eff}}{\lambda_m} = 1 + \left(\frac{\lambda_1 - \lambda_m}{\lambda_m}\right) \cdot f \tag{1.19}$$

and,

$$\frac{\lambda_{eff}}{\lambda_m} = 1 + \frac{2f}{C_1 - f + C_2(0.30584 \cdot f^4 + 0.013363 \cdot f^3 + ...)} \tag{1.20}$$

$$C_1 = \frac{\lambda_1 + \lambda_m}{\lambda_1 - \lambda_m}; C_2 = \frac{\lambda_1 - \lambda_m}{\lambda_1 + \lambda_m}$$

where f : volume ratio of particle,

λ_m, λ_1 : properties of the matrix and particle.

— **Hashin-Shtrinkman**

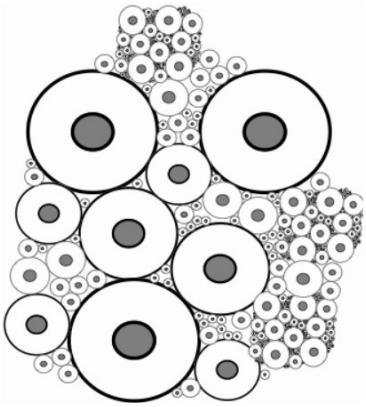

Figure 1.19 – Hashin-Shtrinkman [5]

$$\lambda_{eff} = \lambda_m + \frac{\lambda_m \cdot \frac{V_1}{V_1+Vm}}{\frac{\lambda_m}{\lambda_1-\lambda_m} + \frac{1}{3} \cdot \frac{V_m}{V_1+V_m}} \tag{1.21}$$

where V_m, V_1 : volume ratio of the matrix and particle,
λ_m, λ_1 : properties of the matrix and particle.

These analytical methods are widely used in mechanical problems. Moreover, in the case of heat transfer problem, these analytical methods could not take into account the effect of Thermal Contact Conductance (**TCC**) at the interface between two solids in contact (further detail in section 1.3.3) [178], therefore, numerical methodology are being developed due to recent powerful computational capability [177]. Moreover, the numerical homogenization method will be presented in the next section.

1.2.2.2 Numerical homogenization

The numerical homogenization methods for cement-based materials are also divided into several different scales: microscale (cement paste), sub-mesoscale (mortar), and mesoscale (concrete). Regardless of any scale of cement-based materials, two modelling methods, namely continuum and discrete methods, have been used to produce virtual cement-based materials in both 2D and 3D that represent the real cement-based materials. Furthermore, in the continuum method, there are two approaches: digital image based and parametrization modelling approaches, and in discrete methods, for example, discrete element method (**DEM**), rigid body spring networks, and lattice element methods have been used by researchers for years [53].

1.2.2.3 Geometry generation

As far as the continuum method is concerned, the digital image based approach consists of scanning the real specimen (using either microtomography, X-ray computed tomography (**XCT**) or scanning electron microscopy (**SEM**)) and regenerating the virtual specimen using either finite element mesh or discrete element [53], [179]–[184]. Concerning the parametrization approach, microstructure of cement paste and mesostructure of mortar, and concrete are generated by using either a program and an algorithm. The programs that have been used by researchers are **HYMOSTRUC**, **CEMHYD3D** (figure 1.21), **HydratiCA**, ***µ*ic**, and **Abaqus FEA** and the algorithms that have been developed recently such as single particle, nucleation and growth, random walk, and take-and-place models are used as the complement to the programs [9], [10], [32]–[36], [40]–[44], [46], [47],

[55], [156], [185]–[192]. Moreover, the detail comparison between these two approaches can be found in [53], [184].

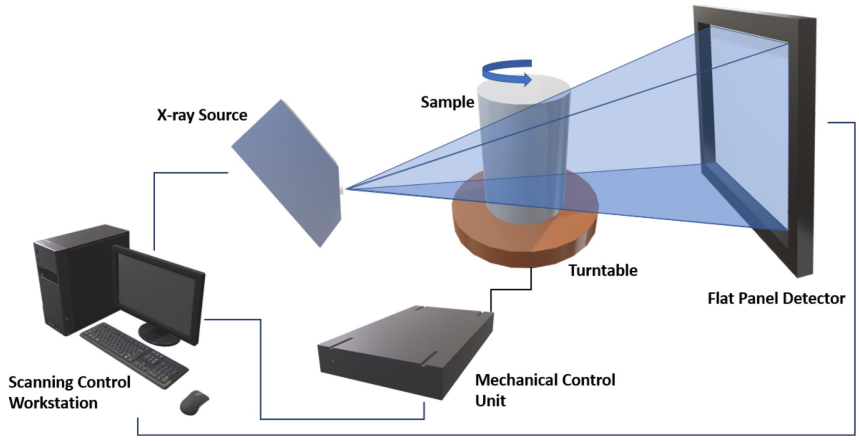

Figure 1.20 – **XCT** scanning system [53]

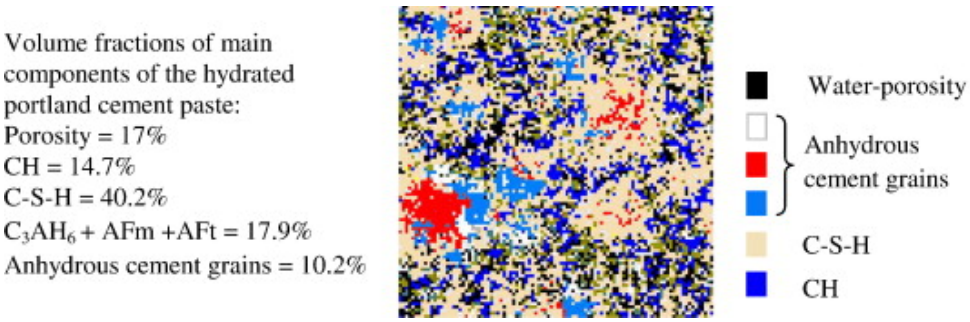

Figure 1.21 – 2D cross section of cement paste from **CEMHYD3D** [9]

Regarding discrete methods, in discrete element method (**DEM**), the geometry of cement-based is composed of several particles that are in contact with each other, and the second law of Newton and the contact law are used to establish the behavior of the interacting particles [53]. Rangari et al. have used the **DEM** to find the tensile strength of concrete and validate the modelling result with experimental result (figure 1.22) [193]. Moreover, spring network models are made up of a given structure split into a large but limited number of stiff segments, which are held together by a spring system distributed throughout the contact boundary surfaces. The deformation of the spring system represents the deformation or propagation of internal forces. The displacement of each segment in such discrete models may be entirely explained by the stiff body movement

of the appropriate centroid (generally, it consists of 6 components) (figure 1.23) [53], [181], [194]–[198]. The initial stage in constructing the lattice network is the partition of the continuous model into multiple cubic cells of equal size with an identically sized cubic core in the middle. Then, a single node is produced randomly within the cubic center for each cell, and special cells, such as corner, edge, and facet cells, have nodes fixed at the continuous model's corner, edge, and facet. As a result, the model is represented as a set of lattice nodes. The lattice nodes are then linked together to build a lattice network using a tetrahedral network generated via 3D Delaunay triangulation and a cube-like network (figure 1.24). Finally, the model with a lattice network is discretized into a sequence of truss elements [199]. Several good example of numerical homogenization can be found, for example, Mazzucco et al. used **Abaqus FEA** to simulate 3D concrete at the mesoscale, using recycled aggregates (**RAs**) derived from topology reconstruction [200]. Bernard et al. employed **CEMHYD3D**, developed by the National Institute of Standards and Technology (**NIST**), to create 3D representative volume elementary (**RVE**) models for cement paste and mortar to analyze the mechanical behavior, sound, and leached mortar using **Abaqus FEA** [9]. Later, the same authors utilized **CEMHYD3D** again to create the microstructure of cement paste and mortar, which was then converted to finite element mesh to analyze mechanical behavior and lattice element mesh to study diffusivity behavior of cement paste and mortar using **Abaqus FEA** [10].

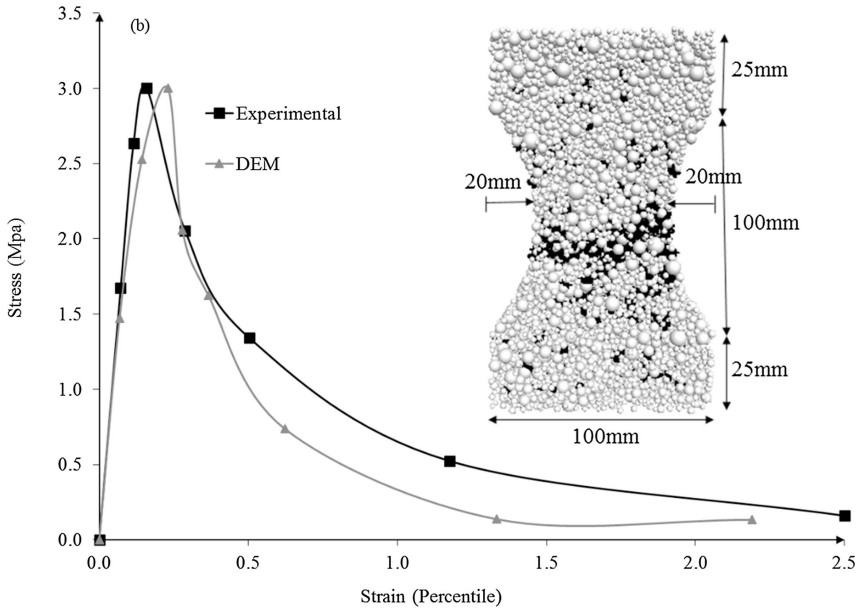

Figure 1.22 – **DEM** result validation with experimental result [193]

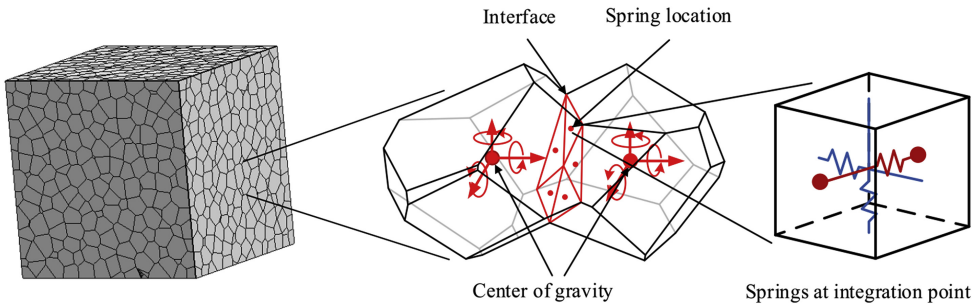

Figure 1.23 – Concrete geometry generation by Voronoi cells [198]

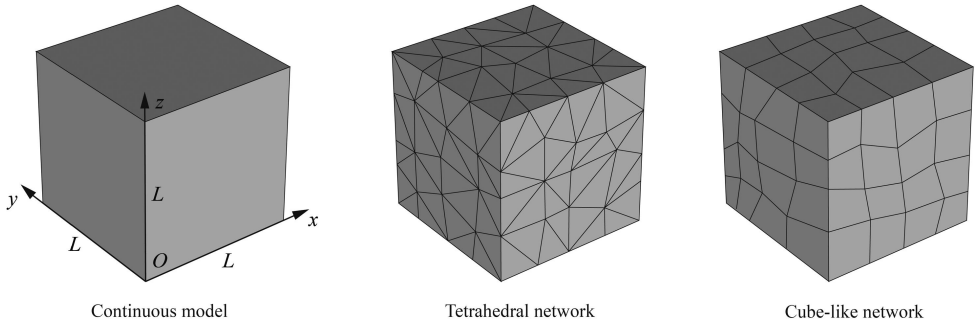

Figure 1.24 – Lattice network of a continuous model [199]

After discussing how to build 2D and 3D models out of cement-based materials, the final part of this section discusses the difference between a pseudo-3D model and a 3D model. Zhou defines the distinction between a pseudo-3D model and a 3D model of concrete at the mesoscale. A 3D model is composed of 3D aggregates of various forms. It requires a specific technique, such as the take-and-place approach mentioned above, to generate a representative 3D model for concrete. Furthermore, a concrete pseudo-3D model is a collection of 2D models that have been sliced from completely 3D models to save computation costs (figure 1.26) [201]. Rhardane et al., for example, studied damage of mortar under mechanical load using pseudo-3D modeling [55].

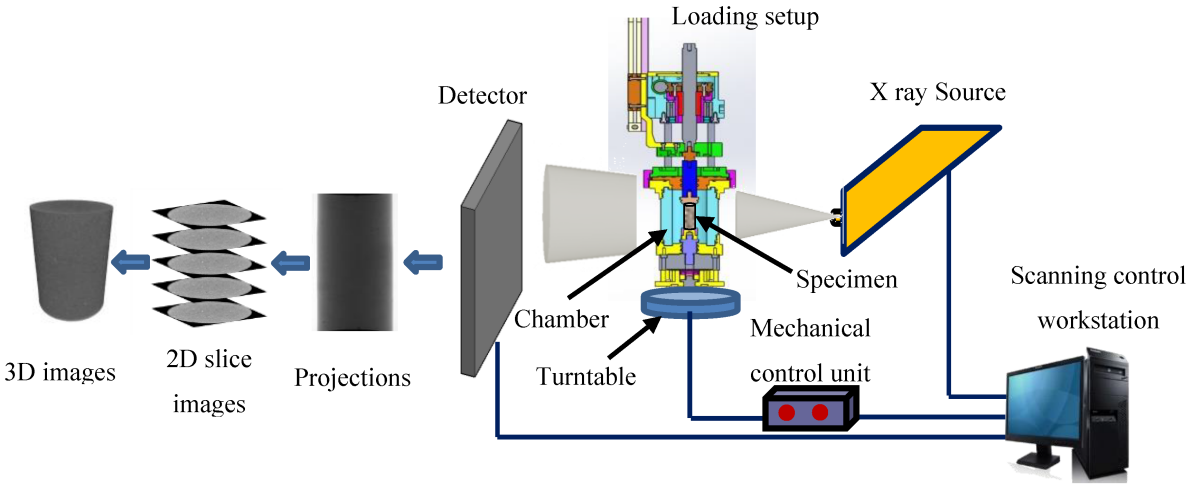

Figure 1.25 – **XCT** scanning for pseudo-3D model [202]

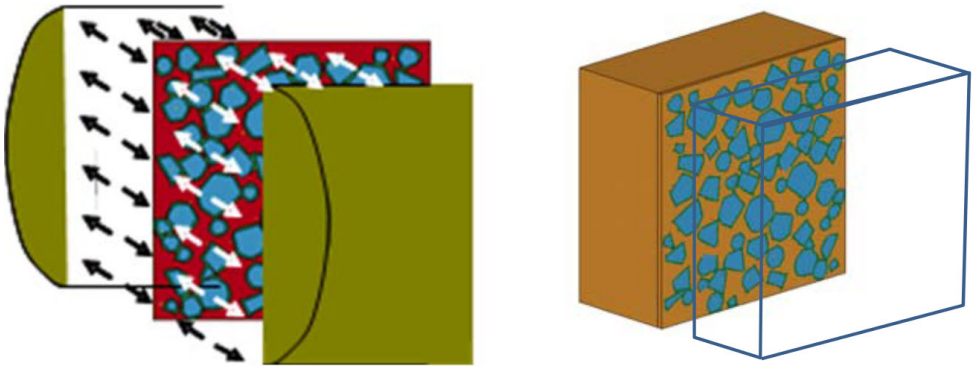

Figure 1.26 – Pseudo-3D mesoscale of concrete [201]

1.2.2.4 Take-and-place method

Take-and-place method is one of the most used method to recreate the virtual concrete specimen with random aggregate distribution. It was initially utilized to generate 2D specimens with various types of inclusion, such as spherical, broken, and defined shape aggregate, to evaluate the elastic modulus and effective coefficient diffusion of cement-based materials [54]. Later, the take-and-place method was also adopted for constructing virtual 3D specimens since it is simple, straightforward, rapid, and produces good results, and the fuller's curve was used as a reference of aggregate particle size distribution [203]–[206]. Moreover, specific finite element meshing technique is required for certain studies,

for example, nonlinear finite element analysis [207], [208].

The take-and-place method generally consists of two essential steps: *take* and *place* [209]. The *take* processes include computing the entire volume of aggregate, defining aggregate size, recalculating aggregate volume, and repeating until no aggregate remains. While the *place* processes consist of defining a random position, checking for overlap between aggregates, and looping till the last aggregate. Furthermore, Rhardane et al. have modified the original take-and-place method by constructing sets of the center of each aggregate class in advance for the *place* process [55]. When an aggregate is placed within the domain, all centers inside the aggregate and a band around it (zone of influence) are removed from the sets (figure 1.27).

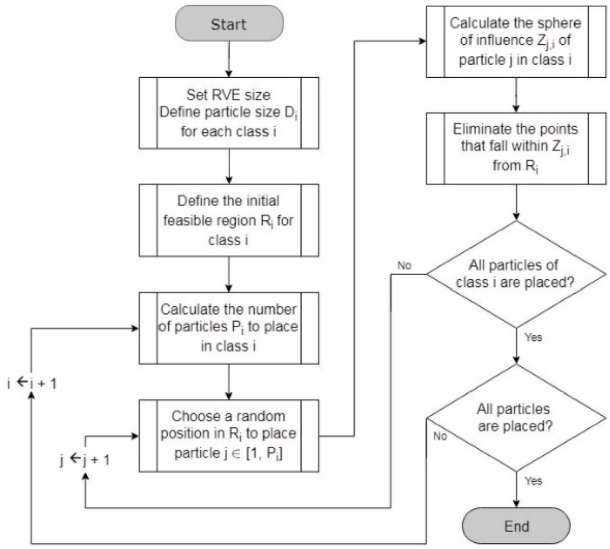

Figure 1.27 – Take-and-place with zone of influence by Rhardane [55]

1.2.2.5 Representative Volume Element (RVE)

Representative Volume Element (**RVE**) is an intermediate volume of a sample that is small enough to represent the whole volume on average and big enough to represent the uniform properties of the domain regardless of boundary conditions [210]. Any volume which is more smaller than the **RVE** is called sub-**RVE**, and it has essential heterogeneity [211]. It is claimed that the size of **RVE** is generally around four to five times the size of the structural parameter (inclusion) [212], and it can be up to an order of magnitude larger depending on the sensitivity of the parameter [213]. In case of cement-based materials,

Rhardane et al. have determined the size of **RVE** with the coefficient of variation below 5% as the criteria. They have found that the minimal size of **RVE** for cement paste is 200 μm [55]. Moreover, Grondin et al. have found the suitable size of **RVE** for concrete is four times larger than the size of the most prominent inclusion, which is consistent with the argument mentioned above [214], [215].

1.2.2.6 Multi-scale Modeling of Computational Concrete (MuMoCC)

MuMoCC is a numerical platform that offers an accurate 3D and multiscale hierarchical approach (section 1.2.1) to model all essential phenomena related to transport processes, chemical, physical, and mechanical degradation processes, and their reciprocal connection. Kamali-Bernard et al. have used this platform to study the influence of crack (tensile) on the diffusivity properties of mortar. First, **CEMHYD3D** is used to construct the microstructure of cement paste and the mesostructure of mortar, which is then converted to a finite element mesh so that the mechanical and diffusivity problems can be modeled using **Abaqus FEA** [56], [185]. In addition, the appropriate outputs at a particular scale are used as input data at the next higher scale [5]. In the reference of this **MuMoCC** platform, Comby-Peyrot et al. have used another software, **Forge3®** by **CEMEF.CEMEF.Forge3®**, to simulate the mechanical problem with application to the alkali-silica reaction at mesoscale of cement-based material [11].

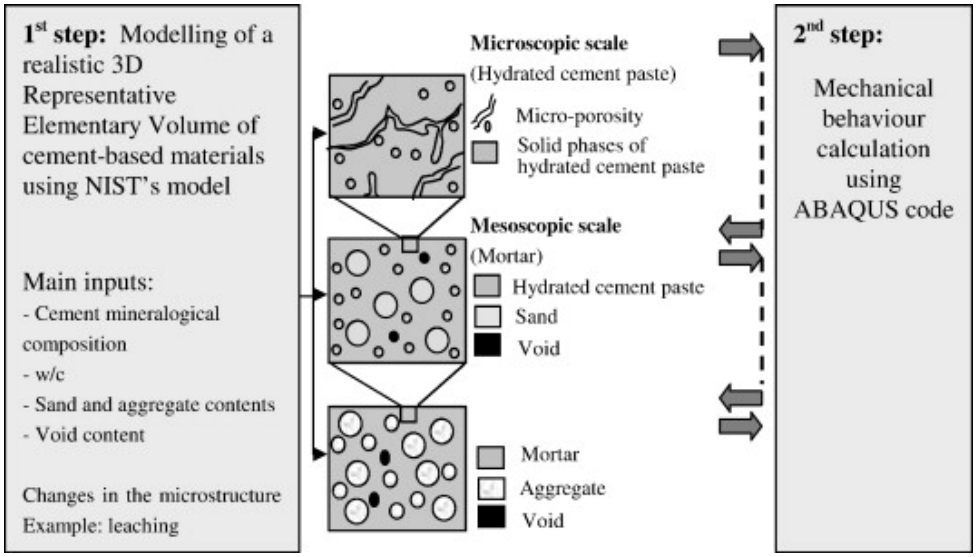

Figure 1.28 – Multi-scale Modeling of Computational Concrete (**MuMoCC**) platform [9]

1.3 Heat transfer problem

Heat transfer is a thermal engineering subject that deals with the generation, storage, transformation, and exchange of heat across physical systems. The mechanism of heat transfer involves of advection, conduction, convection, and radiation.

By definition, heat conduction (heat diffusion) is the mechanism by which heat is transmitted from the hotter to the colder end of a body. Heat conduction has two regimes: transient and steady-state. Transient heat conduction occurs when the temperature within a body changes over time, while steady-state heat conduction occurs when the temperature inside the body is uniform and is referred to as thermal equilibrium. Moreover, the Fourier's law, which is known as the law of heat conduction, asserts that the rate of heat transfer through a body is proportional to the negative gradient in temperature and the area through which the heat flows at right angles to that gradient. The Fourier's law can be expressed as differential form in equation 1.22.

$$q = -k\nabla T \tag{1.22}$$

where q : heat flux (W/m^2),
k : thermal conductivity (W/m.K),
∇T : the temperature gradient (K/m).

The Fourier's law of heat conduction may be stated in differential form in a 3D homogeneous isotropic materials, such as cement-based materials, in equation 1.23.

$$\rho c_p \frac{\partial T}{\partial t} = \frac{\partial}{\partial x}\left(k\frac{\partial T}{\partial x}\right) + \frac{\partial}{\partial y}\left(k\frac{\partial T}{\partial y}\right) + \frac{\partial}{\partial z}\left(k\frac{\partial T}{\partial z}\right) \tag{1.23}$$

where ρ : density of the sample (kg/m^3),
c_p : specific heat (J/kg.K),
T=T(x,y,z,t) : temperature (K) in function of position and time,
x, y, x, t : positions (m) in the sample and time (s).

Moreover, convection is the flow of fluid that causes heat to be transferred from one location to another and radiation is the transmission of thermal energy across the vacuum and clear medium. The fundamental equations for convection and radiation can be found in equation 1.24 and 1.25, respectively.

$$q = H_c(T - T_f) \tag{1.24}$$

where H_c : thermal convection coefficient (W/m^2.K),
T, T_f : temperature of the solid surface and the flux (K), respectively.

$$q = \epsilon\sigma F(T_a^4 - T_b^4) \tag{1.25}$$

where ϵ : emissivity,
σ : Stefan–Boltzmann constant (=5.67×10^{-8}/m^{2}K^4),
T_a, T_b : temperature of object a and b (K), respectively.

1.3.1 Volumetric mass density of cement-based materials

In heat transfer problems, the mass density of cement-based materials is significant in influencing their thermal properties, such as thermal conductivity. For instance, for hemp concrete, thermal conductivity increases with it's density [11]. Several examples of the relationship between density and thermal conductivity of not only hemp concrete but cement-based materials can be found in [216]–[218].

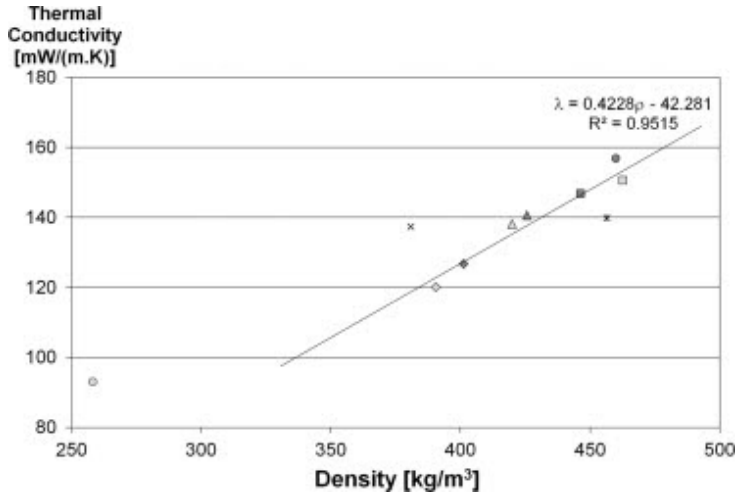

Figure 1.29 – Thermal conductivity and density of hemp concrete [11]

1.3.2 Thermal properties of cement-based materials

Thermal properties of cement-based materials, like other materials, are thermal conductivity ($\mathbf{k}$), specific heat ($\mathbf{C_p}$). In addition, thermal expansion ($\boldsymbol{\alpha}$) is one of the thermal properties; nonetheless, it is connected to expansion, which is one of the mechanical properties that the materials themselves possess. These properties are often investigated in

the context of lowering building energy consumption [11], [219]–[224], fire resistance [225], early-age cracking of massive concrete [226], and radioactive waste repository [227], [228], etc.

The detail of thermal conductivity ($\mathbf{k}$), specific heat ($\mathbf{C_p}$), and thermal expansion ($\boldsymbol{\alpha}$) are described in section 1.3.2.1, 1.3.2.2, and 1.3.2.3, respectively.

1.3.2.1 Thermal conductivity

Thermal conductivity ($\mathbf{k}$) is one of the most important thermal properties of any materials. It is an assessment of its capacity to conduct heat and defines the heat flux across a temperature difference. Furthermore, it is simple to compute using equation 1.26.

$$k = -\frac{q}{\nabla T} \tag{1.26}$$

Thermal conductivity of any material may be determined experimentally using a variety of techniques, including the Steady State Method (Absolute Method), Comparative Technique, Radial Flow Method, Laser-Flash Diffusivity, Pulse-power Method (Maldonado Technique), Parallel Thermal Conductance Technique, and Z-Meters or Harman Technique [229]. If the shape of the inclusion is defined and not random, it is also feasible to compute analytically by employing effective medium methods such as Maxwell, Woodside and Mesmer, Lewis and Nielsen, and Karayacoubian methods [230].

Furthermore, thermal conductivity in cement-based materials is generally influenced by the material's composition and fluctuates with temperature [231]–[233]. For example, various efforts have been made in recent research publications to reduce thermal conductivity in order to reduce energy consumption by employing Supplementary Cementitious Materials (**SCMs**) with low thermal conductivity [11], [219]–[224]. In general, the thermal conductivity values of cement-based materials range from 0.7 to 1.5 for cement paste [234]–[237] and from 1.1 to 1.6 for mortar [7], [238], [239].

1.3.2.2 Specific heat

The specific heat ($\mathbf{C_p}$) is, by definition, the amount of energy required (in **J**) to raise the temperature of one gram of a material by one degree Celsius or Kelvin. As seen in equation 1.23, specific heat has a role in the Fourier's equation. Moreover, it can be theoretically determined by using equation 1.27.

$$C_p = \frac{Q}{m\Delta T} \tag{1.27}$$

where C_p : specific heat (J/kg.K),
Q : heat energy (J),
m : mass (kg),
ΔT : change temperature (K).

Like thermal conductivity, the specific heat ($\mathbf{C_p}$) can be experimentally determined by using calorimetry methods [240], [241]. The calorimetry methods can be divided into three: Differential Thermal Analysis (**DTA**), Differential Scanning Calorimetry (**DSC**) [242]–[246], and alternative conventional calorimetry [240], [241], [247], [248]. Furthermore, these calorimetry analyses follow the same principle of determining the amount of heat necessary to raise the temperature of a sample. Among the alternative conventional calorimetry methods, there are several intriguing methods which are numerical simple and inverse methods. It is important to note that the inverse approach will be employed in this study.

The literature review reveals that the specific heat values for cement-based materials are 736 J/kg.K and 935 J/kg.K for cement paste [237], [245], and 1000 J/kg.K for mortar [239], [249].

1.3.2.3 Coefficient of thermal expansion (coefficient of dilatation)

Thermal expansion is the ability of matter to alter form, area, volume, and density in response to temperature changes, but does not generally include phase transitions [250]. Furthermore, the coefficient of thermal expansion ($\boldsymbol{\alpha}$) measures the change in length, area, or volume per degree temperature. The coefficient of thermal expansion ($\boldsymbol{\alpha}$) is defined in equation 1.28.

$$\alpha_X = \frac{1}{X}\frac{\partial X}{\partial T} \tag{1.28}$$

where α_X : coefficient of thermal expansion (K^{-1}),
X : length (m), area (m^2), or volume (m^3),
T : change temperature (K).

The systematic process of determining the coefficient of thermal expansion involves taking measurements of the sample's length, area, or volume both before and after subjecting it to a predetermined temperature range. However, this technique may need specific

equipment for the accuracy of measurement of some materials [251]–[253]. Finally, equation 1.28 is reduced for simplicity of measurement during the experiment, and the $\boldsymbol{\alpha}$ is computed using equation 1.29.

$$\alpha_X = \frac{1}{X}\frac{\Delta X}{\Delta T} \tag{1.29}$$

The coefficient of (linear) thermal expansion of concrete varies substantially, ranging from 2 to 30×10^{-6}/K, depending on temperature [252].

1.3.3 Thermal Contact Conductance (TCC) effect on heat transfer problem

When two solids come into contact and there is heat transfer from one to the other, the capacity to transfer heat via the interface is referred to as Thermal Contact Conductance (**TCC**) [254]. Each solid has a surface roughness that prevents the two surfaces from making complete microscopic contact. Thus, the space between the solid's surfaces may be filled by interstitial medium, which may or may not have radiation. Finally, heat transfer at the interface of two solids is caused by the solid contact spot (asperities), the interstitial medium, and perhaps radiation.

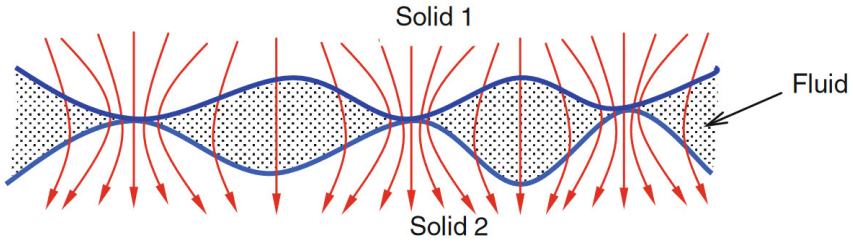

Figure 1.30 – Heat flow at the interface [254]

Furthermore, temperature drop (ΔT) may occur at the interface owing to imperfect contact (figure 1.31). The **TCC** (**h**) may therefore be computed by dividing the heat flow over the surface by the temperature drop (equation 1.30).

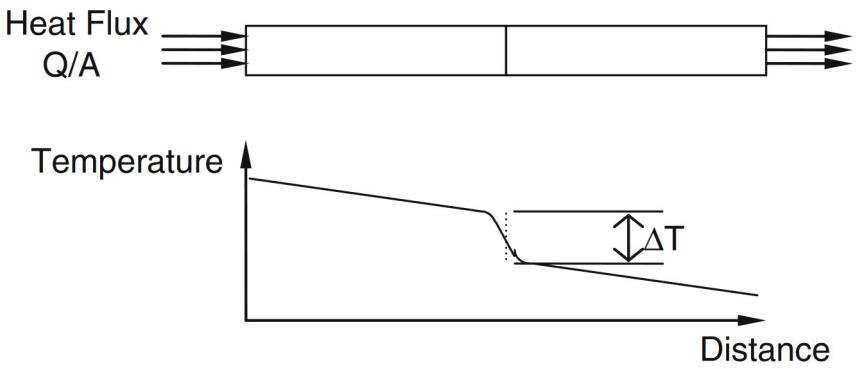

Figure 1.31 – Temperature drop at the interface [254]

$$h_j = \frac{Q/A}{\Delta T} \tag{1.30}$$

where h_j : Thermal Contact Conductance (W/m^{2}K),
Q/A : heat flux (W/m^2),
ΔT : temperature drop (K).

Supposed that there is no radiation at the interface, the heat energy is composed of the heat energy from contact spot ($\mathbf{Q_c}$) and from interstitial medium ($\mathbf{Q_g}$). So, the total **TCC** can be re-written as in equation 1.31.

$$\begin{aligned} h_j &= \frac{(Q_c + Q_g)/A}{\Delta T} \\ &= \frac{Q_c/A}{\Delta T} + \frac{Q_g/A}{\Delta T} \end{aligned}$$

$$h_j = h_c + h_g \tag{1.31}$$

where h_c : TCC of solid contact W/m^{2}K,
h_g : TCC across the gap via intermediate fluid W/m^{2}K.

1.3.3.1 Domain of application

The **TCC** applications include cooling of microelectronic devices, thermal management of space satellites, cryogenic industries, cooling of nuclear reactors, heat exchangers, aircraft structural joints, sliding contacts, and so forth [254]–[259].

1.3.3.2 Interface parameters

In order to precise determine the value of **TCC**, several parameters are needed to study such as surface geometry (roughness and slop), mechanics (pressure and loads), thermophysical (thermal conductivity, hardness), and interface parameters (interstitial fluid, temperature, and heat flow direction) [133], [254], [256], [259]. Furthermore, in the case of cement-based materials, some of these parameters, for example, surface roughness and slop, are very difficult to determine, both experimentally and numerically. As a result, more investigation is required, which will be described in this PhD thesis.

1.3.3.3 Existing theoretical and experimental analyses of TCC

There have been various attempts to comprehend the **TCC** in the domain of application stated in section 1.3.3.1, and some theoretical and experimental findings have been presented. Some models such as Yovanovich's model [257], [260] is very popular to determine the dimensionless gap resistance (**G**) expressed as in equation 1.32.

$$G = \frac{k_g}{h_j Y} \tag{1.32}$$

where G : dimensionless gap resistance,
k_g : thermal conductivity of interstitial gas (W/mK),
h_j : gap conductance or TCC (W/m^2K),
Y : effective gap thickness (m).

Moreover, the Yovanovich's model take into account the interstitial medium at the interface; thus, the gap conductance ($\mathbf{h_j}$) is expressed as in equation 1.33.

$$h_j = \frac{k_g}{\sqrt{2\pi}\sigma} \int_0^\infty \frac{exp[-(Y/\sigma - t/\sigma)^2/2]}{(t+M)/\sigma} d(t/\sigma) \tag{1.33}$$

$$M = \left(\frac{2 - TAC_1}{TAC_1} + \frac{2 - TAC_2}{TAC_2}\right)\left(\frac{2\gamma}{\gamma + 1}\right)\left(\frac{1}{Pr}\right)\Lambda$$

where
σ : surface roughness (μm),
t : local gap thickness (μm),
M : gas parameter,
TAC_1, TAC_2 : thermal accommodation coefficient,
γ : specific heats ratio,
Pr : Prandtl number,
Λ : molecular mean free path (μm).

As seen in equation 1.33, several parameters are unknown in cement-based materials, so the application of this model in cement-based materials is limited, and numerical modelling is required to investigate the possibility of the **TCC** effect on the thermal conductivity of the materials.

Furthermore, there are many additional theories that are worth mentioning in this **TCC** research, such as Resistance of a single contact, Cetinkale and Fishenden, Tachibana, Fenech and Rohsenow, Laming, and Clausing and Chao [261].

1.4 Massive concrete structure problem and solution

By definition, Massive concrete structures have the potential to crack due to the consequences of the hydration heat and autogenous shrinkage of cement-based materials at early-ages [6]. Since the massive concrete structure has large dimensions, the distribution of heat inside the structure is not uniform, which results in a significant temperature differential between the core and the surface of the concrete. In addition, when the concrete is deformation restrained, the difference in temperature creates thermal stress, which may lead to cracking if the thermal stress is greater than the strength of the concrete.

Several example of massive concrete structures have been given in figure 1.32, starting from (a) ground slabs, (b) concrete dams, (c) silos/containment structures, (d) cooling towers, (e) wind turbine foundations, (f) piles, (g) precast segments (top: immersed tunnel, bottom: bridge deck), (h) armour units; (i) bridge piers, and (j) retaining walls.

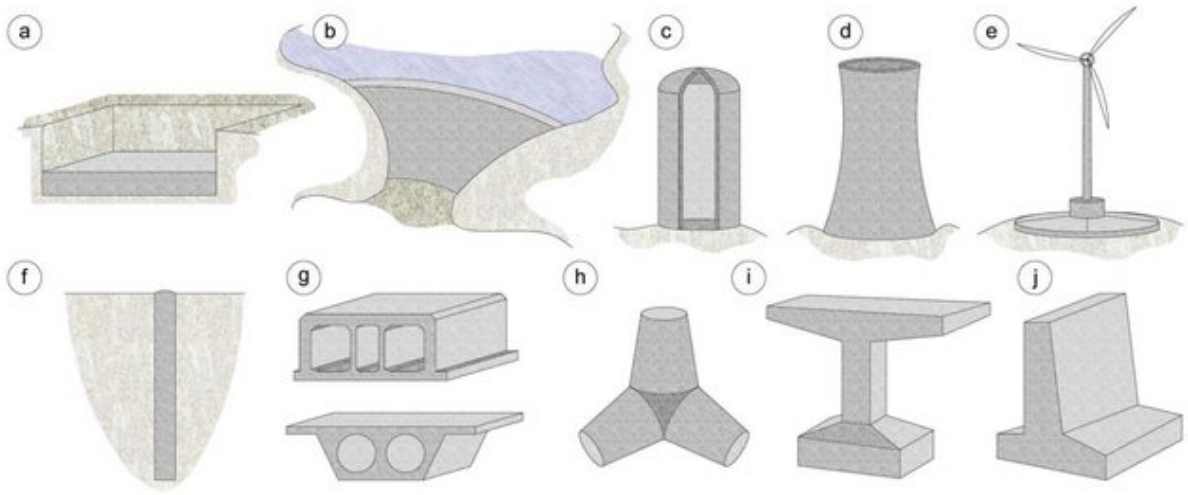

Figure 1.32 – Massive concrete structure examples [262]

The structures shown in Figure 1.32 needed numerical modelling to forecast and prevent thermal cracks from occurring inside the structure. In addition to the heat generated by the concrete itself, thermal loads such as convection, radiation, conduction, and combined emission and absorption are also present in applying heat transfer modelling to massive concrete structures (figure 1.33).

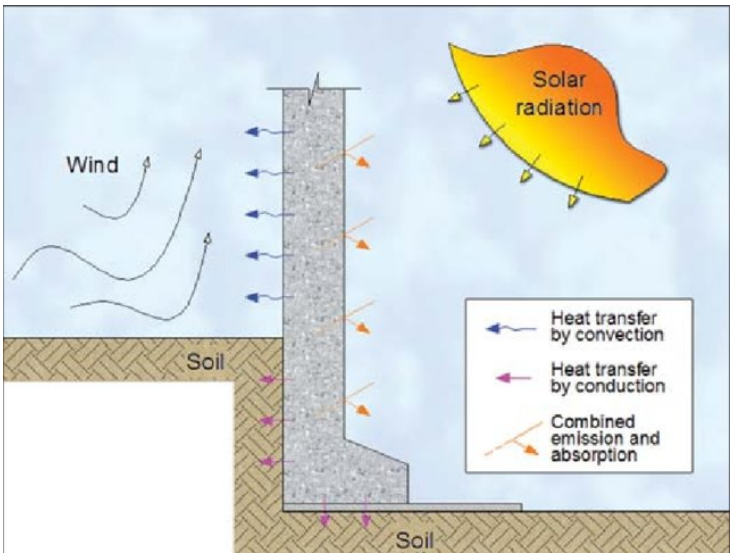

Figure 1.33 – Heat transfer in massive concrete [262]

1.4.1 Early-age crack

Many variables contribute to forming internal cracks inside concrete structures at an early-age. The amount of cement, overall thermal properties of concrete, placement (or initial) temperature, environment (temperature, humidity, and wind), and the dimension of the massive concrete structure, for example, are the factors that control the cause of the early-age crack, such as temperature rise rate, maximum temperature, and temperature differential inside the structure [263].

Only the internal heat generation and concrete structure constraint will be detailed in the next part to serve as a review and hypothesis for the application in section 3.2.

1.4.1.1 Internal heat generation

The heat generated by cement hydration is referred to as internal heat generation. The hydration heat is the energy caused by an exothermic reaction, which generates heat inside the concrete block and releases it into the atmosphere. Moreover, at the structure's core, the heat generation is close to the adiabatic condition. The accumulated heat and it's rate generated by the exothermic reaction in adiabatic conditions can be found in equation 1.34 and 1.35, respectively.

$$Q(t) = Q_\infty e^{\left[-\omega\left(2\varphi e^{\zeta T_0}\frac{t}{60}\right)^{-\xi}\right]} \tag{1.34}$$

where
- Q(t) : accumulated hydration heat (kJ/kg),
- Q_∞ : final amount of accumulated hydration heat (kJ/kg),
- T_0 : initial temperature,
- t : time (min),
- ω, φ, ζ, and ξ : constants.

$$q(t) = W\frac{dQ}{dt} \tag{1.35}$$

where
- q(t) : rate of hydration heat (kJ/m^{3}h),
- W : amount of cement per unit volume concrete (kg/m^3).

The constants, ω, φ, ζ, and ξ, depend on the cement type used. For example, the cement P.O.52.5 Portland cement was used and the hydration heat and rate were plotted in figure 1.34.

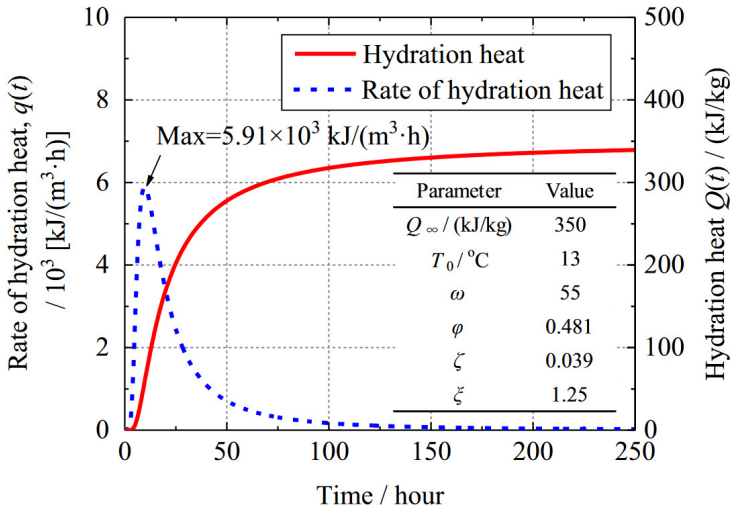

Figure 1.34 – Accumulated hydration heat and rate [264]

1.4.1.2 Restraint in massive concrete structure

Many considerations, such as early-age temperature differentials, embedded reinforcing, and supports, are the restraints of massive concrete [265]. Concerning the early-age temperature differentials, the maximum tensile stress at the core of the structure is expressed in equation 1.36.

$$\sigma_r = -\alpha \times \Delta T \times R \times E_{aaef}, \text{ where } E_{aaef} = \frac{E_c}{1 + \chi\varphi} \tag{1.36}$$

and σ_r : thermal stress (MPa),
ΔT : temperature change (K),
R : restraint factor,
E_{aaef} : age-adjusted effective modulus,
χ : aging coefficient,
φ : tensile creep coefficient.

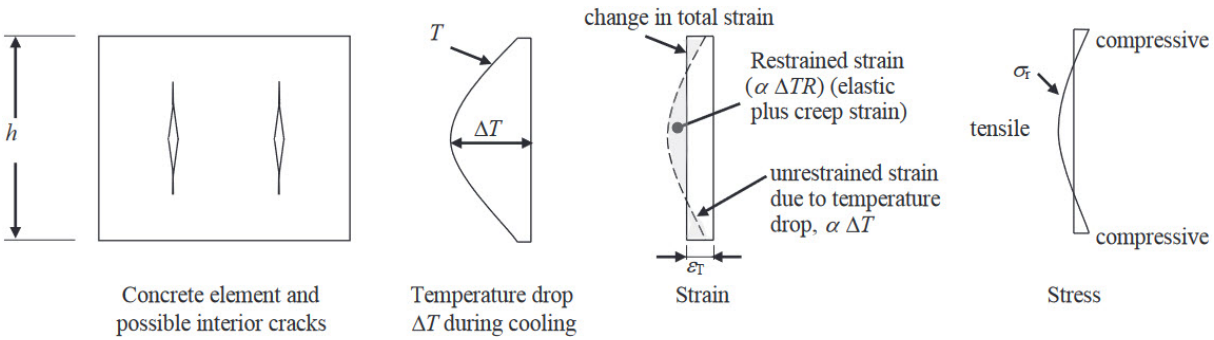

Figure 1.35 – Thermal stress-strain diagram [265]

The constraint by embedded reinforcement and the restraint by structural support are the other two kinds of restraints. When the concrete is extended or contracted due to thermal stress, the embedded reinforcement prevents the concrete from deforming and may cause the concrete to crack. Figures 1.36 and 1.37 show two methods of reinforcement in components of a structure subjected to normal and flexural stress that may prevent the concrete from deforming and cracking.

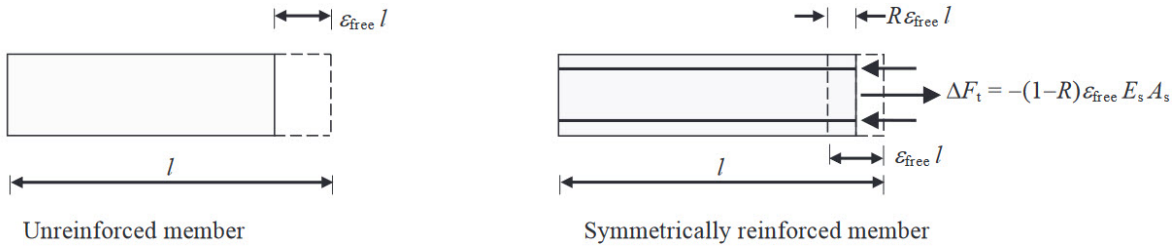

Figure 1.36 – Normal stress structural member [265]

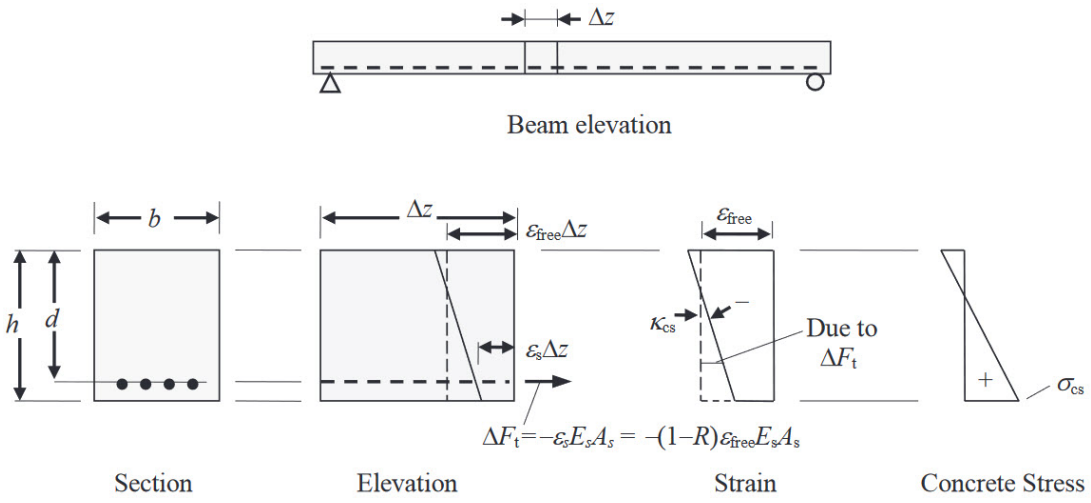

Figure 1.37 – Flexural stress structural member [265]

Furthermore, figure 1.38 depicts the sort of structural support that may be used to restrict concrete deformation.

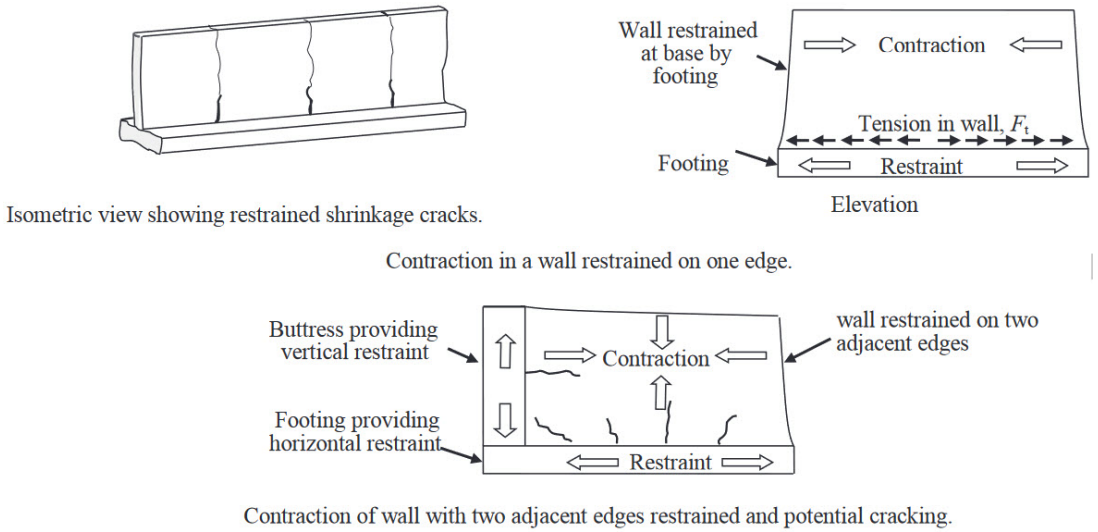

Figure 1.38 – Restraint by supports [265]

1.4.2 Solutions to the problem

Even though cracks may develop at an early age because of the temperature increase caused by the exothermic hydration reaction, there are several known solutions to prevent

early-age cracks from occurring. Adjusting the mix proportions, such as the type of cement, aggregate, SCMs, W/C ratio, and quantity of reinforcement, for example, may improve the early-age properties of concrete. The purpose is to use the right materials so that the overall volume change of the massive concrete is minimal. For example, aggregate type has a significant impact on the total thermal expansion of concrete (figure 1.39).

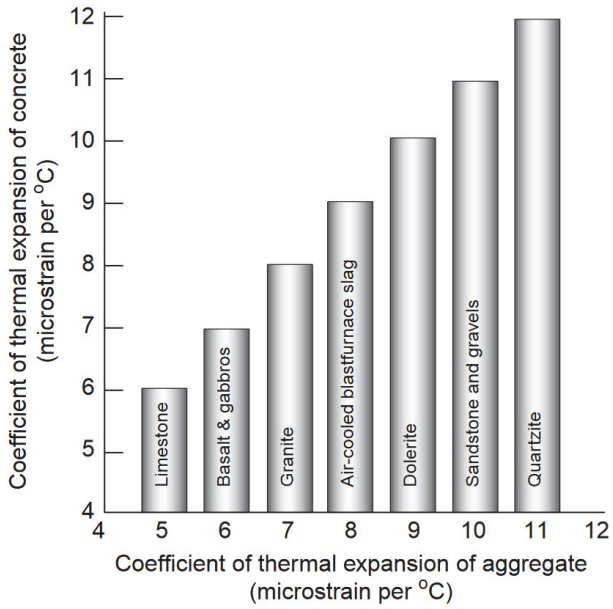

Figure 1.39 – Influence of aggregate on thermal expansion of concrete [266]

Furthermore, temperature control is a common approach utilized to cool down the massive concrete construction. The temperature control has been divided into different stages such as pre-cooling of mix constituents, cooling concrete during the mixing procedures (figure 1.40), controlling temperature during transport and placement, selecting and designing suitable surface measures for temperature control, post-cooling with water or air (figure 1.41), and scheduling of construction stages [6].

Finally, numerical modelling may be used to manage and prevent excessive temperatures within massive concrete. The numerical modelling enables the engineer to foresee and avoid cracks. Engineers have been utilizing coupling models to predict the influence of one phenomenon on another as computer capabilities has improved. The individual models that have been used so far are mechanical, thermal, chemical, and hygro. For exmaple, thermo-chemical coupling model has been used to study the thermal conductivity of cement-based materials in function of microstructure change with time [267]. Fur-



Figure 1.40 – Cooling the concrete truck by injecting nitrogen

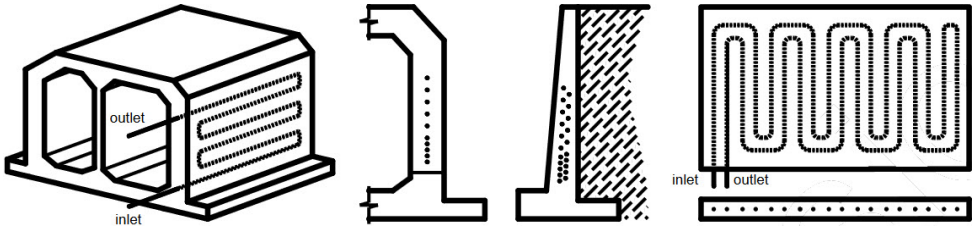

Figure 1.41 – Post cooling concrete pipe layouts in different type of structure [6], [262]

thermore, multi-phase and multiscale modelling, such as **MuMoCC** (see section 1.2.2.6), benefit the engineer by considering all mixed phases to form cement-based materials.

Chapter 2

Theoretical framework, hypotheses, and homogenization

The cement-based materials chosen in this study are cement paste (microscale) and mortar (sub-mesoscale). The platform MuMoCC is developed in this thesis which is devoted to the heat transfer simulation in order to find the thermal properties of cement paste and the result obtained is used as the hypothesis at sub-mesoscale (Mortar). In this study, thermal properties are thermal conductivity (k), specific heat (c_p), and coefficient of thermal expansion (α).

2.1 Cement-based materials

The cement-based materials in this study is the materials that have been studied for radioactive waste disposal over a 300 years period. Adenot and Buil have studied the corrosion of the cement paste by deionized water [268], Mainguy et al. have analysed the leaching of cement paste and mortar by modelling and comparing with experimental result [269], while Le Bellégo et al. [270] have studied the chemo-mechanical effects on mortar that is submerged in aggressive water causing calcium leaching, and Kamali-Bernard et al. [12], [29] have used the multiscale modelling to study the effect of leaching on mechanical properties of the cement paste and mortar. The cement paste and mortar considered in this investigation will be described in detail in sections 2.1.1 and 2.1.2.

2.1.1 Cement paste

The cement paste composition used in this investigation has been reported in various studies about radioactive waste disposal. Cement CEM I 42.5 is used to make cement paste with a water-to-cement ratio (w/b) of 0.4. The hydration degree chosen in this study is 0.27, 0.55, and 0.83. Table 2.1 and 2.2 shows the mineralogical compositions of

CEM I 42.5 and the hydration products of cement paste obtained from **CEMHYD3D** at various hydration degrees.

C_3S	C_2S	C_3A	C_4AF	Gypsum
42.9	13.9	5.15	5.65	3.93

Table 2.1 – Mineralogical composition cement CEM I 42.5 (in %)

Mineralogical compositions	Hydration degree		
	0.27	0.59	0.83
C_3S	13.64	3.64	1.23
C_2S	8.07	5.60	2.76
C_3A	2.49	1.04	0.07
C_4AF	2.21	1.88	0.87
Gypsum	1.34	0.33	0.33
C-S-H	13.71	34.12	43.8
CH	5.28	12.52	15.6
AFt	6.87	7.35	5.62
AFm	0.07	2.65	4.87
C_3AH_6	0.79	2.51	4.61
FH_3	0.38	0.58	1.11
Porosity	45.16	27.79	18.4

Table 2.2 – Mineralogical compositions and hydration products of cement paste (in %)

In terms of porosity (in table 2.2), it is filled with either air, water, or a combination of the two, resulting in varying degrees of saturation. In this investigation, several degrees of hydration were chosen: 0 (no water), 0.25, 0.5, 0.75, and 1 (filled with water).

2.1.2 Mortar

Mortar is a mixture of cement paste (described above) and limestone sand in a 1:1 ratio. Two limestone sands have been used in this study: Sand S_1 0.8/3.15 (diameter ranging from 0.8 to 3.15 mm) and S_2 0.5/1.6 (diameter ranging from 0.5 to 1.6 mm).

2.2 Heat transfer in Multi-scale Modeling of Computational Concrete (MuMoCC)

2.2.1 Analytical homogenization

In order to compute the thermal properties of cement-based materials under analytical homogenization, a morphology of cement-based materials is required. The morphology used in this study (figure 2.1) is the expansion of the composite sphere model in the published article of Bernard et al. [5].

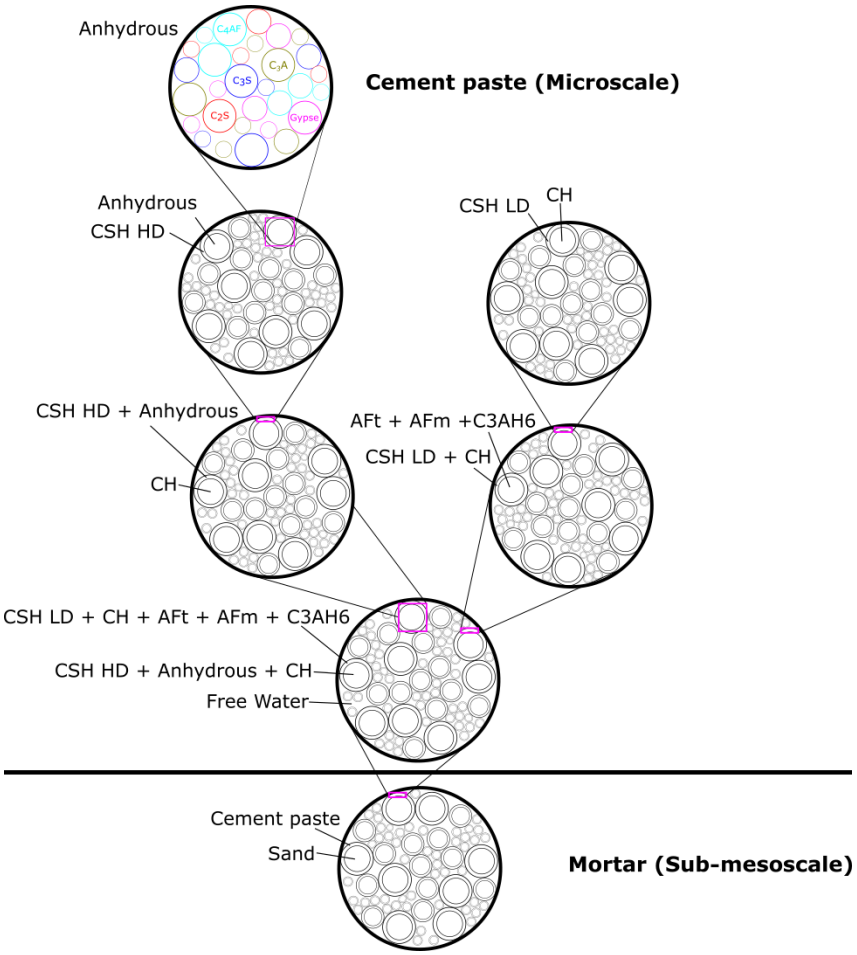

Figure 2.1 – Morphology of cement-based materials for analytical homogenisation

In this morphology, anhydrous is the combination of C_3S, C_2S, C_3A, C_4AF, and gypsum. Moreover, the anhydrous is embedded inside the C-S-H HD. The C-S-H exists in

two forms, C-S-H HD (high density) and C-S-H LD (low density). The C-S-H HD is the C-S-H with a gel porosity of about 24%, while the porosity of C-S-H LD is about 35-37%. Furthermore, the proportion of C-S-H LD may be calculated using the Jenning's relationship (equation 2.1). Then, the C-S-H HD can be found by subtracting the C-S-H LD from the total C-S-H. The portlandite (CH) is embedded in both C-S-H forms; however, AFt, AFm, and C_3AH_6 are only embedded in the C-S-H LD. With the addition of free water, the C-S-H LD is inserted within the C-S-H HD to make the cement paste. Finally, the cement paste finding is upscaled to become the sub-mesoscale mortar hypothesis.

$$r_{\text{LD}} = \frac{m_{\text{C-S-H LD}}}{m_{\text{C-S-H total}}} = \left[3.017\left(\frac{E}{C}\right)\alpha\right] - 1.347\alpha + 0.538 \tag{2.1}$$

where
r_{LD} : ratio of C-S-H LD to total C-S-H,
$m_{\text{C-S-H LD}}$: mass of C-S-H LD,
$m_{\text{C-S-H total}}$: mass of total C-S-H,
$\frac{E}{C}$: water to cement ratio,
α : degree of hydration.

2.2.2 Numerical homogenization

This section requires two steps for numerical homogenization in a FEM framework: geometries generation and FEM Analysis. **CEMHYD3D** is used to build cement paste geometries, whereas the take-and-place method are utilized to create mortar geometries in addition to **CEMHYD3D**. After the geometries are created, they are imported to Abaqus FEA to perform numerical simulations, namely heat transfer or mechanical analysis. As with analytical homogenization and process of MuMoCC, acceptable numerical analysis results at the cement paste scale (microscale) are considered as the hypothesis at the mortar scale (sub-mesoscale).

2.2.2.1 Cement paste representative volume element

As previously mentioned, the geometries of cement paste and mortar are developed individually using **CEMHYD3D**. It is a well-known software which is able to simulate hydration of a dry microstructure of a cement. After the geometries are created, a C++ code has been created which enables the user to transfer geometries to FEM meshes for numerical analysis. As stated in section 2.1.1, three degrees of hydration of cement paste are considered: 0.27, 0.55, and 0.83, requiring three distinct geometries of cement

paste. The cement paste and mortar configuration can be found in figures 2.2 and 2.3, respectively.

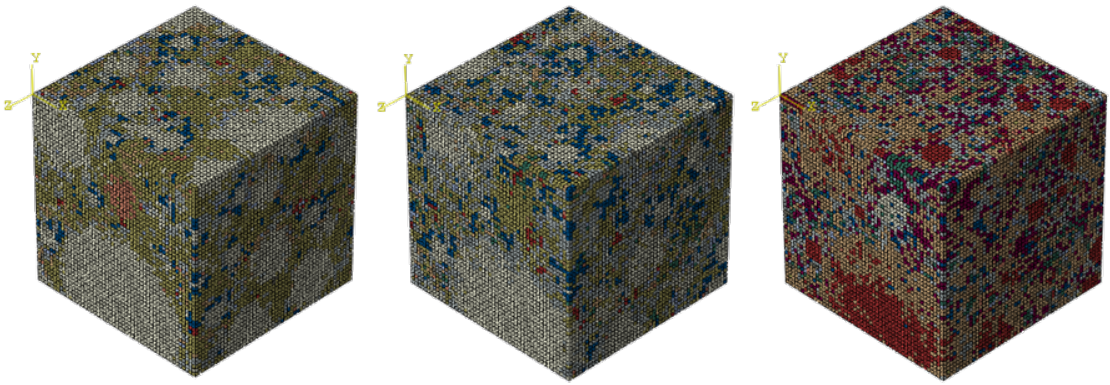

(a) α=0.27 (b) α=0.55 (c) α=0.83

Figure 2.2 – FEM meshes of cement paste imported from **CEMHYD3D** with different degrees of hydration (α)

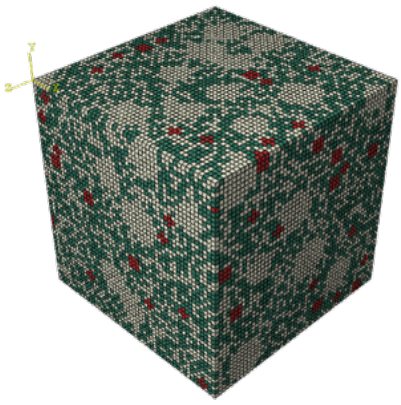

Figure 2.3 – FEM meshes of mortar imported from **CEMHYD3D**

2.2.2.2 Take-and-place methods

In this section deals with the creation of numerical representative volume element of mortar in which aggregates are explicitly taking into account. Moreover, two take-and-place methods are used: the original take-and-place method and improved take-and-place method proposed by Rhardane (figure 1.27) [55]. These methods are only used at the sub-mesoscale (mortar) level, when inclusions (sand grains) are introduced into the

matrix (cement paste). From this point forward, the original take-and-place approach and Rhardane's take-and-place method are referred to as **Method A** and **Method B**, respectively. The particle distribution of the inclusion respect the Fuller's curve as shown in equation 2.2.

$$P(d) = 100\left(\frac{d}{d_{\max}}\right)^{n}, n \in [0.45; 0.7] \tag{2.2}$$

where P(d) : total percentage passing through an opening diameter sieve d,
d : sieve's diamter,
d_{max} : largest inclusion diameter ($d_{max} = 3.15\mu m$),
n : exponent of the Fuller's curve.

The sieve's diameters chosen in this study are the minimum and maximum diameter of the sand inclusion S_1 (0.8 and 3.15 mm) and S_2 (0.5 and 1.6 mm). The Fuller's curve in this study is shown in figure 2.4.

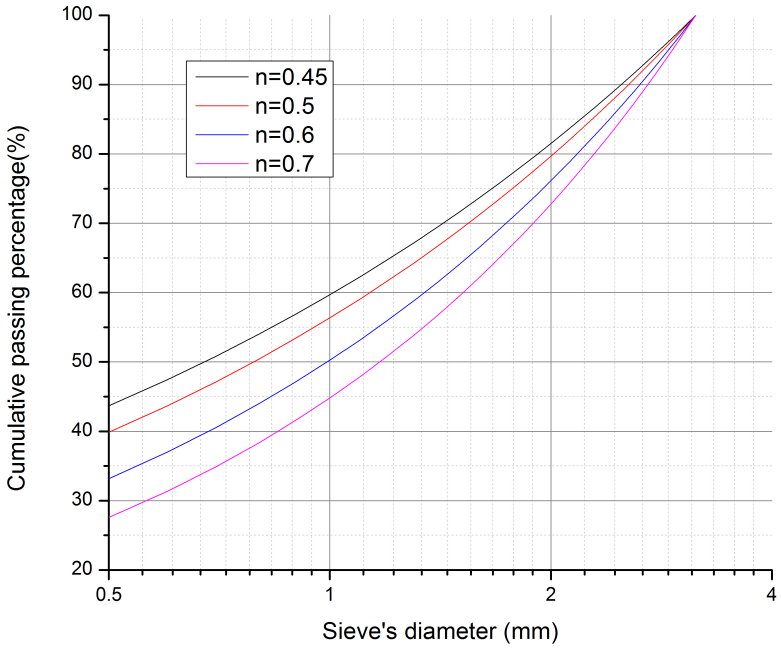

Figure 2.4 – Fuller's grading curve

The total proportion of each diameter (0.5, 0.8, 1.6, and 3.15 mm) of the sand grains could be computed using Fuller's curve (figure 2.4). The value n=0.7 was used in this investigation to minimize the fraction of the smallest particles.

Sand's diameter (mm)	Total percentage (%)	Percentage in mortar (%)
3.15	36.28	18.14
1.6	23.5	11.75
0.8	10.44	5.22
0.5	29.78	14.89

Table 2.3 – Percentage of each sand's diameter

For each case study, a unique algorithm of the take-and-place method is required. figures 2.5 and 2.6 depict the algorithms of Methods A and B in this example. The *placing* process distinguishes Method A from Method B. Method B has no overlap verification phase in the *placing* process, making it a more time efficient method than Method A.

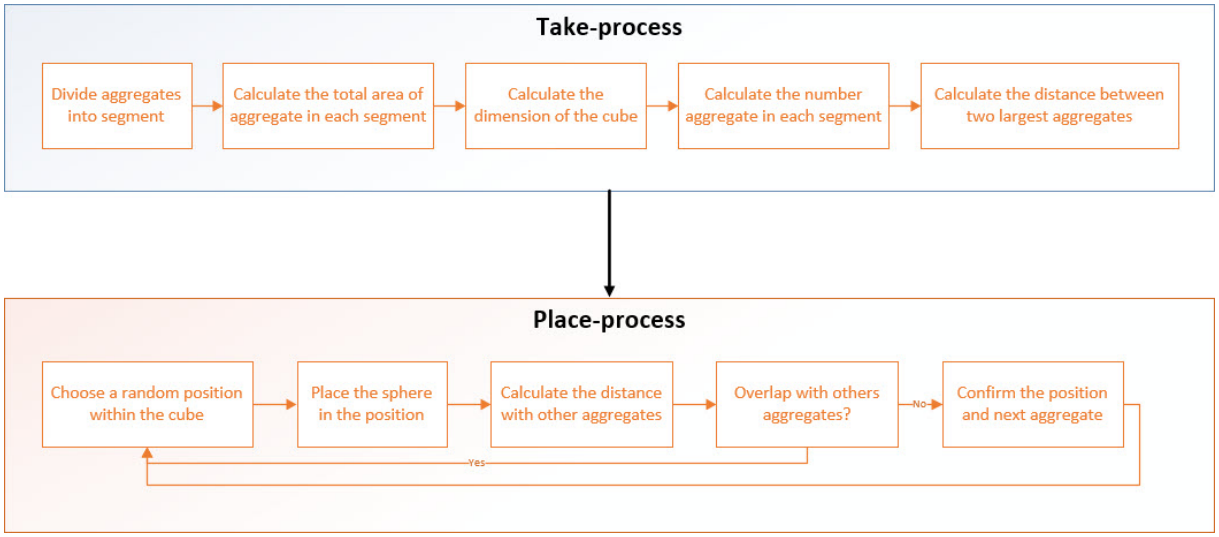

Figure 2.5 – Methodology of original take-and-place (Method A)

Both methods were examined and the results are shown in figures 2.7 and 2.8. Several RVE sizes were evaluated to determine the highest percentage of inclusion that could be accommodated inside the RVE. RVE sizes are represented as L/D (length of the RVE cube to diameter of inclusion) starting from 2.45 (Method A) and 2.33 (Method B) to 3.59.

Two observations could be derived from figures 2.7 and 2.8. First, it is feasible to begin with a smaller RVE size, L/D = 2.33 for Method B, while slightly more prominent, L/D = 2.45 for Method A. Second, it is possible to slightly pack more inclusion with

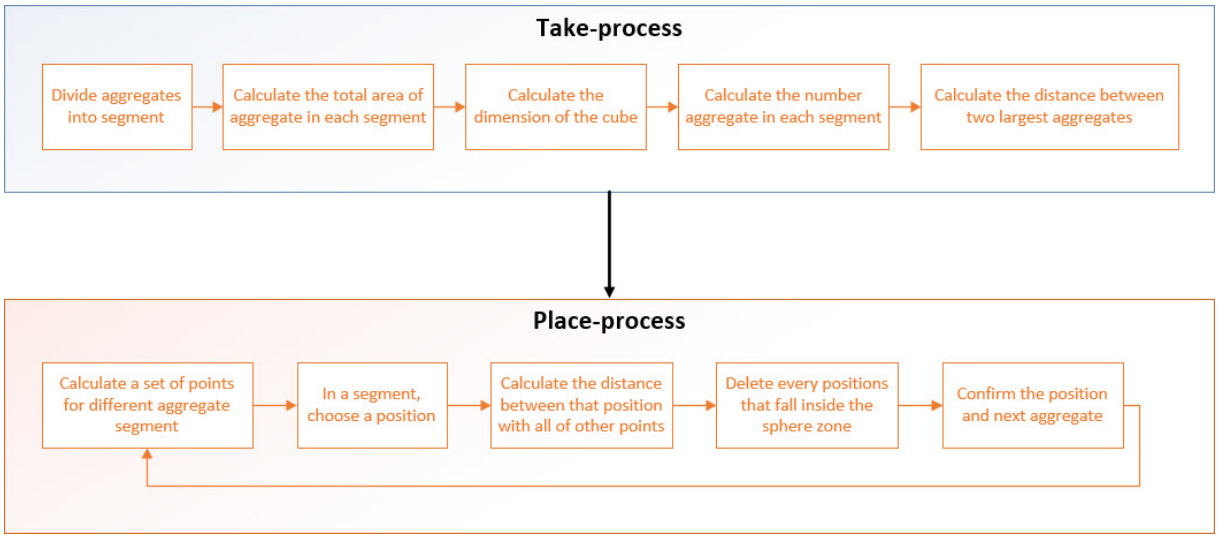

Figure 2.6 – Methodology of improved take-and-place method proposed by Rhardane [55] (Method B)

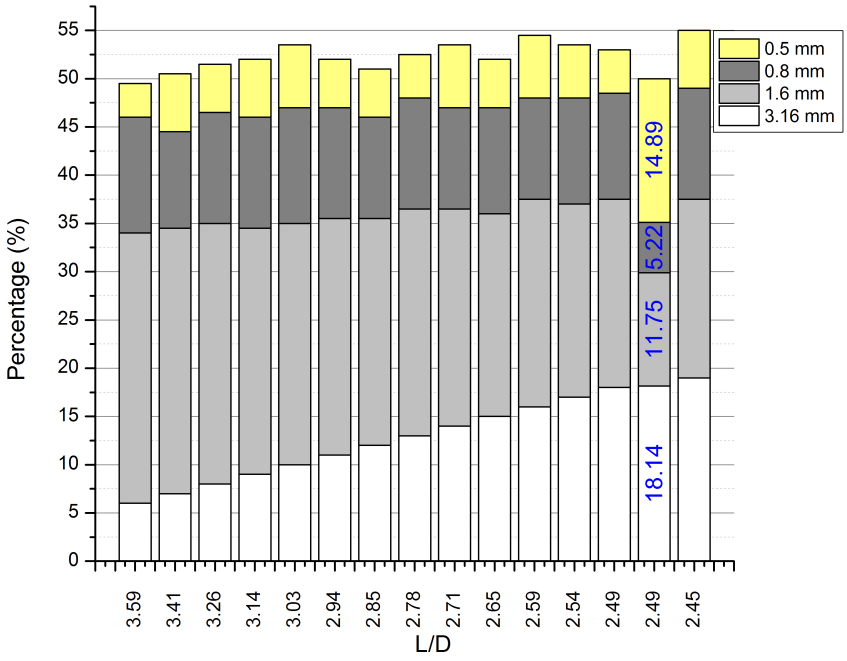

Figure 2.7 – Original take-and-place (Method A)

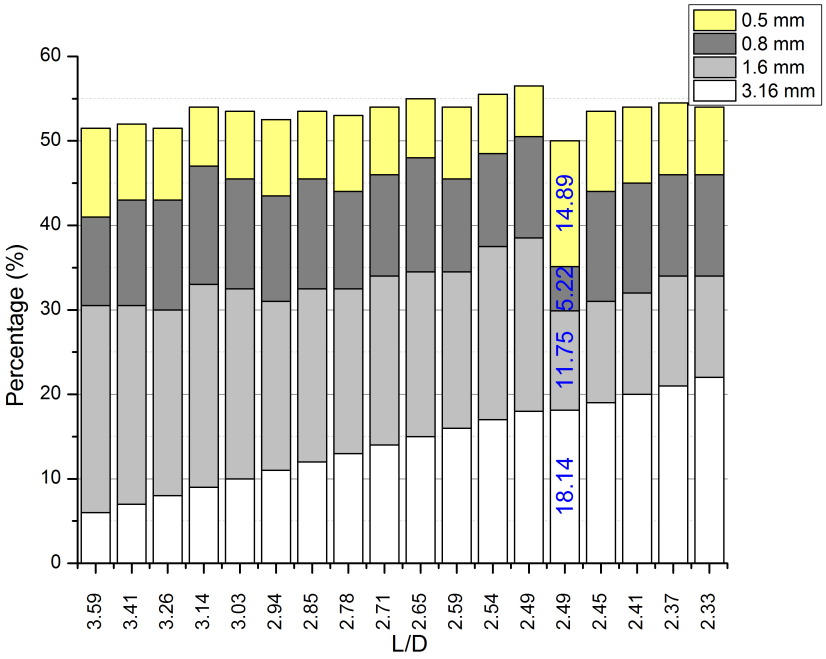

Figure 2.8 – Take-and-place by Rhardane (Method B)

Method B compared to Method A; for example, L/D = 2.49, the maximum packing is 56.5% for Method B and 53% for Method A. Furthermore, by using these methods, it is possible to generate RVE with particle distribution that respects the Fuller's curve at L/D = 2.49. As mentioned by Rhardane et al. [55], one of the advantages of Method B is that it takes less time than Method A. In this case, Method A, for example, can take up to 86 minutes to create an RVE at L/D = 2.49, but Method B takes just 6 minutes. Method B is, therefore, more than 14 times faster than Method A.

2.2.2.3 Heat transfer simulation with Abaqus FEA

Thermal properties of cement-based materials, such as cement paste and mortar, are determined using the commercial Finite Element Analysis software **Abaqus FEA**. Nonetheless, each thermal property necessitated different heat transfer simulations and boundary conditions. Thermo-mechanical properties such as thermal conductivity, specific heat, and coefficient of thermal expansion are examined using various simulations in this study. The following summarizes the simulation type, boundary conditions, loads, and FEA simulation outputs from Abaqus:

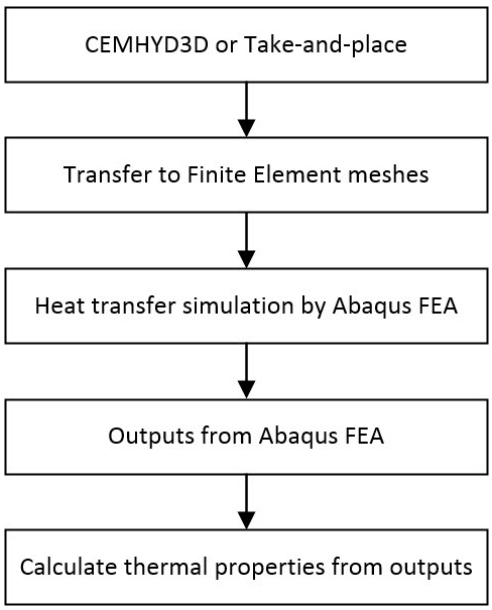

Figure 2.9 – Algorithms for Finite Element Analysis

	Thermal conductivity (h)	Specific heat (Cp)	Coefficient of thermal expansion (α)
Simulation type	Uncoupled heat transfer	Uncoupled heat transfer	Coupled thermal-mechanical
Regime	Steady-state	Transient	Steady-state
Loads	Temperature gradient	Decrease uniform temperature overtime	Increase uniform temperature overtime
Outputs	Heat flux	Temperature profile	Displacement in three directions

Table 2.4 – Heat transfer simulation in Abaqus FEA

2.2.3 Thermal properties of cement-based materials

As discussed in the section 2.1, the components that make up cement-based materials are limestone sand, water, and cement CEM I 42.5. The thermal characteristics of these mixtures are outlined in table 2.5, which may be found here.

Compositions	Thermal conductivity (W/m.K)	Specific heat (J/kg.K)	Coefficient of thermal expansion (10^{-6}/°C)
C_3S	3.45	745	8.56
C_2S	3.45	741	10.42
C_3A	3.45	768	6.46
C_4AF	3.45	813	4.06
Gypse	0.66	1080	48.299
C-S-H	0.98	727	14.5
CH	1.32	1140	23.3
AFt	3.45	1502	35.33
AFm	3.45	1001.55	35.33
C_3AH_6	3.45	893.5	5.44
FH_3	-	-	-
Free water	0.61	4182	200
Air	0.0262	1006	-
Quartz sandstone	2.6	1000	-
Hard stone	1.7	1000	-
Tuffeau limestone	0.6	656	1.43

Table 2.5 – Thermal properties of cement-based materials' compositions [5], [271]–[275]

2.3 Thermal conductivity of cement-based materials

2.3.1 Analytical homogenization of thermal conductivity

The analytical homogenization methods presented in Section 1.2.2.1 are used to assess cement paste and mortar thermal properties with varying degrees of hydration and saturation. The figure 2.10 and 2.11 depict the thermal conductivity of cement paste and mortar in function of hydration degree at saturation degree = 100%.

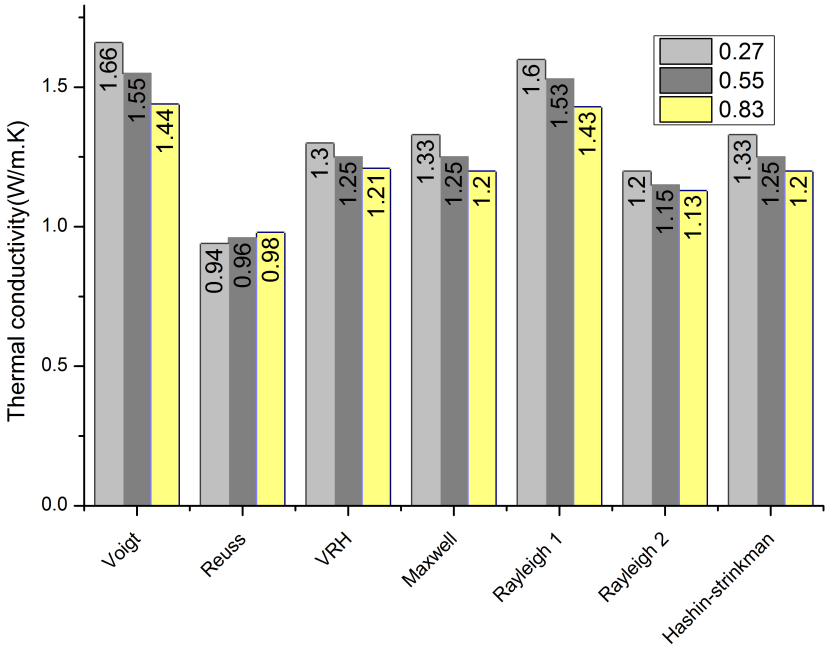

Figure 2.10 – Thermal Conductivity of cement paste in function of hydration degree for various homogenisation schemes

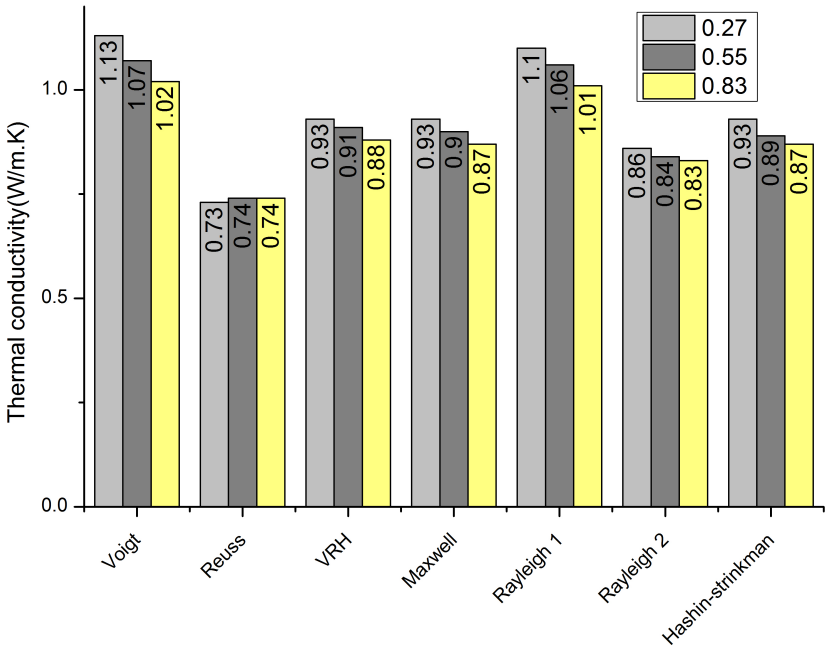

Figure 2.11 – Thermal Conductivity of mortar in function of hydration degree for various homogenisation schemes

The thermal conductivity of cement paste and mortar varies with the degree of hydration (or in function of time). Voigt and Reuss are the upper-bound and lower-bound, and it can be observed that the results from VRH, Maxwell, Rayleigh 1, Rayleigh 2, and Hashin-strinkman are within the bounds. At saturation degree = 100%, the thermal conductivity of cement-based materials decreases with time.

Saturation degree	Thermal conductivity (W/m.K)	Specific heat (J/kg.K)	Coefficient of thermal expansion (10^{-6}/°C)
0	0.026	718	3380
0.25	0.103	1244.756	1632.198
0.5	0.184	1837.791	1083.827
0.75	0.278	2605.814	628.254
1	0.608	4182	200

Table 2.6 – Thermal properties of porosity homogenized with regard to saturation degree

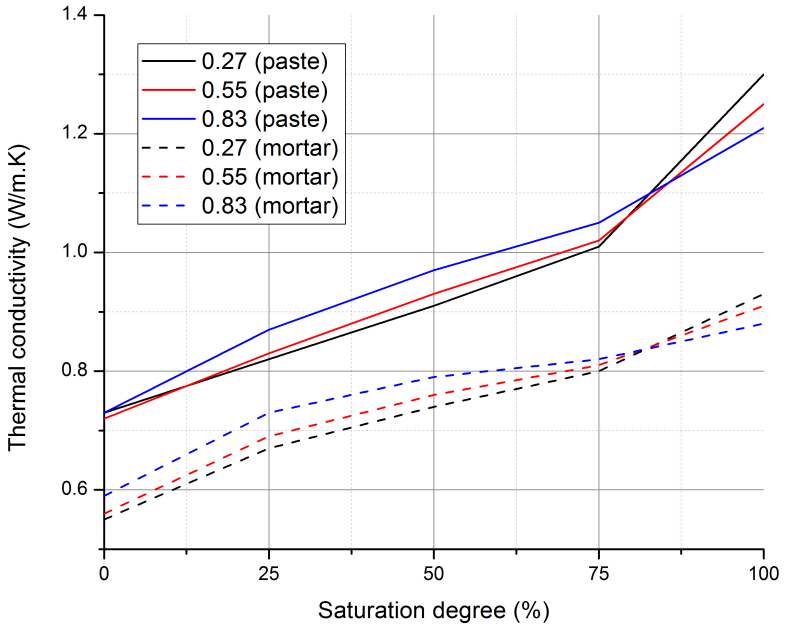

Figure 2.12 – Analytical result of thermal conductivity in function of saturation degree

The results of measuring the thermal conductivity of cement paste and mortar are

shown in figure 2.12, organized according to the saturation degree. Furthermore, the saturation degree is considered by providing the porosity of the homogenized thermal properties between water and air. The VRH homogenisation scheme is used to calculate the value of these homogenized thermal properties. Table 2.6 summarizes the homogenized value of the porosity's thermal properties in relation to the saturation degree. In general, the thermal conductivity of cement paste is lower than that of mortar. It is because the sand, introduced at a sub-mesoscale, has a lower thermal conductivity than cement paste. In addition to the conclusion that was drawn earlier, the result proves that the thermal conductivity of cement-based materials has risen with time at lower saturation degrees (from 0% to 75%).

2.3.2 Numerical homogenization of thermal conductivity

In this section, Abaqus FEA is used to model a heat transfer problem. The steady-state analysis of a heat transfer problem, as discussed in section 2.2.2.3, is utilized to determine the thermal conductivity of cement-based materials. The next section describes the initial and boundary conditions in details.

2.3.2.1 Initial, boundary conditions, and thermal conductivity calculation

The simulations are performed in 3D, and figure 2.13 illustrates the 2D cross-section of the RVE with the boundary conditions used in the simulations. The boundary conditions in this section are the nodal temperatures expressed in kelvin (K). First, the initial condition, $T_{int} = 298.15$ K, is defined at all nodes of the RVE. Then, at the left and right end nodes, the boundary conditions, $T_{hot} = 375.15$ K and $T_{cold} = 298.15$ K, are designated. Such methodology has already been employed to determine the diffusion coefficient in the mass transfer problem [56].

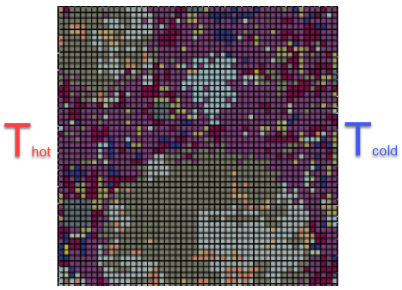

Figure 2.13 – Initial and boundary conditions for thermal conductivity calculation

After the heat transfer simulation has been carried out, the thermal conductivity may be computed by taking outgoing heat flux at the end where the temperature is lower and simplifying the equation 1.26.

$$k = \frac{Q \times L}{T_{\text{hot}} - T_{\text{cold}}} \tag{2.3}$$

where k : thermal conductivity of cement-based material,
Q : outgoing heat flux at where the temperature is equal to T_{cold},
L : length of the sample,
T_{cold}, T_{hot} : lower and higher boundary condition temperatures.

2.3.2.2 Verification of Representative Volume Element (RVE)

By utilizing Take-and-place method and Fuller's curve described in section 2.2.2.2, it is possible to calculate the Representative Volume Element, also known as the RVE, for the thermal conductivity of mortar. The initial conditions and the boundary conditions are implemented in the same manner as described in section 2.3.2.1. First, the RVE estimates the smallest feasible dimension, which in this instance is L/D=2.44, and then gradually increases the size of the dimension until the variance in the sample is low enough that it is possible to disregard the heterogeneity of the mortar. Figure 2.14 presents the outcomes of conducting heat transfer simulations on various volumes.

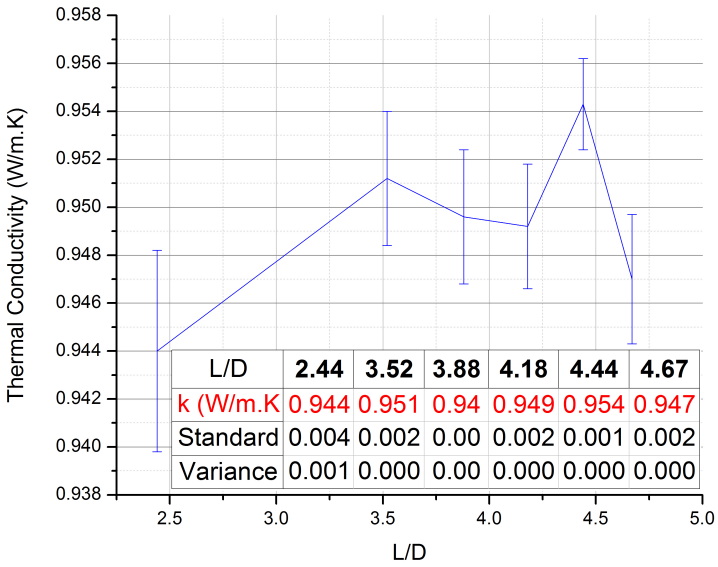

Figure 2.14 – Representative Volume Element's (RVE) size for mortar

It is possible to draw a conclusion that even for a dimension of volume element of 2.44 times the diameter of the largest inclusion can be considered as RVE due to the fact that the variance is very low. More specifically, it is less than 5% mentioned in [55]. In conclusion, the RVE that was evaluated for use in mechanical simulation in previous work [9], [10], [29], [56], [89], [91], [185] may also be utilized in the modeling of heat transfer since its dimension is at least four times that of the largest inclusion.

2.3.2.3 Results from numerical simulation

The result of the numerical simulation for thermal conductivity is shown in figure 2.15. The calculations are performed at various saturation degrees. Since considerable free water has not yet interacted with the cement particle, the impact of saturation degree is more obvious at low hydration degrees. It demonstrates that the degree of saturation does, in fact, affect the thermal conductivity of cement-based materials. The thermal conductivity of cement paste seems to change at different hydration degrees, when the saturation degree is set to 0%. In every other case, the gap decreases as the saturation degree gets higher. When the saturation degree is 100% (fully saturated), the hydration degree has a minor effect on the homogenized value of thermal conductivity.

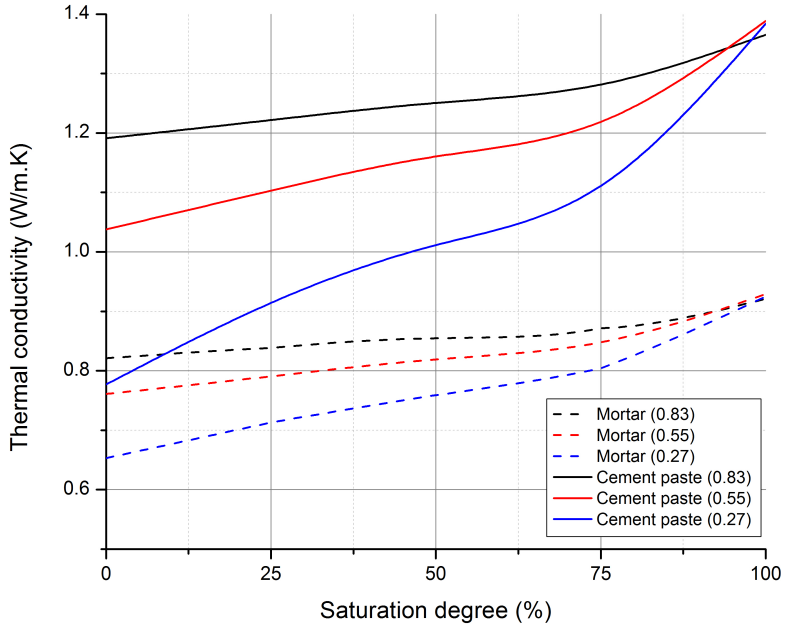

Figure 2.15 – Numerical simulation result of thermal conductivity in function of saturation degree

In addition to the aforementioned results, several simulations were conducted using different types of sand, including Quartz Sandstone, Hard Stone, and Tuffeau limestone. The results, as depicted in Figure 2.16, reveal that the thermal conductivity of the mortar is influenced by the type of sand utilized in the mixture. Notably, the mortar containing Quartz Sandstone exhibited the highest thermal conductivity compared to the mortar with Hard Stone and Tuffeau limestone. This difference can be attributed to the inherently higher thermal conductivity of Quartz Sandstone. Furthermore, the mortar with Hard Stone demonstrated a lower thermal conductivity than the one with Quartz Sandstone but a higher value than the mortar with Tuffeau limestone. This suggests a clear proportionality between the thermal conductivity of the mortar and the thermal conductivity values of its components, including the cement paste and the chosen sand inclusion.

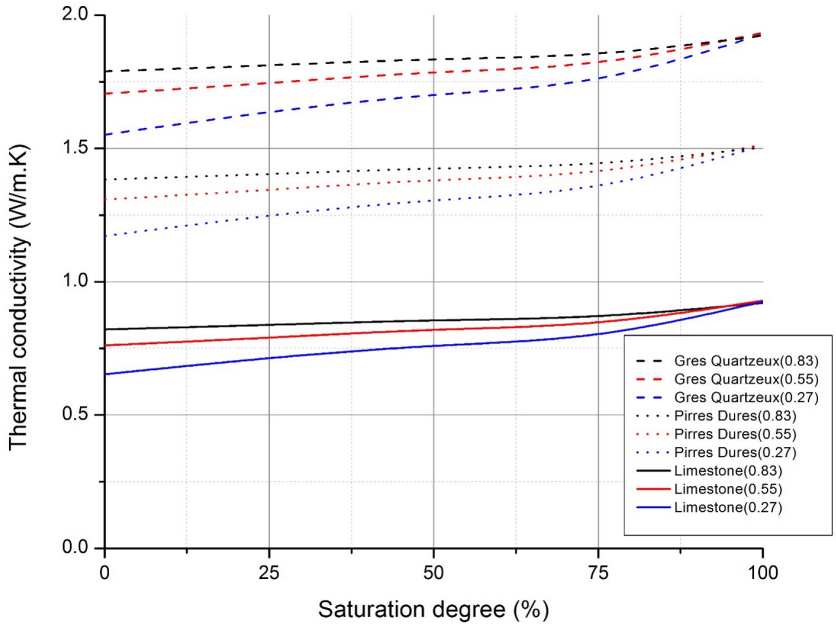

Figure 2.16 – Numerical simulation result of thermal conductivity with different types of sand

2.3.3 Conclusion

This chapter investigates the thermal conductivity of cement-based materials for both analytical and numerical homogenization. The results have been presented, and the conclusions can be drawn as below:

— The thermal conductivity of fully saturated cement paste at high hydration cal-

culated by FEM, around 1.3 W/m^{2}K, matches well with the value obtained from various analytical schemes,

— Due to the incorporation of limestone sand, which has a low thermal conductivity, the thermal conductivity of mortar is often lower than that of cement paste,

— For analytical homogenization, the thermal conductivity does not appear to differ between different hydration degrees at any saturation degree,

— On the other hand, numerical homogenization reveals that when the saturation degree is set to 0%, the thermal conductivity seems to vary depending on the hydration degree. Still, the difference appears to narrow as the saturation degree increases,

— Thermal conductivity of cement paste can be directly used as the hypothesis at sub-mesoscale (mortar level),

— The size of the RVE used for the heat transfer simulation can be as small as L/D = 2.44, which is less than the size used for the mechanical simulation,

— The TCC does have some effect on the thermal conductivity of mortar, but only to the extent that it is less than 10^3 W/m^{2}K,

— The only study case that can cause the TCC to have influence on thermal conductivity of mortar is when there is air gap, which is larger than 30μm, at the interface between limestone sand and cement paste. It could represent the micro-cracks that occur in a real structural member.

In summary, the purpose of this chapter was to illustrate how to determine and homogenize the thermal conductivity of cement-based materials at two separate scales. Comparisons have been made between analytical and numerical homogenization, and the thermal contact conductance (TCC) has also been investigated. Both the degree of hydration and the degree of saturation of the cement-based products have been examined. The findings of this chapter's investigation of thermal conductivity can also be used as hypotheses for analyzing specific heat in the following chapter (chapter 2.4).

2.4 Specific heat of cement-based materials

2.4.1 Analytical homogenization of specific heat

In the same way that analytical homogenization is used to calculate thermal conductivity, analytical methods from section 1.2.2.1 are used to determine the specific heat of

cement-based materials. The specific heat of cement paste and mortar is shown to be a function of hydration degree in figures 2.17 and 2.18, respectively, when the saturation degree is set to 100%.

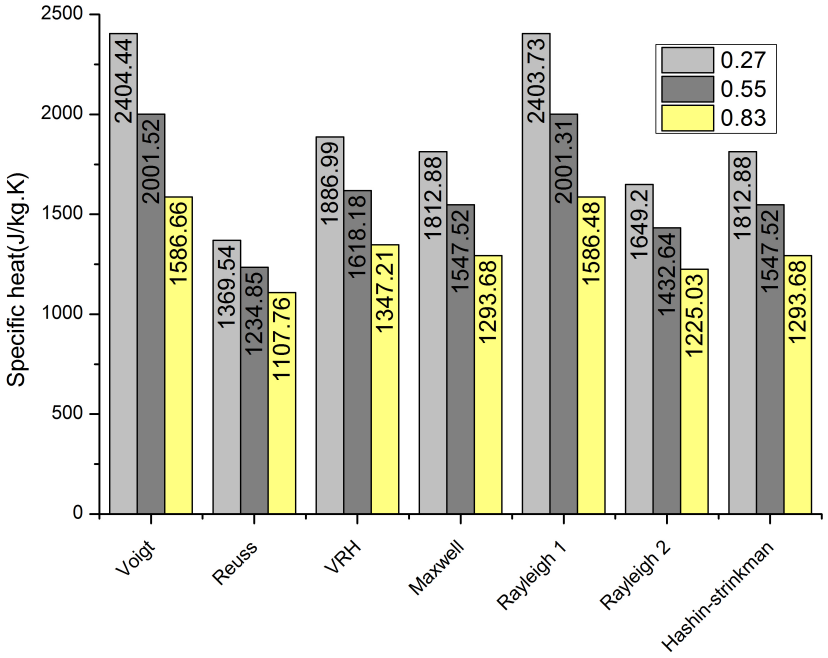

Figure 2.17 – Specific heat of cement paste in function of hydration degree

When the saturation degree approaches 100%, there is a possibility that the specific heat may drop with time. This is also the fact with thermal conductivity. On the other hand, this is not the case when the saturation degree is 0%. There has been a minor rise in the specific heat over time. Another conclusion that may be drawn from figure 2.19 is that compared to the cement paste, the specific heat of mortar appears to be lower. Moreover, it has the same tenancy as cement paste for specific heat.

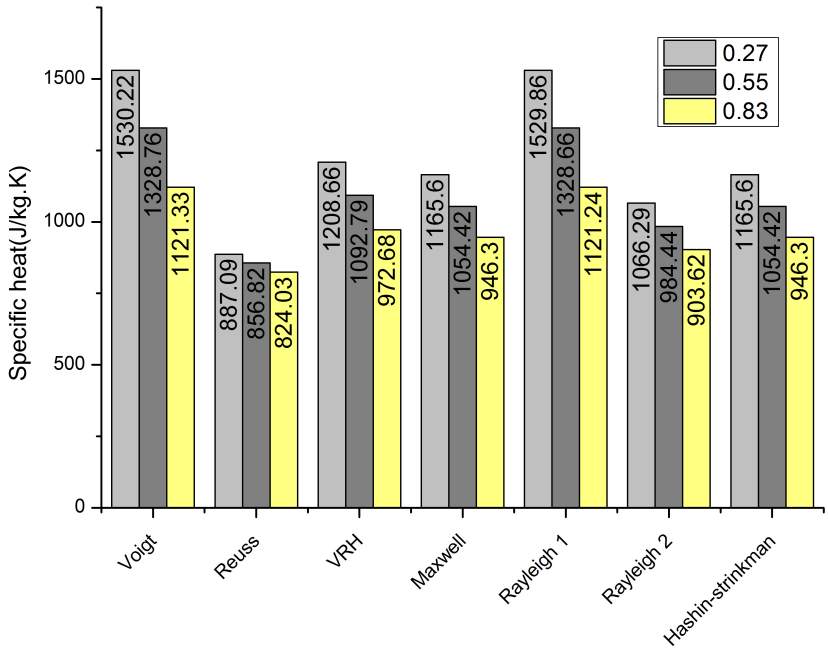

Figure 2.18 – Specific heat of mortar in function of hydration degree

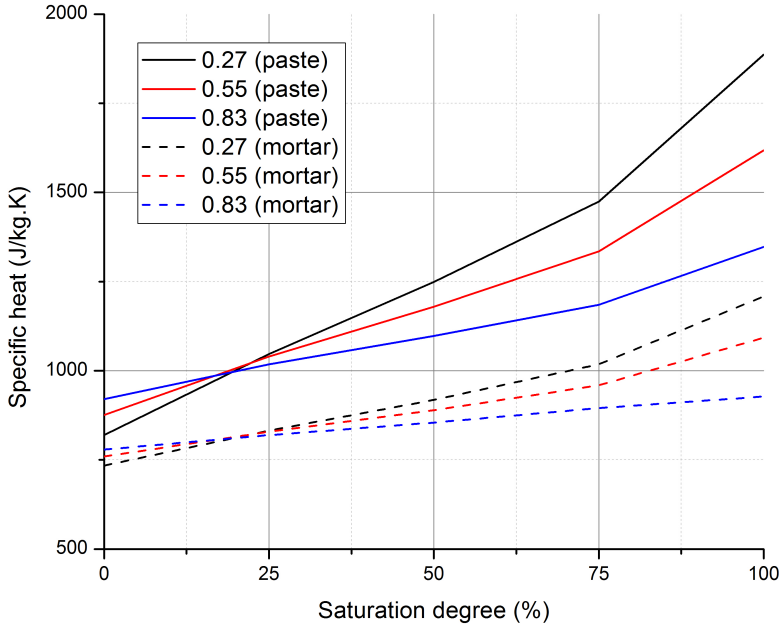

Figure 2.19 – Analytical result of specific heat in function of saturation degree

2.4.2 Numerical homogenization of specific heat

Concerning the numerical homogenisation of specific heat, the same model that was used from **CEMHYD3D** software that was used to study thermal conductivity of cement-based materials (see section 2.3.2) is considered. However, the specific heat cannot be computed directly using simply numerical simulation. In this work, it was proposed to determine it by combining numerical simulation with the inverse analysis approach. Specific heat, unlike thermal conductivity and the diffusion coefficient, has no analog in other physical parameters. Its determination in a FE framework must be specified. The analytical approach presented in section 2.4.2.1 is first considered. This approach allows us to get temperature profiles over the sample. These temperature profiles are then fitted into those obtained by numerical simulation by varying the specific heat. The following section will detail the analytical method and the numerical simulations.

2.4.2.1 Analytical approach in heat conduction problem

The equation of the heat conductance problem (section 2.4.2.1.1) serves as the starting point for this analytical approach. The initial and boundary conditions (section 2.4.2.1.2) are then applied in order to resolve the equation using Fourier solution (section 2.4.2.1.3), which results in the equation of temperature development (or temperature profile) across the sample.

2.4.2.1.1 Equation of heat conduction problem The equation 1.23 is a three-dimensional Cartesian coordinate and it is feasible to employ a one-dimensional problem (equation 2.4) to this specific heat calculation.

$$\rho c_p \frac{\partial T(x,t)}{\partial t} = \frac{\partial}{\partial x}\left(k \frac{\partial T(x,t)}{\partial x}\right) \tag{2.4}$$

It is essential to notice that the heat generated by the material is not accounted for in the equation that was just presented. This equation may be solved, and the result will give the temperature development throughout a thickness of material in the form of a Fourier series [276]. The problem's initial and boundary conditions must be respected to find a solution to this equation.

2.4.2.1.2 Initial and boundary conditions This analytical approach utilizes the identical initial and boundary conditions as the numerical simulation described in table

2.4, which can be seen below. T_{hot}(=298.15K) is set as initial condition which has higher temperature than T_{cold}(=273.15K) which are the boundary conditions.

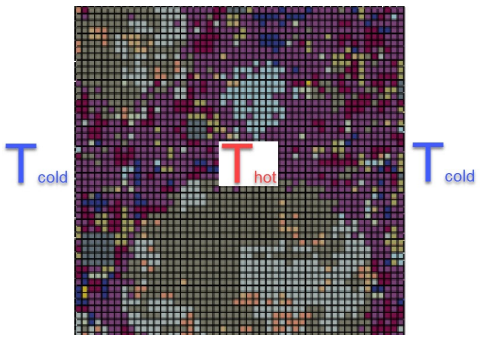

Figure 2.20 – Initial and boundary conditions for specific heat calculation

2.4.2.1.3 Fourier solution After the initial and boundary conditions are applied, the equation 2.4 is resolved and the result is in form of Fourier's series [276], [277] expressed as below.

$$T(x,t) = \frac{4T_0}{\pi} \sum_{n=0}^{\infty} \frac{1}{2n+1} \exp \frac{-\alpha(2n+1)^2\pi^2 t}{L^2} \sin \frac{(2n+1)\pi x}{L} \tag{2.5}$$

and

$$\alpha = \frac{k}{\rho c_p}$$

where T_0 : initial temperature (or T_{cold}),
L : length of the sample (m),
t : time period,
n : 12 is chosen so that the last term is very small.

The temperature profile may be shown by adjusting the specific heat (c_p), and then it can be compared to the one that was obtained from the numerical simulation from section 2.4.2.2.

2.4.2.2 Numerical approach in heat conduction problem

The numerical simulation is carried out on the samples that were transformed to finite element mesh from **CEMHYD3D** (section 2.2.2.1) by employing the initial and boundary conditions in the same way as an analytical approach would (section 2.4.2.1.2).

In addition, it is important to highlight that the simulation is carried out in the transient regime.

Python code is being utilized in this simulation to help speed up and make the process of extracting results (temperature profiles) from Abaqus FEA more straightforward. The samples were initially cut into 51 parallel plans that were equally spaced apart. The first plan may be seen on the far left, and the last plan can be found on the far right (figure 2.21). The average temperature for each plan was computed; the temperature profile was plotted by connecting all of the points of average temperature.

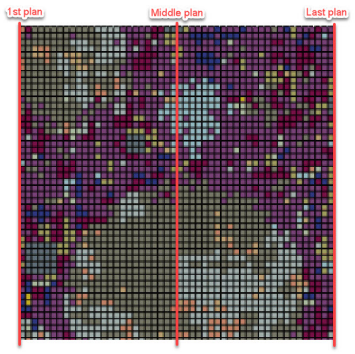

Figure 2.21 – Sample for specific heat calculation (hydrated cement paste)

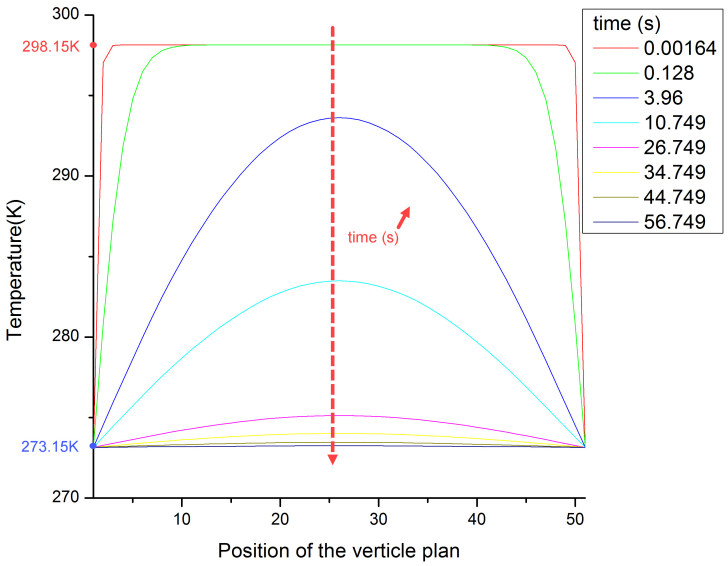

Figure 2.22 – Temperature profile of mortar at α=0.83

Figure 2.22 depicts the example of temperature profile of mortar when α is equal to 0.83. As the time step increases, it is possible to see that the temperature curve tends to fall downward, moving closer and closer to the constant value of the boundary conditions, which is 273.15K.

2.4.2.3 Fitted curve analysis (inverse analysis) for specific heat

After obtaining the temperature profile from Abaqus FEA, the primary objective is to reduce the gap that separates the curve produced from the analytical formulation and the output of numerical simulation by adjusting the c_p value in equation 2.5. It has to be done at every time step and the same time that was retrieved from the numerical simulation. Figure 2.23 depicts the algorithm for estimating the specific heat of the investigated cement-based materials. Therefore, the value of C_p that is considered as the homogenized value of the cement-based materials is the value of C_p that yields the smallest temperature difference at each time step of the computation.

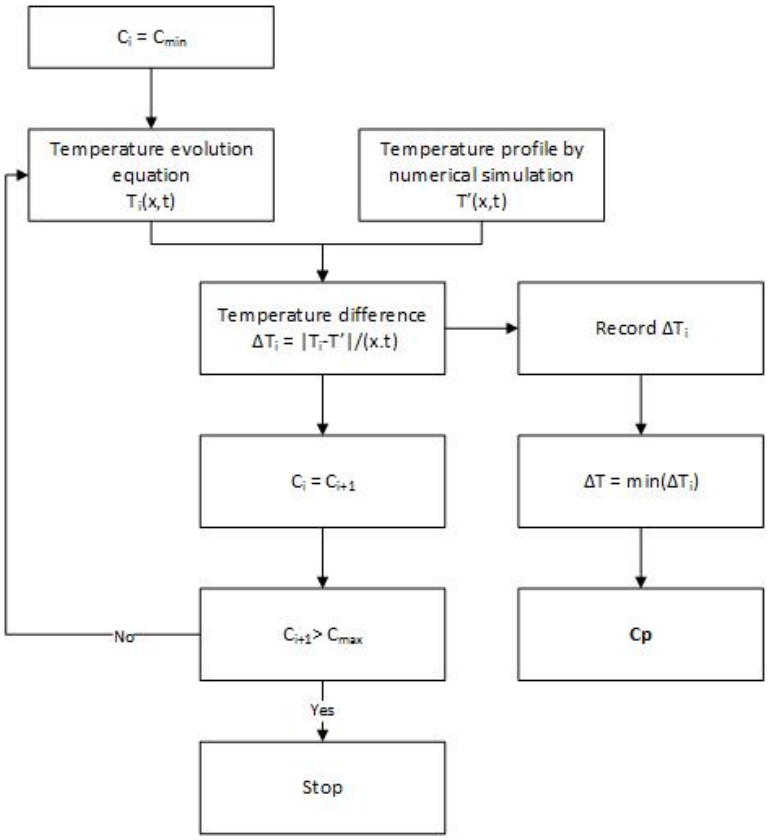

Figure 2.23 – Flowchart for calculating the specific heat

For instance, figure 2.24 depicts the fitted curve of temperature profile of mortar at α=0.83. The curve that was acquired through analytical formulation is shown by the dashed curve, while the curve that was obtained through numerical simulation is represented by the solid curve. Each color of the curve denotes a separate time step; the curves that correspond to the same time step need to be as near to one another as possible.

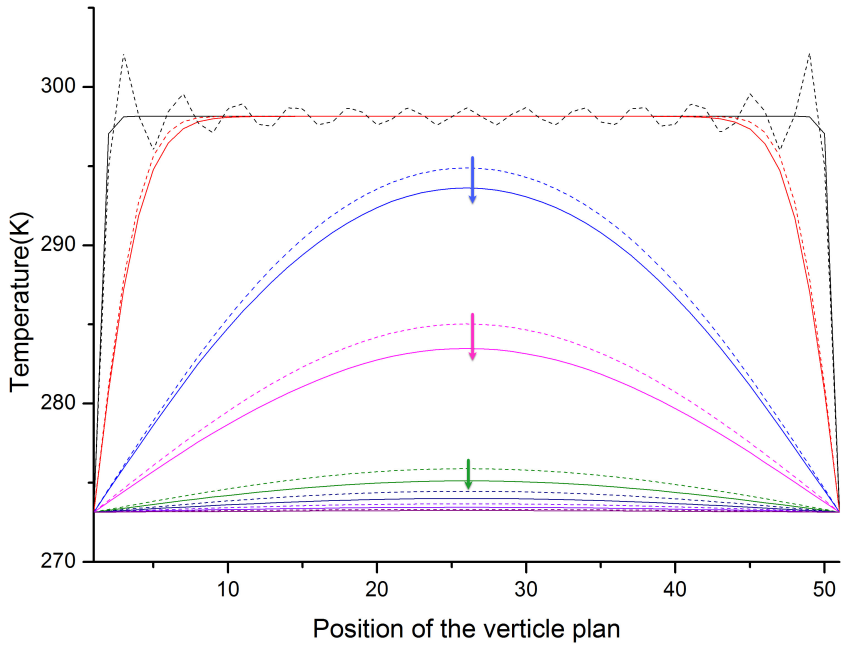

Figure 2.24 – Fitted curve of temperature profile of mortar at α=0.83

2.4.3 Results and discussion

The outcome of the numerical simulation, analytical formulation, and fitted-curve analysis is represented in figure 2.25 as the specific heat of cement paste and mortar as a function of the degree of hydration and degree of saturation. It is clear from this numerical result that at saturation degree = 0%, the specific heat increases with time. However, this is not always the case since the specific heat decreases with time when saturation degree = 100%. It can also be observed that the specific heat reaches its minimum value between 50% and 75% saturation degree.

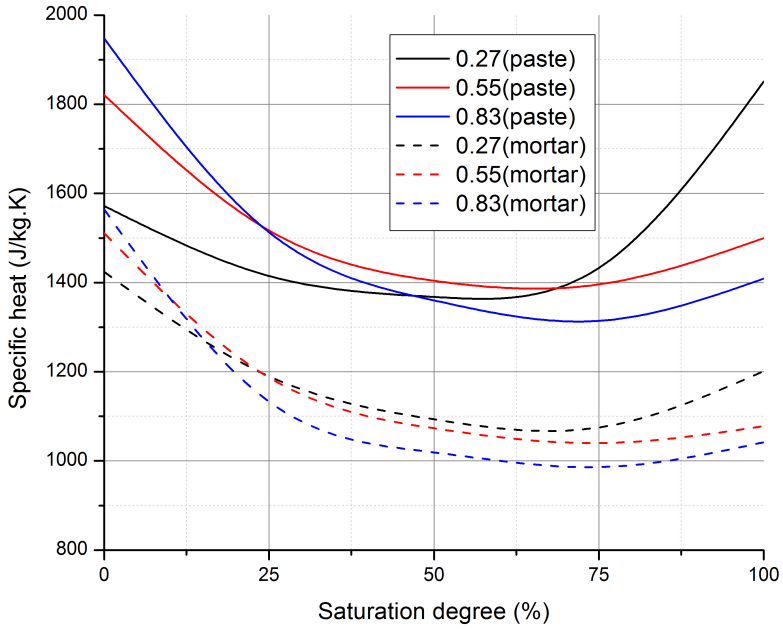

Figure 2.25 – Specific heat from fitted curve analysis

Finally, the outcomes of the analytical and numerical homogenization are presented, and the conclusions can be drawn as below:

— In general, due to the incorporation of the considered sand, which has a low specific heat, the specific heat of mortar is often lower than that of cement paste,

— In both of analytical and numerical homogenisation, the specific heat of cement-based materials rises as hydration increases at 0% saturation, but reduces as hydration increases at 100% saturation,

— Specific heat of cement paste is directly used as the input date at sub-mesoscale (mortar level),

— The findings from analytical and numerical homogenization do not agree and change differently in function of saturation degree,

— The analytical homogenisation shows that the specific heat of cement-based materials increase in function of saturation degree,

— Nonetheless, in numerical homogenisation, the specific heat curve seems like a parabola, with a minimum between 50 and 75% of saturation degree,

— This is most likely owing to the porosity's thermal properties, thermal conductivity, and specific heat, which have an opposite effect on the result,

— Table 2.6 shows that as the saturation degree rises, so do the thermal conductivity and specific heat of the porosity. Increased thermal conductivity indicates that the porosity conducts heat better and requires less energy, but increased specific heat indicates that it requires more energy to raise the temperature at higher saturation degrees,

— This minimum value could not be seen in analytical homogenization since there is no thermal conductivity intervention, and when the specific heat of a phase grows, so does the homogenized specific heat of the material.

In conclusion, this chapter has shown how to determine the specific heat of cement-based materials using analytical and numerical homogenization at two different scales. In addition, the findings have demonstrated that the analytical and numerical methods of homogenization both result in values of specific heat that does not agree well due to the effect of increasing the thermal conductivity in the porosity. In addition, the study results of the specific heat investigation presented in this section, as well as the thermal conductivity assessment presented in the previous section (section 2.3), are utilized as hypotheses to determine the coefficient of thermal expansion presented in the next section(section 2.5).

2.5 Coefficient of thermal expansion (coefficient of dilatation)

2.5.1 Analytical homogenization of coefficient of thermal expansion

Estimating the coefficient of thermal expansion of cement-based materials is accomplished by the application of the same analytical homogenization methods (section 1.2.2.1) as employed in thermal conductivity (section 2.3) and specific heat (section 2.4). However, one can instinctively understand that this homogenization can be discussed for porous materials such as cement-based materials. Indeed, an expansion of the different porosity phases cannot be considered.

When the saturation degree is adjusted to 100%, the coefficient of thermal expansion of cement paste and mortar is shown to be a function of hydration degree in figures 2.26 and 2.27, respectively.

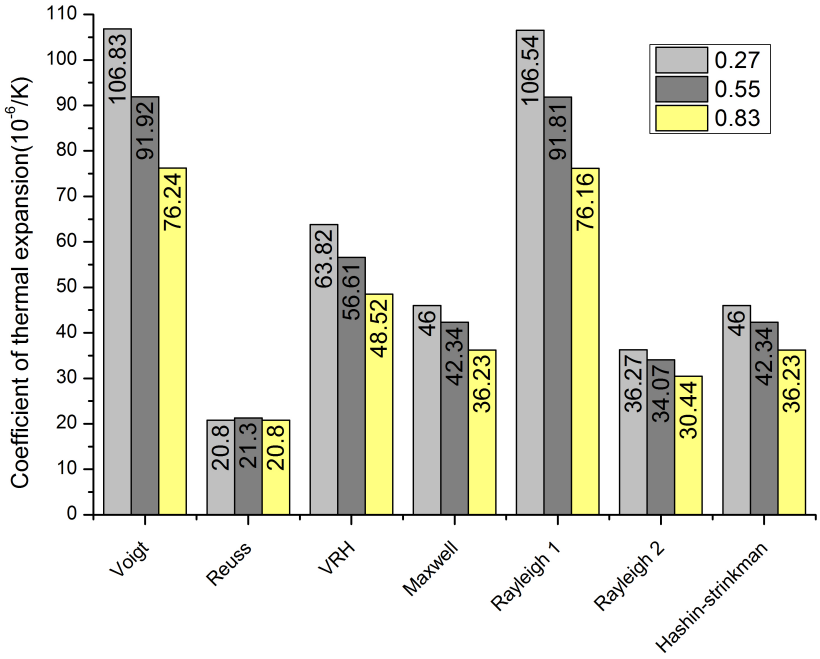

Figure 2.26 – Coefficient of thermal expansion of cement paste in function of hydration degree

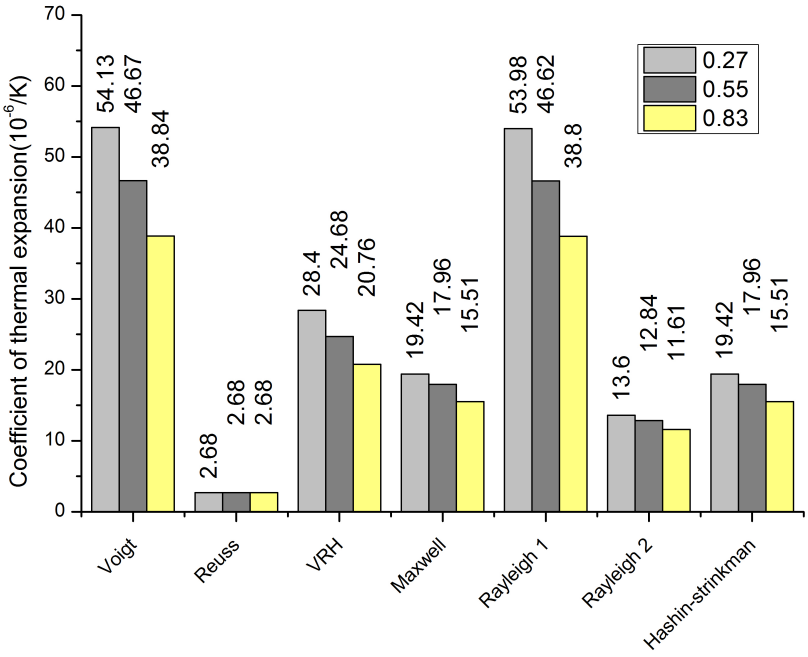

Figure 2.27 – Coefficient of thermal expansion of mortar in function of hydration degree

2.5.2 Numerical homogenization of coefficient of thermal expansion

In relation to the numerical homogenization of the coefficient of thermal expansion, the simulation may be carried out with two different techniques, thermo-mechanical sequential (section 2.5.2.1) and thermo-mechanical coupled simulation (section 2.5.2.2). The thermo-mechanical simulation can also be found in [278]–[280] but it was applied on the thermal barrier coatings. In order to compute the coefficient of thermal expansion, the most important thing to do is to determine the displacement in three different directions. This process is applied regardless of whether the technique is employed.

2.5.2.1 Thermo-mechanical sequential simulation

The thermal (heat transfer) simulation comes first in the sequence of steps that make up the thermo-mechanical sequential simulation, followed by the mechanical simulation as the second step. In Abaqus FEA, element type that are used for heat transfer and mechanical simulations are DC3D8 and C3D8R, respectively.In the end, the coefficient of thermal expansion is computed by using the displacement that was acquired from the three directions of the mechanical simulation (figure 2.28).

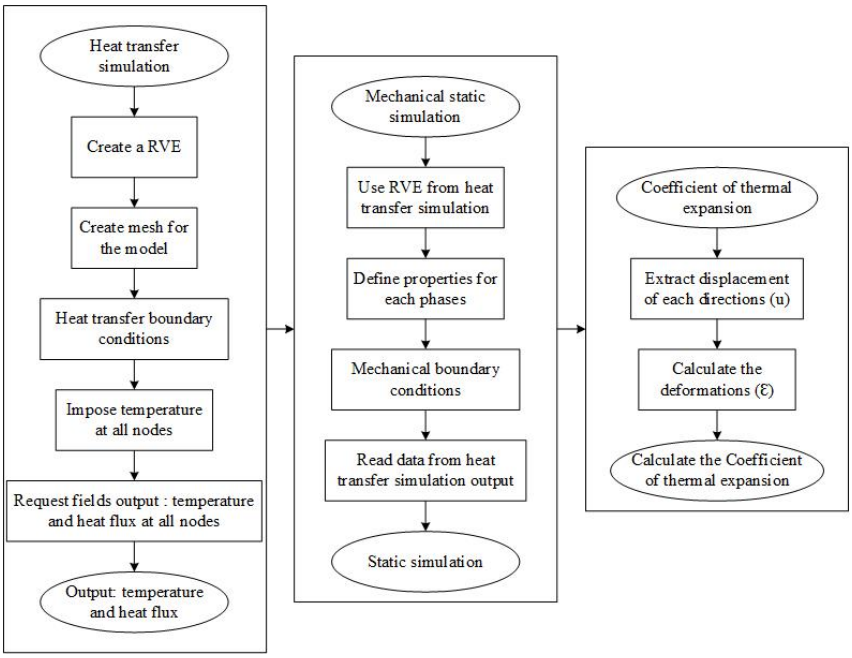

Figure 2.28 – Algorithm for thermo-mechanical sequential simulation in Abaqus FEA

Otherwise, in this simulation, it required specific initial and boundary conditions. The initial and boundary conditions of both of thermal and mechanical simulations are shown in figure 2.29. The simulation of heat transfer begins by first defining the initial temperature ($T_{initial}$=298.15K) over the entirety of the body of the sample. Next, the temperature is raised to a specific value, which in this example is 398.15K as shown in figure 2.29(a). The simulation results are then processed to provide the output, which includes the nodal temperature and the element heat flow. Thereafter, the initial condition, displacement, is set to 0 on one side of the sample (u=0) for the mechanical simulation. In contrast, the displacement on the other side of the sample is free from any constraints (u≠0) as shown in figure 2.29(b). In this mechanical simulation, the outputs of a previous heat transfer simulation are brought into the simulation. As was indicated previously, the coefficient of thermal expansion of the sample is determined by using the displacement, which is on the constrain free side, collected from the three directions of the mechanical simulation.

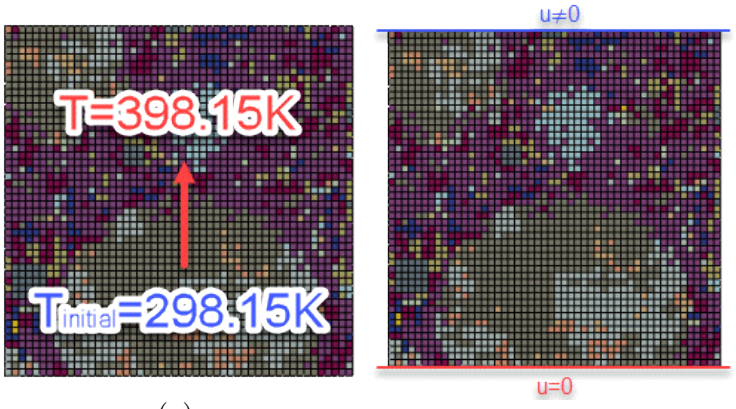

(a) (b)

Figure 2.29 – Initial and boundary conditions for thermo-mechanical sequential simulation

2.5.2.2 Thermo-mechanical coupled simulation

The procedure for carrying out a thermo-mechanical coupled simulation is, more or less, the same as the procedure for carrying out the earlier simulation; however, the heat transfer simulation and the mechanical simulation need to be carried out simultaneously as shown in figure 2.30. Moreover, C3D8T element type is used for this coupled simulation in Abaqus FEA. By the way, the computation for the coefficient of thermal expansion follows the exact same steps as the technique mentioned earlier.

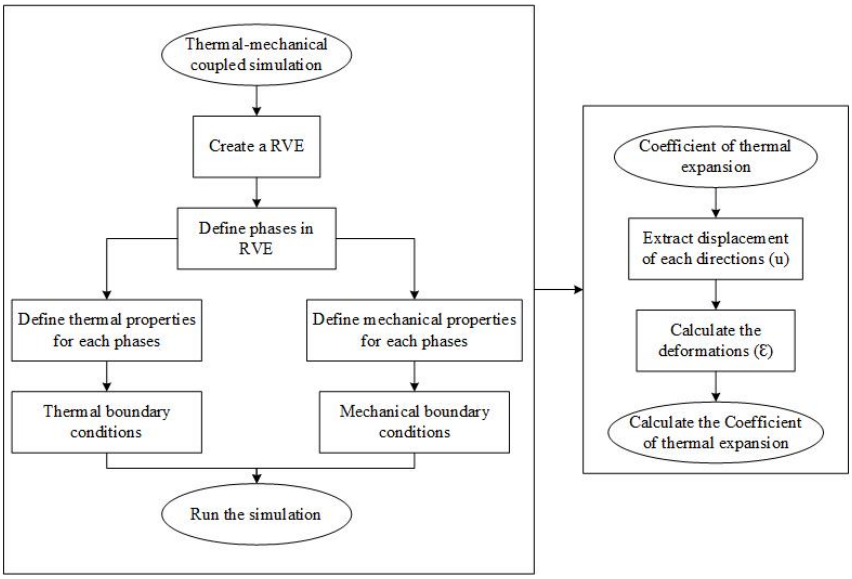

Figure 2.30 – Algorithm for thermo-mechanical coupled simulation in Abaqus FEA

Additionally, specific initial and boundary conditions are essential for this simulation. Because this is a coupled simulation, the heat transfer and mechanical simulations may use the same initial and boundary conditions. In this case, the same initial and boundary conditions used for heat transfer in the previous section are used in this simulation. It means the initial temperature ($T_{initial}$) = 298.15K with the temperature raise until a specific value, 398.15K.

In this scenario, the identical initial and boundary conditions utilized for heat transfer in the preceding section are employed in this simulation. This indicates that the initial temperature ($T_{initial}$) will be 298.15K, and it will continue to rise until it reaches 398.15K.

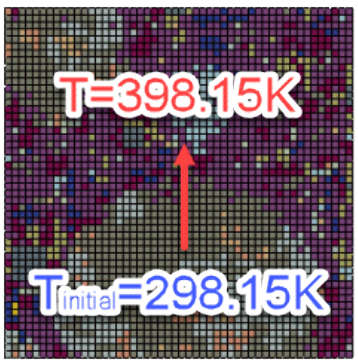

Figure 2.31 – Initial and boundary conditions for thermo-mechanical coupled simulation

2.5.3 Results and discussion

The results from numerical homogenization of coefficient of thermal expansion for cement paste and mortar are presented in the figure 2.32.

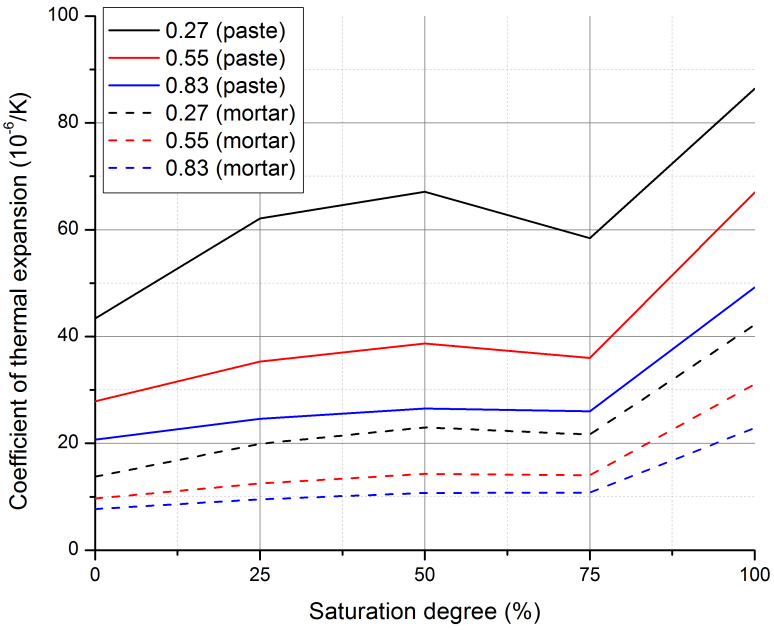

Figure 2.32 – Numerical result of coefficient of thermal expansion in function of saturation degree

Conclusions may be derived from the numerical homogenization result shown in Figure 2.32, including the following:

— The outcome of the thermo-mechanical coupled simulation is the same as that of the thermo-mechanical sequential simulation,
— As the degree of hydration rises, the coefficient of thermal expansion drops. The porosity inside cement-based materials is filled by hydration products with lower coefficients of thermal expansion,
— Unlike thermal conductivity and specific heat, the coefficient of thermal expansion at lower hydration degree is always higher than that of higher hydration degree at any saturation degree,

2.5.4 Comparison with analytical homogenisation methods and discussion

The result of analytical homogenization is shown in figure 2.33. It show that the coefficient of thermal expansion decreases as the degree of saturation increases. It has the same tendency for both of cement paste and mortar. The coefficient of thermal expansion does, in fact, significantly drop with increasing the hydration degree when the saturation degree is 0%. In addition to this, after the saturation level reaches 100%, it does show a tiny drop with hydration degree.

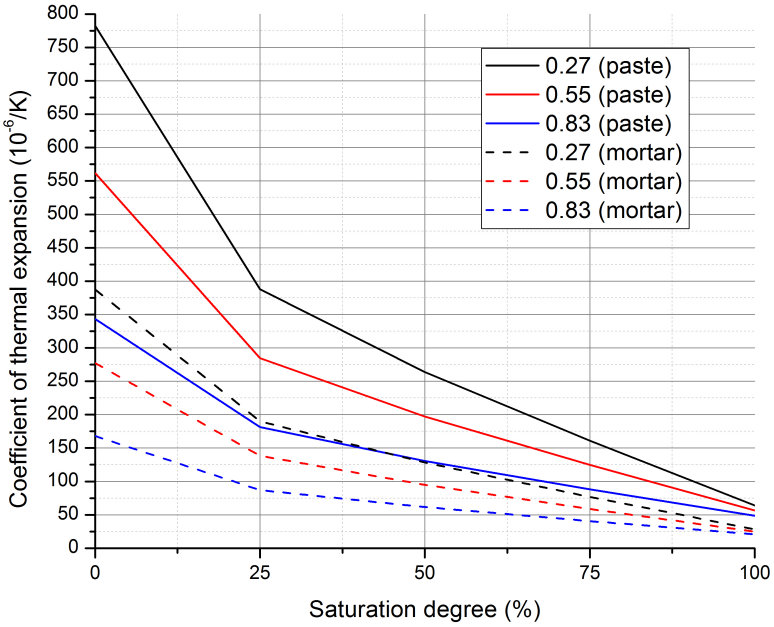

Figure 2.33 – Analytical result of coefficient of thermal expansion in function of saturation degree

Moreover, it can be seen that the results from analytical and numerical homogenization are not matched due to the complicity of mechanical and thermal properties of the cement-based materials. To summarize, the complex evolution of numerous mechanical and thermal properties as a function of saturation degree, particularly the specific heat, has resulted in a nonlinear evolution of the coefficient of thermal expansion. As a result, this homogenization model cannot be utilized to anticipate the complex evolution of the coefficient of thermal expansion.

2.6 The effect of Thermal Contact Conductance (TCC) on thermal conductivity

The TCC is introduced in this work at the mortar (sub-mesoscale) level, when aggregates and cement paste come into contact. Furthermore, attempts have been made to forecast the value of TCC using analytical formulation in section 2.6.1 and numerical simulation in section 2.6.2.

2.6.1 Analytical formulation for TCC

Analytical formulations are the formulations that have been deducted from simplified models of TCC. Like mentioned in section 1.3.3, TCC has been classified into two forms of heat transfer via the interface, solid-to-solid contact points (h_c) and conduction across the gap via intermediate fluid (h_g), in terms of simplified models [254]. The equation 1.31 is used here.

Concerning the solid-to-solid contact points (h_c), Yovanovich provided a formula (equation 2.6) for calculating TCC with just solid-to-solid contact [260]. The equation has multiple parameters that need extra experimental work in order to provide an accurate result.

$$h_c = 1.25m\frac{k_s}{\sigma}\left(\frac{P}{H}\right)^{0.95}, \text{ where } m = \sqrt{m_1^2 + m_2^2} \qquad k_s = \frac{2k_1k_2}{k_1 + k_2} \qquad \sigma = \sqrt{\sigma_1^2 + \sigma_2^2} \tag{2.6}$$

and m_1, m_2 : surface slop for cement paste and inclusion, respectively,
k_s : harmonic mean conductivity of two materials,
k_1, k_2 : thermal conductivity of cement paste and inclusion, respectively,
σ : the effective surface roughness,
P : contact pressure,
H : minimum hardness between the two materials.

Table 2.7 presents the assumptions that are being taken into account in the process of determining the value of h_c.

Materials	m	k (W/m.K)	σ (μm)	P (MPa)	H (GPa)
Limestone	0.03 - 0.3	1.33	11.74	2	0.92
Paste	0.03 - 0.3	0.6	28		

Table 2.7 – Hypotheses for solid-to-solid contact points of TCC

With the value of $m \in [0.03, 0.3]$, the TCC of solid-to-solid contact points varies from 3.017 to 30.169 W/m^{2}K. In such case, these results is insufficient to determine the overall value of TCC since the estimation of TCC across the gap via intermediate fluid is still unknown.

2.6.2 Numerical simulation for TCC

There are two goals to accomplish with the implementation of numerical modeling in this section. The first goal is to determine whether or not TTC affects the thermal properties of cement-based materials, and the second goal is to understand how to determine the precise value of TCC.

2.6.3 TCC influence on cement-based materials

Two simple models are created to understand better the effect that TCC has on the thermal conductivity of cement-based materials. Both the simple model with one inclusion (figure 2.35) and the simple model with 27 inclusions (figure 2.36) are utilized in this investigation. These two simple models allow one get a good grasp on the concept of interface attributes and make it easy to look at the temperature drop at the interface. In addition, in order to build the two simple models, they must meet a condition called the maximum paste thickness (l), which is often used in cement-based materials at the mesoscale [11]. By definition, it is the largest spacing that two particles have ever experienced during such a homogeneous dilatation procedure (figure 2.34) [281]. The maximum paste thickness (l) can be found by applying the equations 2.7 and 2.8.

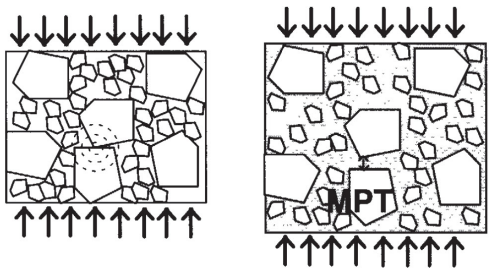

Figure 2.34 – Maximum paste thickness of two particles under homogeneous dilatation procedure [281]

$$g^* = 1 - 0.47\left(\frac{d_{min}}{d_{max}}\right)^{0.22} \tag{2.7}$$

where g^* : maximum aggregates concentration,
d_{min} : minimum size of aggregates,
d_{max} : maximum size of aggregates.

$$l = d_{max}\left(\sqrt[3]{\frac{g^*}{g}} - 1\right) \tag{2.8}$$

where l : maximum paste thickness,
g : aggregates volume in a concrete sample.

After the two simple models have been constructed, the TCC is then applied at the interface between the cement paste and the sand, with the initial value ranging from 10^{-2} to 10^{6} W/m^{2}K. To obtain the results, simulations and boundary conditions identical to those described in section 2.3.2 are being used.

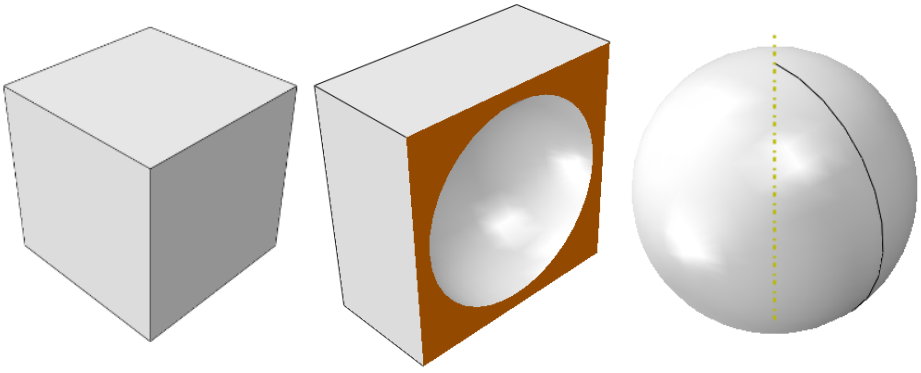

Figure 2.35 – Simple model with one inclusion

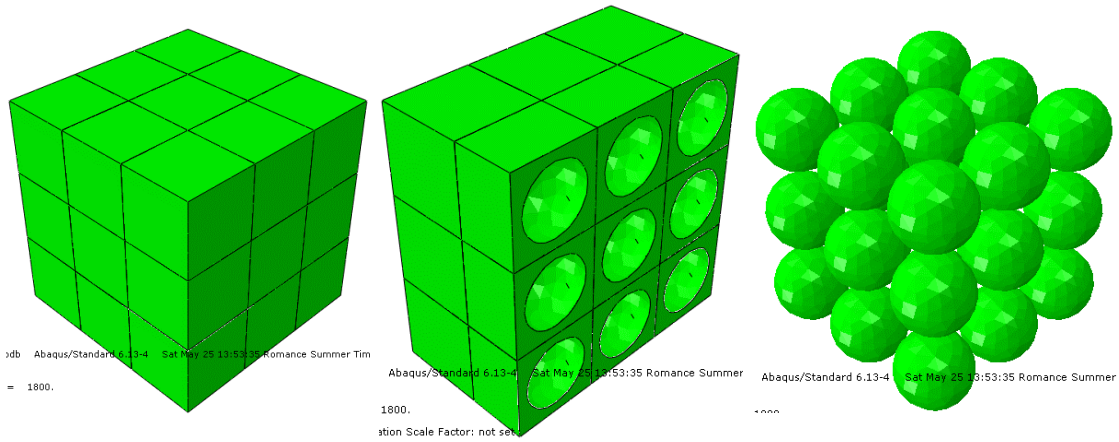

Figure 2.36 – Simple model with 27 inclusions

In a 2D cross section, figure 2.37 displays how the heat flux pass through the 27 inclusion simple model and it's temperature profile without imposing the TCC at the interface between inclusion and matrix. The outcomes of the observation on the effect of TCC on thermal conductivity are presented in figure 2.38. The findings indicate that the TCC does, in fact, impact the thermal conductivity of cement-based materials; however, this influence is only present within limited value ranges, commencing at 10^3 W/m^{2}K or lower.

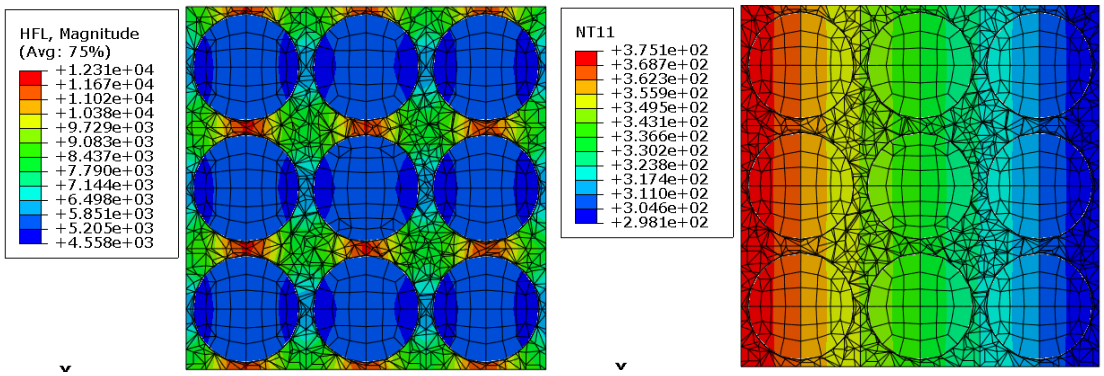

(a) (b)

Figure 2.37 – Flux (a) and temperature (b) profile of the 27 inclusions simple model without TCC

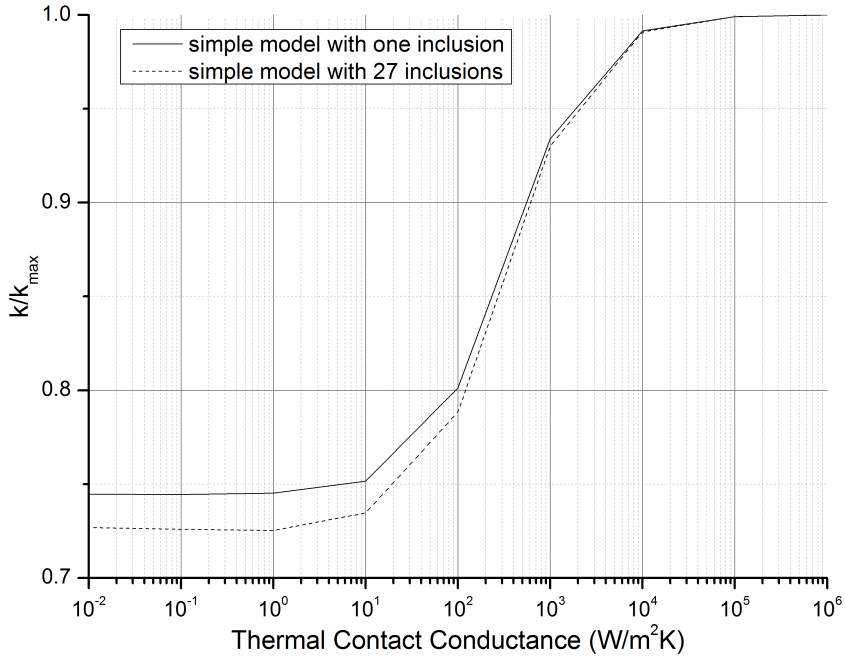

Figure 2.38 – The influence of TCC on thermal conductivity of cement-based material

2.6.4 TCC estimation with numerical simulation

Numerous parameters can be taken into consideration thanks to the capacity of numerical modeling. For instance, asperities, gaps, defects, and ITZ may all be found at the interface between two different materials. For the purposes of this investigation, a particular modelling technique is required. To begin, scanning electron microscopy (SEM) has captured the interface between the matrix and the aggregates, and the geometry model consists of only two components: aggregate and cement paste (figure 2.39). To be more specific, each piece is 165 micrometers long, for a total of 330 micrometers, 330 micrometers thick. The image obtained from the SEM was then submitted to WebPlotDigitizer to have the data (or coordinates) of the interface extracted from it. After that, the dataset was imported into Abaqus/CAE in the form of a sketch. Consequently, the interface profile was recreated by constructing points from the dataset and connecting all of the points using a curve line (figure 2.40). The 2D 3-node linear diffusive heat transfer element is used for meshing at the interface, and the 2D 4-node linear diffusive heat transfer element element is used for everything else. Finally, the surfaces that separate the two halves of the mortar are brought and bound together. It indicates that the temperature

(or heat flux) is transferred straight from one surface to another without any temperature decreases (or heat flux loss).

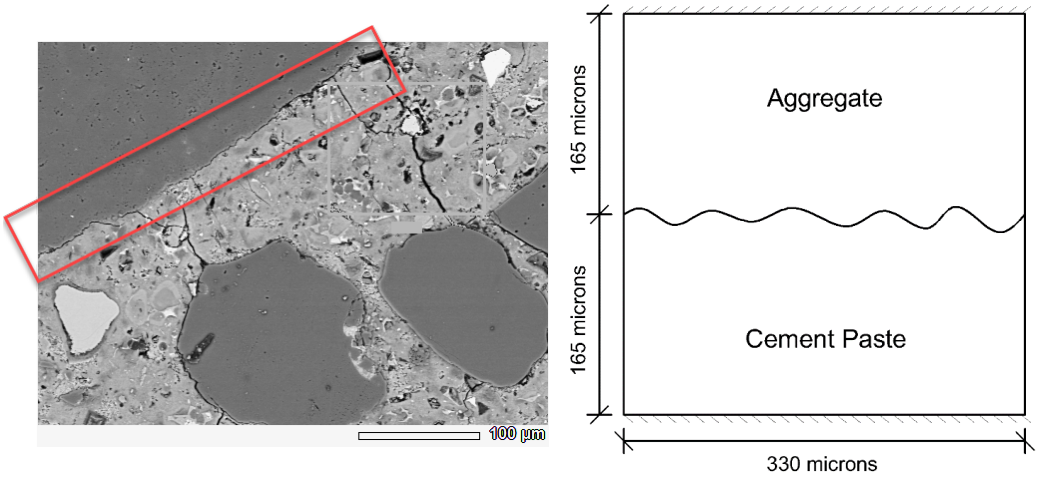

Figure 2.39 – Interface of matrix/aggregates captured by SEM

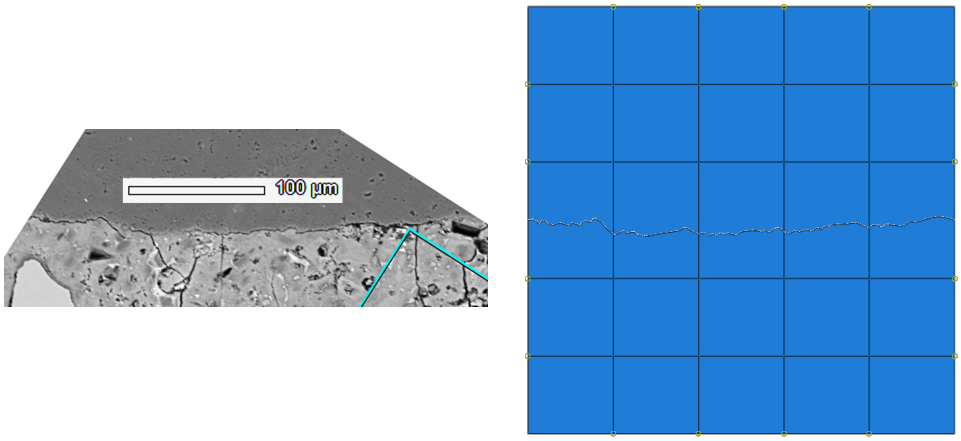

Figure 2.40 – Interface of matrix/aggregates regenerated in Abaqus/CAE

Regarding the topic of the interface between cement paste and sand inclusion, a number of hypotheses have been proposed (figure 2.41), including the non-rough (or smooth) (a) and rough surface (b), gap (c), one and two flaws (d and e), and ITZ (f). These configurations are considered as the representative of real imperfect interfaces that can be found in [282].

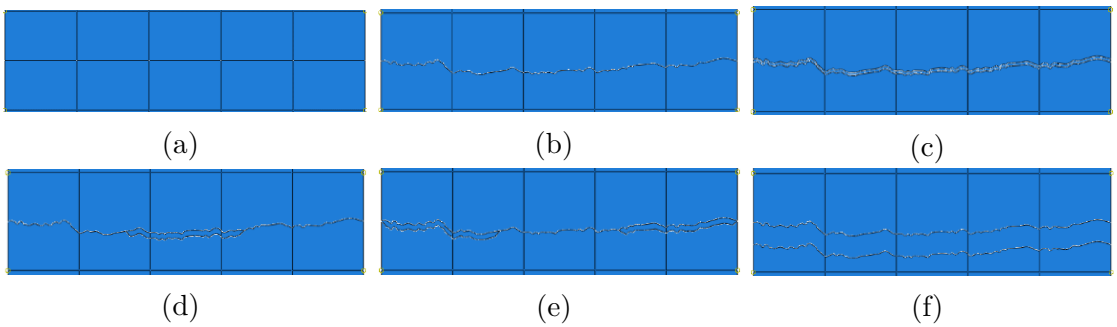

Figure 2.41 – Interface of paste/inclusion hypotheses for FEM simulation

In addition, a summary of all of the hypotheses in this investigation can be seen in table 2.8, which also includes the smooth surface for comparison.

Interface type	Opening (μm)	Length (μm)	figure 2.41
Non-rough	0	0	(a)
Rough	0	0	(b)
Air gap	3, 10, 20, 30, 40	330	(c)
Water gap	3, 10, 20, 30, 40	330	(c)
One air flaw	3, 10, 20, 30, 40	100	(d)
One water flaw	3, 10, 20, 30, 40	100	(d)
Two air flaws	3, 10, 20, 30, 40	2×100	(e)
Two water flaws	3, 10, 20, 30, 40	2×100	(e)
ITZ (α = 1.5, 1.7, 1.85, 2)	20, 40, 60	330	(f)

Table 2.8 – Interface of paste/inclusion hypotheses

In any other case, the original local porosity in cement paste has been reduced as a result of the presence of ITZ. In other words, the increase in porosity in the ITZ is countered by a reduction in porosity in the cement paste core. The new porosity may be determined by applying the equation 2.9 [91], [283].

$$\varphi_{\text{matrix}} = \varphi_{\text{paste}} \left(\frac{V_{\text{matrix}} + V_{\text{ITZ}}}{V_{\text{matrix}} + \alpha V_{\text{ITZ}}} \right) \tag{2.9}$$

where φ_{matrix} : porosity of cement paste with the presence of ITZ,
φ_{paste} : porosity of cement paste without the presence of ITZ,
V_{matrix} : volume of cement paste,
V_{ITZ} : volume of ITZ,
α : porosity ratio between the ITZ and the matrix, from 1.5 to 2.

The thermal properties of the constituents of the mortar are outlined in table 2.9, and the cement paste is analyzed in table 2.10 with regard to the porosity of the paste. A multi-scale modeling strategy has been employed to determine both the thermal conductivity and the specific heat of the ITZ and matrix core.

	Density (kg/m^3)	Specific heat (J/kg.K)	Thermal conductivity (W/m.K)
Limestone	2650	656	0.6
Air	1.208	1006	0.0262
Water	1000	4128	0.608

Table 2.9 – Thermal properties of mortar's composition

	Porosity (%)	Density (kg/m^3)	Specific heat (J/kg.K)	Thermal conductivity (W/m.K)
Cement paste	0.44	1707.371	1724	1.38
	0.31	1857.14	1341	1.39
	0.18	2018.166	1216	1.37

Table 2.10 – Thermal properties of cement paste with porosity

ITZ has a higher porosity in the mortar than the bulk cement paste, and the porosity of the bulk cement paste itself has been adjusted compared to the initial cement paste (before mixing with aggregate). For instance, cement paste with a porosity of 0.18 (table 2.10) changed into ITZ with a porosity of 0.247 and bulk cement paste with a porosity of 0.123 (table 2.11). In conclusion, it is possible to compute the thermal properties of ITZ as well as bulk cement paste by first determining its equivalent porosity through the use of equation 2.9 and then extrapolating the value of thermal properties from table 2.10. In addition, table 2.11 provides information on the thermal properties of ITZ and bulk cement paste in various porosity.

	α	Porosity (%)	Density (kg/m^3)	Specific heat (J/kg.K)	Thermal conductivity (W/m.K)
ITZ	1.5	0.22	1969.224	1253.992	1.376
	1.7	0.231	1954.415	1265.488	1.378
	1.85	0.239	1944.594	1273.112	1.379
	2	0.247	1935.702	1280.015	1.380
Bulk cement paste	1.5	0.146	2059.858	1183.636	1.365
	1.7	0.136	2072.472	1173.844	1.363
	1.85	0.129	2080.838	1167.349	1.362
	2	0.123	2088.413	1161.469	1.361

Table 2.11 – Thermal properties of ITZ and bulk cement paste

In this regard, the initial and boundary conditions described in section 2.3.2.1 are applied, and the thermal conductivity is determined by entering the relevant numbers into equation 2.3. The TCC is defined as the capacity to transfer heat at interface between two bodies in contact, it may be considered as series model and computed using equation 2.10.

$$h_{\mathrm{j}} = \left[\frac{T_{\mathrm{hot}} - T_{\mathrm{cold}}}{Q} - \frac{\Delta L_{\mathrm{limestone}}}{k_{\mathrm{limestone}}} - \frac{\Delta L_{\mathrm{cement\ paste}}}{k_{\mathrm{cement\ paste}}} \right]^{-1} \tag{2.10}$$

where $\mathrm{L_{limestone}}$: length of the limestone sample,
$\mathrm{L_{cement\ paste}}$: length of the cement paste sample,
$\mathrm{k_{limestone}}$: thermal conductivity of limestone,
$\mathrm{k_{cement\ paste}}$: thermal conductivity of cement paste.

2.6.5 Result and discussion on TCC

Following the completion of the heat transfer simulation, the temperature profile, the temperature drop, the thermal conductivity, and the TCC have all been computed.

In order to make comparisons more straightforward, the model has been sectioned up into 12 average planes of equal portions, as seen in figure 2.42 (a). The last step is to determine the average temperature for each plane, as represented in figure 2.42 (b-h). Planes number 6 and 7 illustrate the interfaces between the matrix and the aggregates, respectively.

According to figure 2.42, it is possible to observe that a rough surface (a) causes a temperature drop at the contact that is relatively little, only 0.016%. Since it has a lower thermal conductivity than water, air often causes a more significant temperature drop than water does. When the gap thickness is 40μm, for instance, the temperature drop caused by the intermediate fluid being air, which is 16.18%, is considerably more than the temperature drop caused by water, which is just 3% (figure 2.42 (c) and (d)).

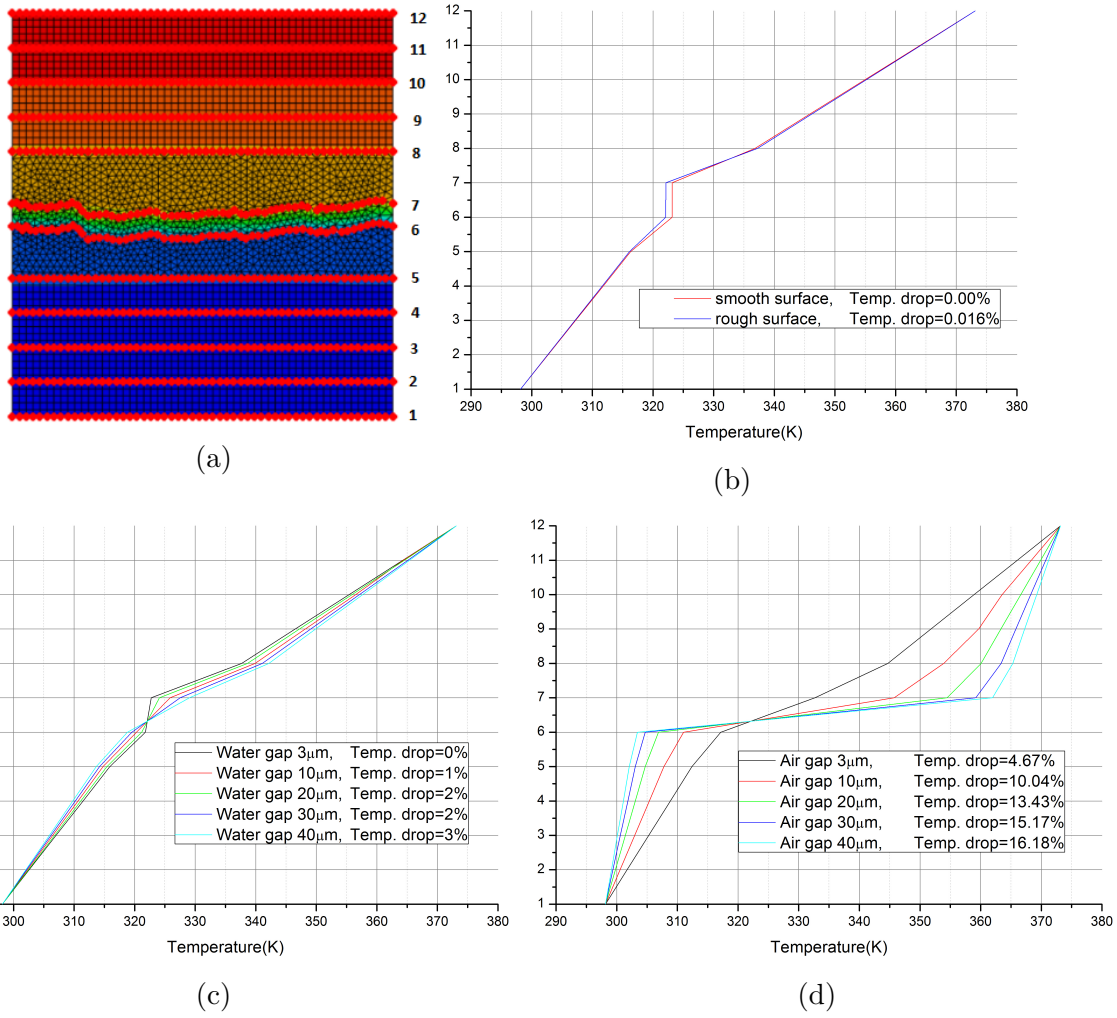

Figure 2.42 – Temperature profile, temperature drop at variety of interfaces (1/2)

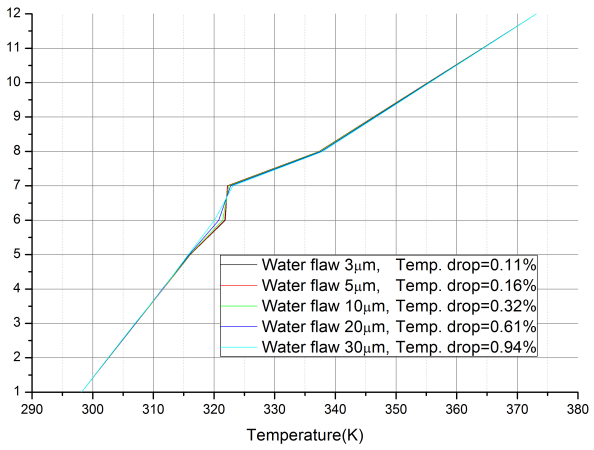

(e)

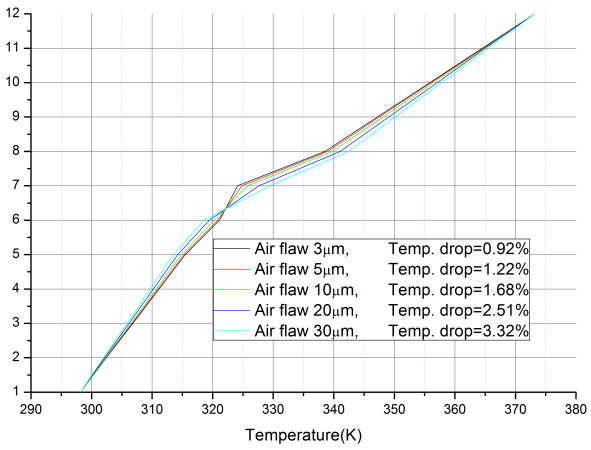

(f)

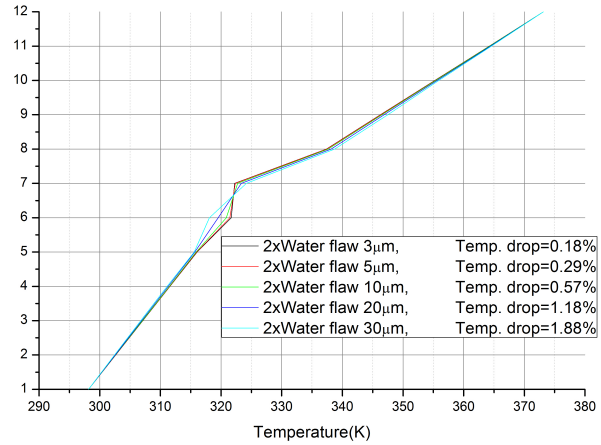

(g)

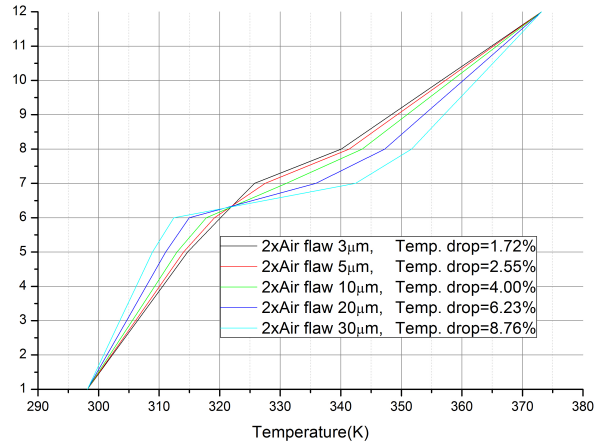

(h)

Figure 2.42 – Temperature profile, temperature drop at variety of interfaces (2/2)

With regard to the TCC, it has been computed, and the results are presented in table 2.12 along side with temperature drop, and thermal conductivity. In accordance with figure 2.38, the impact of TCC on the thermal conductivity of cement-based materials begins with TCC values less than 10^3 W/m^2.K. Thus, only air gap with thickness larger than 30μm can alter the thermal conductivity of cement-based materials. Another conclusion that can be derived from this study is that when the TCC has an impact on the thermal conductivity, it causes a temperature reduction at the interface that is greater than 15%. In reality, such situations might occur when micro-cracks form inside structural elements subjected to mechanical loads. These micro-cracks often form at the interface between

aggregates and matrix. TCCs are pretty high in all other cases of imperfect interfaces and do not affect the homogenized thermal conductivity of mortar. As a result, perfect contact can be regarded.

Interface type	Gap ($\mu m \times \mu$m)	Temp. drop (%)	k (W/m.K)	h_j (W/m^2.K)
Non-rough	0×0	0	0.80	2424240000
Rough	0×0	0.016	0.79	199654.90
Air gap	3×330	4.67	0.63	8730.52
	10×330	10.04	0.44	2724.81
	20×330	13.43	0.31	1362.95
	30×330	**15.17**	**0.23**	**893.16**
	40×330	**16.18**	**0.19**	**667.40**
Water gap	3×330	0	0.79	98066.66
	10×330	1	0.78	45778.14
	20×330	2	0.78	26098.77
	30×330	2	0.77	18251.60
	40×330	3	0.76	14037.08
One Air flaw	3×330	0.92	0.77	47514.83
	5×330	1.22	0.75	37370.28
	10×330	1.68	0.76	27317.05
	20×330	2.51	0.71	18024.27
	30×330	3.32	0.74	13025.06
One Water flaw	3×330	0.11	0.80	170144.27
	5×330	0.16	0.79	156631.13
	10×330	0.32	0.81	130011.84
	20×330	0.61	0.78	96332.96
	30×330	0.94	0.85	74255.89
Two Air flaws	3×330	1.72	0.74	24649.867
	5×330	2.55	0.70	16843.46
	10×330	4	0.67	10681.40
	20×330	6.23	0.57	5998.33
	30×330	8.76	0.52	3492.53

Table 2.12 – Temperature drop, thermal conductivity and TCC of each study case (1/2)

Interface type	Gap ($\mu m \times \mu$m)	Temp. drop (%)	k (W/m.K)	h_j (W/m^2.K)
Two Water flaws	3×330	0.18	0.79	152005.78
	5×330	0.29	0.79	131949.82
	10×330	0.57	0.80	97542.46
	20×330	1.18	0.77	62786.51
	30×330	1.88	0.83	43526.86
ITZ (α=1.5)	20×330	1	0.82	49450.13
ITZ (α=1.7)		1	0.82	49521.27
ITZ (α=1.85)		1	0.82	49554.63
ITZ (α=2)		1	0.82	49588.26
ITZ (α=1.5)	20×330	1	0.82	49450.13
ITZ (α=1.7)		1	0.82	49521.27
ITZ (α=1.85)		1	0.82	49554.63
ITZ (α=2)		1	0.82	49588.26
ITZ (α=1.5)	40×330	2	0.82	28759.36
ITZ (α=1.7)		2	0.82	28799.48
ITZ (α=1.85)		2	0.82	28821.483
ITZ (α=2)		2	0.82	28841.81
ITZ (α=1.5)	60×330	3	0.82	20283.60
ITZ (α=1.7)		3	0.82	20312.41
ITZ (α=1.85)		3	0.82	20326.90
ITZ (α=2)		3	0.82	20341.44

Table 2.12 – Temperature drop, thermal conductivity and TCC of each study case (2/2)

2.7 Conclusion

In the framework of the multi-scale approach, analytical and numerical homogenization methodologies were used. Analytical and numerical homogenization outcomes at the microscale are homogenized and used as input data for analytical and numerical homogenization at the sub-mesoscale, respectively. These results are also used in real-world applications in the next chapter, such as the influence of cracks on thermal conductivity and the effect of specific heat on heat development in massive concrete. In this chapter, additional research on thermal contact conductance **TCC** and the Representative Vol-

ume Element (**RVE**) was conducted to determine whether **TCC** has an impact on the study of thermal conductivity of mortar and to calibrate the size of **RVE** of mortar for thermal homogenization. Furthermore, homogenization is studied at various hydration and saturation degrees.

In analytical homogenization, thermal conductivity (**k**) was determined by combining the thermal conductivity of its constituents. The findings show that heat conductivity is relatively equal at any hydration degree at both scales. Furthermore, it increases as saturation degrees increase. Since the considered sand has a lower thermal conductivity than that of cement paste, so the mortar has a lower thermal conductivity than the cement paste. When numerical homogenization is applied, several results are conceivable. The **RVE** cubes of cement paste and mortar were generated by **CEMHYD3D**, and the heat transfer simulation is done by imposing two temperatures on two opposing sides of the **RVE**. First, two take-and-place procedures were employed to calibrate the size of **RVE** utilized in sub-mesoscale, in addition to the **RVE** acquired from **CEMHYD3D**. For a long time, many researchers used the original take-and-place method, and the new one is the modified take-and-place method developed by Rhardane **rhardane microscopically 2020**. The modified take-and-place method has the benefit of being faster than the original. Furthermore, the size of **RVE** calibrated for heat transfer simulation is 2.44 times the diameter of the largest inclusion (L/D=2.44), which is smaller than that used for mechanical simulation. Furthermore, it was discovered that the **TCC** did not affect the homogenized thermal conductivity of the mortar unless the air gap was larger than 30 μm. Second, the thermal conductivity of cement paste and mortar increases dramatically with increasing hydration degree at 0% saturation degrees. However, it seems to be very comparable in fully saturated materials. Finally, the analytical and numerical homogenization results do not agree at lower saturation degrees, but it works well with fully saturated cement-based materials.

The specific heat ($\mathbf{C_p}$) was calculated in the same manner as thermal conductivity in analytical homogenization. Since the presence of limestone sand, the result shows that the specific heat of mortar is lower than that of cement paste and gradually increases with saturation degrees. It grows somewhat with hydration when the saturation degree is 0% but drops when it is 100%. The inverse analysis approach was employed in numerical homogenization. This inverse analysis approach includes numerical simulations of heat transfer on a **RVE** and analytical formulation of the temperature profile in a sample. After performing the numerical simulation, Python was used to get the temperature

profiles from the model at each time step. The temperature profiles obtained from the numerical simulation were then reproduced using the analytical formulation by changing the value of $\mathbf{C_p}$ and calculating the difference between the two profiles at each time step. The $\mathbf{C_p}$ that gives the minor difference between the two profiles is the $\mathbf{C_p}$ of the cement-based materials. The findings show that the specific heat curve has a minimum as a function of saturation degrees, which might be owing to the influence of opposing thermal properties inside the porosity. As the saturation degrees rise in porosity, so do the thermal conductivity and specific heat. Thus, greater thermal conductivity indicates that the porosity conducts heat better and requires less energy to raise the temperature, but increased specific heat means that the porosity requires more energy. Furthermore, since it is based only on the specific heat of each component and not on thermal conductivity, the analytical homogenization technique could not reproduce the same findings as the numerical method. To conclude, both homogenization methods provide comparable results for completely saturated cement-based materials but not for lower saturation degrees.

In analytical homogenization calculations, the coefficient of thermal expansion ($\boldsymbol{\alpha}$) declines with increasing saturation degrees. It shows that air expansion is greater than water expansion, which is true in open space but not in porosity. The surrounding solid typically confines the porosity, preventing it from expanding. As a result, the analytical homogenization results for porous materials, especially those with closed porosity, are illogical. This work presented two numerical homogenization methods: thermo-mechanical sequential simulation and thermo-mechanical coupled simulation. Thermal simulations were performed first in the thermo-mechanical sequential simulation, followed by mechanical simulation using the previous thermal simulation results. Furthermore, the thermal and mechanical properties were given independently in each simulation. The thermo-mechanical coupled simulation, as compared to the thermo-mechanical sequential simulation, was done just once and included both mechanical and thermal properties. In this situation, both simulations produced the same outcome. Furthermore, at lower hydration degrees, the $\boldsymbol{\alpha}$ of cement-based materials at low hydration is always more significant than that of cement-based materials at higher hydration degrees. Nonetheless, the complex evolution of several mechanical and thermal properties as a function of saturation degree, notably specific heat, has resulted in a nonlinear development of the coefficient of thermal expansion that is difficult to explain.

Chapter 3

Application

In this chapter, the outcomes of the thermal homogenization performed in the previous chapter are utilized as the basis for the hypothesis on the application of actual work of cement-based materials.

In general, in addition to thermal aspects, cement-based materials are also subjected to mechanical stresses, which can lead to the formation of cracks in the materials. Therefore, such cracks have the potential to affect both the mechanical and thermal properties of the materials. In addition, the cement-based materials are susceptible to cracking not only because of mechanical loads but also because of thermal loads. For instance, the massive concrete structure that is able to produce heat on its own at a young age due to the heat that was dissipated during the cement hydration process could generate cracks that, again, could alter the properties of concrete.

In this section of the study, the influence of crack on thermal conductivity, and the role of specific heat on the evolution of heat in massive concrete is being discussed in section 3.1 and 3.2, respectively.

3.1 The influence of crack on thermal conductivity

The study is performed at the mesoscale: the influence of cracks on the mortar thermal conductivity is investigated. The control of cracking and, conversely, quantification of its influence is a problem of prime importance in the context of the insulation of buildings.

As mentioned above, cracks may appear as a result of mechanical and thermal stresses. By the way, the focus of this research is solely on cracks that are produced by the application of mechanical stresses. In this context, the word "mechanical stresses" refers to the compression and tension stresses that have the potential to form cracks in a variety of patterns.

With regard to the method of simulation, the CEMHYD3D and Abaqus FEA software will be utilized once more in this scenario. Furthermore, only mortar will be used as the

cement-based materials. A mortar cube is placed in pure compression and tension in Abaqus FEA until it meets its ultimate load, which causes a fracture displacement (also known as a crack) in the material. The element type for mechanical simulation in Abaqus FEA is 3D 8-node linear brick, reduced integration with hourglass control (C3D8R). The formation of the fracture patterns on the mortar RVE as a result of tensile and compressive loading has been discussed in the past in [89], [185]. After the mechanical simulations have been completed, the kill element option in Abaqus is utilized to identify which element has a significant displacement compared to the limit value. Any local displacement greater than the limit value will result in the mesh being deleted and may be considered a micro-crack. Then, a list of the elements that have been eliminated is provided for it to be utilized to offer the characteristic of the crack in heat transfer simulation. Finally, the thermal conductivity of mortar is calculated in the same manner as described in section 2.3.2 by using equation 2.3.

Figure 3.1 shows the mesh that will be used in mechanical test and it's microstructure can be found in figure 2.3.

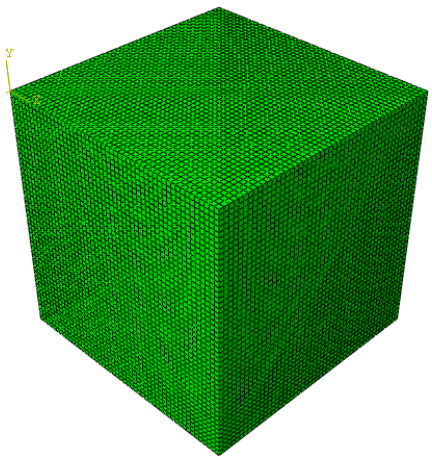

Figure 3.1 – Mortar's mesh for finite element modeling

3.1.1 Brief presentation of the hypotheses of the mechanical simulations

The formation of the fracture patterns on the mortar RVE as a result of tensile and compressive loading has been discussed in previous works [89], [185]. Only a brief description is given here.

It is first essential to precise that failure in cement-based materials is the consequence of highly tensile and shear stresses due to the heterogeneities of the materials. A widely used cohesive crack model is considered to describe the behavior of the paste and the aggregates. In such an approach, macro-cracks are not tracked individually. Instead, their presence enters into the calculations by the way they affect the stress and material stiffness associated with each material calculation point. Thus the model considers the development of the Fracture Process Zone (FPZ) by the stress vs. crack-opening relationship. A crack is assumed to open when stress at the tip of the FPZ reaches the tensile strength f_t (= Rankine criterion). Thus, at the tip of the FPZ, a zero-crack opening is associated with stress equal to f_t. The widening (u) of the tip of the FPZ causes the crack to propagate. The stress at the tip of FPZ decreases gradually to zero as u grows to a critical value u_{ck} where there is no stress transfer between the crack surfaces in the FPZ.

A bi-linear post-peak tensile stress-displacement curve is considered for mortar in this work and defined in the input file in a tabular way. The characteristic points of this curve have been deduced by inverse identification on the computed stress-strain curve on the micro-level and are presented in [10]. The evolution of the post-peak shear stress is assumed to be equal to the tensile stress' one. Furthermore, aggregates are assumed to follow the same kind of constitutive law. Fracture energy of 120 N/m is imposed, which is strictly equivalent to a post-peak stress-displacement curve.

3.1.2 Crack characteristic under compression and tension

The compression and tension test simulation is carried out using the mortar mesh with the boundary conditions being respected (figure 3.2). An imposed displacement of 1 and 15 μm (totaling 2 and 30 μm) is employed and set at two faces of the cube opposite one another for the simulation of tension and compression, respectively. After the simulations are done, elements that have local displacement than the critical value (u_{ck}) will be removed from the mesh.

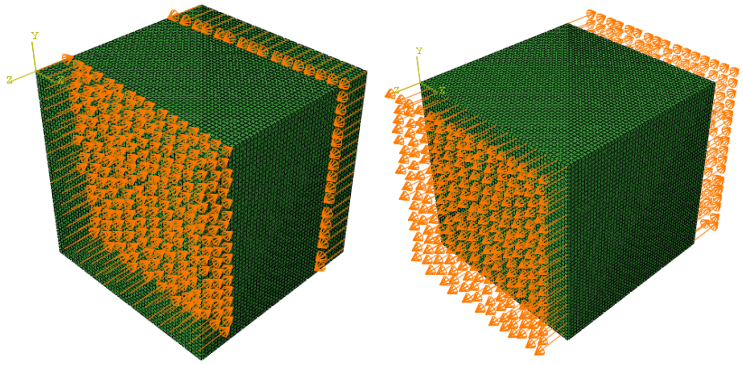

(a) Compressive simulation (b) Tension simulation

Figure 3.2 – Boundary conditions for mechanical simulation

Moreover, the failure of each component defines the mortar's failure criterion. The fracture of the cement paste is related to the result of tension and shear stresses that develop inside the mortar, which is a heterogeneous material at the sub-mesoscale.

Figure 3.3 illustrates the mortar meshes that were, respectively, subjected through the simulations of compressive (a) and tensional (b) stresses. The output of the mechanical simulation is a list of elements that have been removed from the model so that they may be added back in or altered for the following simulation.

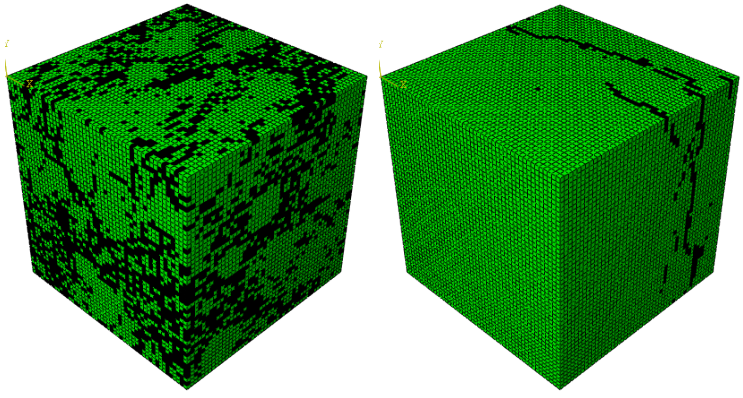

(a) Compressive simulation (b) Tension simulation

Figure 3.3 – Mortar meshes with removed elements (in black)

It is apparent from figure 3.3 that the distributions of cracks in both simulations are distinct from one another. In the case of compression, the cracks are dispersed arbitrarily

across the cube (a), but in the case of tension, the cracks are laid out in the shape of a plane (b) perpendicular to the axis of the force being applied.

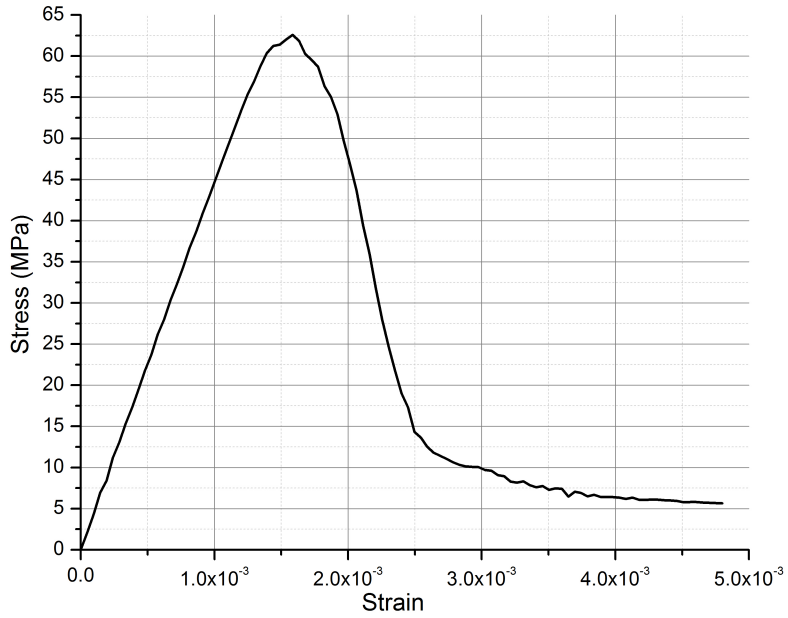

Figure 3.4 – Stress and strain curve for compression test

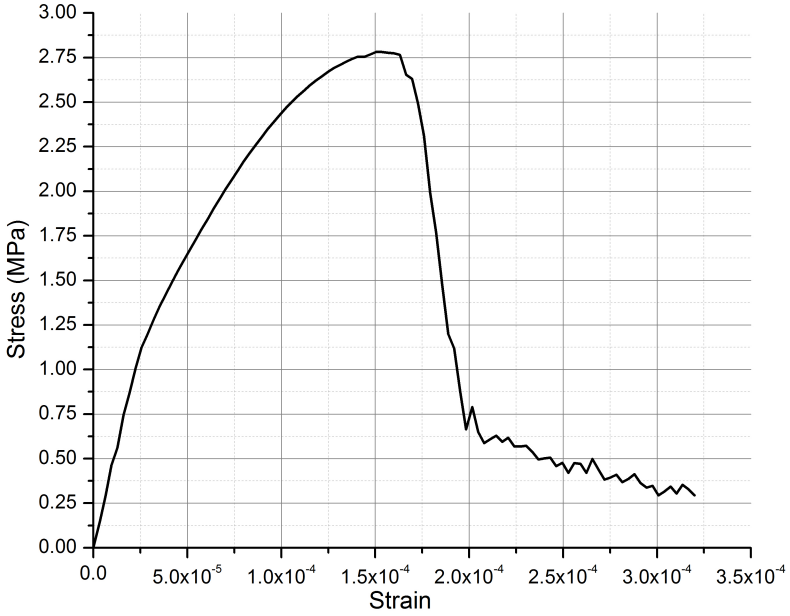

Figure 3.5 – Stress and strain curve for tension test

Moreover, figure 3.4 and 3.5 show the stress and strain curve for both of simulations with number of elements that have been deleted (kill elements). The number of elements removed from the compression test was significantly higher than those removed from the tension test. The damage caused by compressive load might lead to a modification of not just the thermal properties of cement-based materials but any properties they possess. In order to examine the thermal characteristics of cement-based materials using a heat transfer simulation, just a few points, such as when the strain equal to 0, 1.39×10^{-3}, 1.68×10^{-3}, 2.54×10^{-3}, and 4.80×10^{-3} for compressive test and 0, 1.41×10^{-4}, 1.54×10^{-4}, 1.82×10^{-4}, 1.98×10^{-4}, and 3.20×10^{-4}, for tension test, are chosen. Regarding heat transfer simulation, the thermal properties of air will replace the thermal properties of the removed elements.

3.1.3 Heat transfer simulation respect to crack's orientation

Following the mechanical simulation's completion, heat transfer simulation on damaged mortar is carried out utilizing the identical initial and boundary conditions described in section 2.3.2.1. In addition, the thermal conductivity of damaged mortar may be computed in the same way as it is of sound mortar by utilizing equation 2.3. The results of the thermal conductivity simulation on damaged mortar due to compression and tension stresses are shown in figures 3.6 and 3.7, respectively, in the following sections.

3.1.3.1 Thermal conductivity of mortar under compression

This section's results of assessing the thermal conductivity of damaged mortar, which is a result of compression stress, compared to sound mortar (k/k_{max}) are shown in figure 3.6. It can be clearly seen that the cracks does have influence of thermal conductivity of mortar. In this scenario, the values of thermal conductivity decline from 1 to roughly 0.3 of the initial value, yet the isotropy of the material might still be preserved.

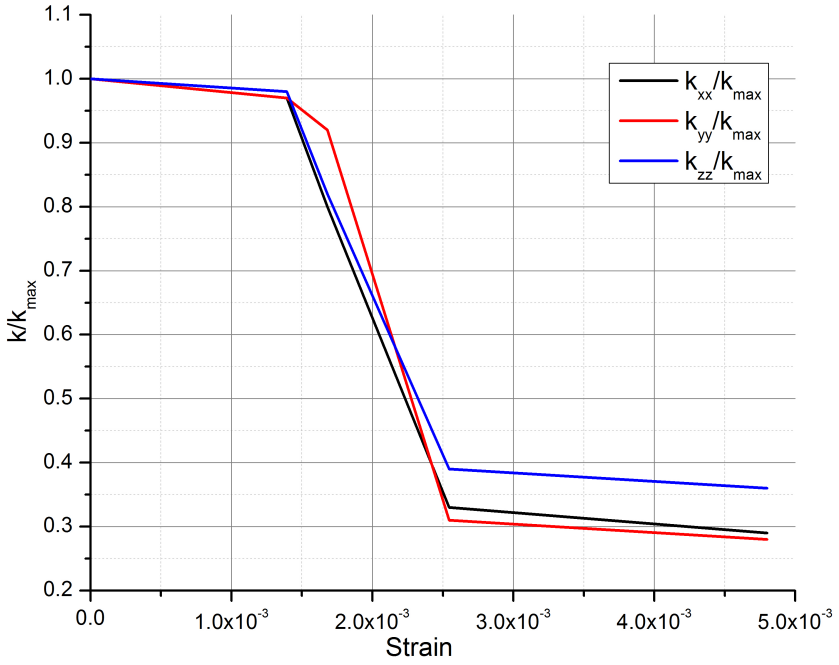

Figure 3.6 – Thermal conductivity of mortar after crack (compression)

3.1.3.2 Thermal conductivity of mortar under tension

As far as the mechanical cracks are concerned, figure 3.7 displays the results of the relative thermal conductivity (k/k_{max}) owing to tension cracks. Cracks, in contrast to the prior section, affect the thermal conductivity of mortar; however, this influence is limited to the direction in which tension force is applied (direction zz). The thermal conductivity is reduced to around 0.75 of the reference value in the direction where the load is applied, whereas in the other two directions it is reduced just slightly to approximately 0.95. It implies that the mortar's isotropy has been altered after being split by mechanical loads.

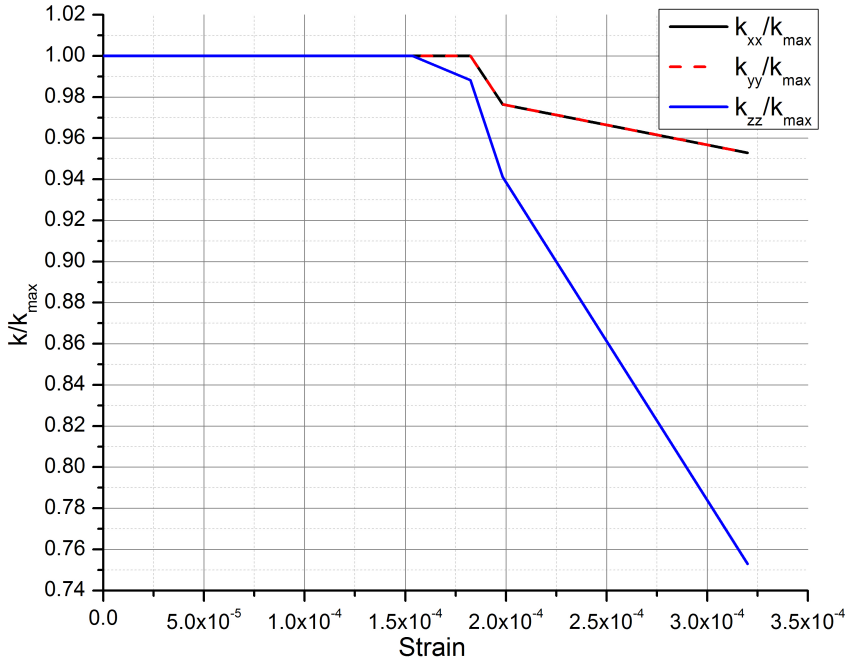

Figure 3.7 – Thermal conductivity of mortar after crack (tension)

3.1.4 Conclusion - Influence of crack on thermal conductivity of cement-based materials

Following the completion of the heat transfer simulation on damaged mortar caused by the tension and compression stresses, it is possible to conclude that cracks brought on by mechanical loads do have an effect on the thermal conductivity of the mortar. In addition, the isotropy of the thermal conductivity of the mortar can be maintained, depending on the characteristics of the cracks, even after the mortar has been subjected to compression stresses; however, it is significantly reduced. Despite this, the isotropy of the thermal conductivity of the mortar is modified after it has been subjected to tension load, although it marginally decreases in all directions.

3.2 The influence of specific heat on heat evolution in massive concrete

In this section, a sequential thermo-mechanical simulation from the micro to the macro-scale is mentioned, based on previous outcomes obtained at the micro-scale (hy-

drated cement paste) and the meso-scale (mortar). The rise in temperature caused by cement hydration heat might cause micro-fissures in the massive structure. Moreover, when the dimension of the massive structure gets larger, the temperature field is heterogeneous, which could cause residual thermal stress inside the structure. The objective is to determine whether or not the generation of heat during cement hydration is relevant for the cracking of massive structure. There have been several simulations, but only with the specific heat constant.

This section consists of a heat transfer simulation utilizing the outcomes of the specific heat constant and varies determined in section 2.4. It is being done in order to gain an understanding of how the temperature changed within the concrete body as well as the temperature difference that existed between the core and the surface of massive concrete. Different set temperatures have also been addressed to determine whether they potentially increase the maximum temperature of the concrete, which in turn might lead to the damage produced by the heat generated by the hydration of cement. After that, a mechanical simulation is implemented to determine if the massive concrete has any possibly fractured regions.

3.2.1 Materials properties

Since heat dissipation from the soil has also been taken into consideration in this simulation, table 3.1 provides additional thermal properties for the soil on which the massive structure is sitting.

Materials	Thermal Conductivity (J/h/m.K)	Specific Heat (J/kg.K)	Density (kg/m^3)
Mortar	6480	-	2433
Soil	2340	800	2000

Table 3.1 – Thermal properties for massive concrete simulation

For this simulation, the value of specific heat as a function of time is taken from figure 3.8, and the specific heat constant is taken as the value in the long term, which is equal to 0.978 J/kg.K.

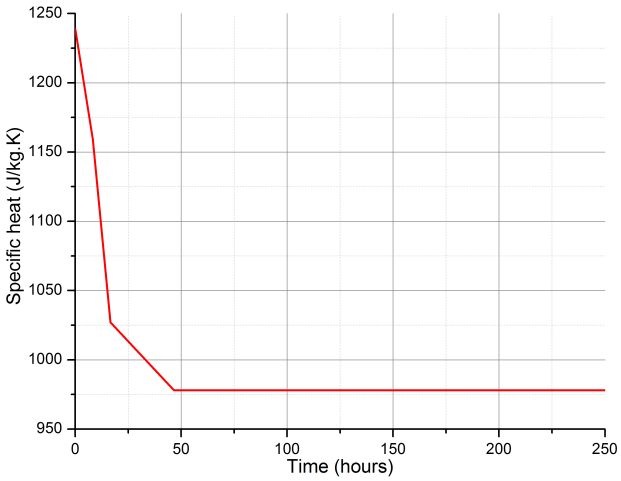

Figure 3.8 – Evolution of specific heat in function of time

3.2.2 Geometries of massive concrete

In terms of its spatial configuration, massive concrete has the shape of a cube block that is 1.5 m in dimension and is positioned on top of soil that is 1 m in height (figure 3.9 (a)). The formwork has a thickness of 2.1 cm, and it holds the concrete block in place. Figure 3.9 (b) illustrates the massive concrete block modeled in Abaqus CAE as a symmetric configuration. Therefore, just a quarter of the concrete blocks and soil are modeled.

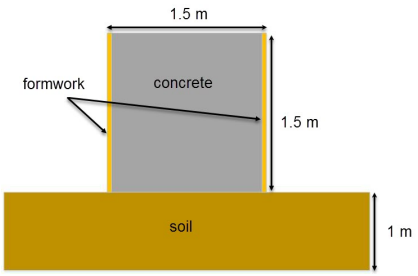

(a) 2D geometry of massive concrete block

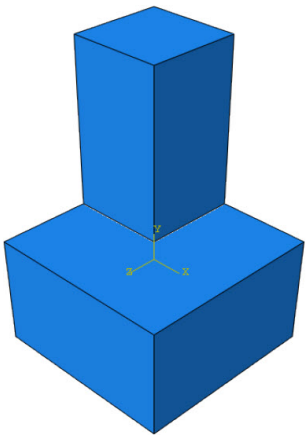

(b) 1/4 massive concrete block in Abaqus

Figure 3.9 – Geometry of massive concrete block

3.2.3 Initial and boundaries conditions

This part discusses the sensitivity analysis of the initial temperature of concrete, therefore different initial conditions, including 20, 25, 30, 35, 40, and 50 °C, have been selected for this study.

Regarding the boundary conditions, the top surface of the concrete is exposed to the solar flux and exchanges its temperature with the ambient temperature. Taken from [284], the coefficients of convection (H_c) and radiation (H_r) are 33.9 and 20.2 kJ/h.m^2.K, respectively; so, the exchange coefficient (H_{c+r}) is 54.2 kJ/h.m^2.K. In addition, the four literal surfaces were sealed by formworks of 2.1 cm thick and subjected to the same environment as the top surface. As a result, the exchange coefficient of convection and radiation is reduced (figure 3.11) and can be estimated by implementing equation 3.1. The bottom surface of the concrete stands on the soil, which has a temperature of 20 °C and the top surface is exposed to solar heat flux which is equal to 829.92 kJ/h.m^2.

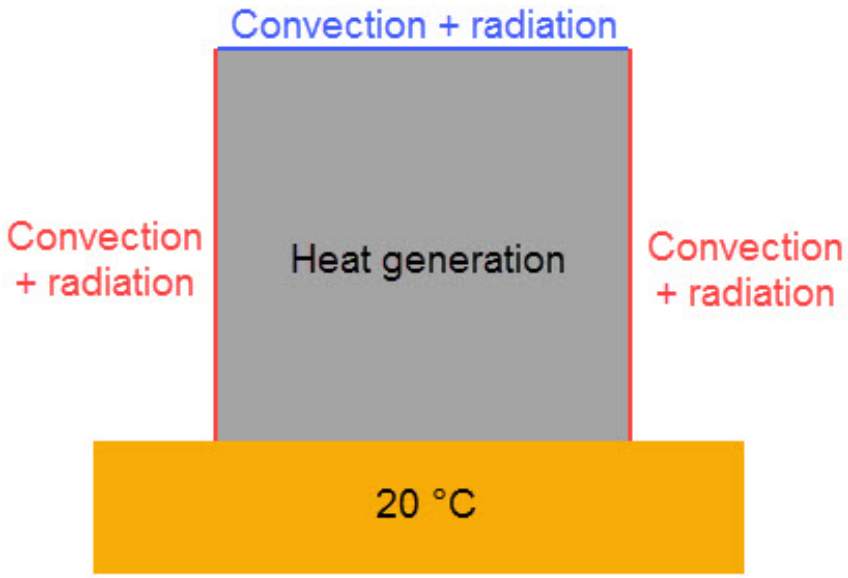

Figure 3.10 – Boundary conditions for massive concrete simulation

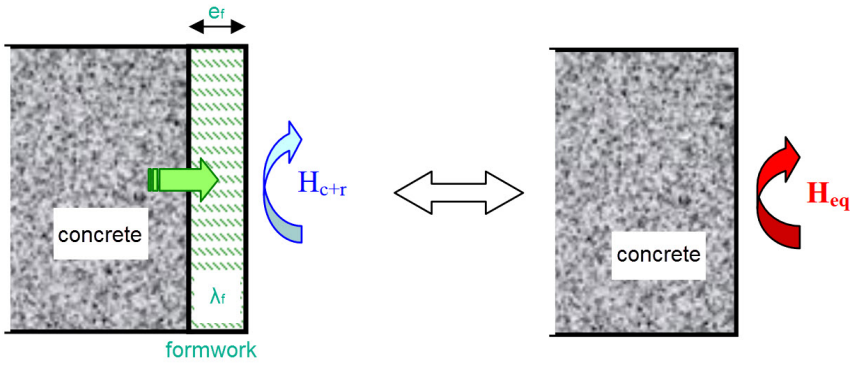

Figure 3.11 – Equivalent exchange coefficient [284]

$$\frac{1}{H_{\text{eq}}} = \frac{1}{H_{\text{c+r}}} + \frac{e_{\text{f}}}{\lambda_{\text{f}}} \tag{3.1}$$

where H_{eq} : equivalent exchange coefficient (kJ/h.m^2.K),
H_{c+r} : exchange coefficient = 54.2 kJ/h.m^2.K,
e_f : thickness of the formwork = 0.021 m,
λ_f : thermal conductivity of formwork = 540 W/m.K.
Thus, the equivalent exchange coefficient equal to 17.4 kJ/h.m^2.K.

3.2.4 Cumulative heat and rate of hydration heat

In this part, the accumulated hydration heat and it's rate from equation 1.34 and 1.35 will be employed.

The equation 1.34 is a function of initial temperature, which indicates that the temperature of the concrete when it was first mixed does have an effect on the overall quantity of heat generated by the hydration of the cement. Moreover, form CEM I 42.5N cement, the value of constants can be found in table 3.2 [264], [285].

Constants	ω	φ	ζ	ξ
Value	55	0.481	0.039	1.25

Table 3.2 – Constants used in equation 1.34

In this case, the ordinary Portland Cement is used in the concrete and the amount of cement per unit volume concrete (W) is equal to 350 kg/m^3.

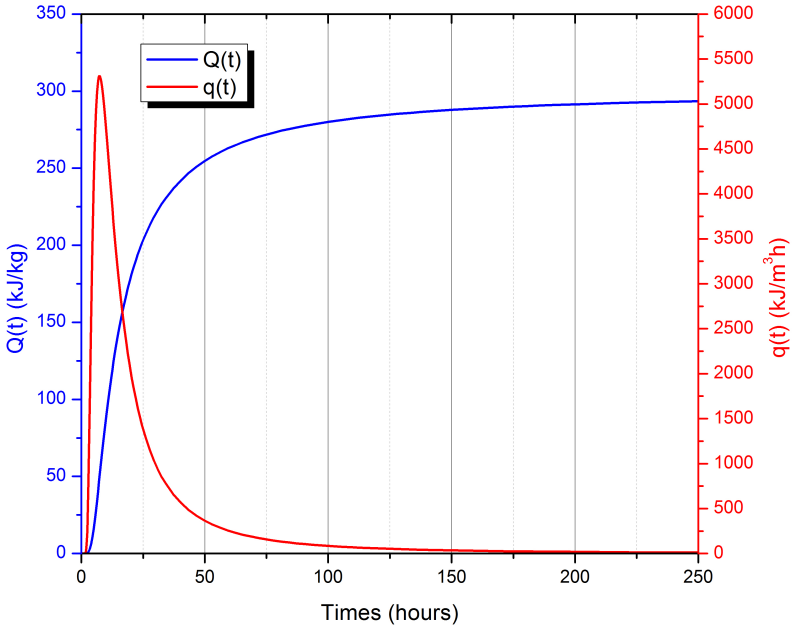

Figure 3.12 – Accumulative hydration heat (blue) and hydration heat rate (red)

The hydration heat (Q) and its rate (q), estimated over a period of 250 hours, are revealed in Figure 3.12. The total hydration heat is about 300 kJ/kg and the maximum heat rate is around 5300 kJ/m^{3}h at 7 hours after mix.

3.2.5 Implement hydration heat rate in Abaqus FEA

A subroutine called "HETVAL" is required in order to simulate heat generation (equation 1.35) from the cement hydration in Abaqus FEA [286]. This subroutine is written using FORTRAN programming language. The rate at which internal heat is generated is given in the subroutine, which is depending on the state variable, changes as the solution evolves, and stores the results as solution-dependent state variables. Moreover, it will be called at each computation increment (figure 3.13).

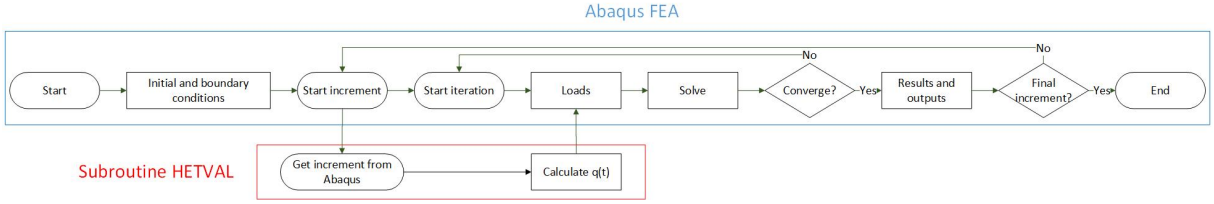

Figure 3.13 – Implement of subroutine HETVAL in Abaqus FEA

3.2.6 Primary results and discussion

As was just mentioned, the primary results will concentrate on the development of temperature inside the block, the influence of change in specific heat, and the initial temperature of the concrete.

3.2.6.1 Temperature evolution inside the concrete block

The change in the temperature within the concrete block during 250 hours is depicted in Figure 3.14, which shows the temperature at three different spots (top, bottom, and center). In this case, the initial temperature is set at 20°C. It is apparent that the maximum temperature inside the concrete might be attained between 25 and 45 hours after mixing. The maximum temperature of the top, bottom, and center of the concrete are 41.7, 42.6, and 52.7°C, respectively. As a result, the greatest difference between the core and the surface of the concrete is roughly 11°C, which might produce residual tension and cracking inside the concrete. Section 3.2.8 will, however, investigate the impact of residual thermal stress on cracking.

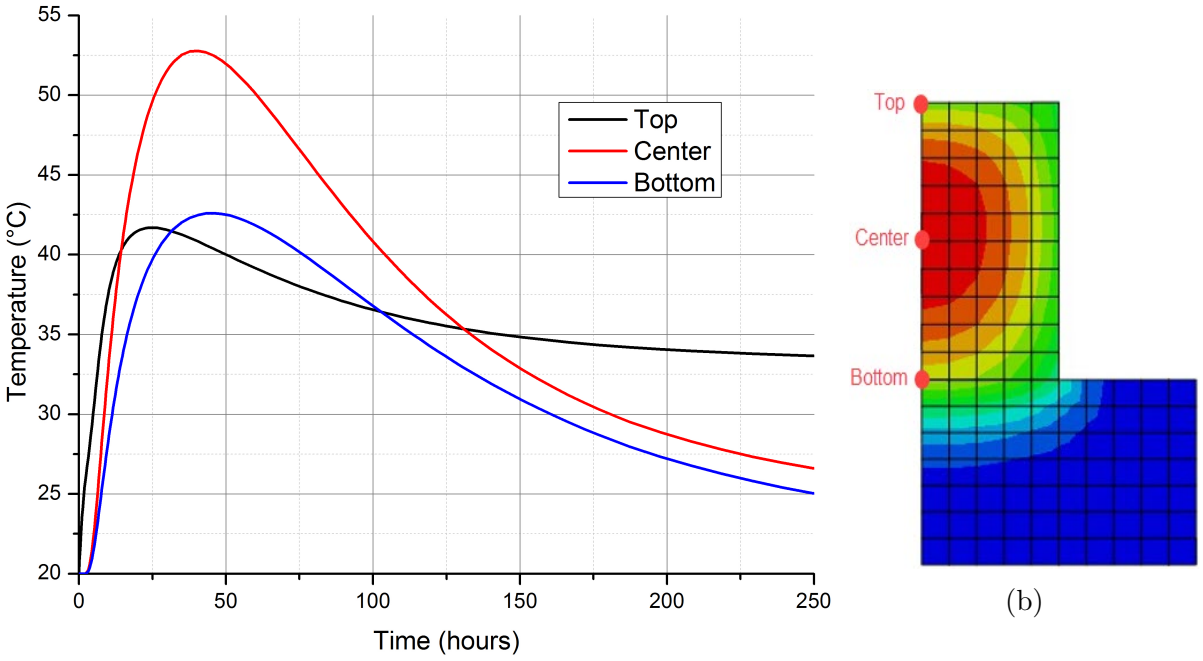

(a) (b)

Figure 3.14 – (a) Temperature evolution at different positions inside concrete block, (b) Temperature cartography

3.2.6.2 Influence of specific heat on temperature development inside concrete

In order to understand the significance of the specific heat result found in Section 2.4 on the temperature evolution of the concrete block, a comprehensive study on heat transfer simulation with specific heat constant and in the function of time (figure 3.8) was conducted. Figure 3.15 illustrates the findings of both simulations.

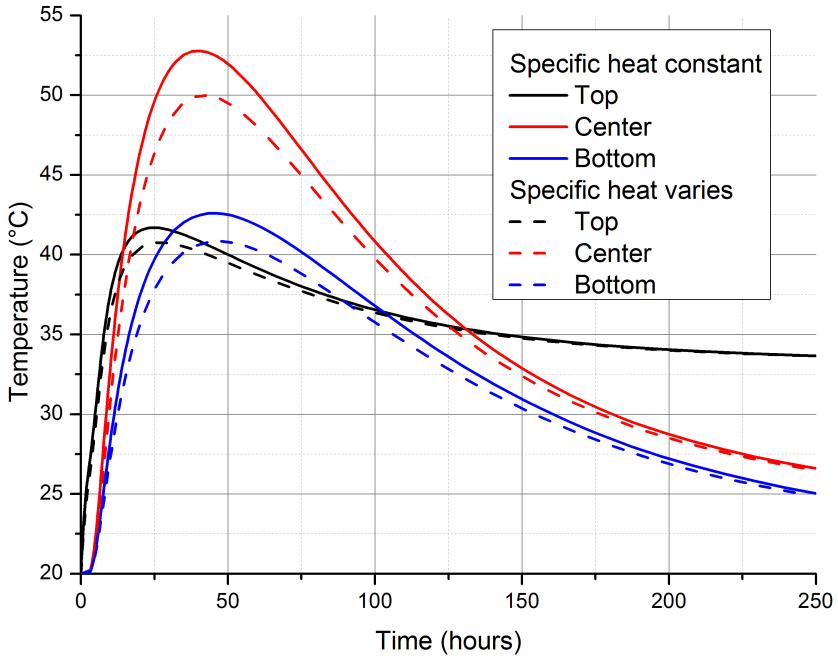

Figure 3.15 – Temperature evolution with specific heat constant (solid lines) and varies (dash lines)

In general, the maximum temperatures are lower for the simulation with specific heat varies in function of time. The Percent Difference (PD) between the two simulations is about 5.12% at the core on concrete. Moreover, the difference between the core and the surface of concrete, being around 9.2°C, is still important for the simulation with specific heat varies.

	$T_{max,\ c_p\ constant}$ (°C)	$T_{max,\ c_p\ varies}$ (°C)	PD (%)
Top	41.7	40.8	2.15
Center	52.7	50	5.12
Bottom	42.6	40.9	3.99

Table 3.3 – Maximum temperature inside the concrete block

3.2.6.3 Influence of initial temperature on the maximum temperature of concrete

In this instance, the initial temperature will be examined to see if it has any effect on the maximum temperature of the concrete. The initial temperatures of 20, 25, 30, 40, and 50°C were chosen, and they will be integrated into the simulation using equation 1.34 and subroutine HETVAL.

Figure 3.16 illustrates the development of temperature at the core of the concrete, where the highest temperature occurs, for each initial temperature. The vertical axis is shown by the ratio of temperature development to maximum temperature at 20°C. As observed, increasing the initial temperature raises the concrete block's maximum temperature at an early age. In addition, the temperature reaches the maximum value sooner when the initial temperature is more significant. This is because the hydration reaction accelerates at higher temperatures, which raises the temperature faster.

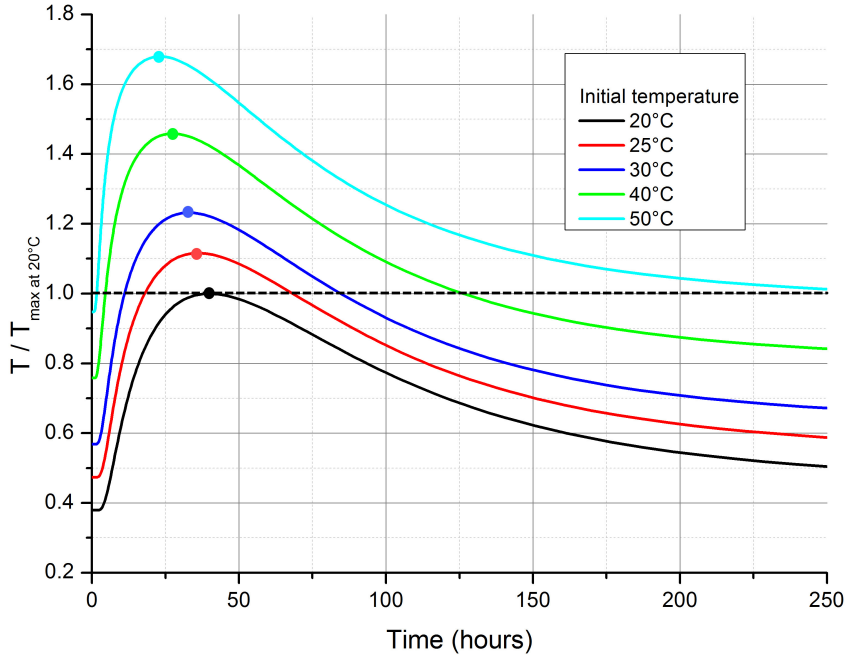

Figure 3.16 – Temperature evolution with different initial temperatures

In addition to figure 3.16, figure 3.17 and 3.18 provide a summary of the maximum temperature, the value representing the difference between the maximum and initial temperature for each initial temperature, and the different temperature between the core and surface of the concrete. It demonstrates that there is a wider gap between the initial

and the maximum temperature when the initial temperature is higher. In addition, it indicates that the temperature difference between the core and the surface also increases (up to 20°C) as the initial temperature rises, which may result in residual stress and the initiation of cracking within the concrete at an early stage.

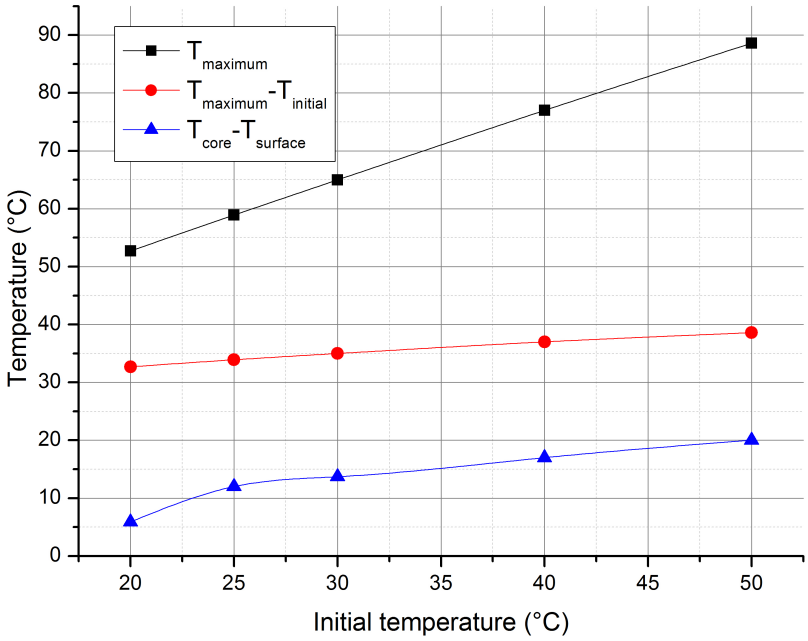

Figure 3.17 – Different temperature between maximum, initial, and surface temperature for each initial temperature

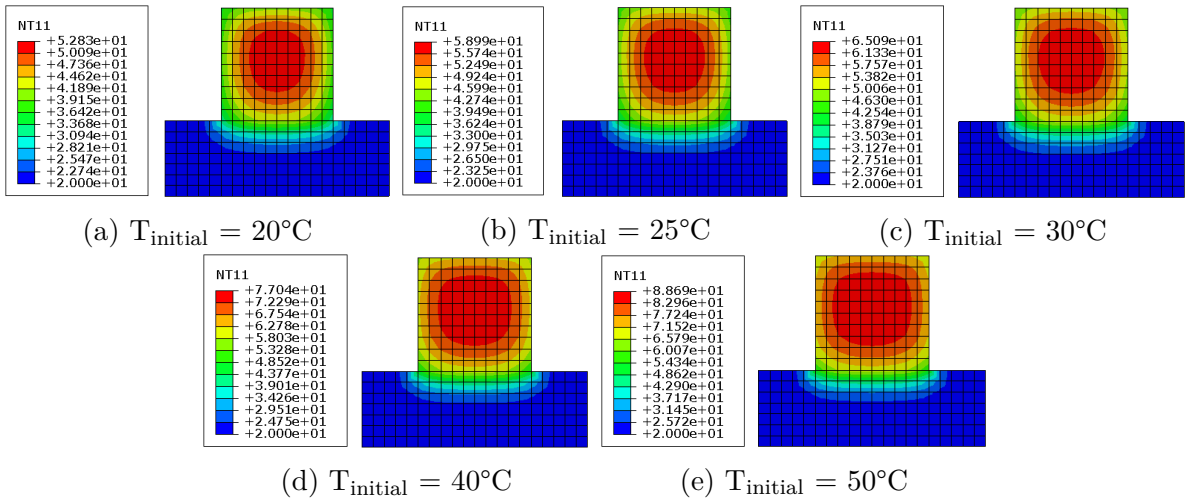

(a) $T_{initial}$ = 20°C (b) $T_{initial}$ = 25°C (c) $T_{initial}$ = 30°C

(d) $T_{initial}$ = 40°C (e) $T_{initial}$ = 50°C

Figure 3.18 – Temperature cartography with different initial temperatures

3.2.7 Equivalent age concrete of massive concrete

Since the hydration rate is a function of temperature, and since the temperature in massive concrete is not uniform, the hydration rate within the concrete block is likewise not uniform. Therefore, the expression of cumulative hydration heat, Q, in equation 1.34 is modified, and the time variable, t, is replaced by the equivalent time, t_e. If t is obtained through finite element software, the t_e is calculated using equation 3.2, which is modified from equation 1.14. Since the temperature within the concrete block changes over time, the t_e will be computed at each time increment. The parameters, ω, φ, ζ, and ξ, of the equation must then be modified. Considering the temperature at the core of the concrete is closest to the quasi-adiabatic condition, it is used to calculate the t_e and to modify the parameters.

$$t_{e,n} = \sum_{i=1}^{n} e^{\left[-\frac{E_a}{R}\left(\frac{1}{\frac{T_i+T_{i-1}}{2}}-\frac{1}{T_s}\right)\right]}(t_i - t_{i-1}) \tag{3.2}$$

where t_i : time at increment i from finite element software (in days or hours),
T_i : temperature at increment i (in K).

Figure 3.19 depicts the calculated t_e and temperature at the core of concrete as a function of t. When the temperature hits its peak at around 40 hours, t_e is nearly triple (112 hours) the normal simulation duration and drops to more than double ($t_e = 530$ hours and t = 239.5 hours) at the completion of simulation. It demonstrates how important it is to include the t_e in the simulation to acquire accurate heat generation from the cement hydration reaction.

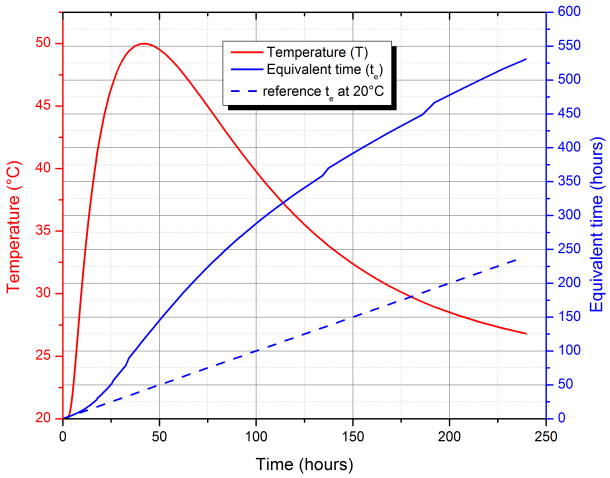

Figure 3.19 – Time equivalent and temperature at core on concrete in function of time

Figure 3.20 and table 3.4 both illustrate the new cumulative hydration heat, as well as new constants to be employed in equation 1.34. The revised curve $Q(t_e)$ is then utilized in the next simulation by implementing the equivalent time (t_e) in the subroutine HETVAL instead of the time (t).

Constants	ω	φ	ζ	ξ
Value	190	0.27	0.12	1.32

Table 3.4 – New constants used in equation 1.34

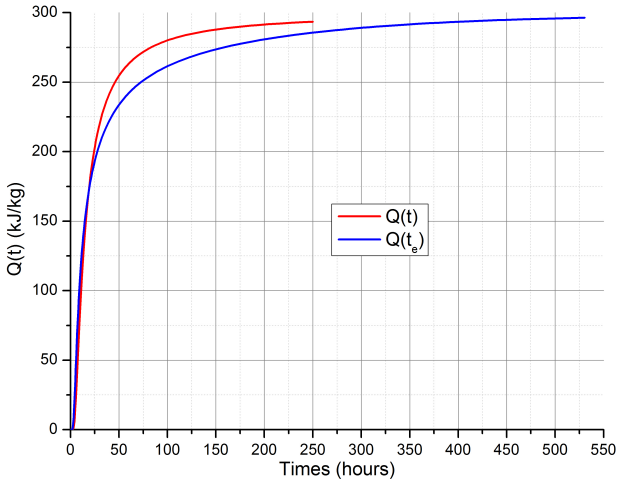

Figure 3.20 – Accumulated hydration heat in function of time and equivalent time

Figure 3.21 illustrates the temperature evolution in the concrete core as a result of the heat transfer simulation using Q(t) and Q(t_e). It demonstrates that the temperature development of the simulation with Q(t_e) achieves a maximum, at 25 hours, earlier than that with Q(t), at 40 hours. Furthermore, its highest peak is also lower than that of the Q(t) simulation, at 42°C and 53°C, respectively.

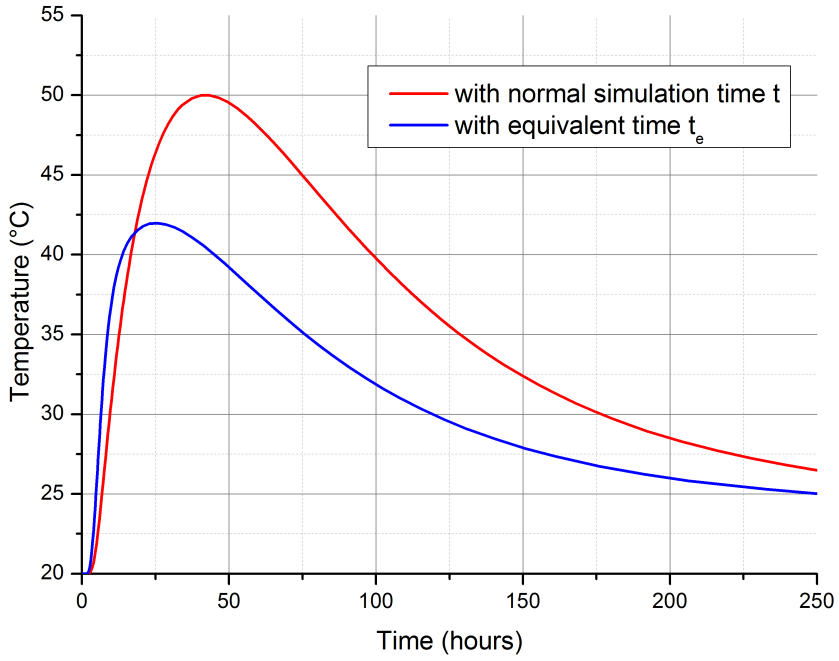

Figure 3.21 – Temperature evolution at the core of concrete simulated with t and t_e

3.2.8 Thermal stress

The fluctuations in temperature may put a body under a variety of strains, one of which is known as thermal stress. Since the thermal stresses may induce cracking or other types of unwanted plastic deformation, it is essential to have a solid grasp of where these stresses come from and what causes them [287]. The heat of cement hydration and the temperature difference between the core and the outside is crucial in massive concrete, as discussed in the preceding section, it generates thermal stresses that produce cracking or plastic deformation inside the massive concrete structural member. Another investigation into the effect of hydration heat on cement, which can lead to thermal stress and crack development, has been carried out in this part of this research.

In general, when a solid cannot deform freely, the thermal stress caused from temper-

ature change from T_i to T_f can be found in equation 3.3.

$$\sigma_T = -E\alpha(T_f - T_i) \tag{3.3}$$

where σ_T : thermal stress (MPa),
E : elastic modulus (MPa),
α : coefficient of thermal expansion (/K) section 2.5,
T_f, T_i : final and initial temperature (K).

If $T_f < T_i$, thermal stress is tensile stress ($\sigma_T>0$); if $T_f > T_i$, it is compressive stress ($\sigma_T<0$).

Thermal and mechanical properties are required in order to examine the effect of thermal stress on massive concrete, such as cracks and plastic deformation. First, compressive and tensile stress and strain curves can be found in section 3.2.8.1; second, the concrete damage plasticity model (CDP) used to study about the cracks is described in section 3.2.8.2.

3.2.8.1 Stress and strain curve from *fib*'s model

The compression and tension stress and strain curves of concrete have been re-plotted in accordance with the CEB-FIP Model Code 1990: Design Code [288] and the Fib Model Code for Concrete Structures 2010 [289] from the International Federation for Structural Concrete (*fib*). These curves account for the plasticity portion of concrete's mechanical behavior and may be used to compute the damage parameters in section 3.2.8.2. Figures 3.22 and 3.23 depict the stress and strain curves for compression and tension from the *fib*'s codes, respectively.

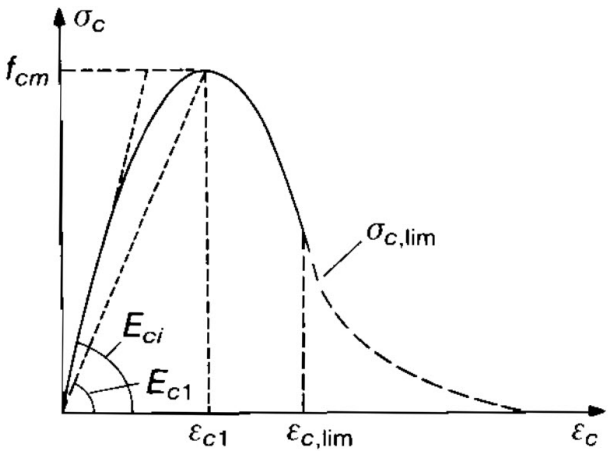

Figure 3.22 – Compression stress and strain curve from the *fib*'s codes [288]

The compression stress and strain curve decomposes into two parts, a part of the curve where $|\varepsilon| < |\varepsilon_{\mathrm{c,lim}}|$ and another part where $|\varepsilon| > |\varepsilon_{\mathrm{c,lim}}|$. The $\varepsilon_{\mathrm{c,lim}}$ is the ultimate strain which may be computed by using equation 3.4.

$$\varepsilon_{c,lim} = \frac{\varepsilon_{c1}}{2}\left(\frac{E_{ci}}{2E_{c1}} + 1\right) + \varepsilon_{c1}\sqrt{\frac{1}{4}\left(\frac{E_{ci}}{2E_{c1}} + 1\right)^2 - \frac{1}{2}} \tag{3.4}$$

with

$$E_{ci} = E_{co}\left(\frac{f_{cm}}{f_{cmo}}\right)^{\frac{1}{3}}$$

$$E_{c1} = \frac{f_{cm}}{0.0022}$$

$$f_{cm} = f_{ck} + 8MPa$$

where $\varepsilon_{c,lim}$: ultimate strain,
ε_{c1} : strain where the compressive stress is maximum = -0.0022,
E_{ci} : tangent modulus (MPa),
E_{c1} : secant modulus from the origin to the peak (MPa),
f_{cm} : compressive strength at 28 days (MPa),
f_{ck} : characteristic strength (MPa),
E_{co} : 2.15×10^4 MPa,
f_{cmo} : 10 MPa.

Moreover, the first part of the compression curve can be found by using equation 3.5.

$$\sigma_c = -\frac{\frac{E_{ci}}{E_{c1}}\frac{\varepsilon_c}{\varepsilon_{c1}} - \left(\frac{\varepsilon_c}{\varepsilon_{c1}}\right)^2}{1 + \left(\frac{E_{ci}}{E_{c1}} - 2\right)\frac{\varepsilon_c}{\varepsilon_{c1}}} f_{cm} \tag{3.5}$$

where σ_c : compressive stress (MPa),
ε_c : compressive strain.

In addition, the second part of the curve can be plotted according to equation 3.6.

$$\sigma_c = -\left[\left(\frac{1}{\varepsilon_{c,lim}/\varepsilon_{c1}}\xi - \frac{2}{(\varepsilon_{c,lim}/\varepsilon_{c1})^2}\right)\left(\frac{\varepsilon_c}{\varepsilon_{c1}}\right)^2 + \left(\frac{4}{\varepsilon_{c,lim}/\varepsilon_{c1}} - \xi\right)\frac{\varepsilon_c}{\varepsilon_{c1}}\right]^{-1} f_{cm} \tag{3.6}$$

with

$$\xi = \frac{4\left[\left(\frac{\varepsilon_{c,lim}}{\varepsilon_{c1}}\right)^2\left(\frac{E_{ci}}{E_{c1}} - 2\right) + 2\frac{\varepsilon_{c,lim}}{\varepsilon_{c1}} - \frac{E_{ci}}{E_{c1}}\right]}{\left[\frac{\varepsilon_{c,lim}}{\varepsilon_{c1}}\left(\frac{E_{ci}}{E_{c1}} - 2\right) + 1\right]^2}$$

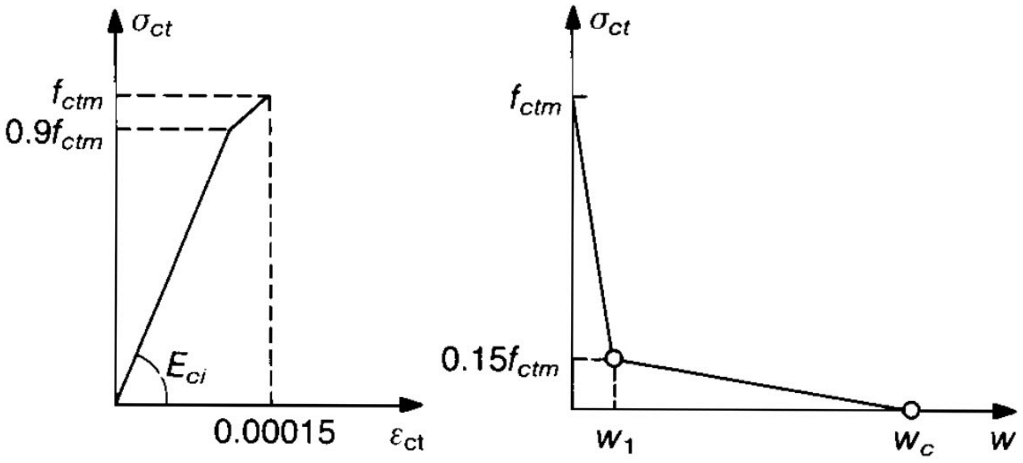

(a) Stress and strain curve (b) Stress and crack opening

Figure 3.23 – Tension stress and strain curve from the *fib*'s codes [288]

The tension stress and strain curve, like the compression curve, is divided into two portions. Figure 3.23(a) can be employed alongside with equations 3.7 and 3.8 for the uncracked concrete section in the first segment.

For $\sigma_{ct} \leq 0.9 f_{ctm}$:

$$\sigma_{ct} = E_{ci}\varepsilon_{ct} \tag{3.7}$$

For $0.9 f_{ctm} < \sigma_{ct} \leq f_{ctm}$:

$$\sigma_{ct} = f_{ctm} - \frac{0.1 f_{ctm}}{0.00015 - 0.9 f_{ctm}/E_{ci}}(0.00015 - \varepsilon_{ct}) \tag{3.8}$$

with

$$f_{ctm} = f_{ctko,m}\left(\frac{f_{ck}}{f_{cko}}\right)^{2/3}$$

where σ_{ct} : tensile stress (MPa),
ε_{ct} : tensile strain,
f_{ctm} : tensile strength (MPa),
$f_{ctko,m}$: 1.40 MPa,
f_{cko} : 10 MPa.

Moreover, figure 3.23(b) is plotted by using equations 3.9 and 3.10 for cracked concrete section in the second segment. The base value of fracture energy (G_{Fo}) and coefficient

(α_F) depend on the maximum size of aggregate and can be found in the CEB-FIP Model Code 1990: Design Code [288].

For $0.15 f_{ctm} \leq \sigma_{ct} \leq f_{ctm}$:

$$\sigma_{ct} = f_{ctm}\left(1 - 0.85\frac{w}{w_1}\right) \tag{3.9}$$

For $0 \leq \sigma_{ct} < 0.15 f_{ctm}$:

$$\sigma_{ct} = \frac{0.15 f_{ctm}}{w_c - w_1}(w_c - w) \tag{3.10}$$

with

$$w_1 = 2\frac{G_F}{f_{ctm}} - 0.15 w_c$$

$$w_c = \alpha_F \frac{G_F}{f_{ctm}}$$

$$G_F = G_{Fo}\left(\frac{f_{cm}}{f_{cmo}}\right)^{0.7}$$

where
- w : crack opening (mm),
- w_1 : crack opening (mm) at $\sigma_{ck} = 0.15 f_{ctm}$,
- w_c : crack opening (mm) at $\sigma_{ct} = 0$,
- G_F : fracture energy (Nmm/mm^2),
- G_{Fo} : base value of fracture energy (Nmm/mm^2),
- α_F : coefficient to estimate w_c.

In this study case, the characteristic strength of concrete (f_{ck}) is 55 MPa and the values of other parameters are computed and presented in table 3.5.

f_{cm} (MPa)	E_{ci} (MPa)	E_{ci} (MPa)	$\varepsilon_{c,lim}$	ξ
63	39708.67	28636.36	-0.00289	19.09

Table 3.5 – Mechanical properties calculated for compression curve

With the parameters shown in table 3.5, the compression stress and strain curve is plotted and shown in figure 3.24.

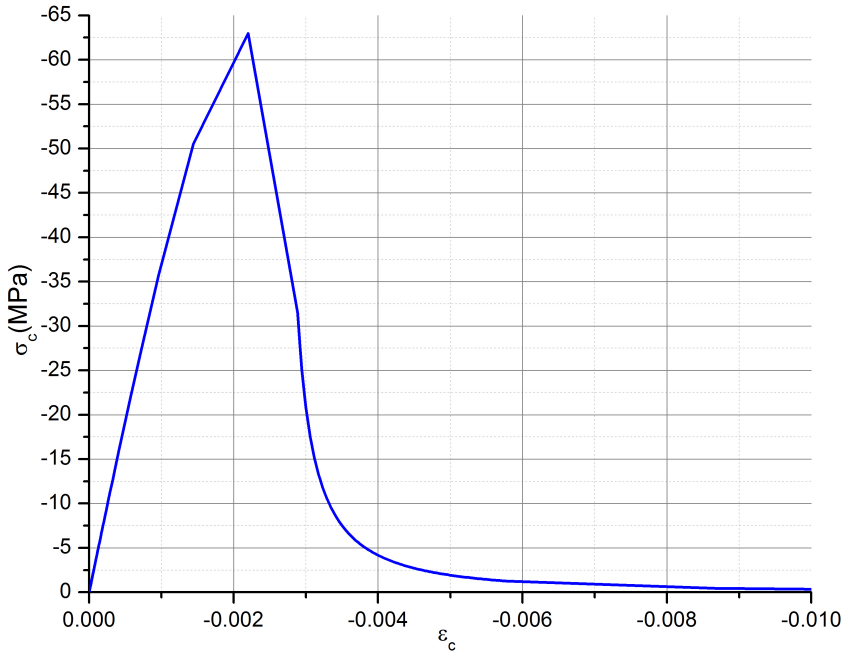

Figure 3.24 – Compression stress and strain curve

Furthermore, the parameters used for tension curve are computed and shown in table 3.6. The tension stress and strain, and stress and crack opening curve are shown in figures 3.25 and 3.26, respectively.

f_{ctm} (MPa)	G_{Fo}	G_F	α_F	w_1 (mm)	w_c (mm)
4.36	0.025	0.09	8	0.017	0.17

Table 3.6 – Mechanical properties calculated for tension curve

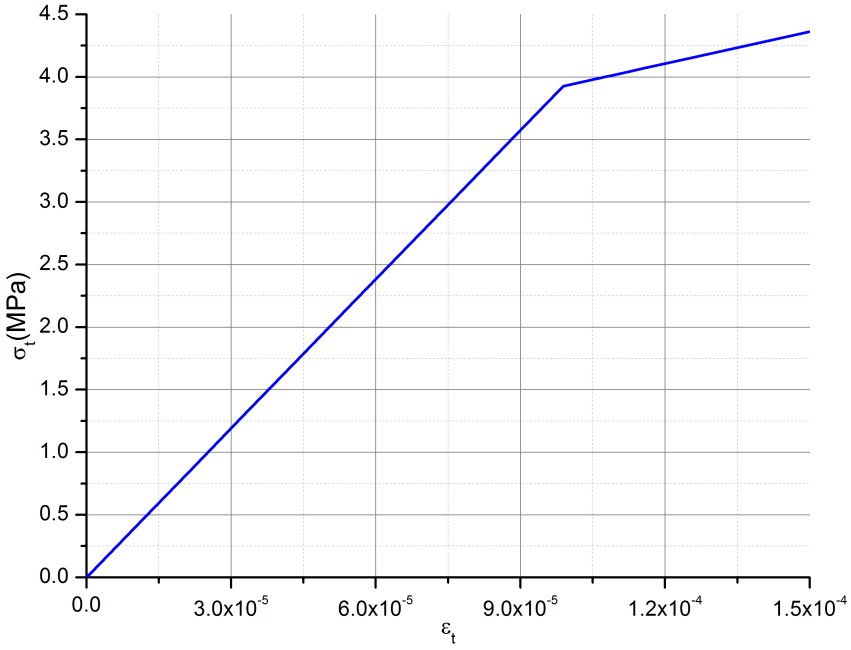

Figure 3.25 – Tension stress and strain curve

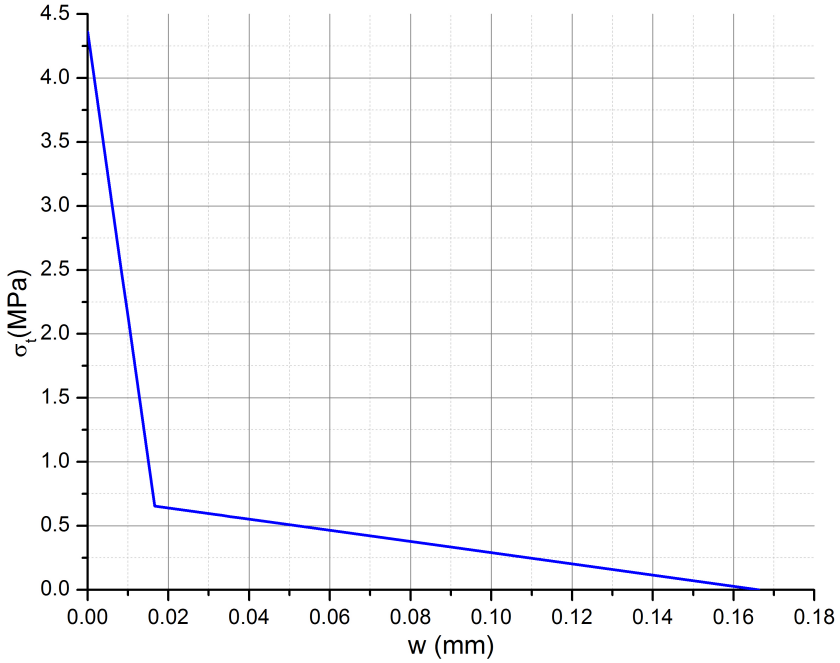

Figure 3.26 – Tension stress and crack opening curve

The curves produced in figures 3.24, 3.25, and 3.26 are utilized in the next section to determine damaged parameters for compression and tension before being input into Abaqus FEA for crack modeling.

3.2.8.2 Concrete Damage Plasticity (CDP) model

In order to study cracking, the Concrete Damage Plasticity (CDP) model may be suitable for use with concrete since it is based on the assumption that plastic degradation only occurs in the softening range [290]. This model takes into consideration the damage variable (d_c and d_t), which indicates the change in elastic modulus that occurs in the concrete during the softening stage ($|\varepsilon_c| > |\varepsilon_{c1}|$ and $|\varepsilon_{ct}| > 0.00015$) when cracks are formed in the matrix [291]. According to the assumptions made by the model, the uniaxial tensile and compressive responses of concrete characterized by damaged plasticity can be seen in figures 3.27 and 3.28, respectively.

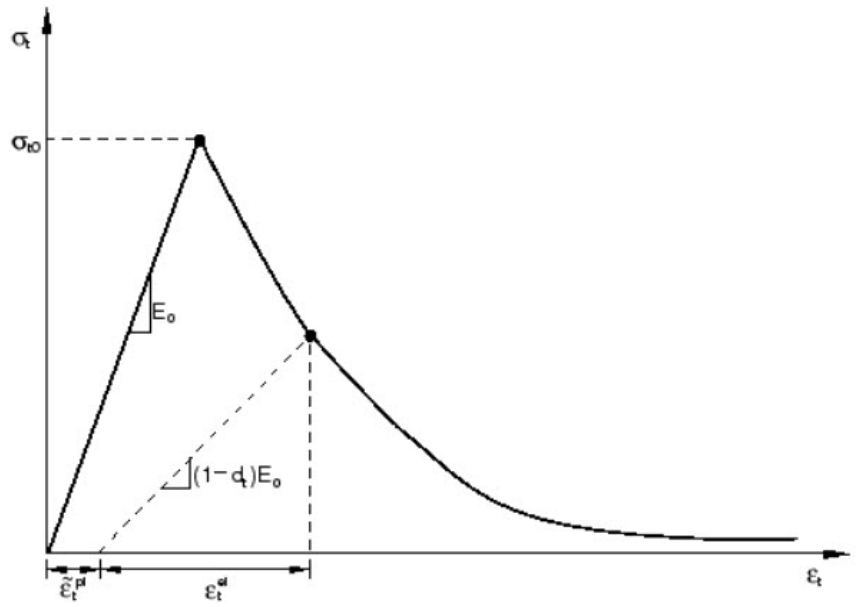

Figure 3.27 – Concrete Damage Plasticity (CDP) model for tension [292]

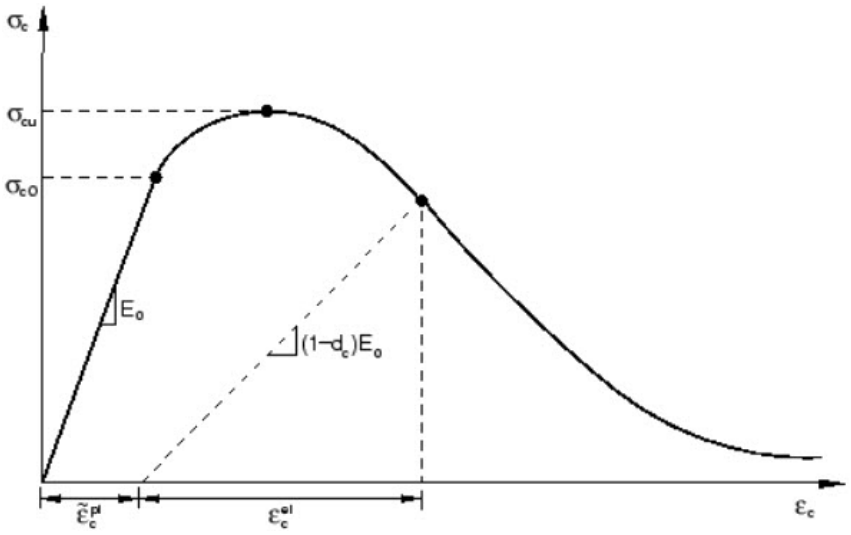

Figure 3.28 – Concrete Damage Plasticity (CDP) model for compression [292]

The relationship between stress and strain during the softening stage of compression and tension is then adjusted as illustrated in equations 3.11 and 3.12, respectively.

$$\sigma_c = (1 - d_c)E_0(\varepsilon_c - \tilde{\varepsilon}_c^{pl}) \tag{3.11}$$

$$\sigma_t = (1 - d_t)E_0(\varepsilon_t - \tilde{\varepsilon}_t^{pl}) \tag{3.12}$$

where E_0 : initial elastic modulus (MPa),
d_c, d_t : compression and tension damage variable,
$\tilde{\varepsilon}_c{}^{pl}$, $\tilde{\varepsilon}_t{}^{pl}$: equivalent plastic strains.

From equations 3.11 and 3.12, the effective cohesion stresses can be defined as in equations 3.13 and 3.14.

$$\bar{\sigma}_c = \frac{1}{(1 - d_c)} = E_0(\varepsilon_c - \tilde{\varepsilon}_c^{pl}) \tag{3.13}$$

$$\bar{\sigma}_t = \frac{1}{(1 - d_t)} = E_0(\varepsilon_t - \tilde{\varepsilon}_t^{pl}) \tag{3.14}$$

The effective stresses, $\bar{\sigma}_c$ and $\bar{\sigma}_t$, represent the boundaries of the yield (or failure) surface in multi-axial behavior; thus, they are identical to f_{cm} and f_{ctm} in uni-axial behavior.

Before the softening stage, the damage parameters, d_c and d_t, are considered as 0

(equation 3.15). Furthermore, the d_c and d_t may be determined during the softening stage by using equation 3.16 [293]. It also is worth mentioning that ε^{peak} is the deformation when the maximum stress reaches. Moreover, if the d_c and d_t are equal to 1, the concrete has completely lost its strength.

For $|\varepsilon| < |\varepsilon^{peak}|$:

$$d_{c,t} = 0 \tag{3.15}$$

For $|\varepsilon| \geq |\varepsilon^{peak}|$ and $\dot{\varepsilon}_t > 0$ or $\dot{\varepsilon}_c < 0$:

$$d_{c,t} = 1 - \frac{\sigma_{c,t}}{f_{cm,ctm}} \tag{3.16}$$

In contrast, when $\dot{\varepsilon}_t < 0$ or $\dot{\varepsilon}_c > 0$ (i.e. during unloading), the damage parameters are regarded to be equal to their maximum values that have been reached.

In Abaqus, the input data needed are stress, inelastic strain ($\varepsilon_{c,inelastic}$) and d_c. The inelastic strain are the strain shown in figure 3.29 and it can be simply calculated by equation 3.17. Moreover, for tension, the data needed are stress, crack opening, and d_t.

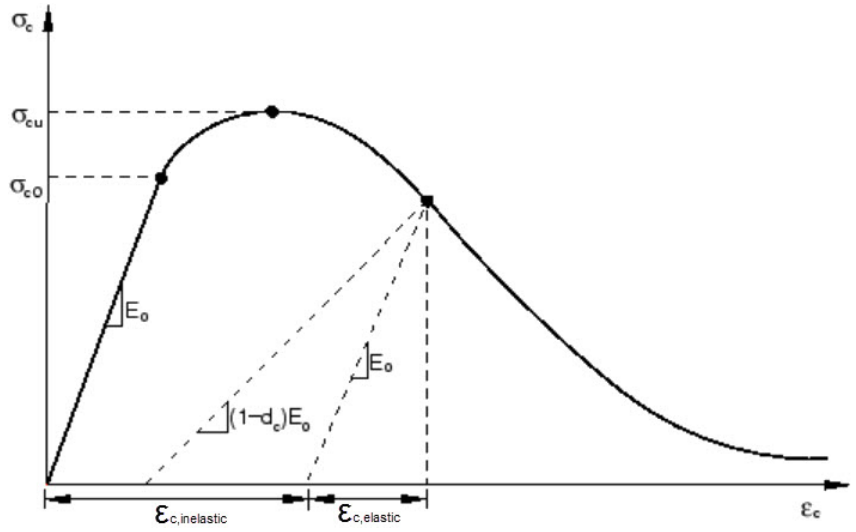

Figure 3.29 – Stress, elastic and inelastic strain for compression

$$\varepsilon_{c,inelastic} = \varepsilon_c - \varepsilon_{c,elastic} \tag{3.17}$$

By using the data from figures 3.24, 3.25, and 3.26 along side with the equations 3.15

and 3.16, the d_c and d_t are computed and depicted in figures 3.30 and 3.31, respectively.

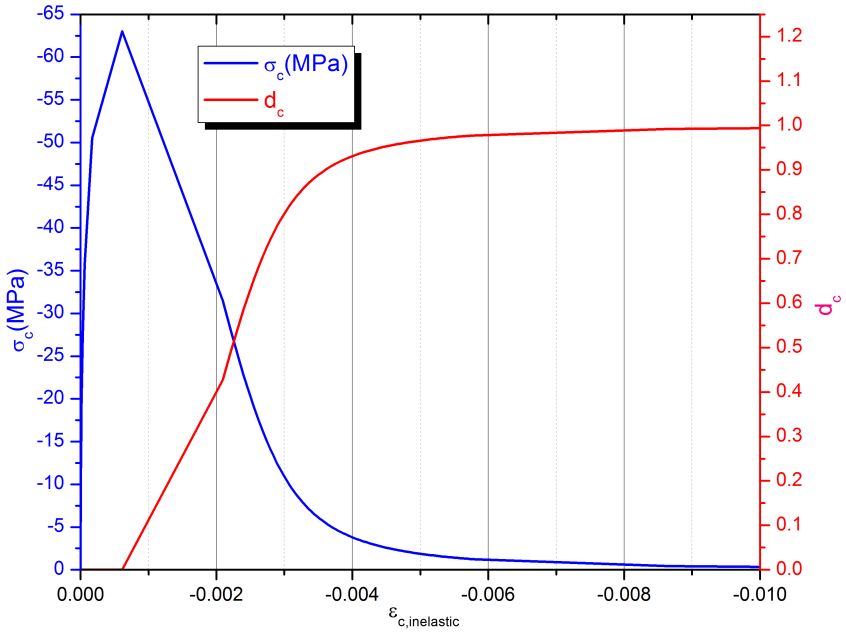

Figure 3.30 – Stress, inelastic strain, and d_c for compression

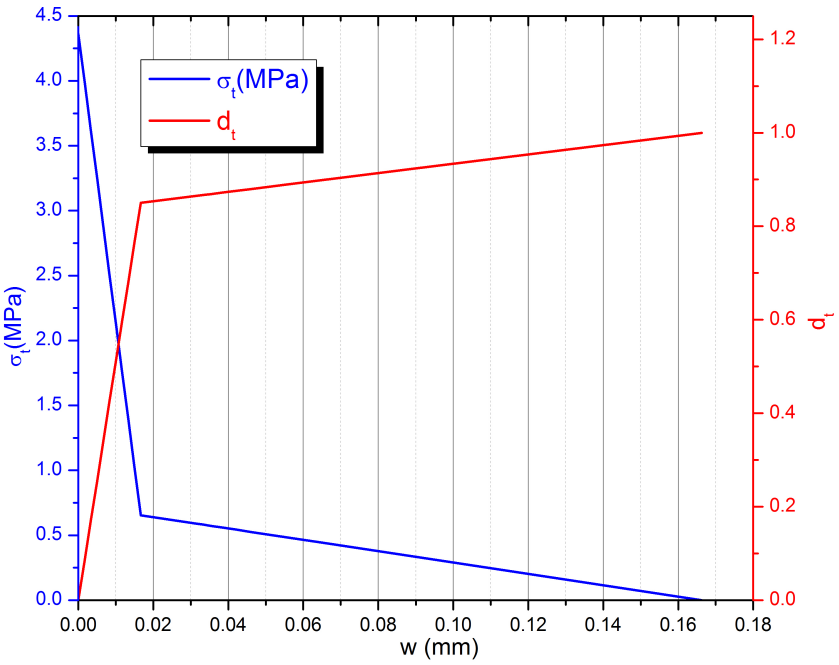

Figure 3.31 – Stress, crack opening, and d_t for tension

3.2.8.3 Time-dependant Mechanical properties

Since the temperature inside the concrete does not evenly distribute, the equivalent time (t_e), as specified in section 3.2.7, was used in the computation. Along the same lines as the heat of hydration, the mechanical properties such as compressive, tensile strength, and elastic modulus vary over time. Due to this, it is necessary to compute these values in a function of equivalent time.

In the CEB-FIP Model Code 1990: Design Code [288], the expression of compressive strength and elastic modulus in function of time are shown in equations 3.18 and 3.19, respectively.

$$f_{cm}(t) = \beta_{cc}(t) f_{cm} \tag{3.18}$$

$$E_{ci}(t) = \beta_E(t) E_{ci} \tag{3.19}$$

with

$$\beta_{cc}(t) = e^{s\left[1-\left(\frac{28}{t/t_1}\right)^{1/2}\right]}$$

$$\beta_E(t) = [\beta_{cc}(t)]^{0.5}$$

where
$f_{cm}(t)$: compressive strength (MPa) at time t days ,
$E_{ci}(t)$: elastic modulus (MPa) at time t days ,
$\beta_{cc}(t)$, $\beta_E(t)$: coefficient depending on time t,
s : coefficient depending on cement type (= 0.2 in this case),
t : time (days),
t_1 : 1 day.

Figure 3.32 illustrates the compressive stress and elastic modulus over the duration of 28 days.

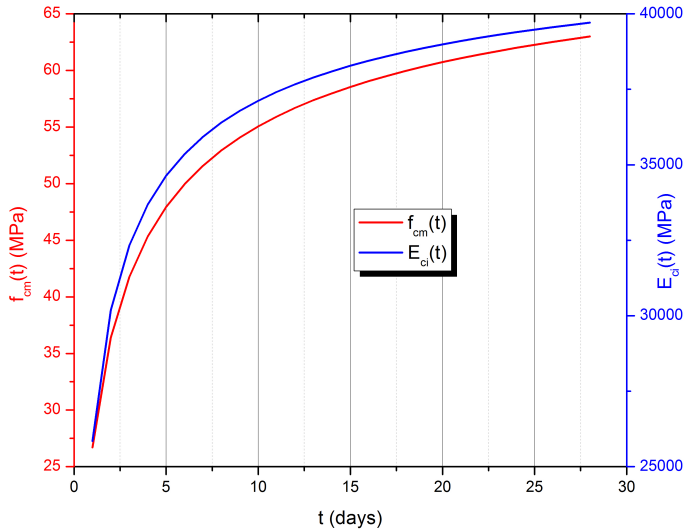

Figure 3.32 – Compressive stress and elastic modulus in function of time

3.2.9 Result and discussion

Since the heat transfer simulation is run first, followed by the mechanical simulation, this final simulation is regarded as a thermo-mechanical sequential simulation (as in section 2.5.2.1). The mechanical simulation uses the temperature outputs from heat transfer simulation (from section 3.2.7) and it has exactly the same geometries as in heat transfer simulation. Equivalent times are also computed in mechanical simulation, and the subroutine USDFLD is used to define field variables (stress and elastic modulus) as a function of time.

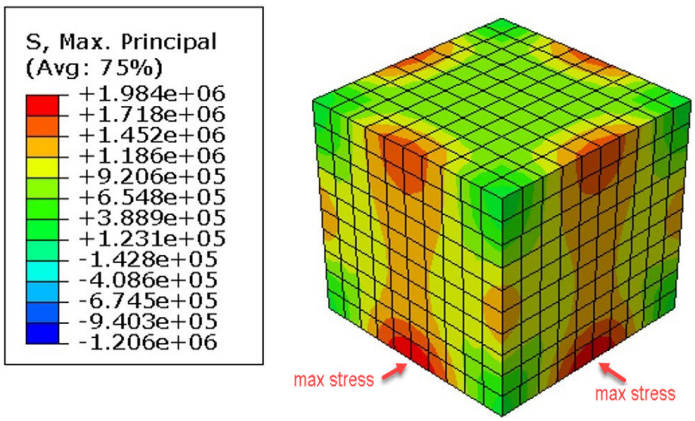

Figure 3.33 – Maximum thermal stress

Figure 3.34 depicts the concrete block's maximum stresses. In the simulation, the most significant stresses locate near the middle of the block's bottom, where it was fixed to the ground. Moreover, figure 3.34 illustrates the evolution of concrete tension strength and stresses, where the maximum stresses locate, over the duration of 7 days. It demonstrates that the thermal stress in tension is always less than the concrete tension strength, resulting in no crack inside the concrete owing to the heat of hydration. However, since the two curves are so near on the first day, the most thorough simulation feasible is required to establish whether or not there is a possibility of damage. In order to acquire accurate results, it is critical to introduce more accurate thermo-mechanical properties, such as those derived from the proposed multi-scale modeling approach. It is also confirmed by the crack status retrieved from Abaqus as shown in figure 3.35.

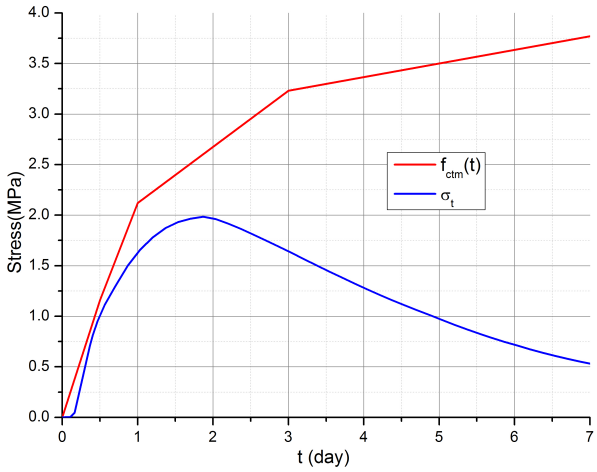

Figure 3.34 – Thermal stress and tension strength of concrete

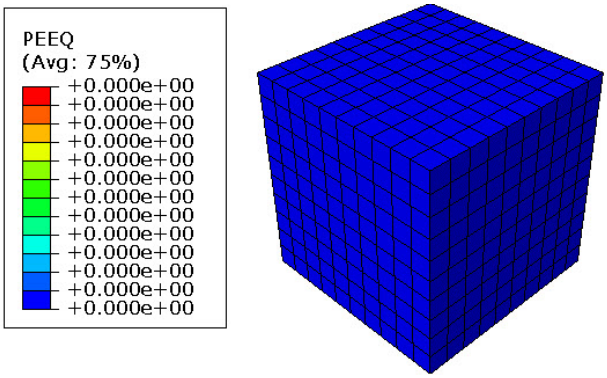

Figure 3.35 – Crack status of at the maximum thermal stress

3.3 Conclusion

In the application section of this PhD thesis, the influence of crack on the thermal conductivity of mortar was first explored. The mortar **RVE** was subjected to mechanical loads such as compression and tension. Since the mortar is made up of cement paste and aggregate, a commonly used cohesive crack model is utilized to describe its behavior. Furthermore, the existence of the crack affects the calculation by influencing the total stress and material stiffness associated with each material calculation point. The Fracture Process Zone (**FPZ**) model is used to examine the stress vs. crack opening relationship. When the tension at the tip of **FPZ** approaches the tensile strength f_t, the crack is considered open (Rankine criterion). Tension and compression are then applied to the mortar by imposing displacements of 1 and 15 μm at the two **RVE** opposing faces. The elements with local displacements greater than the critical value u_{ck} were then eliminated from the mesh. Following the mechanical simulation, a list of the eliminated elements was generated, which was then substituted in the heat transfer simulation by the thermal properties of air. Cracks caused by compression are likewise randomly distributed inside the **RVE**, while cracks caused by tension are spaced out in the shape of a plane. The heat transfer simulation was then conducted. The findings show that the crack pattern has a varied effect on thermal conductivity. The thermal conductivity of the compressed mortar steadily drops while retaining its isotropy. Nonetheless, the thermal conductivity of the tensioned mortar could not maintain its isotropy since the thermal conductivity of the mortar in the direction of applied force gradually decreases while the thermal conductivity in the other two directions just slightly reduces.

The last part of this PhD thesis focuses into the influence of specific heat on heat development. In this last segment, heat transfer and thermo-mechanical sequential simulation are used. First, a heat transfer simulation on the massive structure was performed to determine how specific heat influenced the massive structure's maximum temperature. Furthermore, the hydration heat was considered in this study by implementing the **HETVAL** subroutine in **Abaqus FEA**. The massive structure was placed on the ground and then exposed to the environment, which accounts for ground heat conduction, convection, and radiation. As a result of the specific heat varying with time, the maximum temperature inside the massive structure has been decreased. After then, the sensitivity of the set (or initial) temperature is studied. It is possible to see that when the set temperature increases, so does the maximum temperature. As a consequence, controlling the maxi-

mum temperature of a massive structure with a lower set temperature is preferred. The equivalent time ($\mathbf{t_e}$) is employed since the massive structure has large dimensions and the temperature distribution within the structure is not uniform. The simulation results show that the maximum maximum temperature of the simulation utilizing $\mathbf{t_e}$ is lower and may be reached faster than the maximum temperature of the normal simulation time. The last part discusses thermal stress. The stress and strain curves from the *fib*'s model were then employed. To define the structure's damage behavior, the Concrete Damage Plasticity (**CDP**) model was used.The damage parameters, $\mathbf{d_c}$ and $\mathbf{d_t}$, were calculated and used as input data for the damage model in **Abaqus FEA**. The simulation results show that there is a chance of a crack forming inside the block at a young age (around 0.5 day), but no crack forming throughout the structure overall.

CONCLUSION AND PERSPECTIVE

Conclusion

This PhD thesis aims to investigate the use of hierarchical multi-scale modeling approaches to evaluate the thermal properties of cement-based materials. The Multi-scale Modelling of Computational Concrete (**MuMoCC**) 3D numerical modeling platform was created in this hierarchical approach. **CEMHYD3D** and **Abaqus FEA** are numerical tools adapted for the **MuMoCC** platform. There are also additional software that were used to aide and accelerate the calculation such as Microsoft Excel with Visual Basic Applications (**VBA**), Python, and Fortran.

Furthermore, two crucial keywords in this PhD thesis are thermal property and multi-scale. In terms of thermal properties, thermal conductivity ($\mathbf{k}$), specific heat ($\mathbf{C_p}$), and coefficient of thermal expansion ($\boldsymbol{\alpha}$) are all considered. In addition, the mutlti-scale of cement-based materials employed here are microscale (cement paste) and sub-mesoscale (mortar).

Analytical and numerical homogenization approaches were applied in the context of the multi-scale approach. The homogenized results of analytical and numerical homogenization at the microscale are utilized as input data for analytical and numerical homogenization at the sub-mesoscale, respectively. Furthermore, these findings are utilized in real-world scenarios, such as the effect of cracks on thermal conductivity and the effect of specific heat on heat development in massive structure.

Aside from the literature review, this PhD thesis is separated into two main chapters. A chapter demonstrates the analytical and numerical homogenization of thermal properties and a chapter in which the results from the homogenization are utilized in real applications. Additional research on thermal contact conductance **TCC** and the Representative Volume Element (**RVE**) were conducted in the homogenization chapter to determine whether or not **TCC** has an impact on the study of thermal conductivity of mortar and to calibrate the the size of **RVE** of mortar for thermal homogenization. Furthermore, the homogenization is investigated at different hydration and saturation degrees.

Thermal conductivity (**k**) was estimated in analytical homogenization by combining the thermal conductivity of its constituents. The results reveal that the thermal conductivity is quite comparable at both scales for any hydration degrees. Furthermore, it rises when saturation degrees rises. Due to the addition of soft limestone sand, which has a lower thermal conductivity than cement paste, mortar has a lower thermal conductivity than that of cement paste. Numerous conclusions are possible when numerical homogenization is used. The **RVE** cubes of cement paste and mortar derived from **CEMHYD3D** by imposing two distinct temperatures (293.15 and 373.15 K) at two opposing sides. First, in addition to the **RVE** obtained from **CEMHYD3D**, two take-and-place methods were used to calibrated the size of **RVE** used in sub-mesoscale. Many researchers have utilized the original take-and-place approach for a very long period, and the new one is the modified take-and-place task developed by Rhardane [55]. The advantage of the modified take-and-place method is that it is quicker than the original one. Moreover, the **RVE** is measuring 2.44 times the greatest inclusion's diameter (L/D=2.44) which is less than that for mechanical simulation. Additionally, concerning the **TCC**, it was found out that it has no impact on the mortar's overall thermal conductivity except when there is an air gap larger than 30 μm. Second, both cement paste and mortar's thermal conductivity drastically increase with increasing hydration level at 0% saturation degrees. However, it seems to be fairly similar in the materials that are fully saturated. In conclusion, for lower saturation degrees, the findings of analytical and numerical homogenization do not agree. Additionally, it does very well for fully saturated materials.

In analytical homogenization, the specific heat ($\mathbf{C_p}$) was computed in the same way as thermal conductivity. Due to the presence of limestone sand, the result demonstrates that mortar's specific heat is lower than cement paste's and progressively rises with saturation degrees. It shows a little increase with hydration when the saturation degrees is 0%, but it decreases when the saturation degrees is 100%. In numerical homogenization, the inverse analysis method was used. This inverse analysis method involves numerical simulations of heat transfer on an **RVE** and analytical formulation of the temperature profile in a sample. After running the numerical simulation, the temperature profiles were retrieved from the model at each time-step using Python. Then, using the analytical formulation, the temperature profiles obtained from the numerical simulation were recreated by altering the value of $\mathbf{C_p}$ and calculating the difference between the two profiles at each time step. The $\mathbf{C_p}$ of the materials is the one with the least variation between the two profiles. The results demonstrate that the specific heat curve in function of saturation degrees

has a minimum, which might be due to the influence of opposing thermal properties within the porosity. In the porosity, as the saturation degrees increases, so do the thermal conductivity and the specific heat. Thus, the increased thermal conductivity means that the porosity conduct heat better and require less energy to increase temperature but the increased specific heat mean that it does, in fact, require more energy in the porosity. Furthermore, the analytical homogenization approach could not repeat the same results as the numerical method since it is based only on the specific heat of each component and not on thermal conductivity. To summarize, both homogenization methods provide similar results only for fully saturated cement-based materials and not for lower saturation degrees.

The coefficient of thermal expansion ($\boldsymbol{\alpha}$) decreases with increasing saturation degrees in analytical homogenization results. It indicates that air expansion is more remarkable than that of water, which is true in open space but not in porosity. The porosity is generally confined by the surrounding solid, which prevents it from expanding. As a consequence, the analytical homogenization findings are illogical for porous materials, particularly those with closed porosity. This study proposed two methods for numerical homogenization: thermo-mechanical sequential and thermo-mechanical coupled simulation. Thermal simulations were carried out first in the thermo-mechanical sequential simulation, followed by mechanical simulation by receiving the result from thermal simulation. Furthermore, the thermal and mechanical properties were introduced separately in each simulation. Unlike the thermo-mechanical sequential simulation, the thermo-mechanical coupled simulation was performed just once and included both mechanical and thermal properties. In this case, both of the simulations have given the same result. Moreover, the $\boldsymbol{\alpha}$ of cement-based materials at lower hydration degrees is always higher than that of cement-based materials at higher hydration degrees. Nevertheless, the complex evolution of numerous mechanical and thermal properties as a function of saturation degree, particularly the specific heat, has resulted in a nonlinear evolution of the coefficient of thermal expansion which is difficult to explain.

The effect of crack on the thermal conductivity of mortar was initially investigated in the application section of this PhD thesis. The **RVE** of mortar was submitted to the mechanical stresses such as compression and tension. Since the mortar is composed of cement paste and the aggregate, a widely used cohesive crack model is adopted to describe its behavior. Moreover, the presence of the crack enter the calculation by the way it affect the overall stress and the materials stiffness associated with each material

calculation point. The Fracture Process Zone (**FPZ**) model by stress vs. crack opening relationship is considered. A crack is considered open when the stress at the tip of **FPZ** reaches the tensile strength f_t (Rankine criterion). The mortar is then subjected to tension and compression by imposing displacements of 1 and 15 μm at the two **RVE** opposite faces. Then the elements that have local displacement larger than the critical value u_{ck} was removed from the mesh. Following the mechanical simulation, a list of the removed elements was provided, which was then replaced by the thermal properties of air in the heat transfer simulation. It can also be seen that cracks induced by compression are randomly dispersed inside the **RVE**, but cracks caused by tension are spread out in the form of a plane. Then, the heat transfer simulation was carried out. The results reveal that the crack pattern has a different influence on thermal conductivity. The thermal conductivity of the mortar submitted to compression gradually decreases while maintaining its isotropy. Nonetheless, the thermal conductivity of the mortar submitted to tension could not retain its isotropy since the thermal conductivity of the mortar in the direction of applied force eventually declines while the thermal conductivity in the other two directions just marginally decreases.

The investigation of the impact of specific heat on heat evolution is explored in the last section of this PhD thesis. The heat transfer and thermo-mechanical sequential simulation are employed in this last section. First, a heat transfer simulation on the massive structure was conducted to evaluate how specific heat affected the maximum temperature of the massive structure. Furthermore, in this research, the hydration heat was taken into consideration by introducing the **HETVAL** subroutine in **Abaqus FEA**. The massive structure was positioned on the ground and then exposed to the environment, which takes into account heat conduction from the ground, convection, and radiation. As a consequence, the varying specific heat has resulted in a reduced maximum temperature within the massive structure. The sensitivity of the set (or initial) temperature is then investigated. It can be observed that when the set temperature rises, so does the maximum temperature. As a result, a lower set temperature is preferable to limit the maximum temperature of a massive structure. Because the massive structure has large dimensions and the temperature distribution inside the structure is not uniform, the equivalent time ($\mathbf{t_e}$) is used. The simulation results demonstrate that the maximum temperature of the simulation using $\mathbf{t_e}$ is lower and may be attained sooner than the maximum temperature of the usual simulation time. Thermal stress is addressed in the last section. The *fib*'s model's stress and strain curves were then used. The Concrete Damage Plasticity

(**CDP**) model was utilized to characterize the structure's damage behavior. The damage parameters ($\mathbf{d_c}$ and $\mathbf{d_t}$) were computed and utilized as input data for the damage model in **Abaqus FEA**. The simulation results reveal that there is a chance of crack occurring within the block at an early age (about 0.5 day), but no crack occurs inside the structure overall.

To summarize, analytical and numerical homogenization are utilized to determine the thermal properties of cement-based materials at the microscale (cement paste) and sub-mesoscale (mortar). The results show that only at 100% saturation do both homogenization methods agree well for thermal conductivity and specific heat. It demonstrates that there are certain limitations in analytical homogenization, which solely consider the properties and fraction of the cement-based materials components. For example, the **TCC** and the opposite effect of thermal conductivity ($\mathbf{k}$) and specific heat ($\mathbf{C_p}$) cannot be addressed in analytical homogenization. Furthermore, because of the complex development of thermo-mechanical properties as a function of saturation degree, none of these homogenization methods can determine the coefficient of thermal expansion. Moreover, two take-and-place methods were explored, both of which provide the same outcome, but the newly improved method is more time-efficient. The first section's results were employed in the application of the influence of cracks on thermal conductivity and temperature development within the massive structure. As a consequence, cracks affect heat conductivity differently depending on the direction of applied stress. In terms of temperature evolution, the set temperature, equivalent time ($\mathbf{t_e}$), and time-dependent specific heat affect the structure's maximum temperature. Thus, heat transfer simulation using the equivalent time ($\mathbf{t_e}$) and specific heat is vital to examine thermal stress within the structure, and selecting the proper set temperature is critical to avoiding cracks caused by thermal stress.

Perspective

The use of hierarchical multi-scale modeling methodologies, particularly The Multi-scale Modelling of Computational Concrete (**MuMoCC**) platform, has shown its ability to examine heat transfer problems at the microscale (cement paste) and sub-mesoscale (mortar). Additional research on numerical modeling and experimental studies are necessary for future research.

In terms of numerical modeling, there are various ideas for further study, including:

— Heat transfer simulation on a cement-based material with known thermal properties is required to demonstrate that the methods employed are correct,
— To correctly compute the value of **TCC**, an addition research on **TCC** with different interface configurations is necessary.,
— Heat transfer simulation with sphere inclusion and **TCC** at the interface is also recommended for calculating thermal conductivity exactly,
— Further simulation with alternative boundary conditions for specific heat is also interesting to confirm the conclusion reached in this work,
— Inverse analysis for specific heat using three-dimensional formulation and comparison with one-dimensional formulation is another topic that might be studied,
— Another method for determining the coefficient of thermal expansion is still required.

Furthermore, an experimental campaign is required to confirm the numerical findings. As the example:

— Thermal conductivity of cement-based materials is determined experimentally, allowing the researcher to examine the difference between experimental and simulation results,
— By comparing the two outcomes, it is possible to determine the value of **TCC**,
— Calorimetry experimental campaign for specific heat of cement-based materials,
— Setup for determining the coefficient of thermal expansion.

However, not every verification is achievable since, to the extent of the author's knowledge, the heat transfer properties can only be found at 0 or 100% saturation degrees during in the experimental campaign. Furthermore, verifying the heat conductivity of damaged mortar and measuring the heat development within the massive concrete structure is challenging.

References

[1] M. Jebli, F. Jamin, E. Malachanne, E. Garcia-Diaz, and M. El Youssoufi, « Experimental characterization of mechanical properties of the cement-aggregate interface in concrete », en, *Construction and Building Materials*, vol. 161, pp. 16–25, Feb. 2018, ISSN: 09500618. DOI: 10.1016/j.conbuildmat.2017.11.100.

[2] M. Jebli, F. Jamin, C. Pelissou, E. Malachanne, E. Garcia-Diaz, and M. El Youssoufi, « Leaching effect on mechanical properties of cement-aggregate interface », en, *Cement and Concrete Composites*, vol. 87, pp. 10–19, Mar. 2018, ISSN: 09589465. DOI: 10.1016/j.cemconcomp.2017.11.018.

[3] M. Jebli, F. Jamin, E. Garcia-Diaz, M. El Omari, and M. El Youssoufi, « Influence of leaching on the local mechanical properties of an aggregate-cement paste composite », en, *Cement and Concrete Composites*, vol. 73, pp. 241–250, Oct. 2016, ISSN: 09589465. DOI: 10.1016/j.cemconcomp.2016.05.001.

[4] R. El-Hachem, E. Rozière, F. Grondin, and A. Loukili, « Multi-criteria analysis of the mechanism of degradation of Portland cement based mortars exposed to external sulphate attack », en, *Cement and Concrete Research*, vol. 42, *10*, pp. 1327–1335, Oct. 2012, ISSN: 00088846. DOI: 10.1016/j.cemconres.2012.06.005.

[5] F. Bernard, J. Fu, and S. Kamali-Bernard, « Multiscale modelling approach to determine the specific heat of cementitious materials », *European Journal of Environmental and Civil Engineering*, vol. 23, *5*, pp. 535–551, May 2019, ISSN: 1964-8189. DOI: 10.1080/19648189.2018.1443157.

[6] E. M. Fairbairn and M. Azenha, Eds., *Thermal Cracking of Massive Concrete Structures*, en, ser. RILEM State-of-the-Art Reports. Cham: Springer International Publishing, 2019, vol. 27, ISBN: 978-3-319-76616-4 978-3-319-76617-1. DOI: 10.1007/978-3-319-76617-1.

[7] M. I. Khan, « Factors affecting the thermal properties of concrete and applicability of its prediction models », en, *Building and Environment*, Retrofitting of Office Buildings: Papers from the Research Projec t Office, vol. 37, *6*, pp. 607–614, Jun. 2002, ISSN: 0360-1323. DOI: 10.1016/S0360-1323(01)00061-0.

[8] J. Fu, F. Bernard, and S. Kamali-Bernard, « First-principles calculations of typical anisotropic cubic and hexagonal structures and homogenized moduli estimation based on the Y-parameter: Application to CaO, MgO, CH and Calcite CaCO3 »,

en, *Journal of Physics and Chemistry of Solids*, vol. 101, pp. 74–89, Feb. 2017, ISSN: 00223697. DOI: 10.1016/j.jpcs.2016.10.010.

[9] F. Bernard, S. Kamali-Bernard, and W. Prince, « 3D multi-scale modelling of mechanical behaviour of sound and leached mortar », en, *Cement and Concrete Research*, vol. 38, *4*, pp. 449–458, Apr. 2008, ISSN: 00088846. DOI: 10.1016/j.cemconres.2007.11.015.

[10] F. Bernard and S. Kamali-Bernard, « Predicting the evolution of mechanical and diffusivity properties of cement pastes and mortars for various hydration degrees â€“ A numerical simulation investigation », en, *Computational Materials Science*, vol. 61, pp. 106–115, Aug. 2012, ISSN: 0927-0256. DOI: 10.1016/j.commatsci.2012.03.023.

[11] I. Comby-Peyrot, F. Bernard, P.-O. Bouchard, F. Bay, and E. Garcia-Diaz, « Development and validation of a 3D computational tool to describe concrete behaviour at mesoscale. Application to the alkali-silica reaction », en, *Computational Materials Science*, vol. 46, *4*, pp. 1163–1177, Oct. 2009, ISSN: 09270256. DOI: 10.1016/j.commatsci.2009.06.002.

[12] S. Kamali-Bernard, F. Bernard, and D. Damidot, *Modélisation multi-échelles de la lixiviation des mortiers : effet sur les caractéristiques mécaniques*. Sep. 2005.

[13] F. Grondin, G. Mounajed, A. Hamida, and H. Dumontet, *Digital Concrete: A Multi-scale Approach for the Concrete Behavior*. Sep. 2003, vol. 6, Pages: 208. DOI: 10.1142/9789812704658_0046.

[14] J. fu, F. Bernard, and S. Kamali-Bernard, « Nanoscale Modeling and Elastic Properties of Portlandite and Graphene Based on Atomic Finite Element Method », *Applied Mechanics and Materials*, vol. 711, pp. 137–142, Dec. 2014. DOI: 10.4028/www.scientific.net/AMM.711.137.

[15] F. Grondin, G. Mounajed, H. Boussa, and A. Menou, « Approche multi-échelles pour l'endommagement thermique du béton », Jan. 2004.

[16] F. Bernard, S. Kamali-Bernard, and J. Fu, « Approche de modélisation multi-échelle pour la détermination de la chaleur spécifique des matériaux cimentaires », en, *Academic Journal of Civil Engineering*, vol. 35, *1*, pp. 164–167, 2017, Number: 1, ISSN: 2680-1000. DOI: 10.26168/ajce.35.1.40.

[17] F. Grondin, P. Mounanga, A. Khelidj, and M. Bouasker, « Analyse multi-échelles du retrait endogène des matrices cimentaires », Congrès français de mécanique, A. F. d. Mécanique, Ed., Aug. 2007.

[18] M. Bouasker, F. Grondin, P. Mounanga, and A. Khelidj, *Early age autogenous deformations of cement-based materials*. Lille, France, 2008. DOI: 10.1002/9781118623565.ch30.

[19] F. Grondin, M. Bouasker, P. Mounanga, and A. Khelidj, *A multi-scales approach for the physico-chemical deformations of solidifying cement-based materials*. Delft, Netherlands, May 2008.

[20] F. Mounia, F. Grondin, A. Loukili, and M. Matallah, « Multi-scales computation of creep deformation of concrete at very early-age », *Computational Modelling of Concrete Structures - Proceedings of EURO-C 2014*, vol. 2, pp. 797–804, Mar. 2014, ISSN: 978-1-138-00145-9. DOI: 10.1201/b16645-90.

[21] M. Farah, J. Saliba, F. Grondin, and A. Loukili, *7 - Multi-Scale Methods for the Analysis of Creep-Damage Coupling in Concrete*, en, F. Nicot and O. Millet, Eds. Elsevier, Jan. 2018, pp. 205–241, ISBN: 978-1-78548-278-6. DOI: 10.1016/B978-1-78548-278-6.50007-4.

[22] F. Grondin, M. Bouasker, A. Khelidj, A. Loukili, P. Mounanga, and E. Rozière, *Multi-scales modelling for the delayed deformation and durability of cement-based materials*. Aussois, France, 2007.

[23] F. Bernard and S. Kamali-Bernard, « Performance simulation and quantitative analysis of cement-based materials subjected to leaching », en, *Computational Materials Science*, vol. 50, *1*, pp. 218–226, Nov. 2010, ISSN: 09270256. DOI: 10.1016/j.commatsci.2010.08.002.

[24] L. Sow, F. Bernard, and S. Kamali-Bernard, « Mechanical Behaviour of Cement-Bound Gravels by Experiment-Based 3D Multi-Scale Modelling: Application to Non-Hazardous Waste Incineration Bottom Ashes Aggregates for Use in Road Engineering », en, *International Journal of Engineering Research in Africa*, vol. 54, pp. 71–85, 2021, Conference Name: International Journal of Engineering Research in Africa Vol. 54 ISBN: 9783035727067 Publisher: Trans Tech Publications Ltd, ISSN: 1663-4144. DOI: 10.4028/www.scientific.net/JERA.54.71.

[25] ——, *Mâchefers d'incinération de déchets non dangereux : gisement stratégique de substitution de granulats routiers classiques*. Oct. 2019. DOI: 10.13140/RG.2.2.34948.48006/1.

[26] L. Sow, F. Bernard, S. Kamali-Bernard, and C. Kébé, « Mesoscale modeling of the temperature-dependent viscoelastic behavior of a Bitumen-Bound Gravels », *Coupled systems mechanics an international journal*, vol. 7, pp. 509–524, Oct. 2018. DOI: 10.12989/csm.2018.7.5.509.

[27] F. Fakhari Tehrani, J. Absi, F. Allou, and C. Petit, « Heterogeneous numerical modeling of asphalt concrete through use of a biphasic approach: Porous matrix/inclusions », en, *Computational Materials Science*, vol. 69, pp. 186–196, Mar. 2013, ISSN: 0927-0256. DOI: 10.1016/j.commatsci.2012.11.041.

[28] D. Bentz, *CEMHYD3D: A Three-Dimensional Cement Hydration and Microstructure Development Modeling Package: Version 3.0*. Jun. 2005.

[29] S. Kamali-Bernard, F. Bernard, and W. Prince, « Modélisation tridimensionnelle et multi-échelle du comportement des matériaux cimentaires. Application à la lixiviation », *European Journal of Environmental and Civil Engineering*, vol. 13, pp. 21–32, Jan. 2009. DOI: 10.1080/19648189.2009.9693083.

[30] D. Bentz, « Modeling the Influence of Limestone Filler on Cement Hydration using CEMHYD3D », *Cement and Concrete Composites*, vol. 28, pp. 124–129, Feb. 2006. DOI: 10.1016/j.cemconcomp.2005.10.006.

[31] E. Garboczi and J. Bullard, « Shape Analysis of a Reference Cement », *Cement and Concrete Research*, vol. 34, pp. 1933–1937, Oct. 2004. DOI: 10.1016/j.cemconres.2004.01.006.

[32] G. Ye, E. Koenders, and K. Breugel, *HYMOSTRUC: An Advanced Program for Prediction of Mechanical Properties and Durability of Civil Engineering Structures*, ISBN: 978-1-905088-17-1. DOI: 10.4203/ccp.86.4.

[33] G. Ye, K. Breugel, and J. Hu, « Numerically simulated pore structure and its potential application in high performance concrete », *in*, Jun. 2021, pp. 135–140, ISBN: 978-1-00-321136-5. DOI: 10.1201/9781003211365-19.

[34] G. Ye and K. Breugel, « POTENTIAL USE OF HYMOSTRUC CEMENT HYDRATION MODEL FOR SELF-HEALING OF MICROCRACKS IN CEMENTITIOUS MATERIALS »,

[35] G. Ye, « Characterization of the development of microstructure and porosity of cement-based materials by numerical simulation and ESEM image analysis », *Materials and Structures*, vol. 35, pp. 603–613, Dec. 2002. DOI: 10.1617/13935.

[36] ——, « Experimental Study and Numerical Simulation of the Development of the Microstructure and Permeability of Cementitious Materials », Jan. 2003.

[37] K. van Breugel, « Numerical simulation of hydration and microstructural development in hardening cement-based materials (I) theory », en, *Cement and Concrete Research*, vol. 25, *2*, pp. 319–331, Feb. 1995, ISSN: 00088846. DOI: 10.1016/0008-8846(95)00017-8.

[38] ——, « NUMERICAL SIMULATION OF HYDRATION AND MICROSTRUCTURAL DEVELOPMENT IN HARDENING CEMENT-BASED MATERIALS (H) Applications », en, p. 9,

[39] E. Koenders, « Simulation of Volume Changes in Hardening Cemet-Based Materials », Jan. 1997.

[40] J. Bullard, J. Hagedorn, M. Ley, Q. Hu, W. Griffin, and J. Terrill, « A Critical Comparison of 3D Experiments and Simulations of Tricalcium Silicate Hydration », *Journal of the American Ceramic Society*, vol. 101, Nov. 2017. DOI: 10.1111/jace.15323.

[41] T. Oey, A. Kumar, J. Bullard, N. Neithalath, G. Sant, and G. Scherer, « The Filler Effect: The Influence of Filler Content and Surface Area on Cementitious Reaction Rates », *Journal of the American Ceramic Society*, vol. 96, Jun. 2013. DOI: 10.1111/jace.12264.

[42] J. W. Bullard and R. J. Flatt, « New Insights Into the Effect of Calcium Hydroxide Precipitation on the Kinetics of Tricalcium Silicate Hydration », en, *Journal of the American Ceramic Society*, Mar. 2010, ISSN: 00027820, 15512916. DOI: 10.1111/j.1551-2916.2010.03656.x.

[43] J. Bullard, E. Enjolras, W. George, S. Satterfield, and J. Terrill, « A Parallel Reaction-Transport Model Applied to Cement Hydration and Microstructure Development », *Modelling Simul. Mater. Sci. Eng*, vol. 18, pp. 25 007–16, Mar. 2010. DOI: 10.1088/0965-0393/18/2/025007.

[44] J. Bullard, « A Determination of Hydration Mechanisms for Tricalcium Silicate Using a Kinetic Cellular Automaton Model », *Journal of the American Ceramic Society*, vol. 91, pp. 2088–2097, May 2008. DOI: 10.1111/j.1551-2916.2008.02419.x.

[45] L. Valentini, « Modeling Dissolution–Precipitation Kinetics of Alkali-Activated Metakaolin », *ACS Omega*, vol. 3, pp. 18 100–18 108, Dec. 2018. DOI: 10.1021/acsomega.8b02380.

[46] S. Bishnoi and K. L. Scrivener, « µic: A new platform for modelling the hydration of cements », en, *Cement and Concrete Research*, vol. 39, *4*, pp. 266–274, Apr. 2009, ISSN: 0008-8846. DOI: 10.1016/j.cemconres.2008.12.002.

[47] A. Kumar, G. Sant, C. Patapy, C. Gianocca, and K. L. Scrivener, « The influence of sodium and potassium hydroxide on alite hydration: Experiments and simulations », en, *Cement and Concrete Research*, vol. 42, *11*, pp. 1513–1523, Nov. 2012, ISSN: 0008-8846. DOI: 10.1016/j.cemconres.2012.07.003.

[48] S. Bishnoi and K. L. Scrivener, « Studying nucleation and growth kinetics of alite hydration using µic », en, *Cement and Concrete Research*, vol. 39, *10*, pp. 849–860, Oct. 2009, ISSN: 0008-8846. DOI: 10.1016/j.cemconres.2009.07.004.

[49] A. Kumar, S. Bishnoi, and K. L. Scrivener, « Modelling early age hydration kinetics of alite », en, *Cement and Concrete Research*, vol. 42, *7*, pp. 903–918, Jul. 2012, ISSN: 00088846. DOI: 10.1016/j.cemconres.2012.03.003.

[50] S. Bishnoi, « Vector modelling of hydrating cement microstructure and kinetics », fr, p. 190,

[51] N. Holmes, M. Tyrer, R. West, A. Lowe, and D. Kelliher, « Using PHREEQC to model cement hydration », en, *Construction and Building Materials*, vol. 319, p. 126 129, Feb. 2022, ISSN: 09500618. DOI: 10.1016/j.conbuildmat.2021.126129.

[52] B. Guo, Y. Hong, G. Qiao, and J. Ou, « A COMSOL-PHREEQC interface for modeling the multi-species transport of saturated cement-based materials », en, *Construction and Building Materials*, vol. 187, pp. 839–853, Oct. 2018, ISSN: 09500618. DOI: 10.1016/j.conbuildmat.2018.07.242.

[53] P. Thilakarathna, K. Kristombu Baduge, P. Mendis, V. Vimonsatit, and H. Lee, « Mesoscale modelling of concrete – A review of geometry generation, placing algorithms, constitutive relations and applications », en, *Engineering Fracture Mechanics*, vol. 231, p. 106 974, May 2020, ISSN: 00137944. DOI: 10.1016/j.engfracmech.2020.106974.

[54] F. H. Wittmann, P. E. Roelfstra, and H. Sadouki, « Simulation and analysis of composite structures », en, *Materials Science and Engineering*, vol. 68, *2*, pp. 239–248, Jan. 1985, ISSN: 0025-5416. DOI: 10.1016/0025-5416(85)90413-6.

[55] A. Rhardane, S. Y. Alam, and F. Grondin, « Microscopically informed upscale approach of modelling damage in mortar by considering matrix-to-grain interface and grain micro-fracture characteristics », en, *Theoretical and Applied Fracture Mechanics*, vol. 109, p. 102 725, Oct. 2020, ISSN: 0167-8442. DOI: 10.1016/j.tafmec.2020.102725.

[56] S. Kamali-Bernard, F. Bernard, and W. Prince, « Computer modelling of tritiated water diffusion test for cement based materials », en, *Computational Materials Science*, vol. 45, *2*, pp. 528–535, Apr. 2009, ISSN: 09270256. DOI: 10.1016/j.commatsci.2008.11.018.

[57] E. S. Agence française de normalisation, « NF EN 197 - 1 », p. 38, Apr. 2012.

[58] I. C. Ezema, « Chapter 9 - Materials », *in Sustainable Construction Technologies*, V. W. Y. Tam and K. N. Le, Eds., Butterworth-Heinemann, Jan. 2019, pp. 237–262, ISBN: 978-0-12-811749-1. DOI: 10.1016/B978-0-12-811749-1.00007-9.

[59] C. Chrysostomou, A. Kylili, D. Nicolaides, and P. A. Fokaides, « Life Cycle Assessment of concrete manufacturing in small isolated states: the case of Cyprus », en, *International Journal of Sustainable Energy*, vol. 36, *9*, pp. 825–839, Oct. 2017, ISSN: 1478-6451, 1478-646X. DOI: 10.1080/14786451.2015.1100197.

[60] H. M. Saleh and S. B. Eskander, « 18 - Innovative cement-based materials for environmental protection and restoration », en, *in New Materials in Civil Engineering*, P. Samui, D. Kim, N. R. Iyer, and S. Chaudhary, Eds., Butterworth-Heinemann, Jan. 2020, pp. 613–641, ISBN: 978-0-12-818961-0. DOI: 10.1016/B978-0-12-818961-0.00018-1.

[61] I. Garcia-Lodeiro, A. Palomo, and A. Fernández-Jiménez, « 2 - An overview of the chemistry of alkali-activated cement-based binders », en, *in Handbook of Alkali-Activated Cements, Mortars and Concretes*, F. Pacheco-Torgal, J. A. Labrincha, C. Leonelli, A. Palomo, and P. Chindaprasirt, Eds., Oxford: Woodhead Publishing, Jan. 2015, pp. 19–47, ISBN: 978-1-78242-276-1. DOI: 10.1533/9781782422884.1.19.

[62] J. Beaudoin and I. Odler, « 5 - Hydration, Setting and Hardening of Portland Cement », *in Lea's Chemistry of Cement and Concrete (Fifth Edition)*, P. C. Hewlett and M. Liska, Eds., Fifth Edition, Butterworth-Heinemann, 2019, pp. 157–250, ISBN: 978-0-08-100773-0. DOI: https://doi.org/10.1016/B978-0-08-100773-0.00005-8.

[63] P. C. Taylor, S. H. Kosmatka, and G. F. Voigt, « Integrated Materials and Construction Practices for Concrete Pavement: A State-of-the-Practice Manual », Dec. 2006.

[64] J. W. Bullard, H. M. Jennings, R. A. Livingston, A. Nonat, G. W. Scherer, J. S. Schweitzer, K. L. Scrivener, and J. J. Thomas, « Mechanisms of cement hydration », *Cement and Concrete Research*, vol. 41, *12*, pp. 1208–1223, 2011, Conferences Special: Cement Hydration Kinetics and Modeling, Quebec City, 2009 CONMOD10, Lausanne, 2010, ISSN: 0008-8846. DOI: https://doi.org/10.1016/j.cemconres.2010.09.011.

[65] W. H. Langer and D. H. Knepper, « Geologic characterization of natural aggregate; a field geologist's guide to natural aggregate resource assessment », U.S. Geological Survey, Tech. Rep. 95-582, 1995, ISSN: 2331-1258 Publication Title: Open-File Report. DOI: 10.3133/ofr95582.

[66] E. S. Agence française de normalisation, « NF EN 932-3 », *Afnor EDITIONS*,

[67] *Trap Rock: Dark igneous rocks used to make crushed stone.* [Online]. Available: https://geology.com/articles/trap-rock/.

[68] *Limestone: Rock Uses, Formation, Composition, Pictures.* [Online]. Available: https://geology.com/rocks/limestone.shtml.

[69] *Marble.* [Online]. Available: https://www.sandatlas.org/marble/.

[70] *Gravel is composed of unconsolidated rock fragments that have a general particle size range and include size classes from granule- to boulder-sized fragments.* [Online]. Available: https://www.123rf.com/photo_21949607_gravel-is-composed-of-unconsolidated-rock-fragments-that-have-a-general-particle-size-range-and-incl.html.

[71] S. Marinković and V. Carević, « 10 - Comparative studies of the life cycle analysis between conventional and recycled aggregate concrete », en, *in New Trends in Eco-efficient and Recycled Concrete*, ser. Woodhead Publishing Series in Civil and Structural Engineering, J. de Brito and F. Agrela, Eds., Woodhead Publishing, Jan. 2019, pp. 257–291, ISBN: 978-0-08-102480-5. DOI: 10.1016/B978-0-08-102480-5.00010-5.

[72] A. Albuquerque, J. Pacheco, and J. Brito, « Eurocode Design of Recycled Aggregate Concrete for Chloride Environments: Stochastic Modeling of Chloride Migration and Reliability-Based Calibration of Cover », en, *Crystals*, vol. 11, *3*, p. 284, Mar. 2021, ISSN: 2073-4352. DOI: 10.3390/cryst11030284.

[73] T. Le, S. Rémond, G. Le Saout, and E. Garcia-Diaz, « Fresh behavior of mortar based on recycled sand – Influence of moisture condition », en, *Construction and Building Materials*, vol. 106, pp. 35–42, Mar. 2016, ISSN: 09500618. DOI: 10.1016/j.conbuildmat.2015.12.071.

[74] T. Le, G. Le Saout, E. Garcia-Diaz, D. Betrancourt, and S. Rémond, « Hardened behavior of mortar based on recycled aggregate: Influence of saturation state at macro- and microscopic scales », en, *Construction and Building Materials*, vol. 141, pp. 479–490, Jun. 2017, ISSN: 09500618. DOI: 10.1016/j.conbuildmat.2017.02.035.

[75] B. Wang, L. Yan, Q. N. Fu, and B. Kasal, « A Comprehensive Review on Recycled Aggregate and Recycled Aggregate Concrete », May 2021.

[76] R. K. Dhir, J. de Brito, R. V. Silva, and C. Q. Lye, « Recycled Aggregate Concrete », en, *in Sustainable Construction Materials*, Elsevier, 2019, pp. 365–418, ISBN: 978-0-08-100985-7. DOI: 10.1016/B978-0-08-100985-7.00010-8.

[77] M. Etxeberria, « 13 - The suitability of concrete using recycled aggregates (RAs) for high-performance concrete », en, *in Advances in Construction and Demolition Waste Recycling*, ser. Woodhead Publishing Series in Civil and Structural Engineering, F. Pacheco-Torgal, Y. Ding, F. Colangelo, R. Tuladhar, and A. Koutamanis,

Eds., Woodhead Publishing, Jan. 2020, pp. 253–284, ISBN: 978-0-12-819055-5. DOI: 10.1016/B978-0-12-819055-5.00013-9. (visited on 10/16/2021).

[78] P. J. Nixon, « Recycled concrete as an aggregate for concrete—a review », en, *MatÃ©riaux et Construction*, vol. 11, *5*, p. 371, Sep. 1978, ISSN: 1871-6873. DOI: 10.1007/BF02473878.

[79] T. C. Hansen, « Recycled aggregates and recycled aggregate concrete second state-of-the-art report developments 1945â€“1985 », en, *Materials and Structures*, vol. 19, *3*, pp. 201–246, May 1986, ISSN: 1871-6873. DOI: 10.1007/BF02472036. (visited on 10/29/2021).

[80] I. Sims and B. Brown, « 16 - Concrete Aggregates », en, *in Lea's Chemistry of Cement and Concrete (Fourth Edition)*, P. C. Hewlett, Ed., Oxford: Butterworth-Heinemann, Jan. 1998, pp. 907–1015, ISBN: 978-0-7506-6256-7. DOI: 10.1016/B978-075066256-7/50028-X.

[81] M. Maleki, I. Rasoolan, A. Khajehdezfuly, and A. P. Jivkov, « On the effect of ITZ thickness in meso-scale models of concrete », en, *Construction and Building Materials*, vol. 258, p. 119 639, Oct. 2020, ISSN: 0950-0618. DOI: 10.1016/j.conbuildmat.2020.119639.

[82] K. L. Scrivener, A. K. Crumbie, and P. Laugesen, « The Interfacial Transition Zone (ITZ) Between Cement Paste and Aggregate in Concrete », en, *Interface Science*, vol. 12, *4*, pp. 411–421, Oct. 2004, ISSN: 0927-7056. DOI: 10.1023/B:INTS.0000042339.92990.4c.

[83] J. Xiao, W. Li, Z. Sun, D. A. Lange, and S. P. Shah, « Properties of interfacial transition zones in recycled aggregate concrete tested by nanoindentation », en, *Cement and Concrete Composites*, vol. 37, pp. 276–292, Mar. 2013, ISSN: 09589465. DOI: 10.1016/j.cemconcomp.2013.01.006.

[84] S. Diamond and J. Huang, « The ITZ in concrete â€“ a different view based on image analysis and SEM observations », en, *Cement and Concrete Composites*, Special Theme Issue on Image Analysis, vol. 23, *2*, pp. 179–188, Apr. 2001, ISSN: 0958-9465. DOI: 10.1016/S0958-9465(00)00065-2.

[85] K. Scrivener, « "Characterisation of the ITZ and its quantification by test methods" », *Engineering and transport properties of the interfacial transition zone in cementitious composites*, pp. 3–15, Jan. 1999.

[86] Z. Hashin and P. Monteiro, « An inverse method to determine the elastic properties of the interphase between the aggregate and the cement paste », en, *Cement and Concrete Research*, vol. 32, *8*, pp. 1291–1300, Aug. 2002, ISSN: 00088846. DOI: 10.1016/S0008-8846(02)00792-5.

[87] S. Krishnya, Y. Elakneswaran, and Y. Yoda, « Proposing a three-phase model for predicting the mechanical properties of mortar and concrete », en, *Materials Today Communications*, vol. 29, p. 102 858, Dec. 2021, ISSN: 23524928. DOI: 10.1016/j.mtcomm.2021.102858.

[88] F. Grondin and M. Matallah, « How to consider the Interfacial Transition Zones in the finite element modelling of concrete? », en, *Cement and Concrete Research*, vol. 58, pp. 67–75, Apr. 2014, ISSN: 00088846. DOI: 10.1016/j.cemconres.2014.01.009.

[89] F. Bernard and S. Kamali-Bernard, « Numerical study of ITZ contribution on mechanical behavior and diffusivity of mortars », en, *Computational Materials Science*, vol. 102, pp. 250–257, May 2015, ISSN: 0927-0256. DOI: 10.1016/j.commatsci.2015.02.016.

[90] D. Samal, « Effect of Interfacial Transition Zone on Fracture Energy in Concrete », en, *in Proceedings of the 10th International Conference on Fracture Mechanics of Concrete and Concrete Structures*, IA-FraMCoS, Jun. 2019. DOI: 10.21012/FC10.235522. (visited on 01/06/2022).

[91] S. Kamali-Bernard, D. Keinde, and F. Bernard, « Effect of Aggregate Type on the Concrete Matrix/Aggregates Interface and its Influence on the Overall Mechanical Behavior. A Numerical Study. », en, *Key Engineering Materials*, vol. 617, pp. 14–17, Jun. 2014, ISSN: 1662-9795. DOI: 10.4028/www.scientific.net/KEM.617.14.

[92] D. Bjegović, M. Serdar, I. Stipanovic, F. Jacobs, H. Beushausen, C. Andrade, A. Monteiro, P. Paulini, and S. Nanukuttan, « Test Methods for Concrete Durability Indicators », *in*, vol. 18, Jan. 2016, pp. 51–105, ISBN: 978-94-017-7308-9. DOI: 10.1007/978-94-017-7309-6_4.

[93] L. Basheer, P. Basheer, and A. Long, « Influence of coarse aggregate on the permeation, durability and the microstructure characteristics of ordinary Portland cement concrete », en, *Construction and Building Materials*, vol. 19, *9*, pp. 682–690, Nov. 2005, ISSN: 09500618. DOI: 10.1016/j.conbuildmat.2005.02.022.

[94] C. Yang and S. Cho, « Influence of aggregate content on the migration coefficient of concrete materials using electrochemical method », en, *Materials Chemistry and Physics*, vol. 80, *3*, pp. 752–757, Jun. 2003, ISSN: 02540584. DOI: 10.1016/S0254-0584(03)00112-3.

[95] T. Ji, « Preliminary study on the water permeability and microstructure of concrete incorporating nano-SiO2 », en, *Cement and Concrete Research*, vol. 35, *10*, pp. 1943–1947, Oct. 2005, ISSN: 00088846. DOI: 10.1016/j.cemconres.2005.07.004.

[96] M. Sharma and S. Bishnoi, « The Interfacial Transition Zone: Microstructure, Properties, and Its Modification », en, *in Recent Advances in Structural Engineering, Volume 2*, A. R. M. Rao and K. Ramanjaneyulu, Eds., vol. 12, Series Title: Lecture Notes in Civil Engineering, Singapore: Springer Singapore, 2019, pp. 745–754, ISBN: 9789811303647 9789811303654. DOI: 10.1007/978-981-13-0365-4_63.

[97] L. Wu, X. Ju, M. Liu, L. Guan, Y. Ma, and M. Li, « Influences of multiple factors on the chloride diffusivity of the interfacial transition zone in concrete composites », en, *Composites Part B: Engineering*, vol. 199, p. 108 236, Oct. 2020, ISSN: 13598368. DOI: 10.1016/j.compositesb.2020.108236.

[98] C. Yang and J. Su, « Approximate migration coefficient of interfacial transition zone and the effect of aggregate content on the migration coefficient of mortar », en, *Cement and Concrete Research*, vol. 32, *10*, pp. 1559–1565, Oct. 2002, ISSN: 00088846. DOI: 10.1016/S0008-8846(02)00832-3.

[99] C. Fu, Y. Ling, and K. Wang, « An innovation study on chloride and oxygen diffusions in simulated interfacial transition zone of cementitious material », en, *Cement and Concrete Composites*, vol. 110, p. 103 585, Jul. 2020, ISSN: 09589465. DOI: 10.1016/j.cemconcomp.2020.103585.

[100] Y. Wang, L. Wu, Y. Wang, C. Liu, and Q. Li, « Effects of coarse aggregates on chloride diffusion coefficients of concrete and interfacial transition zone under experimental drying-wetting cycles », en, *Construction and Building Materials*, vol. 185, pp. 230–245, Oct. 2018, ISSN: 09500618. DOI: 10.1016/j.conbuildmat.2018.07.049.

[101] C. Yang, « Effect of the percolated interfacial transition zone on the chloride migration coefficient of cement-based materials », en, *Materials Chemistry and Physics*, vol. 91, *2-3*, pp. 538–544, Jun. 2005, ISSN: 02540584. DOI: 10.1016/j.matchemphys.2004.12.022.

[102] D. Bentz, J. Hwang, C. Hagwood, E. Garboczi, K. Snyder, N. Buenfeld, and K. Scrivener, « Interfacial Zone Percolation in Concrete: Effects of Interfacial Zone Thickness and Aggregate Shape », *MRS Proceedings*, vol. 370, Jan. 1994. DOI: 10.1557/PROC-370-437.

[103] H. Bao, G. Xu, M. Yu, Q. Wang, R. Li, M. Saafi, and J. Ye, « Evolution of ITZ and its effect on the carbonation depth of concrete under supercritical CO2 condition », en, *Cement and Concrete Composites*, vol. 126, p. 104 336, Feb. 2022, ISSN: 09589465. DOI: 10.1016/j.cemconcomp.2021.104336.

[104] « Chapter 10 - Cement additives », en, *in Petroleum Engineer's Guide to Oil Field Chemicals and Fluids (Second Edition)*, J. Fink, Ed., Boston: Gulf Professional Publishing, Jan. 2015, pp. 317–367, ISBN: 978-0-12-803734-8. DOI: 10.1016/B978-0-12-803734-8.00010-2.

[105] K. H. Khayat, « Viscosity-enhancing admixtures for cement-based materials â€" An overview », en, *Cement and Concrete Composites*, vol. 20, *2-3*, pp. 171–188, Jan. 1998, ISSN: 09589465. DOI: 10.1016/S0958-9465(98)80006-1.

[106] P. Mukkala, C. Venkatesh, and S. Habibunnisa, « Evaluation of mix ratios of light weight concrete using geopolymer as binder », en, *Materials Today: Proceedings*, S2214785321078664, Dec. 2021, ISSN: 22147853. DOI: 10.1016/j.matpr.2021.12.140.

[107] Y. Zhou, M. Fall, and S. Haruna, « Flow ability of cemented paste backfill with chloride-free antifreeze additives in sub-zero environments », en, *Cement and Concrete Composites*, vol. 126, p. 104 359, Feb. 2022, ISSN: 09589465. DOI: 10.1016/j.cemconcomp.2021.104359.

[108] D. Kamorny, A. Safonov, K. Boldyrev, E. Abramova, E. Tyupina, and O. Gorbunova, « Modification of the Cement Matrix with Organic Additives for Stabilizing Pertechnetate Ions », en, *Journal of Nuclear Materials*, vol. 557, p. 153 295, Dec. 2021, ISSN: 00223115. DOI: 10.1016/j.jnucmat.2021.153295.

[109] J. Biernacki, « International Summit on Cement Hydration Kinetics and Modeling Special Edition Québec City, July 27, 28 and 29, 2009 », *Cement and Concrete Research - CEM CONCR RES*, vol. 41, pp. 1206–1207, Dec. 2011. DOI: 10.1016/j.cemconres.2011.08.002.

[110] J. W. Martin, « 4 - Glasses and ceramics », en, *in Materials for Engineering (Third Edition)*, J. W. Martin, Ed., Woodhead Publishing, Jan. 2006, pp. 133–158, ISBN: 978-1-84569-157-8. DOI: 10.1533/9781845691608.2.133.

[111] A. D'Aloia, « Early age kinetics: Activation energy, maturity and equivalent age », en, *in Early Age Cracking in Cementitious Systems - Report of RILEM Technical Committee 181-EAS - Early age shrinkage induced stresses and cracking in cementitious systems*, RILEM Publications SARL, 2003, pp. 127–148, ISBN: 978-2-912143-63-1. DOI: 10.1617/2912143632.015.

[112] J. Hong, R. Kim, C. H. Lee, and H. Choi, « Evaluation of stiffening behavior of concrete based on contactless ultrasonic system and maturity method », en, *Construction and Building Materials*, vol. 262, p. 120 717, Nov. 2020, ISSN: 09500618. DOI: 10.1016/j.conbuildmat.2020.120717.

[113] M. Soutsos, F. Kanavaris, and M. Elsageer, « Accuracy of maturity functionsâ€™ strength estimates for fly ash concretes cured at elevated temperatures », en, *Construction and Building Materials*, vol. 266, p. 121 043, Jan. 2021, ISSN: 09500618. DOI: 10.1016/j.conbuildmat.2020.121043.

[114] Q. Li, J. Guan, Z. Wu, W. Dong, and S. Zhou, « Equivalent maturity for ambient temperature effect on fracture parameters of site-casting dam concrete », en, *Construction and Building Materials*, vol. 120, pp. 293–308, Sep. 2016, ISSN: 09500618. DOI: 10.1016/j.conbuildmat.2016.05.111.

[115] M. Soutsos and F. Kanavaris, « Compressive strength estimates for adiabatically cured concretes with the Modified Nurse-Saul (MNS) maturity function », en, *Construction and Building Materials*, vol. 255, p. 119 236, Sep. 2020, ISSN: 09500618. DOI: 10.1016/j.conbuildmat.2020.119236. (visited on 01/28/2022).

[116] M. Soutsos, A. Vollpracht, and F. Kanavaris, « Applicability of fib model codeâ€™s maturity function for estimating the strength development of GGBS concretes », en, *Construction and Building Materials*, vol. 264, p. 120 157, Dec. 2020, ISSN: 09500618. DOI: 10.1016/j.conbuildmat.2020.120157.

[117] M. Benaicha, Y. Burtschell, and A. H. Alaoui, « Prediction of compressive strength at early age of concrete â€“ Application of maturity », en, *Journal of Building Engineering*, vol. 6, pp. 119–125, Jun. 2016, ISSN: 23527102. DOI: 10.1016/j.jobe.2016.03.003.

[118] Z. Mi, Y. Hu, Q. Li, and H. Zhu, « Elevated temperature inversion phenomenon in fracture properties of concrete and its application to maturity model », en, *Engineering Fracture Mechanics*, vol. 199, pp. 294–307, Aug. 2018, ISSN: 00137944. DOI: 10.1016/j.engfracmech.2018.05.040.

[119] M. Velay-Lizancos, I. Martinez-Lage, and P. Vazquez-Burgo, « The effect of recycled aggregates on the accuracy of the maturity method on vibrated and self-compacting concretes », en, *Archives of Civil and Mechanical Engineering*, vol. 19, *2*, pp. 311–321, Mar. 2019, ISSN: 16449665. DOI: 10.1016/j.acme.2018.11.004.

[120] N. J. Jin, I. Seung, Y. S. Choi, and J. Yeon, « Prediction of early-age compressive strength of epoxy resin concrete using the maturity method », en, *Construction and Building Materials*, vol. 152, pp. 990–998, Oct. 2017, ISSN: 09500618. DOI: 10.1016/j.conbuildmat.2017.07.066.

[121] T. A. Yikici and H.-L. (Chen, « Use of maturity method to estimate compressive strength of mass concrete », en, *Construction and Building Materials*, vol. 95, pp. 802–812, Oct. 2015, ISSN: 09500618. DOI: 10.1016/j.conbuildmat.2015.07.026.

[122] M.-C. Han and C.-G. Han, « Use of maturity methods to estimate the setting time of concrete containing super retarding agents », en, *Cement and Concrete Composites*, vol. 32, *2*, pp. 164–172, Feb. 2010, ISSN: 09589465. DOI: 10.1016/j.cemconcomp.2009.11.008.

[123] Y. A. Abdel-Jawad, « The maturity method: Modifications to improve estimation of concrete strength at later ages », en, *Construction and Building Materials*, vol. 20, *10*, pp. 893–900, Dec. 2006, ISSN: 09500618. DOI: 10.1016/j.conbuildmat.2005.06.022.

[124] A. Vollpracht, M. Soutsos, and F. Kanavaris, « Strength development of GGBS and fly ash concretes and applicability of fib model code's maturity function – A critical review », en, *Construction and Building Materials*, vol. 162, pp. 830–846, Feb. 2018, ISSN: 09500618. DOI: 10.1016/j.conbuildmat.2017.12.054.

[125] S. Ghahri Saremi and D. Goulias, « Concrete strength gain monitoring with non-destructive methods for potential adoption in quality assurance », en, *Construction and Building Materials*, vol. 260, p. 120 464, Nov. 2020, ISSN: 09500618. DOI: 10.1016/j.conbuildmat.2020.120464.

[126] M. Soutsos, G. Turuâ€™allo, K. Owens, J. Kwasny, S. Barnett, and P. Basheer, « Maturity testing of lightweight self-compacting and vibrated concretes », en, *Construction and Building Materials*, vol. 47, pp. 118–125, Oct. 2013, ISSN: 09500618. DOI: 10.1016/j.conbuildmat.2013.04.045.

[127] G. De Schutter, « Applicability of degree of hydration concept and maturity method for thermo-visco-elastic behaviour of early age concrete », en, *Cement and Concrete Composites*, vol. 26, *5*, pp. 437–443, Jul. 2004, ISSN: 09589465. DOI: 10.1016/S0958-9465(03)00067-2.

[128] A. G. A. Saul, « Principles underlying the steam curing of concrete at atmospheric pressure », en, *Magazine of Concrete Research*, vol. 2, *6*, pp. 127–140, Mar. 1951, ISSN: 0024-9831, 1751-763X. DOI: 10.1680/macr.1951.2.6.127.

[129] R. W. Nurse, « Steam curing of concrete », en, *Magazine of Concrete Research*, vol. 1, *2*, pp. 79–88, Jun. 1949, ISSN: 0024-9831, 1751-763X. DOI: 10.1680/macr.1949.1.2.79.

[130] « ASTM C1074. Practice for Estimating Concrete Strength by the Maturity Method », en, ASTM International, Tech. Rep. DOI: 10.1520/C1074-11.

[131] N. J. Carino and H. S. Lew, « The Maturity Method: From Theory to Application », en, *in Structures 2001*, Washington, D.C., United States: American Society of Civil Engineers, May 2001, pp. 1–19, ISBN: 978-0-7844-0558-1. DOI: 10.1061/40558(2001)17.

[132] N. Kumar and K. Jayakumar, « The early-age prediction of concrete strength using maturity models: a review », *Journal of Building Pathology and Rehabilitation*, vol. 6, Dec. 2021. DOI: 10.1007/s41024-020-00102-1.

[133] M. Siddiqui and K. Riding, « Effect of Calculation Methods on Cement Paste and Mortar Apparent Activation Energy », *Advances in Civil Engineering Materials (ACEM)*, vol. 1, p. 19, Sep. 2012. DOI: 10.1520/ACEM20120011.

[134] H. Kada-Benameur, E. Wirquin, and B. Duthoit, « Determination of apparent activation energy of concrete by isothermal calorimetry », en, *Cement and Concrete Research*, vol. 30, *2*, pp. 301–305, Feb. 2000, ISSN: 00088846. DOI: 10.1016/S0008-8846(99)00250-1.

[135] E. Wirquin, M. Broda, and B. Duthoit, « Determination of the apparent activation energy of one concrete by calorimetric and mechanical means Influence of a superplasticizer », en, *Cement and Concrete Research*, p. 7, 2002.

[136] M. I. Sánchez de Rojas Gómez and M. Frías Rojas, « 4 - Natural pozzolans in eco-efficient concrete », en, *in Eco-Efficient Concrete*, ser. Woodhead Publishing Series in Civil and Structural Engineering, F. Pacheco-Torgal, S. Jalali, J. Labrincha, and V. M. John, Eds., Woodhead Publishing, Jan. 2013, pp. 83–104, ISBN: 978-0-85709-424-7. DOI: 10.1533/9780857098993.2.83.

[137] V. Baroghel-Bouny, « Hydration and moisture distribution », en, *in Early Age Cracking in Cementitious Systems - Report of RILEM Technical Committee 181-EAS - Early age shrinkage induced stresses and cracking in cementitious systems*, RILEM Publications SARL, 2003, pp. 39–45, ISBN: 978-2-912143-63-1. DOI: 10.1617/2912143632.007.

[138] G. De Schutter, « Hydration and temperature development of concrete made with blast-furnace slag cement », en, *Cement and Concrete Research*, vol. 29, *1*, pp. 143–149, Jan. 1999, ISSN: 00088846. DOI: 10.1016/S0008-8846(98)00229-4.

[139] O. Linderoth, L. Wadsö, and D. Jansen, « Long-term cement hydration studies with isothermal calorimetry », en, *Cement and Concrete Research*, vol. 141, p. 106 344, Mar. 2021, ISSN: 00088846. DOI: 10.1016/j.cemconres.2020.106344.

[140] A. J. MacLeod, F. G. Collins, and W. Duan, « Effects of carbon nanotubes on the early-age hydration kinetics of Portland cement using isothermal calorimetry », en, *Cement and Concrete Composites*, vol. 119, p. 103 994, May 2021, ISSN: 09589465. DOI: 10.1016/j.cemconcomp.2021.103994.

[141] A. Bogner, J. Link, M. Baum, M. Mahlbacher, T. Gil-Diaz, J. LÃ¼tzenkirchen, T. Sowoidnich, F. Heberling, T. Schäfer, H.-M. Ludwig, F. Dehn, H. MÃ¼ller, and M. Haist, « Early hydration and microstructure formation of Portland cement paste studied by oscillation rheology, isothermal calorimetry, 1H NMR relaxometry, conductance and SAXS », en, *Cement and Concrete Research*, vol. 130, p. 105 977, Apr. 2020, ISSN: 00088846. DOI: 10.1016/j.cemconres.2020.105977.

[142] L. Wadsö and M. Arndt, « An international round robin test on isothermal (conduction) calorimetry for measurement of three-day heat of hydration of cement », en, *Cement and Concrete Research*, vol. 79, pp. 316–322, Jan. 2016, ISSN: 00088846. DOI: 10.1016/j.cemconres.2015.10.004.

[143] X. Pang, D. P. Bentz, C. Meyer, G. P. Funkhouser, and R. Darbe, « A comparison study of Portland cement hydration kinetics as measured by chemical shrinkage and isothermal calorimetry », en, *Cement and Concrete Composites*, vol. 39, pp. 23–32, May 2013, ISSN: 09589465. DOI: 10.1016/j.cemconcomp.2013.03.007.

[144] X. Pang, P. Boul, and W. Cuello Jimenez, « Isothermal calorimetry study of the effect of chloride accelerators on the hydration kinetics of oil well cement », en, *Construction and Building Materials*, vol. 77, pp. 260–269, Feb. 2015, ISSN: 09500618. DOI: 10.1016/j.conbuildmat.2014.12.077.

[145] A. Betioli, P. Gleize, D. Silva, V. John, and R. Pileggi, « Effect of HMEC on the consolidation of cement pastes: Isothermal calorimetry versus oscillatory rheometry », en, *Cement and Concrete Research*, vol. 39, *5*, pp. 440–445, May 2009, ISSN: 00088846. DOI: 10.1016/j.cemconres.2009.02.002.

[146] M. Bligh, M. d'Eurydice, R. Lloyd, C. Arns, and T. Waite, « Investigation of early hydration dynamics and microstructural development in ordinary Portland cement using 1H NMR relaxometry and isothermal calorimetry », en, *Cement and Concrete Research*, vol. 83, pp. 131–139, May 2016, ISSN: 00088846. DOI: 10.1016/j.cemconres.2016.01.007.

[147] R. Ylmén, L. Wadsö, and I. Panas, « Insights into early hydration of Portland limestone cement from infrared spectroscopy and isothermal calorimetry », en, *Cement and Concrete Research*, vol. 40, *10*, pp. 1541–1546, Oct. 2010, ISSN: 00088846. DOI: 10.1016/j.cemconres.2010.06.008.

[148] M. Gerstig and L. Wadsö, « A method based on isothermal calorimetry to quantify the influence of moisture on the hydration rate of young cement pastes », en, *Cement and Concrete Research*, vol. 40, *6*, pp. 867–874, Jun. 2010, ISSN: 00088846. DOI: 10.1016/j.cemconres.2010.02.005.

[149] EN 196-11:2018 (E), « Methods of testing cement - Part 11 : Heat of hydration - Isothermal Conduction Calorimetry method », French standard institute (AFNOR), French Standard, Dec. 2018.

[150] EN 196-9:2010 (E), « Methods of testing cement - Part 9 : Heat of hydration - Semi-adiabatic method », French standard institute (AFNOR), French Standard, Dec. 2010.

[151] EN 196-8:2010 (E), « Methods of testing cement - Part 8 : Heat of hydration - Solution method », French standard institute (AFNOR), French Standard, Mar. 2010.

[152] X. Kang, H. Lei, and Z. Xia, « A comparative study of modified fall cone method and semi-adiabatic calorimetry for measurement of setting time of cement based materials », en, *Construction and Building Materials*, vol. 248, p. 118 634, Jul. 2020, ISSN: 09500618. DOI: 10.1016/j.conbuildmat.2020.118634.

[153] E. Hernández Bautista, D. Bentz, S. Sandoval Torres, and P. Cano Barrita, « Numerical simulation of heat and mass transport during hydration of Portland cement mortar in semi-adiabatic and steam curing conditions », *Cement and Concrete Composites*, vol. 69, pp. 38–48, May 2016. DOI: 10.1016/j.cemconcomp.2015.10.014.

[154] D. Bentz, S. Jones, M. Peltz, and P. Stutzman, *Influence of Internal Curing on Properties and Performance of Cement-Based Repair Materials*. Aug. 2015. DOI: 10.6028/NIST.IR.8076.

[155] A. Durán-Herrera, C. Juárez, P. Valdez, and D. Bentz, « Evaluation of sustainable high-volume fly ash concretes », en, *Cement and Concrete Composites*, vol. 33, *1*, pp. 39–45, Jan. 2011, ISSN: 09589465. DOI: 10.1016/j.cemconcomp.2010.09.020.

[156] J. J. Thomas, J. J. Biernacki, J. W. Bullard, S. Bishnoi, J. S. Dolado, G. W. Scherer, and A. Luttge, « Modeling and simulation of cement hydration kinetics and microstructure development », en, *Cement and Concrete Research*, Conferences Special: Cement Hydration Kinetics and Modeling, Quebec City, 2009 & CONMOD10, Lausanne, 2010, vol. 41, *12*, pp. 1257–1278, Dec. 2011, ISSN: 0008-8846. DOI: 10.1016/j.cemconres.2010.10.004.

[157] D. Bentz, « Three-Dimensional Computer Simulation of Portland Cement Hydration and Microstructure Development », *Journal of the American Ceramic Society*, vol. 80, pp. 3–21, Jan. 1997. DOI: 10.1111/j.1151-2916.1997.tb02785.x.

[158] J. W. Bullard, « Approximate Rate Constants for Nonideal Diffusion and Their Application in a Stochastic Model », en, *The Journal of Physical Chemistry A*, vol. 111, *11*, pp. 2084–2092, Mar. 2007, ISSN: 1089-5639, 1520-5215. DOI: 10.1021/jp0658391.

[159] ——, « A three-dimensional microstructural model of reactions and transport in aqueous mineral systems », en, *Modelling and Simulation in Materials Science and Engineering*, vol. 15, *7*, pp. 711–738, Oct. 2007, ISSN: 0965-0393, 1361-651X. DOI: 10.1088/0965-0393/15/7/002.

[160] J. fu, *Atomistic Simulation of Anistropic Crystal Structures at Nanoscale*. May 2019, ISBN: 978-1-83880-201-1. DOI: 10.5772/intechopen.84597.

[161] M. Laanaiya, A. Bouibes, and A. Zaoui, « Structural stability of belite sulfoaluminate clinkering polymorphs », en, *Solid State Ionics*, vol. 365, p. 115 641, Jul. 2021, ISSN: 0167-2738. DOI: 10.1016/j.ssi.2021.115641.

[162] M. Laanaiya and A. Zaoui, « Piezoelectric response and failure behavior of cement paste under external loading », en, *Cement and Concrete Research*, vol. 139, p. 106 257, Jan. 2021, ISSN: 00088846. DOI: 10.1016/j.cemconres.2020.106257.

[163] ——, « Preventing cement-based materials failure by embedding Fe2O3 nanoparticles », en, *Construction and Building Materials*, vol. 260, p. 120 466, Nov. 2020, ISSN: 09500618. DOI: 10.1016/j.conbuildmat.2020.120466.

[164] M. Laanaiya, A. Bouibes, and A. Zaoui, « Understanding why Alite is responsible of the main mechanical characteristics in Portland cement », en, *Cement and Concrete Research*, vol. 126, p. 105 916, Dec. 2019, ISSN: 00088846. DOI: 10.1016/j.cemconres.2019.105916.

[165] W. Sekkal and A. Zaoui, « Enhancing the interfacial bond strength of cement nanocomposite with carbonate nanostructure », en, *Composites Part B: Engineering*, vol. 124, pp. 111–119, Sep. 2017, ISSN: 13598368. DOI: 10.1016/j.compositesb.2017.05.057.

[166] T. Honorio, F. Masara, W. Barbosa, and F. Benboudjema, « The Multi-scale Multi-technique Multi-physics Framework Required to Model the Thermal Properties of Cement-Based Materials », *in*, Jan. 2023, pp. 150–159, ISBN: 978-3-031-07745-6. DOI: 10.1007/978-3-031-07746-3_15.

[167] F. Masara, T. Honorio, and F. Benboudjema, « Modeling C-S-H Sorption at the Molecular Scale: Effective Interactions, Stability, and Cavitation », *in*, Jan. 2023, pp. 218–229, ISBN: 978-3-031-07745-6. DOI: 10.1007/978-3-031-07746-3_22.

[168] T. Sayari, T. Honorio, F. Benboudjema, R. Tabchoury, J.-L. Adia, and C. Clergue, *Numerical and Experimental Investigation of Wall Effect in Concrete*. Jul. 2022, ISBN: 978-3-031-07745-6. DOI: 10.1007/978-3-031-07746-3_31.

[169] J. Claverie, F. Bernard, J. M. M. Cordeiro, and S. Kamali-Bernard, « Water's behaviour on Ca-rich tricalcium silicate surfaces for various degrees of hydration: A molecular dynamics investigation », en, *Journal of Physics and Chemistry of Solids*, vol. 132, pp. 48–55, Sep. 2019, ISSN: 00223697. DOI: 10.1016/j.jpcs.2019.03.020.

[170] P. E. Smith, « 3 - Design and specification of marine concrete structures », en, *in Marine Concrete Structures*, M. G. Alexander, Ed., Woodhead Publishing, Jan. 2016, pp. 65–114, ISBN: 978-0-08-100905-5. DOI: 10.1016/B978-0-08-100081-6.00003-9.

[171] A. CastaÃ±eda, F. Corvo, J. Albear, M. Rigoberto, and A. Fernandez, « Atmospheric Corrosion Behaviors of Reinforcement Steel in Reinforced Concrete in a Coastal City as Havana, Cuba », *in*, Jan. 2020, pp. 283–291, ISBN: 978-3-030-22033-4. DOI: 10.1007/978-3-030-22034-1_32.

[172] J. Belkowitz and D. Armentrout, « An investigation of nano silica in the cement hydration process », *American Concrete Institute, ACI Special Publication*, Jan. 2009.

[173] A. Cwirzen and V. Penttala, « Aggregateâ€“cement paste transition zone properties affecting the saltâ€“frost damage of high-performance concretes », en, *Cement and Concrete Research*, vol. 35, *4*, pp. 671–679, Apr. 2005, ISSN: 0008-8846. DOI: 10.1016/j.cemconres.2004.06.009.

[174] D. H. Allen, « Homogenization principles and their application to continuum damage mechanics », en, *Composites Science and Technology*, p. 8, 2001.

[175] J. Eshelby, « The Determination of the Elastic Field Of An Ellipsoidal Inclusion and Related Problems », *Proceedings of the Royal Society of London. Series A. Mathematical and Physical Sciences*, vol. 241, Aug. 1957. DOI: 10.1098/rspa.1957.0133.

[176] J. D. Eshelby and R. E. Peierls, « The elastic field outside an ellipsoidal inclusion », *Proceedings of the Royal Society of London. Series A. Mathematical and Physical Sciences*, vol. 252, *1271*, pp. 561–569, Oct. 1959, Publisher: Royal Society. DOI: 10.1098/rspa.1959.0173.

[177] M. Wang and N. Pan, « Predictions of effective physical properties of complex multiphase materials », en, *Materials Science and Engineering: R: Reports*, vol. 63, *1*, pp. 1–30, Dec. 2008, ISSN: 0927796X. DOI: 10.1016/j.mser.2008.07.001.

[178] K. Pietrak and T. WiÅ›niewski, « A review of models for effective thermal conductivity of composite materials », *J. Power Technol.*, vol. 95, pp. 14–24, Jan. 2014.

[180] J. Escoda, D. Jeulin, F. Willot, and C. Toulemonde, « Three-dimensional morphological modelling of concrete using multiscale Poisson polyhedra: 3D MORPHOLOGICAL MODELLING OF CONCRETE », en, *Journal of Microscopy*, vol. 258, *1*, pp. 31–48, Apr. 2015, ISSN: 00222720. DOI: 10.1111/jmi.12213.

[181] E. N. Landis and J. E. Bolander, « Explicit representation of physical processes in concrete fracture », en, *Journal of Physics D: Applied Physics*, vol. 42, *21*, p. 214 002, Nov. 2009, ISSN: 0022-3727, 1361-6463. DOI: 10.1088/0022-3727/42/21/214002.

[182] W. Ren, Z. Yang, R. Sharma, C. Zhang, and P. J. Withers, « Two-dimensional X-ray CT image based meso-scale fracture modelling of concrete », en, *Engineering Fracture Mechanics*, vol. 133, pp. 24–39, Jan. 2015, ISSN: 0013-7944. DOI: 10.1016/j.engfracmech.2014.10.016.

[183] Y. Gan, H. Zhang, L. Minfei, E. Schlangen, K. Breugel, and B. Å avija, « A numerical study of fatigue of hardened cement paste at the microscale », *International Journal of Fatigue*, vol. 151, p. 106 401, Jun. 2021. DOI: 10.1016/j.ijfatigue.2021.106401.

[184] J. Wang, A. Jivkov, D. Engelberg, and Q. Li, « Image-Based vs. Parametric Modelling of Concrete Meso-Structures », *Materials*, vol. 15, p. 704, Jan. 2022. DOI: 10.3390/ma15030704.

[185] S. Kamali-Bernard and F. Bernard, « Effect of tensile cracking on diffusivity of mortar: 3D numerical modelling », en, *Computational Materials Science*, vol. 47,

1, pp. 178–185, Nov. 2009, ISSN: 09270256. DOI: 10.1016/j.commatsci.2009.07.005.

[186] D. Bentz, *Guide to using CEMHYD3D: A three-dimensional cement hydration and microstructure development modelling package*. Jan. 1997.

[187] D. Bentz, « CEMHYD3D: A Three-Dimensional Cement Hydration and Microstructure Development Modeling Package. Version 2.0 », Apr. 2000.

[188] D. Bentz, X. Feng, C.-J. Haecker, and P. Stutzman, *Analysis of CCRL Proficiency Cements 135 and 136 Using CEMHYD3D*. May 2000.

[189] D. Bentz and J. Conway, « Computer modeling of the replacement of "coarse" cement particles by inert fillers in low w/c ratio concretes: Hydration and strength », *Cement and Concrete Research*, vol. 31, pp. 503–506, Mar. 2001. DOI: 10.1016/S0008-8846(01)00456-2.

[190] G. Ye, K. Breugel, and A. Fraaij, « Experimental study on ultrasonic pulse velocity evaluation of the microstructure of cementitious material at early age », *HERON, vol. 46 (3), 2001*, vol. 46, Jan. 2001.

[191] R. A. Patel, J. Perko, D. Jacques, G. De Schutter, G. Ye, and K. Van Bruegel, « Effective diffusivity of cement pastes from virtual microstructures: Role of gel porosity and capillary pore percolation », en, *Construction and Building Materials*, vol. 165, pp. 833–845, Mar. 2018, ISSN: 0950-0618. DOI: 10.1016/j.conbuildmat.2018.01.010.

[192] A. Bazzoni, S. Ma, Q. Wang, X. Shen, M. Cantoni, and K. L. Scrivener, « The Effect of Magnesium and Zinc Ions on the Hydration Kinetics of C_3S », en, *Journal of the American Ceramic Society*, vol. 97, *11*, G. Scherer, Ed., pp. 3684–3693, Nov. 2014, ISSN: 00027820. DOI: 10.1111/jace.13156.

[193] S. Rangari, K. Murali, and A. Deb, « Effect of meso-structure on strength and size effect in concrete under compression », en, *Engineering Fracture Mechanics*, vol. 195, pp. 162–185, May 2018, ISSN: 0013-7944. DOI: 10.1016/j.engfracmech.2018.04.006.

[194] J. E. Bolander and S. Saito, « Fracture analyses using spring networks with random geometry », en, *Engineering Fracture Mechanics*, vol. 61, *5*, pp. 569–591, Nov. 1998, ISSN: 0013-7944. DOI: 10.1016/S0013-7944(98)00069-1.

[195] D. Asahina, E. N. Landis, and J. E. Bolander, « Modeling of phase interfaces during pre-critical crack growth in concrete », en, *Cement and Concrete Composites*, vol. 33, *9*, pp. 966–977, Oct. 2011, ISSN: 0958-9465. DOI: 10.1016/j.cemconcomp.2011.01.007.

[196] Z. Wang, F. Lin, and X. Gu, « Numerical simulation of failure process of concrete under compression based on mesoscopic discrete element model », *Tsinghua Science and Technology*, vol. 13, *S1*, pp. 19–25, Oct. 2008, Conference Name: Tsinghua Science and Technology, ISSN: 1007-0214. DOI: 10.1016/S1007-0214(08)70121-4.

[197] T. Kawai, « New discrete models and their application to seismic response analysis of structures », en, *Nuclear Engineering and Design*, vol. 48, *1*, pp. 207–229, Jun. 1978, ISSN: 00295493. DOI: 10.1016/0029-5493(78)90217-0.

[198] U. Farooq, H. Nakamura, T. Miura, and Y. Yamamoto, « Proposal of bond behavior simulation model by using discretized voronoi mesh for concrete and beam element for reinforcement », en, *Cement and Concrete Composites*, vol. 110, p. 103 593, Jul. 2020, ISSN: 0958-9465. DOI: 10.1016/j.cemconcomp.2020.103593.

[199] Z. Pan, A. Chen, R. Ma, D. Wang, and H. Tian, « Three-dimensional lattice modeling of concrete carbonation at meso-scale based on reconstructed coarse aggregates », en, *Construction and Building Materials*, vol. 192, pp. 253–271, Dec. 2018, ISSN: 0950-0618. DOI: 10.1016/j.conbuildmat.2018.10.052.

[200] G. Mazzucco, G. Xotta, B. Pomaro, C. Majorana, F. Faleschini, and C. Pellegrino, *Mesoscale Modelling of Concrete with Recycled Aggregates*. Sep. 2015, Pages: 863. DOI: 10.1061/9780784479346.101.

[201] R. Zhou, *Holistic mesoscale modelling of concrete â€“ Recent developments*. Mar. 2020.

[202] L. Mao, H. Liu, Y. Zhu, Z. Zhu, R. Guo, and F.-p. Chiang, « 3D Strain Mapping of Opaque Materials Using an Improved Digital Volumetric Speckle Photography Technique with X-Ray Microtomography », en, *Applied Sciences*, vol. 9, *7*, p. 1418, Apr. 2019, ISSN: 2076-3417. DOI: 10.3390/app9071418.

[203] G. De Schutter and L. Taerwe, « Random particle model for concrete based on Delaunay triangulation », *Matériaux et Constructions*, vol. 26, pp. 67–73, Jan. 1993. DOI: 10.1007/BF02472853.

[204] Z. Wu, J. Zhang, H. Yu, Q. Fang, H. Ma, and L. Chen, « Three-Dimensional Mesoscopic Investigation on the Impact of Specimen Geometry and Bearing Strip Size on the Splitting-Tensile Properties of Coral Aggregate Concrete », en, *Engineering*, S2095809921005300, Dec. 2021, ISSN: 20958099. DOI: 10.1016/j.eng.2021.02.024.

[205] M. Pundir and G. Anciaux, « Numerical Generation and Contact Analysis of Rough Surfaces in Concrete », *Journal of Advanced Concrete Technology*, vol. 19, pp. 864–885, Jul. 2021. DOI: 10.3151/jact.19.864.

[206] X. Long, M. Mao, C. Lu, R. Li, and F. Jia, « Modeling of heterogeneous materials at high strain rates with machine learning algorithms trained by finite element simulations », *Journal of Micromechanics and Molecular Physics*, vol. 06, p. 2 150 001, Jun. 2021. DOI: 10.1142/S2424913021500016.

[207] A. K. H. Kwan, Z. M. Wang, and H. C. Chan, « Mesoscopic study of concrete II: nonlinear Â®nite element analysis », en, *Computers and Structures*, p. 12, 1999.

[208] Z. M. Wang, A. K. H. Kwan, and H. C. Chan, « Mesoscopic study of concrete I: generation of random aggregate structure and finite element mesh », en, *Computers & Structures*, vol. 70, *5*, pp. 533–544, Mar. 1999, ISSN: 0045-7949. DOI: 10.1016/S0045-7949(98)00177-1.

[209] P. Wriggers and S. O. Moftah, « Mesoscale models for concrete: Homogenisation and damage behaviour », en, *Finite Elements in Analysis and Design*, The Seventeenth Annual Robert J. Melosh Competition, vol. 42, *7*, pp. 623–636, Apr. 2006, ISSN: 0168-874X. DOI: 10.1016/j.finel.2005.11.008.

[210] R. Hill, « Elastic properties of reinforced solids: Some theoretical principles », en, *Journal of the Mechanics and Physics of Solids*, vol. 11, *5*, pp. 357–372, Sep. 1963, ISSN: 00225096. DOI: 10.1016/0022-5096(63)90036-X.

[211] P. Stroeven, J. Hu, and H. Chen, « Stochastic heterogeneity as fundamental basis for the design and evaluation of experiments », en, *Cement and Concrete Composites*, vol. 30, *6*, pp. 506–514, Jul. 2008, ISSN: 0958-9465. DOI: 10.1016/j.cemconcomp.2007.12.001.

[212] W. J. Drugan and J. R. Willis, « A micromechanics-based nonlocal constitutive equation and estimates of representative volume element size for elastic compos-

ites », en, *Journal of the Mechanics and Physics of Solids*, vol. 44, *4*, pp. 497–524, Apr. 1996, ISSN: 0022-5096. DOI: 10.1016/0022-5096(96)00007-5.

[213] P. Stroeven and J. Hu, « On Science Aspects of Simulating Practical Manifestations of Concrete », en, *in Brittle Matrix Composites 8*, A. M. Brandt, V. C. Li, and I. H. Marshall, Eds., Woodhead Publishing, Jan. 2006, pp. 421–430, ISBN: 978-1-84569-031-1. DOI: 10.1533/9780857093080.421.

[214] F. Grondin, H. Dumontet, A. Ben Hamida, G. Mounajed, and H. Boussa, « Multi-scales modelling for the behaviour of damaged concrete », en, *Cement and Concrete Research*, vol. 37, *10*, pp. 1453–1462, Oct. 2007, ISSN: 0008-8846. DOI: 10.1016/j.cemconres.2007.05.012.

[215] F. A. Grondin, « Modélisation multi-échelles du comportement thermo-hydro-mécanique des matériaux hétérogènes. Applications aux matériaux cimentaires sous sollicitations sévères. », fr, Ph.D. dissertation, Université Pierre et Marie Curie - Paris VI, Paris, Dec. 2015.

[216] J. J. del Coz Díaz, F. P. Álvarez Rabanal, P. J. García Nieto, J. Domínguez Hernández, B. Rodríguez Soria, and J. M. Pérez-Bella, « Hygrothermal properties of lightweight concrete: Experiments and numerical fitting study », en, *Construction and Building Materials*, Special Section on Recycling Wastes for Use as Construction Materials, vol. 40, pp. 543–555, Mar. 2013, ISSN: 0950-0618. DOI: 10.1016/j.conbuildmat.2012.11.045.

[217] M. Bederina, L. Marmoret, K. Mezreb, M. M. Khenfer, A. Bali, and M. Quéneudec, « Effect of the addition of wood shavings on thermal conductivity of sand concretes: Experimental study and modelling », en, *Construction and Building Materials*, Fracture, Acoustic Emission and NDE in Concrete (KIFA-4), vol. 21, *3*, pp. 662–668, Mar. 2007, ISSN: 0950-0618. DOI: 10.1016/j.conbuildmat.2005.12.008.

[218] S. Benfratello, C. Capitano, G. Peri, G. Rizzo, G. Scaccianoce, and G. Sorrentino, « Thermal and structural properties of a hempâ€“lime biocomposite », en, *Construction and Building Materials*, vol. 48, pp. 745–754, Nov. 2013, ISSN: 0950-0618. DOI: 10.1016/j.conbuildmat.2013.07.096.

[219] M. H. Yassin, Z. Hjaj, and R. Lakys, *Experimental Study on the Thermal Characterization of PTF Concrete*. Oct. 2022. DOI: 10.11159/iccste22.188.

[220] M. M. Alsaadawi, M. Amin, and A. M. Tahwia, « Thermal, mechanical and microstructural properties of sustainable concrete incorporating Phase change materials », en, *Construction and Building Materials*, vol. 356, p. 129 300, Nov. 2022, ISSN: 09500618. DOI: 10.1016/j.conbuildmat.2022.129300.

[221] H. Cui, J. Zou, Z. Gong, D. Zheng, X. Bao, and X. Chen, « Study on the thermal and mechanical properties of steel fibre reinforced PCM-HSB concrete for high performance in energy piles », en, *Construction and Building Materials*, vol. 350, p. 128 822, Oct. 2022, ISSN: 09500618. DOI: 10.1016/j.conbuildmat.2022.128822.

[222] J. Xiao, L. Hao, W. Cao, and T. Ye, « Influence of recycled powder derived from waste concrete on mechanical and thermal properties of foam concrete », en, *Journal of Building Engineering*, vol. 61, p. 105 203, Dec. 2022, ISSN: 23527102. DOI: 10.1016/j.jobe.2022.105203.

[223] A. K. Pal, P. K. S. Rathore, and M. K. Gupta, « Design, development, and analysis of modified concrete block integrated with thermal energy storage material for regulating indoor temperature », en, *Materials Today: Proceedings*, S2214785322056401, Sep. 2022, ISSN: 22147853. DOI: 10.1016/j.matpr.2022.08.447.

[224] L. Hao, J. Xiao, J. Sun, B. Xia, and W. Cao, « Thermal conductivity of 3D printed concrete with recycled fine aggregate composite phase change materials », en, *Journal of Cleaner Production*, vol. 364, p. 132 598, Sep. 2022, ISSN: 09596526. DOI: 10.1016/j.jclepro.2022.132598.

[225] M. El Marzak, H. Karim Serroukh, M. Benaicha, A. Hafidi Alaoui, and Y. Burtschell, « Analysis of the thermal behavior of rubber concrete at elevated temperatures based on the humidity levels: Numerical and mathematical modeling », en, *Advances in Engineering Software*, vol. 172, p. 103 182, Oct. 2022, ISSN: 09659978. DOI: 10.1016/j.advengsoft.2022.103182.

[226] J. Xin, X. Jiang, Z. Chen, L. Zuo, G. Zhang, Z. Wang, C. Qi, L. Zhang, and Y. Liu, « Early age thermal cracking resistance of basalt fiber-reinforced concrete for mass concrete structures under restraint condition », en, *Structures*, vol. 45, pp. 1189–1198, Nov. 2022, ISSN: 23520124. DOI: 10.1016/j.istruc.2022.09.101.

[227] T.-x. Da, T. Chen, W.-k. He, T. Elshaikh, Y. Ma, and Z.-f. Tong, « Applying machine learning methods to estimate the thermal conductivity of bentonite for a high-level radioactive waste repository », en, *Nuclear Engineering and Design*, vol. 392, p. 111 765, Jun. 2022, ISSN: 00295493. DOI: 10.1016/j.nucengdes.2022.111765. (visited on 10/24/2022).

[228] Y. Seok, K. Min-Jun, C. Seeun, and L. Gi-Jun, « Evaluation on the buffer temperature by thermal conductivity of gap-filling material in a high-level radioactive waste repository », en, *Nuclear Engineering and Technology*, Publisher: Elsevier, ISSN: 1738-5733. DOI: 10.1016/j.net.2022.06.008.

[229] T. M. Tritt, Ed., *Thermal conductivity: theory, properties, and applications*, en, ser. Physics of solids and liquids. New York: Kluwer Academic/Plenum Publishers, 2004, ISBN: 978-0-306-48327-1.

[230] L. Zhou and L. Yang, « A method to calculate the effective thermal conductivity of spherical particle-laden composite », en, *IOP Conference Series: Materials Science and Engineering*, vol. 493, p. 012 049, Mar. 2019, ISSN: 1757-899X. DOI: 10.1088/1757-899X/493/1/012049.

[231] K. Makarian and S. Santhanam, *Utility of 2D Finite Element Simulations for Predicting Effective Thermomechanical Properties of Particle-Reinforced Composites*. Nov. 2018. DOI: 10.1115/IMECE2018-87031.

[232] J. K. Carson, S. J. Lovatt, D. J. Tanner, and A. C. Cleland, « An analysis of the influence of material structure on the effective thermal conductivity of theoretical porous materials using finite element simulations », en, *International Journal of Refrigeration*, vol. 26, *8*, pp. 873–880, Dec. 2003, ISSN: 0140-7007. DOI: 10.1016/S0140-7007(03)00094-X.

[233] A. M. Thiele, A. Kumar, G. Sant, and L. Pilon, « Effective thermal conductivity of three-component composites containing spherical capsules », en, *International Journal of Heat and Mass Transfer*, vol. 73, pp. 177–185, Jun. 2014, ISSN: 0017-9310. DOI: 10.1016/j.ijheatmasstransfer.2014.02.002.

[234] Y. Du and Y. Ge, « Multiphase Model for Predicting the Thermal Conductivity of Cement Paste and Its Applications », *Materials*, vol. 14, *16*, Aug. 2021, ISSN: 1996-1944. DOI: 10.3390/ma14164525.

[235] A. Abdelalim, S. Abdallah, K. Easawi, S. Negm, and M. Talaat, « Thermal properties of hydrated cement pastes studied by the photoacoustic technique », *Journal of Physics: Conference Series*, vol. 214, p. 012 136, Apr. 2010. DOI: 10.1088/1742-6596/214/1/012136.

[236] M. Baghban, P. Hovde, and S. Jacobsen, « Analytical and experimental study on thermal conductivity of hardened cement pastes », *Materials and Structures*, vol. 46, pp. 1871–6873, Sep. 2013. DOI: 10.1617/s11527-012-9995-y.

[237] D. Mikulić, B. Milovanović, and I. Gabrijel, « Analysis of Thermal Properties of Cement Paste During Setting and Hardening », *Nondestruct Test Mater Struct*, vol. 6, Jan. 2013, ISSN: 978-94-007-0722-1. DOI: 10.1007/978-94-007-0723-8_66.

[238] P. Mounanga, A. Khelidj, and G. Bastian, « Experimental study and modelling approaches for the thermal conductivity evolution of hydrating cement paste », *Advances in Cement Research*, vol. 16, *3*, pp. 95–103, Jul. 2004, ISSN: 0951-7197. DOI: 10.1680/adcr.2004.16.3.95.

[239] V. F. Mendes, W. Fardin, R. R. Barreto, L. F. Caetano, and J. C. Mendes, « Sensitivity analysis of coating mortars according to their specific heat, specific gravity, thermal conductivity, and thickness in contribution to the global thermal performance of buildings », en, *Sustainable Materials and Technologies*, vol. 31, e00381, Apr. 2022, ISSN: 2214-9937. DOI: 10.1016/j.susmat.2021.e00381. [Online]. Available: https://www.sciencedirect.com/science/article/pii/S2214993721001366.

[240] M. Pomianowski, P. Heiselberg, R. L. Jensen, R. Cheng, and Y. Zhang, « A new experimental method to determine specific heat capacity of inhomogeneous concrete material with incorporated microencapsulated-PCM », en, *Cement and Concrete Research*, vol. 55, pp. 22–34, Jan. 2014, ISSN: 00088846. DOI: 10.1016/j.cemconres.2013.09.012.

[241] Y. Zhang and Y. Jiang, « A simple method, the T-history method, of determining the heat of fusion, specific heat and thermal conductivity of phase-change materials », *Measurement Science and Technology*, vol. 10, p. 201, Mar. 1999. DOI: 10.1088/0957-0233/10/3/015.

[242] Y. Xu and D. D. L. Chung, « Increasing the specific heat of cement paste by admixture surface treatments », en, *Cement and Concrete Research*, vol. 29, *7*, pp. 1117–1121, Jul. 1999, ISSN: 0008-8846. DOI: 10.1016/S0008-8846(99)00080-0.

[243] X. Fu and D. D. L. Chung, « Effects of silica fume, latex, methylcellulose, and carbon fibers on the thermal conductivity and specific heat of cement paste », en, *Cement and Concrete Research*, vol. 27, *12*, pp. 1799–1804, Dec. 1997, ISSN: 0008-8846. DOI: 10.1016/S0008-8846(97)00174-9.

[244] Y. Xu and D. Chung, « Cement of high specific heat and high thermal conductivity, obtained by using silane and silica fume as admixtures », en, *Cement and Concrete Research*, vol. 30, *7*, pp. 1175–1178, Jul. 2000, ISSN: 00088846. DOI: 10.1016/S0008-8846(00)00296-9. (visited on 10/25/2022).

[245] ——, « Effect of sand addition on the specific heat and thermal conductivity of cement », en, *Cement and Concrete Research*, vol. 30, *1*, pp. 59–61, Jan. 2000, ISSN: 00088846. DOI: 10.1016/S0008-8846(99)00206-9. (visited on 10/25/2022).

[246] H. Song, W. S. Yum, S. Sim, D. Jeon, S. Yoon, and J. E. Oh, « Proposed specific heat capacity model for a concrete wall containing phase change material (PCM) under field experiment conditions », en, *Construction and Building Materials*, vol. 336, p. 127 381, Jun. 2022, ISSN: 09500618. DOI: 10.1016/j.conbuildmat.2022.127381.

[247] Ł. Czajkowski, W. Olek, J. Weres, and R. Guzenda, « Thermal properties of wood-based panels: specific heat determination », *Wood Science and Technology*, vol. 50, May 2016. DOI: 10.1007/s00226-016-0803-7.

[248] X.-H. Yang and J. Liu, « A novel method for determining the melting point, fusion latent heat, specific heat capacity and thermal conductivity of phase change materials », en, *International Journal of Heat and Mass Transfer*, vol. 127, pp. 457–468, Dec. 2018, ISSN: 0017-9310. DOI: 10.1016/j.ijheatmasstransfer.2018.07.117.

[249] M. Talebi, M. A. Borhani, S. M. M. Zadeh, and G. R. Ansarifar, « Experimental analysis of forced convection heat transfer of Hybrid Nanofluids in a vertical annulus with cosine heat flux », en, *Progress in Nuclear Energy*, vol. 153, p. 104 438, Nov. 2022, ISSN: 0149-1970. DOI: 10.1016/j.pnucene.2022.104438.

[250] P. Tipler and G. Mosca, *Physics for Scientists and Engineers*, ser. Physics for Scientists and Engineers ptie. 133. W. H. Freeman, 2007, ISBN: 978-1-4292-0124-7.

[251] I. Maruyama and A. Teramoto, « Strain and thermal expansion coefficients of various cement pastes during hydration at early ages », *Materials and Structures*, Mar. 2013. DOI: 10.1617/s11527-013-0042-4.

[252] E. Tsolakis, C. Kalligeros, P. Tzouganakis, D. Koulocheris, and V. Spitas, « A novel experimental setup for the determination of the thermal expansion coefficient of concrete at cryogenic temperatures », en, *Construction and Building Materials*, vol. 309, p. 125 134, Nov. 2021, ISSN: 09500618. DOI: 10.1016/j.conbuildmat.2021.125134.

[253] S.-L. Cha, S.-S. Jin, G.-H. An, and J.-K. Kim, « A prediction approach of concrete properties at early ages by using a thermal stress device », en, *Construction and Building Materials*, vol. 178, pp. 120–134, Jul. 2018, ISSN: 09500618. DOI: 10.1016/j.conbuildmat.2018.05.143.

[254] C. V. Madhusudana, *Thermal Contact Conductance*, en, ser. Mechanical Engineering Series. Cham: Springer International Publishing, 2014, ISBN: 978-3-319-01275-9 978-3-319-01276-6. DOI: 10.1007/978-3-319-01276-6.

[255] P.G. Siddappa and Andallib Tariq, « Contact area and thermal conductance estimation based on the actual surface roughness measurement »,

[256] R. Dou, T. Ge, X. Liu, and Z. Wen, « Effects of contact pressure, interface temperature, and surface roughness on thermal contact conductance between stainless steel surfaces under atmosphere condition », en, *International Journal of Heat and Mass Transfer*, vol. 94, pp. 156–163, Mar. 2016, ISSN: 00179310. DOI: 10.1016/j.ijheatmasstransfer.2015.11.069.

[257] S. Song, M. M. Yovanivich, and F. O. Goodman, « Thermal Gap Conductance of Conforming Surfaces in Contact », *Journal of heat transfer*, vol. 115, pp. 553–540, 1993.

[258] J. Salerno, P. Kittel, and A. Research, « Thermal Contact Conductance », en, p. 22,

[259] X. Pan, X. Cui, S. Liu, Z. Jiang, Y. Wu, and Z. Chen, « Research Progress of Thermal Contact Resistance », en, *Journal of Low Temperature Physics*, vol. 201, *3-4*, pp. 213–253, Nov. 2020, ISSN: 0022-2291, 1573-7357. DOI: 10.1007/s10909-020-02497-0.

[260] M. Yovanovich, « Thermal contact correlations », *Progress in Astronautics and Aeronautics*, vol. -1, pp. 83–95, Jan. 1982. DOI: 10.2514/6.1981-1164.

[261] L. Fletcher, *Heat Transfer Between Surfaces in Contact: An Analytical and Experimental Study of Thermal Contact Resistance of Metallic Interfaces*. 1971.

[262] I. Sfikas, J. Ingham, and J. Baber, « Using finite-element analysis to assess the thermal behaviour of concrete structures », *Concrete (London)*, pp. 50–52, Feb. 2017.

[263] B. Klemczak, M. Batog, M. Pilch, and A. Żmij, « Analysis of Cracking Risk in Early Age Mass Concrete with Different Aggregate Types », en, *Procedia Engineering*, International Conference on Analytical Models and New Concepts in Concrete and Masonry Structures, vol. 193, pp. 234–241, Jan. 2017, ISSN: 1877-7058. DOI: 10.1016/j.proeng.2017.06.209.

[264] J. Liu, Y. Liu, N. Zhang, Z. Ma, and Y. Bai, « Research on temperature action and cracking risk of steel–concrete composite girder during the hydration process », en, *Archives of Civil and Mechanical Engineering*, vol. 20, *2*, p. 47, Jun. 2020, ISSN: 1644-9665. DOI: 10.1007/s43452-020-00050-0.

[265] R. I. Gilbert, « Cracking Caused by Early-age Deformation of Concrete – Prediction and Control », en, *Procedia Engineering*, Modern Building Materials, Structures and Techniques, vol. 172, pp. 13–22, Jan. 2017, ISSN: 1877-7058. DOI: 10.1016/j.proeng.2017.02.012.

[266] P. K. Mehta and P. J. M. Monteiro, *Concrete: microstructure, properties, and materials*, en, 3rd ed. New York: McGraw-Hill, 2006, ISBN: 978-0-07-146289-1.

[267] P. Mounanga, « Étude expérimentale du comportement de pâtes de ciment au très jeune âge : hydratation, retraits, propriétés thermophysiques », fr-FR, Ph.D. dissertation, Université de Nantes, Saint Nazaire, 2004.

[268] F. Adenot and M. Buil, « Modelling of the corrosion of the cement paste by deionized water », en, *Cement and Concrete Research*, Special Double Issue Proceedings of Symposium D of the E-MRS Fall Meeting 1991, vol. 22, *2*, pp. 489–496, Mar. 1992, ISSN: 0008-8846. DOI: 10.1016/0008-8846(92)90092-A.

[269] M. Mainguy, C. Tognazzi, J.-M. Torrenti, and F. Adenot, « Modelling of leaching in pure cement paste and mortar », en, *Cement and Concrete Research*, vol. 30, *1*, pp. 83–90, Jan. 2000, ISSN: 0008-8846. DOI: 10.1016/S0008-8846(99)00208-2.

[270] C. Le Bellégo, B. Gérard, and G. Pijaudier-Cabot, « Chemo-Mechanical Effects in Mortar Beams Subjected to Water Hydrolysis », *Journal of Engineering Mechanics - ASCE*, vol. 126, *3*, pp. 266–272, 2000, Publisher: American Society of Civil Engineers. DOI: 10.1061/(ASCE)0733-9399(2000)126:3(266).

[271] T. Honorio, B. Bary, and F. Benboudjema, « Thermal properties of cement-based materials: Multiscale estimations at early-age », en, *Cement and Concrete Composites*, vol. 87, pp. 205–219, Mar. 2018, ISSN: 09589465. DOI: 10.1016/j.cemconcomp.2018.01.003.

[272] M. J. Abdolhosseini Qomi, F.-J. Ulm, and R. J.-M. Pellenq, « Physical Origins of Thermal Properties of Cement Paste », en, *Physical Review Applied*, vol. 3, *6*, p. 064 010, Jun. 2015, ISSN: 2331-7019. DOI: 10.1103/PhysRevApplied.3.064010.

[273] J. Liu, S. Xu, and Q. Zeng, « A multi-scale micromechanical investigation on thermal conductivity of cement-based composites », en, *IOP Conference Series: Materials Science and Engineering*, vol. 167, p. 012 069, Jan. 2017, ISSN: 1757-8981, 1757-899X. DOI: 10.1088/1757-899X/167/1/012069.

[274] W. Suthabanditpong, C. Takai, H. Razavi-Khosroshahi, Y. Okada, M. El-Salmawy, and M. Fuji, « Influence of CaCO3 pore-forming agent on porosity and thermal conductivity of cellulose acetate materials prepared by non-solvent induced phase separation », en, *Advanced Powder Technology*, vol. 30, *1*, pp. 207–213, Jan. 2019, ISSN: 09218831. DOI: 10.1016/j.apt.2018.10.024.

[275] S. Mohaine, « Etude des propriétés thermiques et mécaniques des bétons isolants structurels incorporant des cénosphères », Ph.D. dissertation, Oct. 2018.

[276] A. O. Mydin, « MODELING OF TRANSIENT HEAT TRANSFER IN FOAMED CONCRETE SLAB », en, vol. 8, p. 18, 2013.

[277] H. S. Carslaw, *Introduction to the mathematical theory of the conduction of heat in solids*. London, 1921.

[278] M. Ranjbar-Far, J. Absi, S. Shahidi, and G. Mariaux, « Impact of the non-homogenous temperature distribution and the coatings process modeling on the thermal barrier coatings system », en, *Materials & Design*, vol. 32, *2*, pp. 728–735, Feb. 2011, ISSN: 0261-3069. DOI: 10.1016/j.matdes.2010.07.034.

[279] M. Ranjbar-far, J. Absi, G. Mariaux, and D. S. Smith, « Crack propagation modeling on the interfaces of thermal barrier coating system with different thickness of the oxide layer and different interface morphologies », en, *Materials & Design*, vol. 32, *10*, pp. 4961–4969, Dec. 2011, ISSN: 0261-3069. DOI: 10.1016/j.matdes.2011.05.039.

[280] M. Ranjbar-Far, J. Absi, G. Mariaux, and F. Dubois, « Simulation of the effect of material properties and interface roughness on the stress distribution in thermal barrier coatings using finite element method », en, *Materials & Design*, vol. 31, *2*, pp. 772–781, Feb. 2010, ISSN: 02613069. DOI: 10.1016/j.matdes.2009.08.005.

[281] F. d. Larrard, *Concrete mixture proportioning: a scientific approach*, en, 1. publ, ser. Modern concrete technology series 9. London: E & FN Spon, 1999, ISBN: 978-0-419-23500-2.

[282] A. Nadeem, S. A. Memon, and T. Y. Lo, « Qualitative and quantitative analysis and identification of flaws in the microstructure of fly ash and metakaolin blended high performance concrete after exposure to elevated temperatures », en, *Construction and Building Materials*, 25th Anniversary Session for ACI 228 - Building on the Past for the Future of NDT of Concrete, vol. 38, pp. 731–741, Jan. 2013, ISSN: 0950-0618. DOI: 10.1016/j.conbuildmat.2012.09.062.

[283] W. Dridi, « ANALYTICAL MODELLING OF THE COUPLING BETWEEN MICROSTRUCTURE AND EFFECTIVE DIFFUSIVITY OF CEMENT BASED MATERIALS », en, p. 9, 2008.

[284] L. Buffo-Lacarriére, « Prévision et évaluation de la fissuration précoce des ouvrages en béton », Ph.D. dissertation, INSA Toulouse, Oct. 2007.

[285] C. Cristofari, G. Notton, and A. Louche, « Study of the thermal behaviour of a production unit of concrete structural components », en, *Applied Thermal Engineer-*

ing, vol. 24, *7*, pp. 1087–1101, May 2004, ISSN: 1359-4311. DOI: 10.1016/S1359-4311(03)00161-3.

[286] *ABAQUS User Subroutines Reference Manual (v6.6)*. [Online]. Available: https://classes.engineering.wustl.edu/2009/spring/mase5513/abaqus/docs/v6.6/books/sub/default.htm?startat=ch01s01asb12.html#sub-rtn-uhetval.

[287] W. D. Callister, *Materials Science and Engineering*, en. New York: Wiley, 2019, OCLC: 1083469263, ISBN: 978-1-119-40543-6.

[288] *CEB-FIP Model Code 1990: Design Code*, en. fib Fédération internationale du béton, Jan. 1993, ISBN: 978-0-7277-1696-5.

[289] *Fib Model Code for Concrete Structures 2010*, en. Ernst & Sohn, a Wiley brand, 2013, ISBN: 978-3-433-60421-2.

[290] J. Lubliner, J. Oliver, S. Oller, and E. Oñate, « A plastic-damage model for concrete », en, *International Journal of Solids and Structures*, vol. 25, *3*, pp. 299–326, 1989, ISSN: 00207683. DOI: 10.1016/0020-7683(89)90050-4.

[291] H. Le Minh, S. Khatir, M. Abdel Wahab, and T. Cuong-Le, « A concrete damage plasticity model for predicting the effects of compressive high-strength concrete under static and dynamic loads », en, *Journal of Building Engineering*, vol. 44, p. 103 239, Dec. 2021, ISSN: 23527102. DOI: 10.1016/j.jobe.2021.103239.

[292] *Abaqus Analysis User's Guide (6.14)*. [Online]. Available: http://130.149.89.49:2080/v6.14/books/usb/default.htm?startat=pt05ch23s06abm39.html.

[293] G. Abada, F. Bernard, S. Lim, and M. Tehami, « Simulations of push-out tests: influence of several parameters and structural arrangements », en, *Proceedings of the Institution of Civil Engineers - Structures and Buildings*, vol. 172, *5*, pp. 340–357, May 2019, ISSN: 0965-0911, 1751-7702. DOI: 10.1680/jstbu.17.00109.

DOCTORAT BRETAGNE LOIRE / SCIENCES POUR L'INGENIEUR

INSA RENNES

Titre : Modélisation multi-échelle des propriétés thermiques des matériaux cimentaires

Mot clés : modélisation multi-échelle, transfert thermique, conductivité thermique, chaleur spécifique, coefficient dilatation, take-and-place, matériaux cimentaire

Résumé : Ce travail porte sur la modélisation multi-échelle des propriétés thermiques des matériaux cimentaires, prenant explicitement en compte leurs hétérogénéités aux différentes échelles telles que la microscopique (pâte de ciment) et la sous-méso-échelle (mortier). Des logiciels tels que **CEMHYD3D**, **Abaqus FEA** et des algorithmes Take-and-place sont utilisés pour générer et simuler le transfert thermique. Les propriétés obtenues à une échelle sont considérées comme données d'entrée à l'échelle immédiatement supérieure. La conductivité thermique est tout d'abord calculée par le biais de simulations Eléments Finis sur maillage hétérogène. L'influence de la conductance de contact (**TCC**) à l'interface matrice-granulat sur la conductivité thermique a été quantifiée. Une démarche originale, mêlant calculs Eléments Finis et comparaison avec un profil de température théorique de l'équation de la chaleur, a ensuite permis de calculer la chaleur spécifique de la pâte de ciment et du mortier. Les coefficients de dilatation ont été calculés par modélisations thermo-mécaniques séquentielles et couplées. Ce travail a ensuite été appliqué, d'abord au calcul de l'évolution de la conductivité thermique du mortier ayant subi des tests mécaniques de traction et de compression, et l'évolution des températures au sein d'un massif en béton.

Title: Multi-scale modeling of thermal properties of cement-based materials

Keywords: Multi-scale modeling, heat transfer, thermal conductivity, specific heat, coefficient of thermal expansion, take-and-place, cement-based materials

Abstract: This work focuses on the multi-scale modeling of the thermal properties of cement-based materials, explicitly taking into account their heterogeneities at the different scales such as microscale (cement paste) and sub-mesoscale (mortar). Software such as **CEMHYD3D**, **Abaqus FEA**, and Take-and-place algorithms are used to generate and simulate heat transfer simulation. The properties obtained at one scale are considered input data at the following higher scale. The thermal conductivity is first calculated through Finite Element simulations of heat transfer on a heterogeneous mesh. The influence of Thermal Contact Conductance (**TCC**) at the matrix-aggregate interface on thermal conductivity has been quantified. An original approach, comparing the temperature profile from Finite Element Analysis and heat transfer equation, has made it possible to calculate the specific heat of cement paste and mortar. The coefficients of thermal expansion are calculated by means of sequential and fully coupled thermo-mechanical modellings. After the thermal properties calculation, the results were then applied, first to calculate the evolution of the thermal conductivity of the mortar having undergone mechanical stresses such as traction and compression, and temperature evolution within a concrete block.